

Energy dissipation in fiber-polymer composites adhesive joints under cyclic loading

Présentée le 1^{er} décembre 2023

Faculté de l'environnement naturel, architectural et construit
Laboratoire de construction en composites
Programme doctoral en génie civil et environnement

pour l'obtention du grade de Docteur ès Sciences

par

Ghazaleh ESLAMI

Acceptée sur proposition du jury

Prof. E. Brühwiler, président du jury
Prof. T. Keller, Dr A. Movahedirad, directeurs de thèse
Prof. Y. Bai, rapporteur
Prof. R. D. Adams, rapporteur
Prof. V. Michaud, rapporteuse

Endurance is not just the ability to bear a hard thing,
but to turn it into glory.
— William Barclay



To my father, Ebrahim, for being my role model;
To my mother, Heshmat, for her infinite support and guidance;
To my husband, Arash, for his boundless love;
To my sisters, Fatemeh, and Sara for their endless kindness.

Preface

Composite materials often exhibit an undesired brittle failure behavior, particularly in fiber-dominated response cases. Lacking ductility on the material level can however be compensated on the structural system level - for instance, by combining brittle composite members with ductile adhesive joints. Since this type of ductility is not related to yielding, as in case of steel, but to progressive damage and viscoelastic energy dissipation, the term “pseudo-ductility” is used in this work.

Due to the viscoelastic nature of adhesives, their possible pseudo-ductility depends on the material state, temperature and strain rate. Elastomer thermoset adhesives, as used in this work, can exhibit pseudo-ductility at ambient temperature and moderate strain rates, as it has already been demonstrated in previous works at CCLab, on linear lap joints. In that type of joint, the strain rate is constant along the joint overlap. One of the novelties in this work is the investigation of angle joints, as used in frame structures. The angle joints are hybrid, i.e., they have a central bolt to ensure joint integrity, and the angle bending moment is transmitted by torsion in the adhesive layers. This torsion causes a radial strain rate distribution which is not constant anymore and thus complicates the analysis compared to linear lap joints.

In addition to quasi-static loading conditions, cyclic conditions are also investigated for linear lap joints, to study the possible pseudo-ductility and energy dissipation capacity in cases of seismic loading.

I would like to thank Fiberline, Denmark, and Sika, Switzerland, for their continuous support of our research.

Lausanne, July 2023

Prof. Dr. Thomas Keller

Acknowledgements

This doctoral thesis signifies the culmination of four exhilarating years of rigorous but rewarding endeavors at CCLab. It has offered an opportunity for both immense professional growth and personal enrichment. Along this complex yet gratifying journey, I have been blessed to cross paths with a host of remarkable individuals whose unwavering encouragement and support have been instrumental in reaching this pivotal stage.

A river of gratitude flows to my esteemed supervisor, Prof. Thomas Keller, whose faith in my abilities allowed me to become a Ph.D. student at EPFL and ignited the spark that fueled my academic quest. Your sagacious guidance, relentless support, and professionalism have not only enhanced my analytical acumen and communication skills but also instilled a sense of integrity that I will carry with me. Standing shoulder to shoulder with me through the ebbs and flows of this journey, my co-supervisor and friend, Dr. Abdolvahid Movahedirad, has been a compass, guiding me safely through my academic journey.

In the realm of academic enlightenment, I am profoundly grateful for the wisdom of my thesis defense committee: Prof. Robert Adams (Bristol, England), Prof. Yu Bai (Monash, Australia), Prof. Véronique Michaud (LPAC, EPFL, Switzerland), and Prof. Eugen Brühwiler (MCS, EPFL, Switzerland), the president of the jury. Their insightful scrutiny and invaluable feedback have sharpened my perspectives, challenging me to reach new intellectual heights.

My deep respect goes to Prof. Anastasios Vassilopoulos, whose enriching dialogues, insightful mentorship, and dedication to improving our communication with laboratory technicians have been priceless. Dr. Sonia Yanes Armas, you are the cornerstone of my initial years at CCLab. Our collaboration, your mentorship, and your unwavering friendship have been the source of both inspiration and comfort. Dr. Julia de Castro, our enlightening conversations and the opportunity to contribute to your courses have kindled a joy of teaching in me that I will forever cherish.

Acknowledgements

To Saira, the diligent engine of CCLab, your tireless administrative work and efforts are the wheels that keep us all moving forward. My sincerest appreciation to Sylvain and Gilles, the resilient pillars of EPFL's Structural Engineering Laboratory. Their constant support and wise guidance have been instrumental in my experimental endeavors. Gilles, thanks to you for your valuable and essential assistance in laboratory management and installing the experimental set-ups and performing and monitoring the experiments. I will always remember your commitment during all the many hours we spent working together in the laboratory. I would like to acknowledge Fredrique, for your incredibly meticulous, precise and high-quality work regarding the preparation of my specimens and the fabrication of the fixtures. Thank you also for being always proactive and respectful regarding my sometimes tight deadlines and for always keeping a kind smile on your face. I owe a world of gratitude to Armin, Serge, Luca, Gerald, and François, the extraordinary technicians who were always there whenever I needed their help with my experiments.

The soul of CCLab has been the friendships formed within its walls. Niloufar, my kind and steadfast friend, your positive attitude was the ray of hope in times of uncertainty. Aida, your spirit dances in my memory even after graduation and relocation to Geneva. Your continuous motivation and encouragement heightened my aims. To Lulu, my energetic colleague, and Congzhe and Shayan, my fellow academic companions, your presence has enriched my journey. Tara, our friendship that took root in our master's university in Iran has blossomed in the halls of CCLab. Dharun, your lively spirit breathes life into CCLab, infusing it with vibrancy.

To my officemates: Lingfeng, Yunton, Shengchen, and Mateus, who recently embraced fatherhood, sharing space with you has brought moments of joy, companionship, and scientific discussions. And the indomitable spirit of CCLabians: Gisele, Ting, Geovane, Guangjian, Yun, Changyuan, Aloys, and the forever radiant Viviana, have imprinted my heart with unforgettable moments and shared discoveries.

Beyond academia, I found a constellation of friendships that provided a shining array of unforgettable memories and unwavering support. Maryam, Niloufar and Amir, Solmaz and Mahdi, Sahar and Hamed, Tahereh and Farshad, Saya and Haris; you have become my best friends, illuminating my path with warmth and companionship.

In the quiet corners of my heart, my love for my husband, Arash, reverberates with a resonance that words can scarcely capture. His faith in me a reflection that reveals the vast potential within my soul. With his loving encouragement, he pushes not just me, but us, to ascend together, hand-in-hand. His influence fuels a shared dream, an

Acknowledgements

ambition that is not just about excelling in our individual paths, but growing together, fostering a synergistic dance that intertwines our destinies. His love is a solace that eases all worries, a force that binds me to him with a love so profound, so enduring, it transcends the boundaries of the spoken word.

A heartfelt embrace of gratitude to my sisters, Fatemeh and Sara, who have generously offered me their ears, words of encouragement, and a reservoir of hope. My sweet niece and nephews, Bardia, Ghazal, Arshia, and Ashkan, who brought countless smiles and sparkled my life with youthful joy.

And at the very core of my existence, my parents. My father, Zibarou, you are my rock, my pillar of strength, and the personification of resilience and hard work. Your life is a masterclass in perseverance, and I strive to live by your example. My beloved mother, Zendegim, you are so much more than just a parent to me. You are my guiding lighthouse, reliable in the tumultuous sea of life, leading me safe through the darkest nights. You are my wellspring of energy, infinite and constant, inspiring me to reach for the stars. Your tranquil spirit and masterful management have served as my greatest lessons, teaching me not just to endure the challenges life throws my way, but to rise above them, stronger and wiser. Your influence is woven into the fabric of who I am, and for that, I am eternally grateful.

Finally, the moment when my friends, colleagues, and loved ones gathered under the Swiss sky in Vevey, at my wedding, is a memory forever etched in the canvas of my heart. To each soul mentioned and those silently acknowledged, your support, guidance, and friendship have shaped this journey in more ways than words can capture.

From the bottom of my heart, thank you.

Lausanne, July 2023

G. Eslami

Abstract

Sustainable development has emerged as a paramount consideration in various fields of industry, including construction, to preserve the environment and its finite resources. Lightweight structures, such as fiber-polymer composite structures, address both sustainability and earthquake resistance concerns. Despite their reduced weight, which lowers seismic input energy, the inherent brittleness of composite structures limits their energy dissipation capacity. This challenge can be addressed through implementing pseudo-ductility by using pseudo-ductile adhesives, through which energy dissipation in beam-column connections is enhanced by enabling a nonlinear structural response due to progressive damage. The capability of pseudo-ductile adhesives to dissipate inelastic energy through mechanisms such as viscoelastic friction, plasticity, or damage substantiates them as a potential solution to the concerns on seismic performance of composite structures' connections.

The performance of pseudo-ductile adhesive and bolted double-lap joints composed of pultruded glass composite profiles were experimentally investigated and compared. The effects of applied displacement rates on the behavior of the pseudo-ductile adhesive and configurations of bolted joints were studied through monotonic and cyclic experiments. The adhesive joints showed significantly higher energy dissipation than bolted joints at lower displacement rates while maintaining similar or greater strength under monotonic loading.

A phenomenological model comprised of two parallel Maxwell units, one conventional-linear, and one extended-nonlinear, was developed. The model captured effectively pre- and post-yield monotonic and cyclic responses of pseudo-ductile adhesive double lap joints under various displacement rates. The developed phenomenological model's advantage over other constitutive models lies in its fewer parameters and computational efficiency.

Seismic forces might induce variable strain rates in the form of torsional moments in the joint area. Therefore, a novel angle joint configuration was designed, with a bolt

Abstract

positioned at the geometric centroid of the joint area that permitted relative rotation while restricting relative displacements, leading to pure torsion in the adhesive layer. The angle joints were then subjected to various rates of monotonic displacement-controlled loadings. It was observed that with an increase in the range of strain rates, the ultimate strength of the experimented angle joints increased while their energy dissipation capacity and failure rotation decreased. An analytical model was introduced to predict the torsional behavior of pseudo-ductile adhesive joints using a bilinear material behavior. The analytical model effectively predicted angle joints' torsional behavior.

In conclusion, this thesis provides insight into the mechanical behavior of a pseudo-ductile adhesive in composite joints and their energy dissipation capacity. The developed phenomenological model can serve as a useful tool for future engineers and researchers to design and analyze adhesively bonded composite joints, taking into consideration the complex and highly nonlinear cyclic behavior of the pseudo-ductile adhesive. Furthermore, the novel angle joint configuration designed in this study contributes to a better understanding of the effects of variable strain rates on the behavior of pseudo-ductile adhesive joints, expanding the scope of potential applications and enhancing the seismic performance of composite structures.

Keywords: *Pseudo-ductile adhesive joint, glass composite double-lap joints, rate-dependent behavior, variable strain rate, angle joint, torsion-rotation capacity, energy dissipation capacity, cyclic behavior.*

Résumé

Le développement durable est apparu comme une considération primordiale dans divers domaines de l'industrie, y compris la construction, afin de préserver l'environnement et ses ressources finies. Les structures légères, telles que les structures composites en fibres-polymères, répondent à la fois aux préoccupations de durabilité et de résistance aux séismes. Malgré leur poids réduit, qui diminue l'énergie sismique entrante, la fragilité inhérente des structures composites limite leur capacité à dissiper l'énergie. Ce défi peut être relevé en mettant en œuvre une pseudo-ductilité à l'aide d'adhésifs pseudo-ductiles, grâce auxquels la dissipation d'énergie dans les connexions poutre-colonne est améliorée en permettant une réponse structurelle non linéaire due à des dommages progressifs. La capacité des adhésifs pseudo-ductiles à dissiper l'énergie inélastique par des mécanismes tels que le frottement viscoélastique, la plasticité ou les dommages les consolide comme une solution potentielle aux préoccupations sur la performance sismique des connexions de structures composites. Les performances des joints adhésifs pseudo-ductiles et des joints double boulonnés composés de profils composites en verre pultrudés ont été expérimentalement étudiées et comparées. Les effets des taux de déplacement appliqués sur le comportement de l'adhésif pseudo-ductile et des configurations des joints boulonnés ont été étudiés à travers des expériences monotones et cycliques. Les joints adhésifs ont montré une dissipation d'énergie nettement supérieure aux joints boulonnés à des taux de déplacement plus faibles tout en conservant une force similaire ou supérieure sous charge monotone.

Un modèle phénoménologique composé de deux unités Maxwell parallèles, l'une conventionnelle-linéaire, et l'autre étendue-non linéaire, a été développé. Le modèle a efficacement capturé les réponses monotones et cycliques pré et post-rendement des joints adhésifs double boulon pseudo-ductiles sous divers taux de déplacement. L'avantage du modèle phénoménologique développé sur les autres modèles constitutifs réside dans ses paramètres plus restreints et son efficacité computationnelle.

Résumé

Les forces sismiques pourraient induire des taux de déformation variables sous forme de moments de torsion dans la zone de joint. Par conséquent, une nouvelle configuration de joint d'angle a été conçue, avec un boulon positionné au centroïde géométrique de la zone de joint qui permettait une rotation relative tout en restreignant les déplacements relatifs, conduisant à une torsion pure dans la couche adhésive. Les joints d'angle ont ensuite été soumis à divers taux de charges contrôlés par déplacement monotone. Il a été observé qu'avec une augmentation de la plage des taux de déformation, la résistance ultime des joints d'angle expérimentés augmentait tandis que leur capacité de dissipation d'énergie et leur rotation de rupture diminuaient. Un modèle analytique a été introduit pour prédire le comportement de torsion des joints adhésifs pseudo-ductiles en utilisant un comportement de matériau bilinéaire. Le modèle analytique a efficacement prédit le comportement de torsion des joints d'angle.

En conclusion, cette thèse offre un aperçu du comportement mécanique d'un adhésif pseudo-ductile dans les joints composites et leur capacité à dissiper l'énergie. Le modèle phénoménologique développé peut servir d'outil utile pour les futurs ingénieurs et chercheurs afin de concevoir et d'analyser les joints composites collés, en prenant en compte le comportement cyclique complexe et hautement non linéaire de l'adhésif pseudo-ductile. De plus, la nouvelle configuration de joint d'angle conçue dans cette étude contribue à une meilleure compréhension des effets des taux de déformation variables sur le comportement des joints adhésifs pseudo-ductiles, élargissant ainsi le champ des applications potentielles et améliorant la performance sismique des structures composites.

Mots clés : *Joint adhésif pseudo-ductile, joints à double lamelle en composite de verre, comportement dépendant de la vitesse, taux de déformation variable, joint angulaire, capacité de torsion-rotation, capacité de dissipation d'énergie, comportement cyclique.*

Abstract (Persian)

توسعه پایدار به عنوان یک اصل مهم در بسیاری از حوزه‌های صنعتی، از جمله ساخت و ساز، به منظور حفاظت از محیط زیست و منابع محدود آن، مورد توجه است. سازه‌های سبک، همچون سازه‌های کامپوزیت پلیمری-الیافی، به صورت همزمان به اهداف توسعه پایدار و مقاومت در برابر زلزله کمک می‌کنند. علیرغم وزن کمتر سازه‌های سبک که سبب کاهش انرژی ورودی زلزله می‌شود، شکنندگی ذاتی این نوع سازه‌ها قدرت جذب انرژی آنها را محدود می‌کند. این چالش با استفاده از چسب‌های شبه-انعطاف پذیر که با شکست تدریجی سبب افزایش ظرفیت جذب انرژی از طریق ایجاد پاسخ غیر خطی در سازه می‌شوند، می‌تواند پاسخ داده شود. قابلیت جذب انرژی غیر الاستیک این چسب‌ها از طریق مکانیزم‌هایی مانند اصطکاک ویسکوالاستیک، پلاستیسیته، یا شکست، آن‌ها را به گزینه‌ای مناسب برای حل مساله عملکرد لرزه ای اتصالات در سازه‌های کامپوزیتی تبدیل می‌کند.

در این تحقیق، عملکرد اتصالات شبه-انعطاف پذیر چسبی و پیچی که از پروفیل‌های کامپوزیتی با الیاف شیشه ساخته شده بودند، مورد آزمایش و مقایسه قرار گرفت. تأثیر سرعت اعمال جابجایی بر رفتار اتصالات چسبی شبه-انعطاف پذیر و تأثیر آرایش پیچ‌ها بر رفتار اتصالات پیچی با استفاده از آزمایش‌های مونوتونیک و چرخه‌ای مورد بررسی قرار گرفتند. در آزمایش‌های چرخه ای با نرخ جابجایی کمتر، اتصالات چسبی قابلیت جذب انرژی بسیار بیشتری نسبت به اتصالات پیچی نشان دادند، در حالی که در آزمایشات مونوتونیک، این اتصالات مقاومت مشابه یا حتی بیش تری نسبت به اتصالات پیچی داشتند.

یک مدل رفتاری شامل دو المان ماکسول به صورت موازی، یکی خطی و دیگری غیر خطی، توسعه یافت. این مدل قادر به شبیه‌سازی پاسخ اتصالات چسبی در هر دو نوع بارگذاری مونوتونیک و چرخه‌ای قبل و بعد از نقطه تسلیم در نرخ‌های جابجایی مختلف است. ویژگی متمایز کننده این مدل رفتاری نسبت به دیگر مدل‌های موجود، تعداد کمتر پارامترهای آن و کارایی محاسباتی بالای آن است.

نیروهای لرزه ای ممکن است باعث ایجاد نرخ‌های جابجایی متغیر در ناحیه اتصال به صورت لنگر پیچشی شوند. بنابراین، یک پیکربندی جدید از اتصال چسبی طراحی شد که با داشتن زاویه عمود و یک پیچ در مرکز هندسی ناحیه اتصال، امکان چرخش نسبی را فراهم می‌کند در حالی که جابجایی‌های نسبی را محدود می‌کند. این طراحی به چرخش خالص در لایه چسبی اتصال انجامید. سپس، اتصالات زاویه دار تحت نرخ‌های مختلف جابجایی به صورت مونوتونیک مورد بررسی قرار گرفتند. مشاهدات نشان داد که با افزایش دامنه نرخ‌های جابجایی ایجاد شده در ناحیه اتصال، مقاومت نهایی اتصال افزایش می‌یابد، در حالی که ظرفیت جذب انرژی و میزان چرخش نهایی آن کاهش می‌یابند. برای پیش‌بینی رفتار پیچشی اتصالات چسبی شبه-انعطاف‌پذیر یک مدل تحلیلی با در نظر گرفتن رفتار دوخطی برای ماده چسبی معرفی شد. این مدل تحلیلی توانست رفتار پیچشی در اتصالات زاویه‌دار را به صورت موثری پیش‌بینی کرد.

به صورت کلی، این پایان‌نامه اطلاعاتی در مورد رفتار مکانیکی چسب شبه-انعطاف‌پذیر در اتصالات کامپوزیتی و ظرفیت جذب انرژی آنها ارائه می‌دهد. مدل رفتاری توسعه یافته، با توجه به رفتار چرخه‌ای پیچیده و بسیار غیر خطی چسب شبه-انعطاف‌پذیر، می‌تواند به عنوان یک ابزار مفید برای مهندسان و محققان آینده برای طراحی و تجزیه و تحلیل اتصالات کامپوزیتی چسبی استفاده شود. علاوه بر این، پیکربندی جدید اتصال زاویه‌دار که در این مطالعه طراحی شد، منجر به درک بهتری از اثرات نرخ‌های جابجایی متغیر بر رفتار اتصالات چسبی شبه-انعطاف‌پذیر می‌شود و همچنین گسترش کاربرد و بهبود عملکرد لرزه‌ای سازه‌های کامپوزیتی را میسر می‌سازد.

کلمات کلیدی: اتصالات چسبی شبه-انعطاف‌پذیر، اتصالات پروفیل‌های الیاف شیشه، رفتار وابسته به نرخ جابجایی، نرخ کرنش متغیر، اتصالات زاویه‌دار، ظرفیت پیچش-دوران، ظرفیت جذب انرژی، رفتار چرخه‌ای

Contents

Preface	i
Acknowledgements	iii
Abstract	vii
Résumé	ix
Abstract (Persian)	xi
1 Introduction	3
1.1 Context and motivation	3
1.2 Objectives	6
1.3 Methodology	7
1.4 Thesis organization	8
References	12
2 Energy dissipation in adhesive and bolted pultruded GFRP double-lap joints under cyclic loading	17
2.1 Introduction	17
2.2 Experimental set-up	19
2.2.1 Joint geometry and preparation	19
2.2.2 Materials	20
2.2.3 Adhesive joint manufacturing	21
2.2.4 Instrumentation	21
2.2.5 Experimental program	22
2.3 Experimental results	25
2.3.1 Monotonic experiments	25
2.3.1.1 Adhesive joints	25

xiii

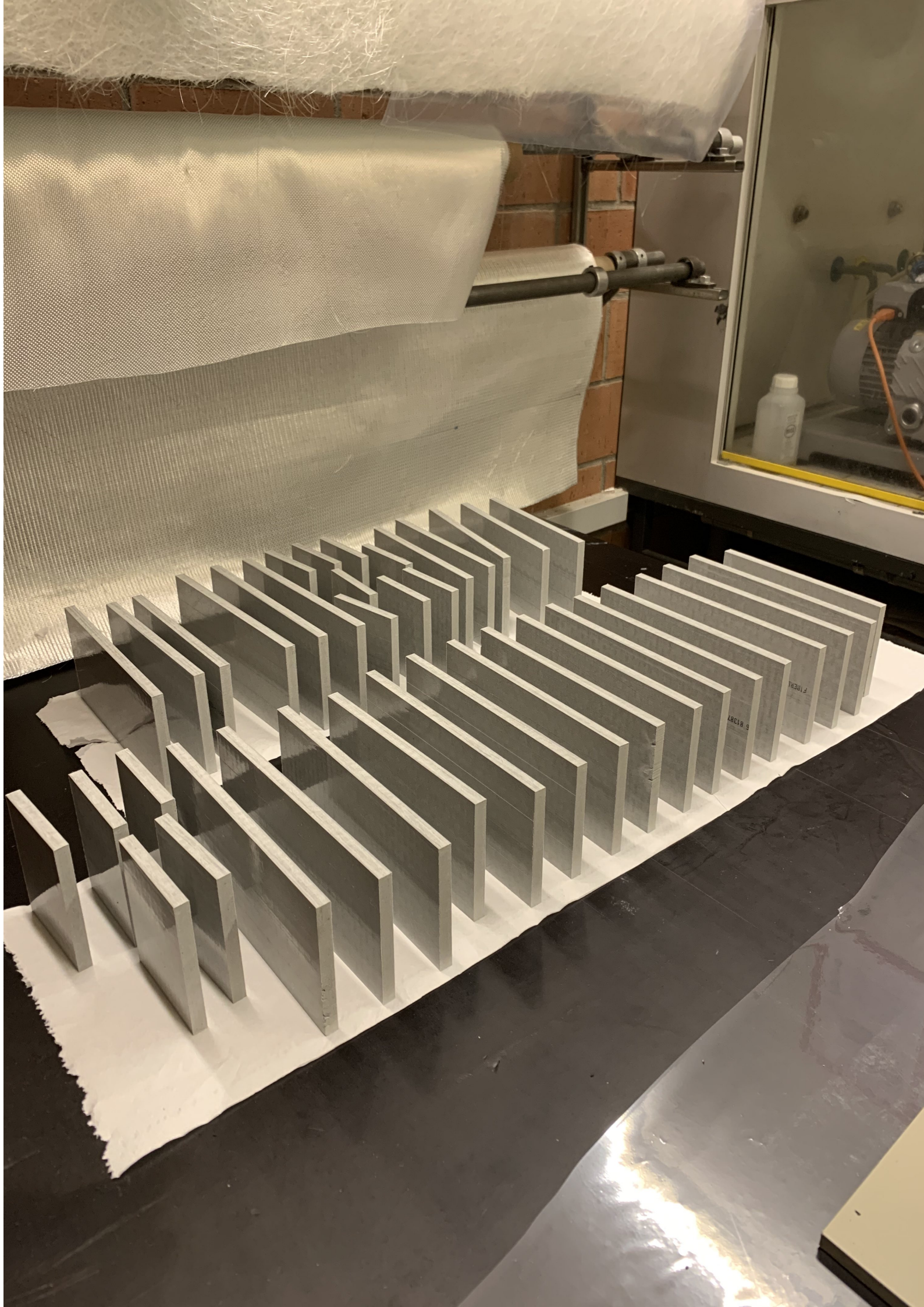
Contents

2.3.1.2	Bolted joints	26
2.3.1.3	Derivation of cyclic reference displacements	29
2.3.2	Cyclic experiments	29
2.3.2.1	Adhesive joints	29
2.3.2.2	Bolted joints	31
2.4	Discussion	34
2.4.1	Comparison of monotonic and cyclic behavior	34
2.4.2	Stiffness degradation	35
2.4.3	Energy dissipation capacity	36
2.4.3.1	Energy dissipation per cycle	36
2.4.3.2	Cumulative energy dissipation	37
2.4.3.3	Normalized energy dissipation	39
2.5	Conclusions	40
	References	42
3	Viscoelastic adhesive modeling of ductile adhesive-composite joints during cyclic loading	47
3.1	Introduction	47
3.2	Summary of experimental work	51
3.2.1	Experimental setup	51
3.2.2	Experimental results	52
3.3	General phenomenological model	53
3.3.1	Constitutive equation	55
3.3.2	Parameter optimization method	57
3.3.2.1	Nonlinear least square problem	57
3.3.2.2	Trust Region Reflective (TRF) algorithm	57
3.3.2.3	Parameter initial values	58
3.3.2.4	Parameter bounds	59
3.4	Monotonic and cyclic viscoelastic parameter results	59
3.4.1	Rate-dependent monotonic viscoelastic parameters	59
3.4.2	Rate-dependent cyclic viscoelastic parameters	61
3.4.2.1	Cycle decomposition	61
3.4.2.2	Cyclic viscoelastic parameter estimation procedure	62
3.4.2.3	Cyclic viscoelastic parameter development	63
3.4.2.4	Cyclic viscoelastic parameter constant development	66

3.5	Model validation and application	68
3.5.1	Contributions of first and second Maxwell units	68
3.5.2	Full cycle and envelope curves comparisons	69
3.5.3	Energy dissipation	70
3.6	Conclusions	70
	Appendix	72
3.A.1	General relationships	72
3.A.2	Solution for the first Maxwell unit	72
3.A.3	Solution for the second Maxwell unit	73
	References	75
4	Experimental investigation of rotational behavior of pseudo-ductile adhesive angle joints exhibiting variable strain rate	81
4.1	Introduction	81
4.2	Angle joint concept and experimental program	84
4.2.1	Angle joint experimental approach	84
4.2.2	Specimen geometry and fabrication	86
4.2.2.1	Single-lap experiments	86
4.2.2.2	Angle joint experiments	87
4.2.3	Materials	88
4.2.4	Setup, instrumentation, and experimental procedure	88
4.2.4.1	Single-lap experiments	88
4.2.4.2	Angle joint experiments	89
4.2.5	Experimental results	90
4.2.5.1	Single-lap experiments	90
4.2.5.2	Angle joint experiments	92
4.3	Analytical model	99
4.4	Discussion	103
4.4.1	Analytical model validation and discussion	103
4.4.2	Variable strain rate effect	106
4.4.3	Effect of adhesive layer thickness	107
4.4.4	Effect of the adhesive joint type on ductility	107
4.5	Conclusions	110
	References	112
5	Conclusions and future work	117

Contents

5.1	Conclusion	117
5.2	Original contributions	120
5.3	Recommendations for future work	122
5.3.1	Phenomenological model of the pseudo-ductile adhesive containing failure criteria	122
5.3.2	Time evolution, thickness, and geometry effects	122
5.3.3	Cycle amplitude effects in tension and torsion	123
5.3.4	Frame application	123
5.3.5	Exploring a predictive model using machine learning methods	124
	References	125
A	Fabrication process and experiments on linear adhesive and bolted glass composite double-lap joints	127
B	Phenomenological constitutive model development and Python program	137
C	Tensile experiments on adhesive dog-bone specimens	151
3.1	Experimental set-up	151
3.2	Experimental results	153
	References	158
D	Adhesive glass composite angle double-lap and single-lap experiments	159
	Curriculum Vitae	165



Introduction

1.1 Context and motivation

Seismic resistance in structures relies on two key factors: 1) the input energy to the structure, and 2) the capacity of the structure to absorb and dissipate the input energy [1]. Lightweight construction enhances the seismic resilience of the structures as the internal forces induced within the structural elements are directly proportional to the structure's weight. Fiber-polymer composite elements (Fig. 1.1(a)) have become increasingly popular in lightweight construction, as they offer a high strength-to-weight ratio and corrosion resistance. Glass composites also provide low thermal conductivity and the potential for translucency or transparency [2], [3].

Composites have been used in pedestrian (Fig. 1.1(b)) and highway bridge decks [4], [5] due to their cost-effectiveness [6] and aforementioned superior properties; however, their use in building construction is less widespread due to their low fire resistance. Additionally, in bridges and buildings, the composites' lack of inelastic energy dissipation capacity raises concerns for efficient earthquake-resistant design, maintaining serviceability, and global failure prevention in high seismicity areas. Although extensive research has been conducted on individual composite structural members, such as beams [7], columns [8], and roofs [9], the development of all-composite structures remains yet limited. One notable example of a nearly all-composite structure is the five-story Eyecatcher building [10], illustrated in (Fig. 1.1(c)).

Contrary to ductility in metals which indicates a nonlinear response due to yielding, pseudo-ductility designates a nonlinear response caused by progressive failure or

Chapter 1. Introduction

damage [11]. Thus, to address the challenges regarding the seismic resilience of structures composed of brittle members such as composite elements, pseudo-ductility can be introduced by either designing redundant (statically indeterminate) structural systems or using pseudo-ductile joints [12]. In the following, the pseudo-ductile term is used on all levels, such as system, joint, component, and material, including polymers if progressive damage occurs [13], [14]. Pseudo-ductility can be implemented into joints by using pseudo-ductile adhesives to dissipate inelastic energy through viscosity-related friction and damage, as it has already been shown in [15]–[17].

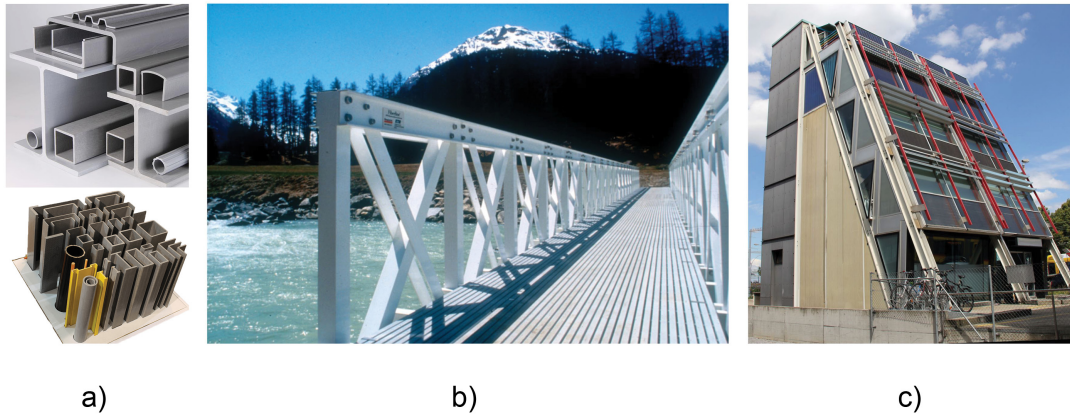


Figure 1.1: a) Composite profiles, b) Pontresina Bridge 1997, c) Eyecatcher Building 1999.

The adhesives used for structural purposes are mostly thermoset polymers and exhibit viscoelastic behavior [18], [19]. In thermoset polymers, the viscoelastic behavior results from molecular chain movements, which is both strain rate- and temperature-dependent [20]. Different applied strain rates can result in different mechanical responses in the thermoset polymer, varying from brittle to pseudo-ductile, with different yield load and post-yield behavior [21]. The thermoset molecular chain structure consists of both primary bonds (in the chains and cross-links between the chains, mainly covalent bonds) and secondary bonds (Van der Waals and hydrogen bonds). The molecular chains in lightly cross-linked thermosets, denominated elastomer thermosets, are formed in random coils and are in an amorphous state [22]. Coiled chains can uncoil and reach their yield point at a low displacement rate, as they have sufficient time. After the yield point, chains lose secondary bonds and become aligned or stretched, leading to decreased stiffness and increased deformability, possibly resulting in hardening behavior. During unloading, the stretched chains coil back, and secondary bonds are reformed [23]. Broken primary bonds contribute

to the initiation and propagation of damage and energy dissipation in viscoelastic polymers [24]. Depending on the amount of energy dissipation, the response could be either brittle (low amount of energy dissipation, at high strain rate or low temperature) or pseudo-ductile (high amount of energy dissipation, at low strain rate or high temperature). Therefore, understanding the behavior of molecular chains in the thermoset polymers and the respective amount of dissipated energy during loading and unloading is crucial for accurate analysis and design of viscoelastic materials.

Due to the high costs, lengthy durations, and impracticality of conducting a plethora of experiments under diverse conditions, constitutive models have become indispensable for designing and analyzing viscoelastic materials which require much fewer experiments for calibration purposes. One of the most common mechanical model for characterizing viscoelastic behavior involves a spring representing the elastic component with a modulus of elasticity of E and a dashpot representing the viscous component with the viscosity η [25]. Specific viscoelastic responses can be generated by integrating these elements in various arrangements. The Maxwell and Kelvin models, which involve coupling a linear spring and a dashpot in series and parallel configurations, respectively, offer the most elementary depictions of viscoelastic behavior [26]. Since 1952, the combination of a spring and a dashpot element has been employed to simulate the rate-dependent behavior of different varieties of viscoelastic materials [27]. Simplicity is a vital aspect of understanding and modeling procedures. However, to date, no model has been developed that can effectively and simply capture the cyclic behavior of rate-dependent pseudo-ductile adhesive materials.

In the realm of all-composite structures, energy dissipation can be achieved through the use of pseudo-ductile adhesive beam-column joints. Consequently, it is imperative to understand and predict their rate-dependent cyclic performance, as well as analyze their behavior under other critical conditions. Typically, connections between pultruded profile beam-columns employ a cleat plate, which can be positioned between the beam flange and the column [28], or between the beam web and the column [29], [30] (Fig. 1.2). In some cases, when a vertical load is applied to the beam within these configurations, torsional moments could be generated in the joint. If the joint is of bonded type [31], a torsional moment would be formed within the adhesive layer.

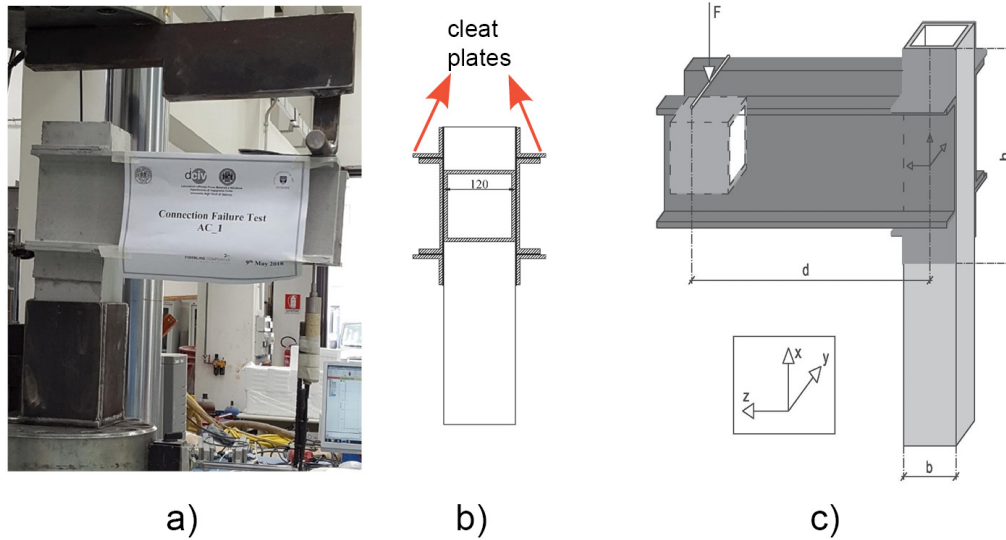


Figure 1.2: Pultruded profile channel-beam web to box-column connections using cleats a) experiment setup [30], b) schematic front view representation [30] and c) schematic 3D representation [31].

Under torsional loading, if the relative displacements are prevented, each point within the adhesive layer of the connection undergoes a distinct strain rate contingent on its distance to the center of rotation. This variability in strain rates complicates the determination of shear stress distribution and the analysis of adhesively bonded beam-column connections using conventional methods. Since the existing literature has focused on the investigation of pseudo-ductile adhesives under uniform strain rate and stress distribution across the examined joint, a more comprehensive understanding of these connections under variable strain rates is essential for practical applications and structural design.

1.2 Objectives

The primary objective of this research was to explore pseudo-ductility in pseudo-ductile adhesive glass composite connections by assessing their energy dissipation capacity in comparison to bolted connections, deriving the viscoelastic properties of a pseudo-ductile adhesive, and evaluating their performance under variable strain rates reflecting more realistic scenarios. Consequently, the following objectives have been established:

1. Experimental investigation of the monotonic tension performance of adhesive and bolted linear double-lap joints. Determination of the basis for cyclic loading pattern under different displacement rates for adhesive joints and one rate for bolted joints.
2. Experimental investigation of cyclic tension-compression performance of adhesive and bolted linear double-lap joints. Comparison of the effects of applied displacement rates and bolt configurations on the energy dissipation capacity of double-lap joints.
3. Establishment of a constitutive model for load-bearing behavior of pseudo-ductile adhesive joints to predict their cyclic performance when subjected to a given displacement rate.
4. Experimental investigation of the response of a pseudo-ductile adhesive under variable strain rates using a novel angle double-lap joint configuration, a semi-rigid joint that allows relative rotation while restricting relative displacements in the joint area.
5. Analytical investigation of nonuniform stress distribution in the pseudo-ductile adhesive layer under torsional moment by developing a rate-dependent bilinear model.

1.3 Methodology

The methodology adopted to attain the objectives of this research is as follows:

- 1.a. Design of one adhesive and two bolted linear double-lap joint configurations providing identical strength capacities under tension loading.
- 1.b. Conduct monotonic tension loading experiments at three different levels of displacement rate for adhesive joints and a single rate for bolted joints, extracting the reference displacement for cyclic loading pattern.
- 1.c. Performing cyclic tension-compression loading experiments at three different levels of displacement rate for adhesive joints and a single rate for bolted joints, comparing their energy dissipation capacities.

Chapter 1. Introduction

- 2.a. Developing a simple yet accurate constitutive model based on monotonic experimental results, accounting for the power-law rate dependency of viscoelastic parameters for the pseudo-ductile adhesive model.
- 2.b. Expanding the developed model from monotonic to cyclic experimental results, considering the loading-unloading viscoelastic behavior of the pseudo-ductile adhesive under different displacement rate levels.
- 3.a. Designing a new adhesive double-lap joint configuration, i.e., angle joint, to provide pure torsion, causing variable strain rates within the adhesive layer.
- 3.b. Conducting monotonic loading experiments at three different displacement rates, creating different ranges of strain rates across the adhesive layer.
- 4.a. Performing monotonic tension experiments on standard ductile single-lap joints under six different strain rates.
- 4.b. Developing a bilinear model with rate-dependent power-law relations.
- 4.c. Analytically analyze the pseudo-ductile adhesive behavior under variable strain rates, utilizing the developed bilinear model as a supporting framework.

1.4 Thesis organization

The research work presented in this thesis is divided into three core chapters, which address the objectives introduced in Section 1.2, and an additional chapter summarizing the conclusions of the research and future prospects. The general organization of the core chapters of the thesis is shown in Table 1.1.

A summary of the main content of each chapter is presented in the following:

- **Chapter 2:** Experimental investigation of pseudo-ductile adhesive and bolted double-lap joints was conducted under displacement-controlled monotonic tension and cyclic tension-compression, focusing on their rate-dependent performance and energy dissipation capacity in the context of seismic events. Double-lap adhesive joints by minimizing the eccentricities enable the study of shear transfer in adhesive materials while serving as a common benchmark for

comparison. The adhesive joints were subjected to different displacement rates in a monotonic tension regime, while two bolted joint configurations, single-column with two-rows and dual-column with two-rows bolts, were examined under a single displacement rate. CUREE protocol [32], which assess how ordinary seismic activity, with a 10% chance of being surpassed in 50 years, impacts the capacity of various components in lightweight structures, was used for the cyclic experiments. Following the CUREE protocol, tension-compression cyclic displacements were applied to both adhesive and bolted joint types, and their failure modes, maximum cycle numbers, stiffness degradation, and total energy dissipation were analyzed. The dissipated energy per cycle, represented by the enclosed area in the load-displacement curve, underscores the significance of adhesive joints in maintaining structural integrity and stability during seismic events. Insights gained from this investigation on the rate-dependent performance and energy dissipation capacity of pseudo-ductile adhesive joints in the context of seismic events form the foundation for the subsequent theoretical modeling in Chapter 3.

- **Chapter 3:** A phenomenological constitutive model was developed to accurately simulate the pseudo-ductile adhesive joints behavior under different displacement rates, accounting for their viscoelasticity and capturing their stiffening and softening responses. The developed constitutive model was composed of fundamental elements, spring and dashpots, and a new spring with variable constant, whose configurations and arrangements were established based on the distinct pre- and post-yield branches of the monotonic load-bearing response and experimental observations. Model parameters were calibrated using both monotonic and decomposed segments of cyclic experimental data resulting in power-law relations between the viscoelastic parameters versus either the displacement rate or maximum cycle displacement. These relations can be utilized to develop a robust predictive model for the materials under investigation. To further extend the findings from this chapter, and to investigate the behavior of pseudo-ductile beam-column joints, studying joints with a different configuration and under different loading conditions is covered in the next chapter.
- **Chapter 4:** A novel pseudo-ductile adhesive glass composite double-lap joint, termed the angle double-lap joint, has been designed to examine the adhesive

Chapter 1. Introduction

behavior under variable strain rates induced by pure torsion. This configuration features an inner laminate oriented perpendicularly to the outer laminates with a bolt at the joint area's geometric centroid, creating a semi-rigid joint that allows relative rotation but prevents in-plane displacements in the adhesive layer. The angle joint was subjected to monotonic displacement-controlled experiments with different displacement rates.

A new analytical method was developed to predict the stress distribution over the joint area and resultant torsion at each time step. Stress was calculated at each point using a bilinear model calibrated with the monotonic results of standard pseudo-ductile adhesive single-lap joints subjected to different strain rates. Finally, the experimental torsion-rotation responses of the angle joints were compared to the predictions of the newly developed analytical method.

- **Chapter 5:** The research's main conclusions are presented, and suggestions for future research are formulated.

Supplementary information to the main chapters of the thesis is provided in three appendices (see Table 1.1):

- **Appendix A:** Fabrication process and experiments on linear adhesive and bolted glass composite double-lap joints.
- **Appendix B:** Phenomenological constitutive model development and Python program.
- **Appendix C:** Tensile experiments on adhesive dog-bone specimens.
- **Appendix D:** Adhesive glass composite angle double-lap and single-lap experiments.

The results of this thesis have been consolidated into three journal articles, of which two have been published, and one has been submitted. The three papers are listed below and correspond to the three main chapters of the thesis (see Table 1.1):

1. G. Eslami, S. Yanes-Armas, T. Keller, **Energy dissipation in adhesive and bolted pultruded GFRP double-lap joints under cyclic loading**, *Compos. Struct.* 248 (2020) 112496. <https://doi.org/10.1016/j.compstruct.2020.112496>.

2. G. Eslami, A.V. Movahedi-Rad, T. Keller, **Viscoelastic adhesive modeling of ductile adhesive-composite joints during cyclic loading**, *Int. J. Adhes. Adhes.* 119 (2022) 103241. <https://doi.org/10.1016/j.ijadhadh.2022.103241>.
3. G. Eslami, A.V. Movahedi-Rad, T. Keller, **Experimental investigation of rotational behavior of pseudo-ductile adhesive angle joints exhibiting variable strain rate**, *Submitted*.

Table 1.1: Thesis core chapter organization.

Investigated lap joint	Loading condition	Methodology	Main chapter	Appendix	Paper
Bolted double-lap	Monotonic and cyclic at 0.1 mm/s	Development of experimental set-up and procedure	Chapter 2	A	1
		Experimental investigation			
Pseudo-ductile adhesive linear double-lap	Monotonic and Cyclic at 0.1, 0.5, and 1.0 mm/s	Development of experimental set-up and procedure			
		Experimental investigation			
		Development of phenomenological model	Chapter 3	B	2
Pseudo-ductile adhesive single-lap	Monotonic at 0.01, 0.05, 0.1, 0.5, 1.0, 5.0 mm/s	Experimental investigation	Chapter 4	D	3
		Development of bilinear model			
Pseudo-ductile adhesive angle double-lap	Monotonic at 0.1, 0.5, 2.0 mm/s	Development of experimental set-up and procedure			
		Experimental investigation			
		Analytical investigation based on developed bilinear model			

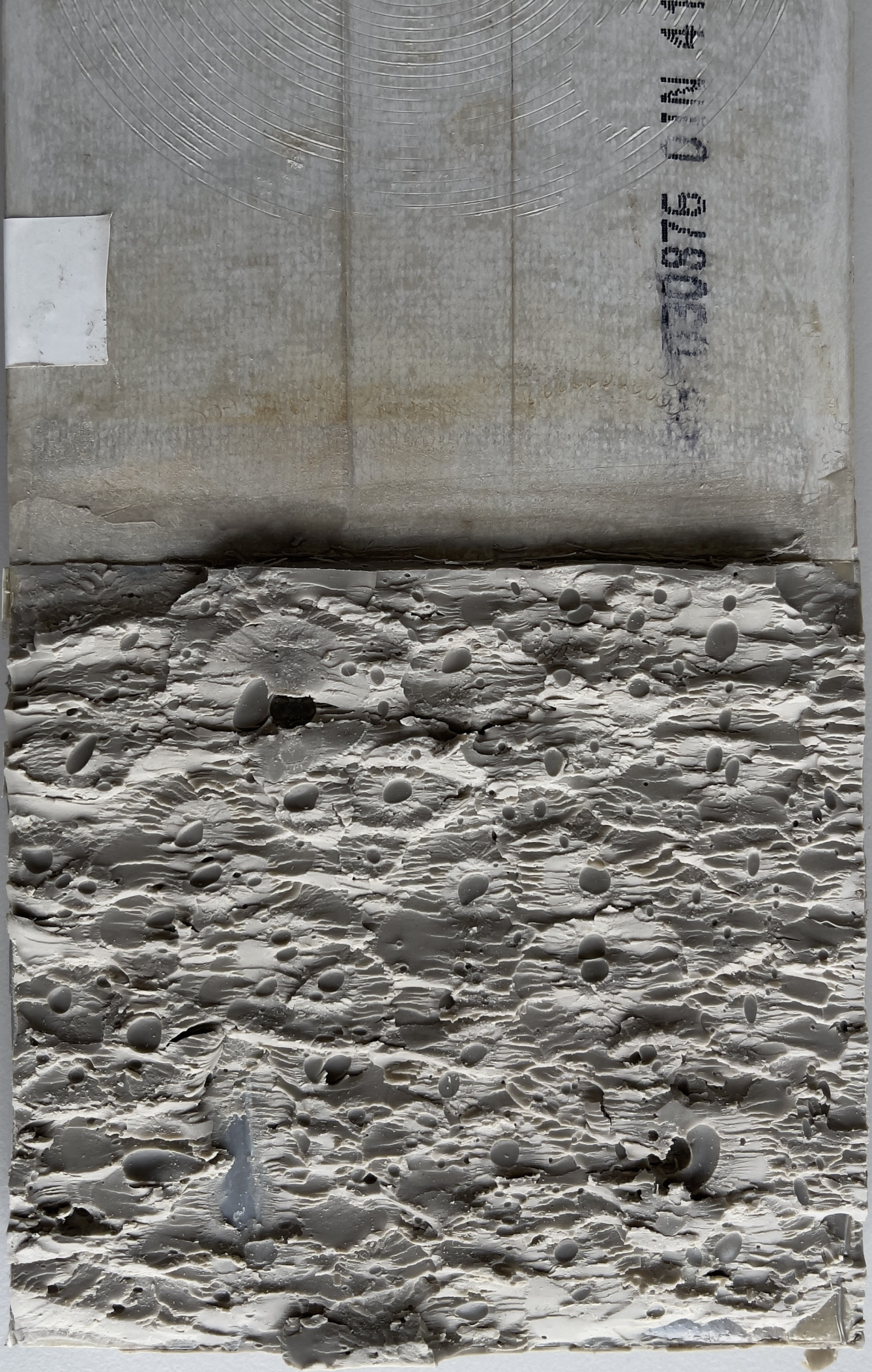
References

- [1] J. Bai, S. Jin, and H. Chen, “Method of seismic resistance design—case studies”, in *Seismic Evaluation, Damage, and Mitigation in Structures*, Elsevier, 2023, pp. 99–141.
- [2] C. E. Bakis, L. C. Bank, V. Brown, *et al.*, “Fiber-reinforced polymer composites for construction—state-of-the-art review”, *Journal of composites for construction*, vol. 6, no. 2, pp. 73–87, 2002.
- [3] T. Keller, “Recent all-composite and hybrid fibre-reinforced polymer bridges and buildings”, *Progress in Structural Engineering and Materials*, vol. 3, no. 2, pp. 132–140, 2001.
- [4] T. Keller and M. Schollmayer, “Plate bending behavior of a pultruded gfrp bridge deck system”, *Composite Structures*, vol. 64, no. 3-4, pp. 285–295, 2004.
- [5] A. Zhou and T. Keller, “Joining techniques for fiber reinforced polymer composite bridge deck systems”, *Composite Structures*, vol. 69, no. 3, pp. 336–345, 2005.
- [6] B. R. Suratno, L. Ye, and Y.-W. Mai, “Simulation of temperature and curing profiles in pultruded composite rods”, *Composites Science and Technology*, vol. 58, no. 2, pp. 191–197, 1998.
- [7] J. R. Correia, F. Branco, N. Silva, D. Camotim, and N. Silvestre, “First-order, buckling and post-buckling behaviour of gfrp pultruded beams. part 1: Experimental study”, *Computers & Structures*, vol. 89, no. 21-22, pp. 2052–2064, 2011.
- [8] G. Turvey and Y. Zhang, “A computational and experimental analysis of the buckling, postbuckling and initial failure of pultruded grp columns”, *Computers & Structures*, vol. 84, no. 22-23, pp. 1527–1537, 2006.
- [9] T. Keller, C. Haas, and T. Vallée, “Structural concept, design, and experimental verification of a glass fiber-reinforced polymer sandwich roof structure”, *Journal of composites for construction*, vol. 12, no. 4, pp. 454–468, 2008.
- [10] T. Keller, N. A. Theodorou, A. P. Vassilopoulos, and J. de Castro, “Effect of natural weathering on durability of pultruded glass fiber-reinforced bridge and building structures”, *Journal of Composites for Construction*, vol. 20, no. 1, p. 04015025, 2016. DOI: 10.1061/(ASCE)CC.1943-5614.0000589.

- [11] U. Meier, T. Triantafillou, and N. Deskovic, “Innovative design of frp combined with concrete: Short-term behaviour”, *J. Struct. Eng*, vol. 121, no. 7, pp. 1069–1078, 1995.
- [12] T. Keller and J. de Castro, “System ductility and redundancy of frp beam structures with ductile adhesive joints”, *Composites Part B: Engineering*, vol. 36, no. 8, pp. 586–596, 2005.
- [13] L. C. Bank, “Progressive failure and ductility of frp composites for construction”, *Journal of Composites for Construction*, vol. 17, no. 3, pp. 406–419, 2013.
- [14] S. Yanes-Armas, J. De Castro, and T. Keller, “Energy dissipation and recovery in web–flange junctions of pultruded gfrp decks”, *Composite Structures*, vol. 148, pp. 168–180, 2016.
- [15] J. de Castro and T. Keller, “Ductile double-lap joints from brittle gfrp laminates and ductile adhesives, part i: Experimental investigation”, *Composites Part B: Engineering*, vol. 39, no. 2, pp. 271–281, 2008.
- [16] M. Angelidi, A. P. Vassilopoulos, and T. Keller, “Ductile adhesively-bonded timber joints–part 1: Experimental investigation”, *Construction and Building Materials*, vol. 179, pp. 692–703, 2018.
- [17] L. Liu, X. Wang, Z. Wu, and T. Keller, “Tension-tension fatigue behavior of ductile adhesively-bonded frp joints”, *Composite Structures*, vol. 268, p. 113 925, 2021.
- [18] J. Lancaster, “The use of adhesives for making structural joints”, *Metallurgy of Welding*, vol. 6, pp. 54–84, 1999.
- [19] L. Hollaway, *Key issues in the use of fiber-reinforced polymer (frp) composites in the rehabilitation and retrofitting of concrete structures: Chapter 1, service life estimation and extension of civil engineering structures*, 2011.
- [20] I. M. Ward and J. Sweeney, *Mechanical properties of solid polymers*. John Wiley & Sons, 2012.
- [21] M. Angelidi, A. P. Vassilopoulos, and T. Keller, “Displacement rate and structural effects on poisson ratio of a ductile structural adhesive in tension and compression”, *International Journal of Adhesion and Adhesives*, vol. 78, pp. 13–22, 2017.

Chapter 1. Introduction

- [22] M. Leary, “Chapter 8 - material extrusion”, in *Design for Additive Manufacturing*, ser. Additive Manufacturing Materials and Technologies, M. Leary, Ed., Elsevier, 2020, pp. 223–268. DOI: <https://doi.org/10.1016/B978-0-12-816721-2.00008-7>.
- [23] D. R. Askeland, P. P. Phulé, W. J. Wright, and D. Bhattacharya, “The science and engineering of materials”, 2003.
- [24] R. A. Deblieck, D. Van Beek, K. Remerie, and I. M. Ward, “Failure mechanisms in polyolefines: The role of crazing, shear yielding and the entanglement network”, *Polymer*, vol. 52, no. 14, pp. 2979–2990, 2011.
- [25] H. F. Brinson, L. C. Brinson, *et al.*, “Polymer engineering science and viscoelasticity”, *An introduction*, pp. 99–157, 2008.
- [26] T. Alfrey and P. Doty, “The methods of specifying the properties of viscoelastic materials”, *Journal of applied physics*, vol. 16, no. 11, pp. 700–713, 1945.
- [27] F. Schwarzl and A. Staverman, “Time-temperature dependence of linear viscoelastic behavior”, *Journal of Applied Physics*, vol. 23, no. 8, pp. 838–843, 1952.
- [28] J. Mottram and Y. Zheng, “Further tests of beam-to-column connections for pultruded frames: Flange-cleated”, *Journal of Composites for Construction*, vol. 3, no. 3, pp. 108–116, 1999.
- [29] J. Qureshi, Y. Nadir, and S. K. John, “Bolted and bonded frp beam-column joints with semi-rigid end conditions”, *Composite Structures*, vol. 247, p. 112 500, 2020.
- [30] A. Razaqpur, F. Ascione, M. Lamberti, S. Spadea, and M. Malagic, “Gfrp hollow column to built-up beam adhesive connection: Mechanical behaviour under quasi-static, cyclic and fatigue loading”, *Composite Structures*, vol. 224, p. 111 069, 2019.
- [31] F. Ascione and L. Granata, “Mechanical models for predicting the strength and stiffness of a beam-to-column adhesively-bonded connection between pultruded profiles”, in *Structures*, Elsevier, vol. 43, 2022, pp. 493–507.
- [32] H. Krawinkler, F. Parisi, L. Ibarra, A. Ayoub, and R. Medina, *Development of a testing protocol for woodframe structures*. CUREe Richmond, CA, 2001, vol. 102.



Energy dissipation in adhesive and bolted pultruded GFRP double-lap joints under cyclic loading

Authors: Ghazaleh Eslami*, Sonia Yanes-Armas*, Thomas Keller*

* Composite Construction Laboratory, École Polytechnique Fédérale de Lausanne (EPFL), Switzerland

Published: *Composite Structures*, 248, art. no. 112496, Cited 9 times,

DOI: [10.1016/j.compstruct.2020.112496](https://doi.org/10.1016/j.compstruct.2020.112496)

2.1 Introduction

Fiber-reinforced polymer (FRP) composites are characterized by their high specific strength and stiffness and are thus ideally suited for lightweight construction. Their lightweight, i.e. their low mass, also provides an advantage in resisting earthquake actions since the inertial forces are reduced. However, an efficient earthquake-resistant structural design also requires a high inelastic energy dissipation capacity and in this respect, FRP composites are less appropriate due to their brittle behavior.

Possibilities for overcoming brittle material behavior do exist however, e.g. by implementing an inelastic energy dissipation capacity on the structural system level, i.e. by implementing system ductility or system pseudo-ductility (instead of material ductility) [1]. Ductility and pseudo-ductility are mainly differentiated by the formation of irreversible damage, which only occurs in the latter case. System ductility can be achieved by combining brittle and ductile members in a structure, e.g. a glass-FRP (GFRP) bridge deck with steel girders [2], where inelastic energy is dissipated by the ductile members. In a structure composed of only brittle members, pseudo-ductility can be obtained by designing redundant (statically

Contributions: *Ghazaleh Eslami conceived, designed and performed the experimental campaign under the supervision of Dr. Sonia Yanes-Armas and Prof. Thomas Keller. The analysis of the results was carried out by Ghazaleh Eslami in collaboration with Dr. Sonia Yanes-Armas and Prof. Thomas Keller.*

Chapter 2. Pseudo-ductile adhesive and bolted linear double lap joints

indeterminate) structural systems, which enable progressive failure of the brittle members and thus dissipation of inelastic energy [3].

Specific “members” that can dissipate inelastic energy through ductile or pseudo-ductile failure mechanisms are the joints between structural members. System ductility or pseudo-ductility can be achieved for instance by using flexible adhesives [1], [4]. The adhesive layer may dissipate inelastic energy through viscoelastic friction, plasticity or damage. Since such adhesives are flexible however, their behavior is strain rate-dependent and their energy dissipation capacity strongly depends on the applied strain or loading rate [4], [5]. Furthermore, bolted joints can exhibit a pseudo-ductile behavior in the case of FRP members, if bearing (crushing) failure occurs, which is activated by appropriately selecting the edge distances of the bolts and thus preventing brittle shear-out or net-tension failure mechanisms [6], [7].

Similar to FRP structures, timber and cold-formed steel (CFS) structures may behave in a brittle manner, for different reasons however. The reason in the first case is, as for FRP materials, the brittle behavior of timber. In the second case, although the material is ductile, pre-yield local buckling of the thin CFS sheets can occur and lead to a brittle failure nevertheless. To achieve system ductility in timber buildings, glued-in steel rod connections can provide a high energy dissipation capacity at each cycle after the yielding of the rods [8], [9]. In the case of CFS sections, the activation of bolt slippage prior to local buckling, in bolted connections, can significantly improve the energy dissipation capacity [10], [11].

Only a limited amount of research has been performed on the cyclic energy dissipation capacity of structures composed of FRP members. Due to the elastic-brittle behavior of FRP members, the potential energy dissipation in an FRP frame structure is mainly concentrated in its connections [12]. Studies of the cyclic performance of bonded steel sleeve connections for joining tubular GFRP beams and columns were conducted in [13], [14], in terms of their ductility and energy dissipation capacity. The joint experiments showed that excellent ductility and energy dissipation capacity could be achieved through the yielding of the steel endplates before the final connection failure. Another experimental and numerical investigation of the cyclic behavior of a novel tubular GFRP beam-to-column sleeve connection system was conducted in [15]. Several bolt configurations were studied and it was found that increasing the edge distance of the bolts leads to a significant enhancement of the hysteretic behavior of the connections. It should be noted that no previous studies were found on the energy dissipation in adhesive joints composed of FRP members and flexible adhesives, subjected to cyclic loading, and their performance comparison to bolted joints.

In this work, a series of monotonic tension and reversed cyclic loading experiments was

designed and conducted to study and compare the load-displacement behavior and the energy dissipation capacity of adhesive and bolted GFRP double-lap joints. The applied cyclic loading was considered as being able to simulate a deformation history to which light-frame buildings are likely to be subjected during earthquakes. A flexible adhesive and stainless-steel bolts were used to connect the brittle GFRP profiles. The joints were designed to have similar geometry and monotonic strength to allow the comparison of energy dissipation during cyclic loading. Further parameters of the investigation were the applied displacement rate in the case of the adhesive joints and the bolt configuration in the case of the bolted joints.

2.2 Experimental set-up

2.2.1 Joint geometry and preparation

Double-lap joints were selected to minimize the eccentricities; the joints consisted of two outer laminates of 230 mm length and 100 mm width and an inner laminate of 200 mm length and 100 mm width; all three laminates were of 10 mm thickness, see Fig. 2.1. The outer laminates thus bore only half of the load of the inner laminate. A laminate piece of 85×100×10 mm was placed between the outer laminates at the joint end where the axial displacement was applied by the machine grips; the other joint end, i.e. the inner laminate, was directly fixed in the machine. The compact joint configuration was chosen in order to prevent buckling during the compression cycles. Due to the high deformability of the adhesive, the stress distribution was nevertheless uniform along and across the joint overlaps; the local load transfer mechanism in the bolted joints was not affected by the vicinity of the machine grips either.

The overlap length of the adhesive joints was 100 mm. The adhesive thickness was selected as 5 mm, to be representative of typical applications in GFRP bridge and building construction [2], [16]. Two types of bolted joints were studied: four-bolt and two-bolt joints. The overlap length of the two-bolt joints was 100 mm and thus identical to that of the adhesive joints, while that of the four-bolt joints was 110 mm. The diameter of the bolts was 10 mm, i.e. identical to the laminate thickness, and thus fulfilling the condition in [6]; the bolt hole clearance was 1 mm. To prevent early shear-out failure, the distances between the centerlines of bolts and laminate edge (a in Fig. 2.1), and between the two rows of bolts (a'), were selected as being $3.5\times$ and $4\times$ the bolt diameter, respectively, in the four-bolt joints, according to [6]. In the two-bolt joints, the laminate length between bolts and laminate edge of the inner laminate was thus doubled from 30 to 60 mm. In the transverse direction, the edge distance was $2.5\times$ the bolt diameter in all bolted joints.

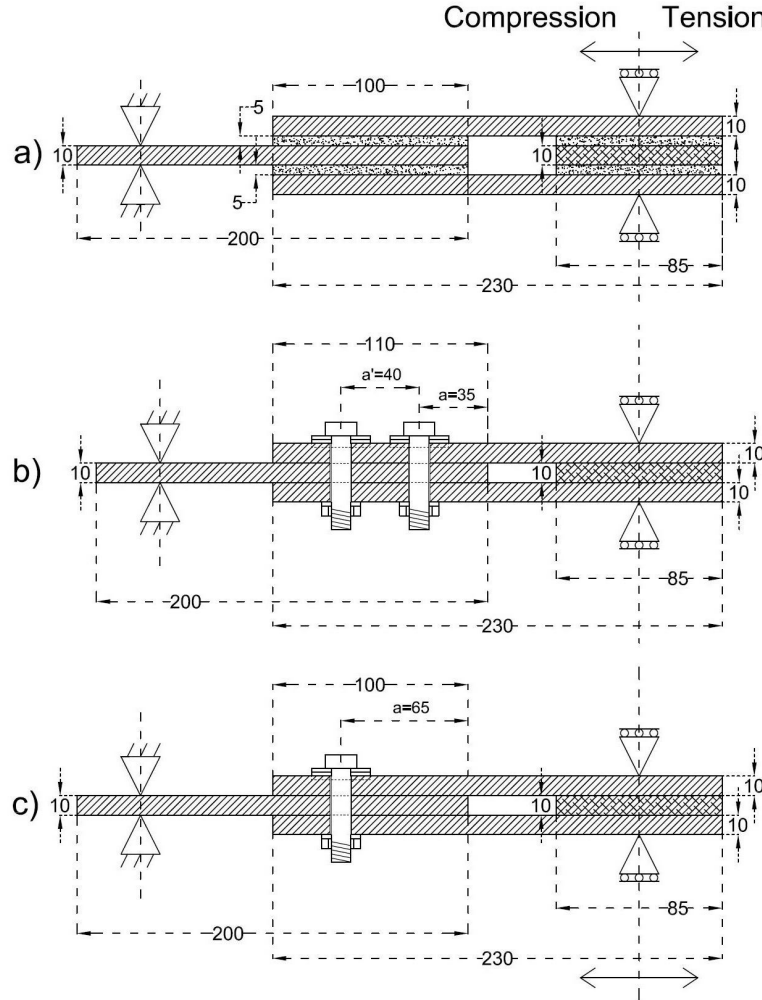


Figure 2.1: Specimen dimensions (mm) in longitudinal section of a) adhesive, b) four-bolt, c) two-bolt joint (two bolts across the width in each case).

2.2.2 Materials

The GFRP laminates were pultruded by Fiberline, Denmark. They were composed of E-glass fibers and an isophthalic polyester resin matrix with a fractional fiber weight of 60%. The laminate architecture consisted of approximately 70% unidirectional rovings in the central part and two outer combined mats. A polyester surface veil covered the outsides. The corresponding measured longitudinal elastic modulus was 33.3 ± 0.7 GPa and the tensile strength 240 MPa (manufacturer data).

The adhesive was a flexible structural two-part system based on acrylic double performance (ADP) polymer technology, SikaFast®-5221 NT, supplied by Sika, Switzerland. The two com-

ponents (SikaFast5221NT and SikaFast5200) were mixed at a ratio of 10:1 (by volume). The adhesive, whose response is highly rate-dependent, exhibits pseudo-ductile behavior at low and moderate displacement rates [17]. Elastic moduli of 140 MPa up to 368 MPa were measured on standardized dogbone specimens at 0.03 mm/s up to 0.83 mm/s displacement rates [17].

Grade 80 stainless steel bolts M10 were used, with an unthreaded length of 35 mm. The nuts were hand-tightened to prevent the bolts from being pre-stressed.

2.2.3 Adhesive joint manufacturing

The surface of the GFRP laminates was firstly roughened with sandpaper to remove the polyester surface veil until the combined mat layer was revealed at an approximately 0.5 mm depth. Based on preliminary experiments, to avoid early adhesion failure, a thin epoxy adhesive layer (of approximately 0.5 mm thickness, Sikadur-330) was applied as an adhesion promoter and cured for four hours at 60 °C [17]. The two-part ductile adhesive was then applied using a mixing gun, and four steel beads of 5 mm diameter were placed in the bonding area to guarantee the targeted layer thickness. One-day curing under ambient laboratory conditions (21 ± 3 °C and $38 \pm 10\%$ relative humidity) was applied for each lap. Subsequently, the joint was stored for five days in the same room prior to the experiments.

2.2.4 Instrumentation

The joint axial and through-thickness deformations were measured, in monotonic and cyclic experiments, by a video-extensometer, at a rate of 10 Hz and ± 0.003 mm to ± 0.015 mm accuracy. The distances and the numbering of the corresponding measuring points on the laminate side faces are shown in Fig. 2.2, (a) for adhesive, (b) four-bolt, and (c) two-bolt joints. Additional points were fixed on the bolt heads (nos. 22 and 23 in four-bolt and 19 in two-bolt joints) and at the ends of the inner laminates (no. 24 in four-bolt and 20 in two-bolt joints). These additional points allowed to derive the laminates' crushing deformations from the differential displacements of the target pairs 8–22 and 14–23 in four-bolt, and 8–19 in two-bolt joints. Similarly, the shear-out deformations could be obtained from the target pairs 20–24 and 17–20 in the four- and two-bolt joints respectively, see Fig. 2.3. The loads and total specimen displacements were also measured by the loading machine at a rate of 100 Hz for the specimens at 1 mm/s displacement rate (see below), and 10 Hz for the remaining specimens.

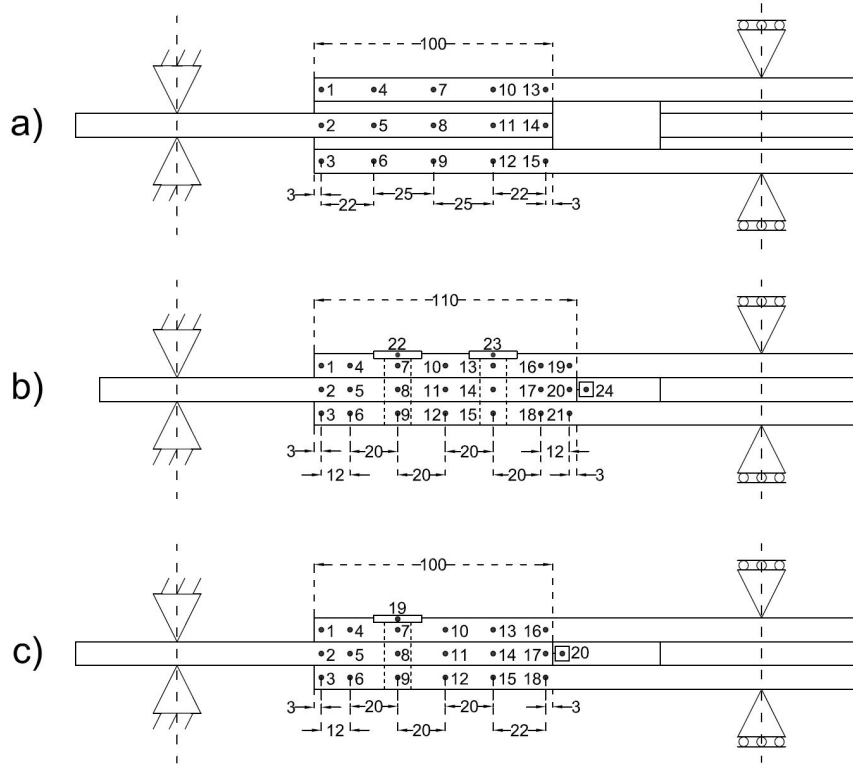


Figure 2.2: Video-extensometer target points and distances (mm), a) adhesive, b) four-bolt, c) two-bolt joints.

2.2.5 Experimental program

Monotonic tension and cyclic tension–compression experiments were performed on all joint types. Since cyclic loading protocols for GFRP joints do not yet exist, a protocol developed for joints in timber frames was selected, i.e. the CUREE protocol [18], which is also included in the ASTM E2126 standard [19], specified there as “Test Method C”. The protocol is a “realistic and conservative representation of the cyclic deformation history to which a component of a wood structure likely is subjected in earthquakes” (citation from [19]).

According to [18], [19], the reference displacement or amplitude of the applied cycles, Δ , is defined based on the load–displacement curves obtained from monotonic experiments. The reference displacement is equal to 60% of the joint displacement at 80% of the maximum load, F_{max} , taken in the after-peak softening branch, $\Delta_{0.8F_{max}}$. The applied load history then consists of primary cycles, whose amplitude is a fraction of Δ , and intermediate trailing cycles (two after the initial phase) of 75% of the amplitude of the previous primary cycle, see Fig. 2.4.

As far as the displacement rate is concerned, in [18] reference is made to ISO 16,670 [20], where

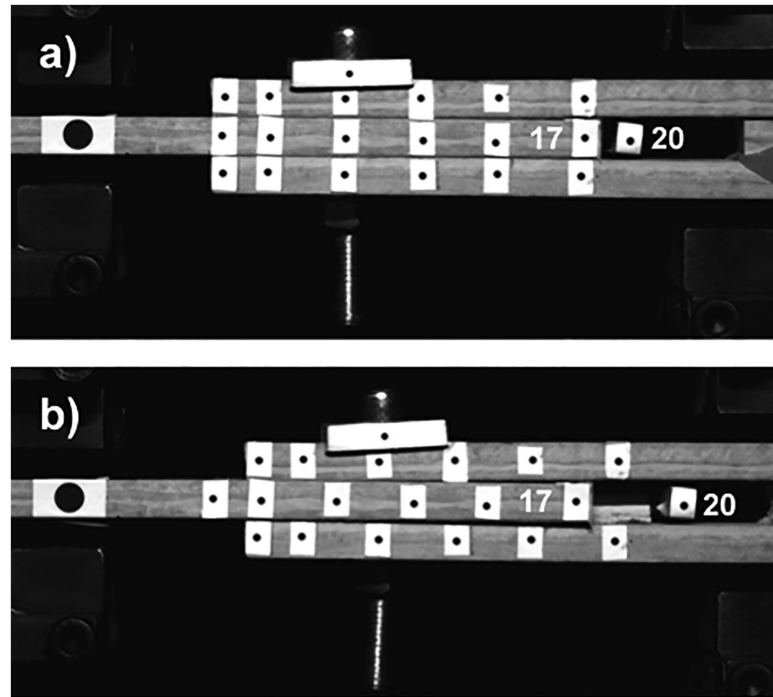


Figure 2.3: Shear-out deformation measured by targets 17 and 20 in two-bolt joints, a) initial target positions, b) target positions after shear-out failure.

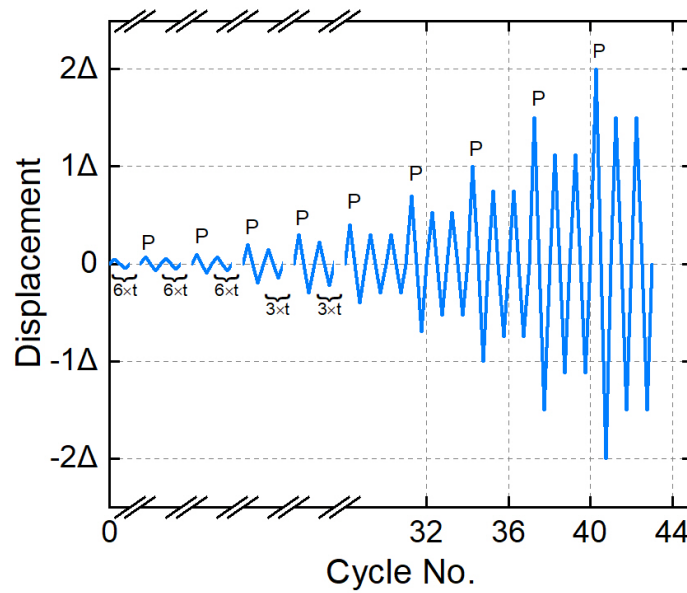


Figure 2.4: Cyclic displacement scheme [19] (P = primary cycle, t = trailing cycle).

values between 0.1 and 10 mm/s are recommended. In view of the high rate sensitivity of the adhesive and the results obtained in [17], three displacement rates of 0.1, 0.5 and 1.0 mm/s

Chapter 2. Pseudo-ductile adhesive and bolted linear double lap joints

were selected for the adhesive joints, in monotonic and cyclic experiments, denominated low, medium and high rate in the following. Consequently, the effect of the displacement rate on the energy dissipation capacity of the adhesive joints was also evaluated. The bolted joints were subjected to only one rate, i.e. the lowest, 0.1 mm/s, since the sensitivity to the displacement rate was considered to be much less than that of the adhesive joints, in view of the approximately 100× higher elastic modulus of the GFRP laminates compared to that of the adhesive and their mainly unidirectional architecture. Selecting the lowest rate also provided the most favorable condition in view of high energy dissipation.

The displacement rate was applied by the machine to the whole specimen and thus included the small elastic deformation of the laminates outside of the joint; the rate applied to the joint part was thus insignificantly lower. Since the displacement rate was kept constant during each experiment, the frequency of the cycles varied and decreased during the experiments due to the increase of the displacement amplitudes, see Fig. 2.5.

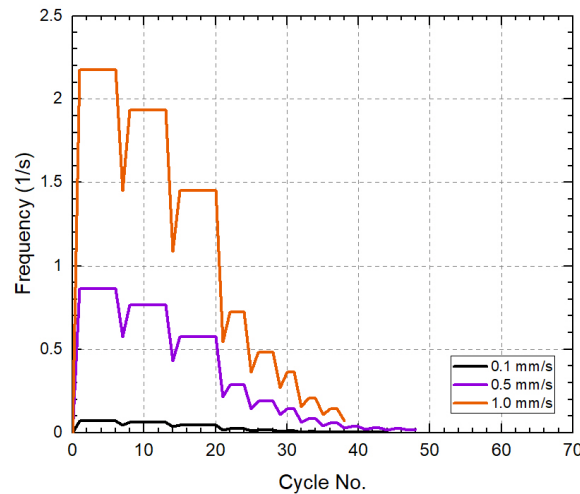


Figure 2.5: Frequency variations during cyclic scheme for each type of specimen.

Two experiments were performed for each parameter combination in monotonic and cyclic investigations. The joint denominations included the joint type (A, B4 or B2), loading type (S or C), rate (0.1, 0.5, 1.0) and joint replicate (a or b). “B4-C0.1a” for instance indicates the first four-bolt joint under cyclic loading at a rate of 0.1 mm/s, while “A-S1.0b” denominates the second adhesive joint under monotonic (static) loading at a rate of 1.0 mm/s.

A Walter + Bai type LFV universal experimental machine was used with a capacity of 200 kN in tension and compression and a maximum displacement of 200 mm. Both monotonic and cyclic experiments were conducted in a laboratory environment at ambient temperature (21 ± 3 °C).

2.3 Experimental results

2.3.1 Monotonic experiments

2.3.1.1 Adhesive joints

The load-joint displacement responses of the adhesive joints under monotonic loading are shown and summarized in Fig. 2.6 and Table 2.1. The joint displacements were obtained from the target pairs 2–13, see Fig. 2.2; the joints exhibited a bilinear behavior. The displacement rate significantly influenced the initial (tangential) stiffness, S , the yield load, F_y (determined as the intersection of two tangent lines to the almost linear segments), and the displacement at failure, Δ_{fail} , the former two increasing and the latter decreasing as the rate increased from 0.1 to 1.0 mm/s. The remaining results, i.e. yield displacement, Δ_y , and maximum load, F_{max} , exhibited only a slight dependency on the rate. The highest maximum loads and maximum displacements at failure were achieved at the low rate. At the low rate, furthermore, a significant hardening occurred in the second part of the curves between yield and maximum load. The two joints per configuration exhibited similar and consistent behaviors.

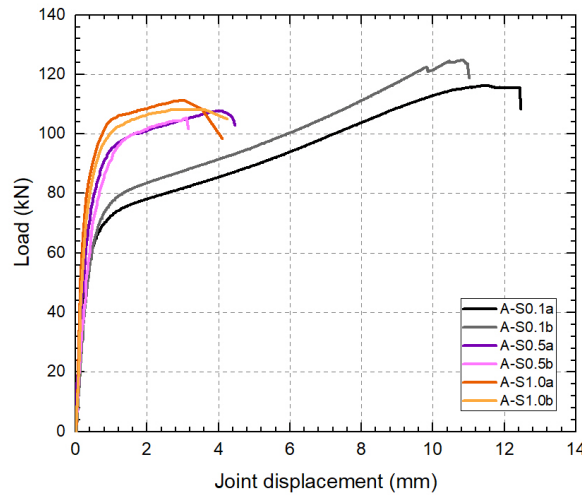


Figure 2.6: Load-joint displacement responses of adhesive joints.

The shear strain distributions in the adhesive layers were derived from the through-thickness target pairs; they are shown in Fig. 2.7 at three load levels, i.e. below and at the yield load and at the maximum load. The resulting strain distributions were almost uniform at all load levels and did not exhibit peaks at the overlap ends (typical for stiffer, e.g. epoxy adhesives). The through-thickness strains were also derived, but they were small, only approximately 10% of the shear strains, and are thus not shown.

Chapter 2. Pseudo-ductile adhesive and bolted linear double lap joints

Table 2.1: Results obtained from monotonic experiments for adhesive and bolted joints.

Joint	S (kN/mm)	Δ_y (mm)	F_y (kN)	F_{max} (kN)	Δ_{fail} (mm)	Δ (mm)
A-S0.1a	200.3	0.40	71.8	116.1	12.6	7.6
A-S0.1b	192.2	0.42	77.4	124.6	11.1	6.7
A-S0.5a	231.7	0.36	95.3	107.7	5.6	3.4
A-S0.5b	210.8	0.37	95.6	105.3	3.9	2.4
A-S1.0a	364.6	0.32	102.9	111.8	3.8	2.3
A-S1.0b	307.9	0.33	103.2	108.1	3.9	2.3
B4-S0.1a	52.2	–	–	123.9	2.7	1.6
B4-S0.1b	54.4	–	–	115.4	2.8	1.7
B2-S0.1a	43.5	–	–	88.0	5.1	3.1
B2-S0.1b	43.7	–	–	84.8	4.8	2.9

Note: 1-mm clearance was discounted in Δ_{fail} of bolted joints.

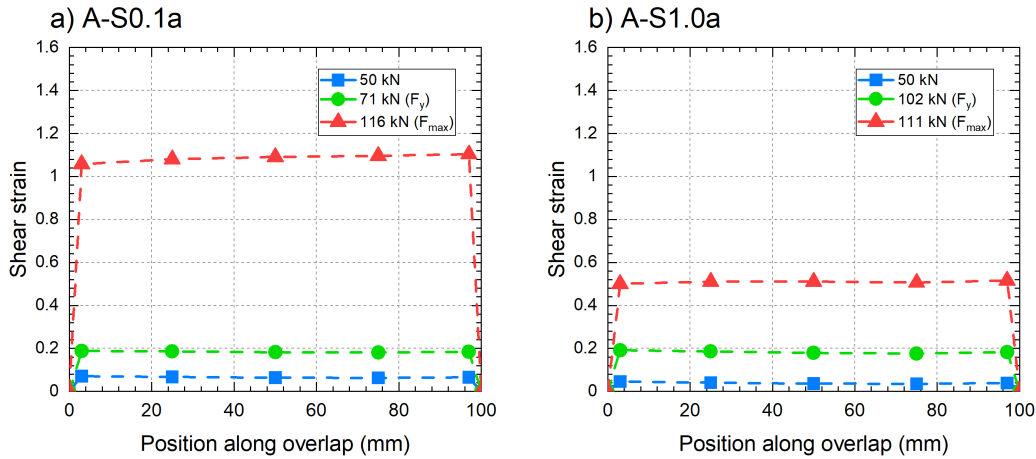


Figure 2.7: Shear strain distributions along overlap of adhesive joints at different load levels, a) A-S0.1a, b) A-S1.0a.

Failure of all joints occurred in the inner laminate. The failure mode was a fiber-tear failure according to [21]; Fig. 2.8 shows the failure plane, located within the visible combined mats of the inner laminate. The failure mode was not affected by the displacement rate.

2.3.1.2 Bolted joints

The load-joint displacement responses and results obtained for the bolted joints under monotonic loading are shown in Fig. 2.9 and summarized in Table 2.1. The joint displacements were obtained from the target pairs 2–19 and 2–16 for the four- and two-bolt joints, see Fig. 2.2. Also

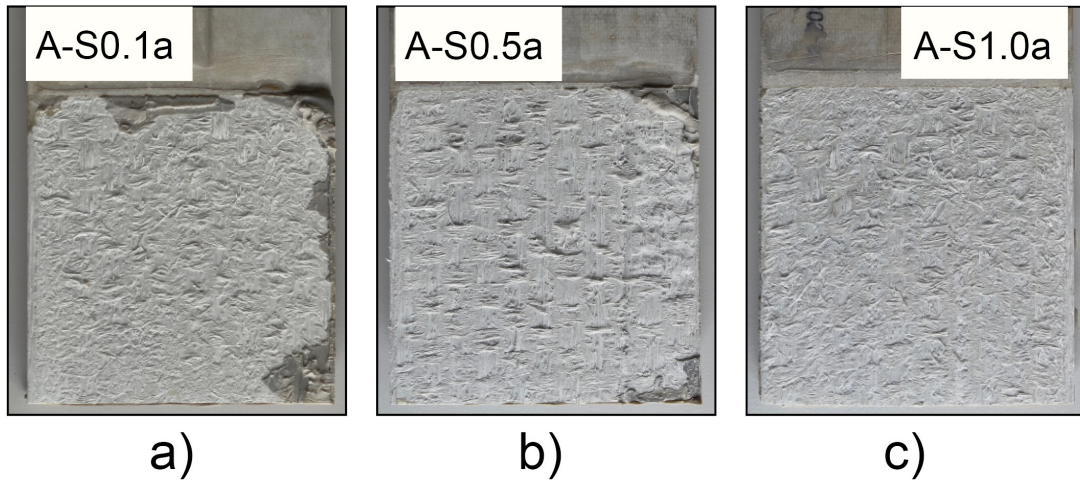


Figure 2.8: Fiber-tear failure modes of adhesive joints under monotonic loading, a) A-S0.1a, b) A-S0.5a, c) A-S1.0a.

shown in Fig. 2.9 are the points of crushing and shear-out initiation (indicated by star and square symbols). In both four- and two-bolt joints, the load-joint displacement curves consisted of five segments, (i) clearance compensation up to approx. 1 mm of displacement, (ii) linear behavior up to crushing initiation, (iii) stiffness reduction during crushing up to shear-out initiation, (iv) further stiffness reduction during simultaneous crushing and shear-out up to the maximum load, and (v) significant drop of the load during only small displacements in the four-bolt and more significant displacements in the two-bolt joints.

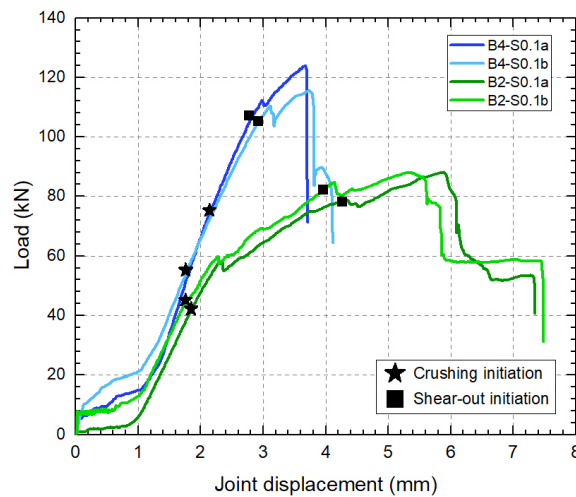


Figure 2.9: Load-joint displacement responses of bolted joints.

Crushing initiation occurred simultaneously in both rows of the four-bolt joints. They exhibited a much stiffer behavior after crushing initiation and higher maximum loads (38% on

Chapter 2. Pseudo-ductile adhesive and bolted linear double lap joints

average) than two-bolt joints since the bolts in the former transferred only half of the load of the latter and crushing and shear-out initiation thus occurred at higher loads. The crushing deformations up to failure in the four-bolt case were less than half of those of the two-bolt case, as shown in Fig. 2.10; the shear-out deformations before failure were however similar. After the maximum load, crushing no longer occurred. The combined crushing/shear-out failure modes of both joint types are shown in Fig. 2.11. Failure occurred only in the inner laminates, the outer laminates remained undamaged since they bore only half of the load. The steel bolts also remained undamaged.

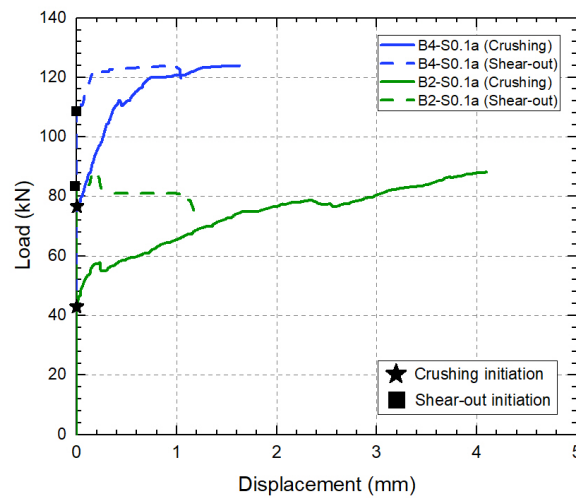


Figure 2.10: Crushing and shear-out behavior of B4-S0.1a and B2-S0.1a bolted joints.

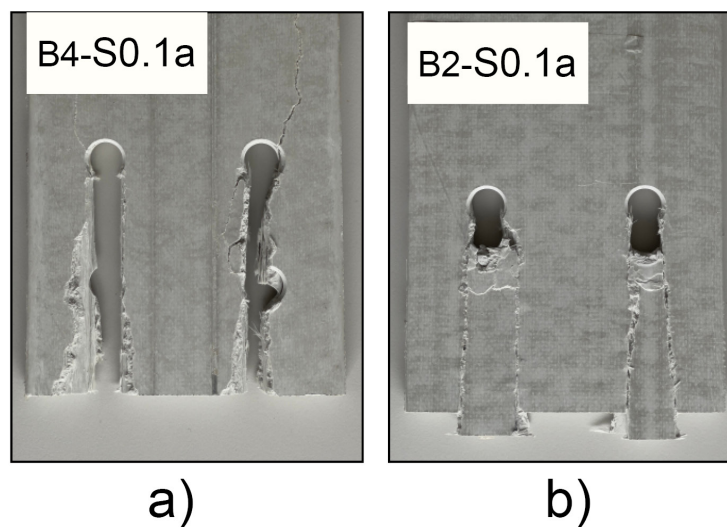


Figure 2.11: Combined crushing and shear-out failure modes of bolted joints under monotonic loading, a) B4-S0.1a, b) B2-S0.1a.

2.3.1.3 Derivation of cyclic reference displacements

The cyclic reference displacements, Δ , were derived from the monotonic experiments, as described above. Since no clear softening behavior was obtained and values $\Delta_{0.8F_{max}}$ in the softening branches could thus not be determined, the 60% fraction was applied to Δ_{fail} , see Table 2.1. In the latter values, the clearance of the bolted joints was discounted. The average Δ values of both specimens were taken as reference and applied in the cyclic experiments, see Table 2.2.

Table 2.2: Results obtained from cyclic experiments for adhesive and bolted joints.

Specimen	Δ (mm)	F_{max} (kN)	Δ_{fail} (mm)	N_{fail}
A-S0.1a	7.15	93.7	17.5	44
A-S0.1b	7.15	90.5	17.7	44
A-S0.5a	2.90	87.8	14.3	59
A-S0.5b	2.90	94.1	14.4	59
A-S1.0a	2.30	110.1	3.2	38
A-S1.0b	2.30	109.8	3.1	38
B4-S0.1a	1.65	115.1	5.9	47
B4-S0.1b	1.65	114.7	5.8	47
B2-S0.1a	3.00	92.4	9.9	47
B2-S0.1b	3.00	91.3	8.4	44

Note: F_{max} values refer to tensile loading.

2.3.2 Cyclic experiments

2.3.2.1 Adhesive joints

The load-joint displacement responses of the adhesive joints under cyclic loading are shown in Fig. 2.12. One of the two specimens of each displacement rate was selected (which both showed consistent behavior); only the primary cycles are shown and their number is indicated. The trailing cycles always overlapped each other and also overlapped the subsequent primary cycle. Table 2.2 furthermore summarizes the maximum loads reached during each loading history, F_{max} ; the joint displacements at the failure cycle, Δ_{fail} ; and the cycle numbers when failure occurred, N_{fail} .

The hysteresis loops were almost tension–compression symmetric in all cases. In a first phase, the tensile and compressive reversals had a parabolic shape, i.e. the cyclic responses exhibited a softening behavior, as also occurred in the monotonic experiments. In the second phase however, the shapes changed to sigmoid, i.e. the responses showed a hardening behavior,

Chapter 2. Pseudo-ductile adhesive and bolted linear double lap joints

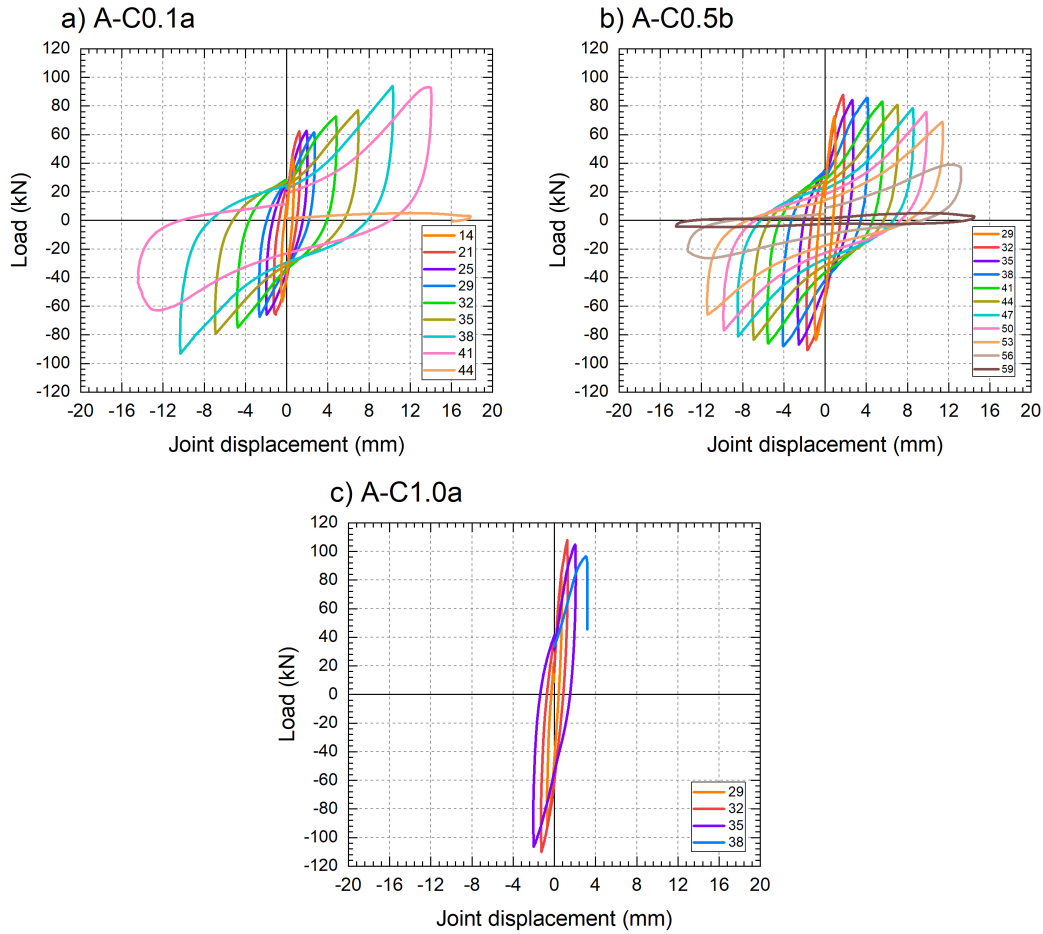


Figure 2.12: Load-joint displacement responses of adhesive joints under cyclic loading, a) A-C0.1a, b) A-C0.5b, c) A-C1.0a.

again similar to the monotonic experiments. The changes of these behaviors occurred in cycles no. 32 and 41 at the low and medium rates respectively, while the specimens at the high rate failed before entering the second phase. The hardening behavior was attributed to a stretching of the molecule chains and their alignment to the load direction, which was possible at the low and medium rates. In the last cycles prior to failure, subsequent to hardening and prior to the peak load, the joints again exhibited a short softening behavior.

The peak loads were similar at the low and medium rates while at the high rate they were slightly higher, see Table 2.2. Specimens at the medium rate exhibited the highest number of cycles up to failure, followed by those at the low and high rates. However, the displacements at failure were similar at the low and medium rates.

2.3 Experimental results

The envelope curves of the responses shown in Fig. 2.12, i.e. the curves connecting the cyclic peak loads, are presented in Fig. 2.13. The tension envelopes were denominated as previously explained, while the denomination of the compression envelopes was complemented by “-c”. The envelope curves confirmed the almost symmetric behavior; they also exhibited a softening after the peak at the medium and high rates and hardening at the low rate up to the penultimate primary cycle. Two mechanisms apparently worked against each other at the low and medium rates, softening due to damage formation and hardening due to molecule chain stretching. At the low rate, hardening dominated up to the penultimate primary cycle while softening dominated at the medium rate.

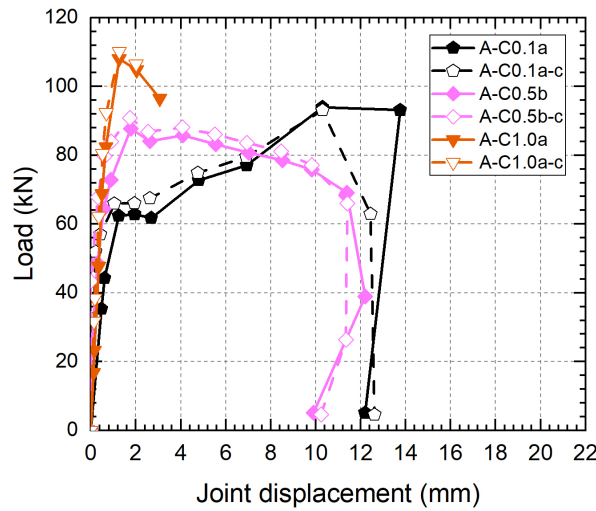


Figure 2.13: Envelope curves of load-joint displacement responses of adhesive joints.

Two different failure modes were observed, see Fig. 2.14. At the low and medium rates, cohesive failure occurred in the adhesive, while at the high rate the joints exhibited fiber-tear failure in the inner laminate, as was the case in the monotonic experiments.

2.3.2.2 Bolted joints

The load-joint displacement responses of the bolted joints under cyclic loading are shown in Fig. 2.15 (again primary cycles only) and the results are summarized in Table 2.2. The specimens exhibited linear behavior up to the initiation of crushing, which is indicated by star symbols in Fig. 2.15 and occurred on both sides of the holes, depending on tension or compression loading. The responses then became nonlinear up to the initiation of shear-out under tensile loading (indicated by square symbols). The maximum load was reached in the cycle in which shear-out initiated or in the following one. Subsequently, the load rapidly

Chapter 2. Pseudo-ductile adhesive and bolted linear double lap joints

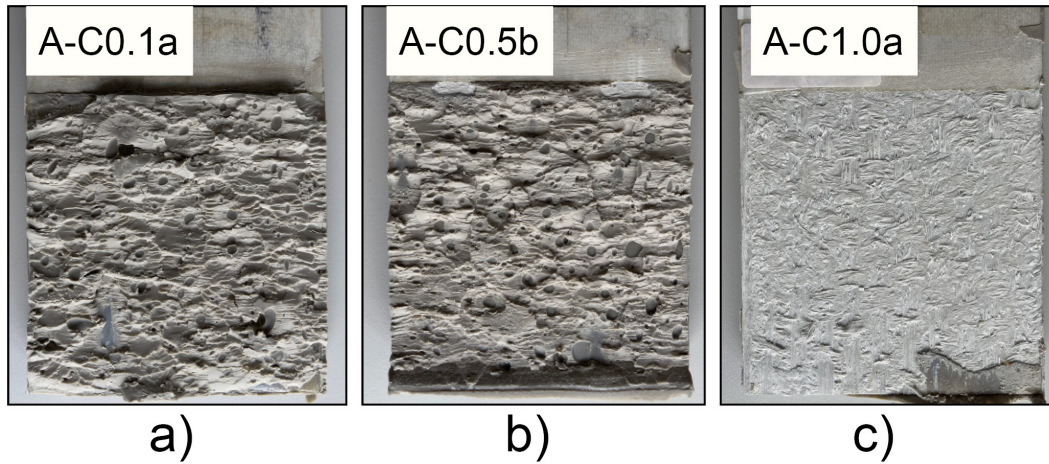


Figure 2.14: Failure modes of adhesive joints under cyclic loading, cohesive failure in a) A-C0.1a and b) A-C0.5b, fiber-tear failure in c) A-C1.0a.

dropped in the tension cycles while under compression loading, where no shear-out was possible, the load dropped at a much lower rate. The displacements obtained from the target pairs that measured the cumulated crushing and shear-out values (see above), were almost the same as those obtained for the whole joints in Fig. 2.15 and are thus not shown; the only differences were the small elastic displacements of the laminates.

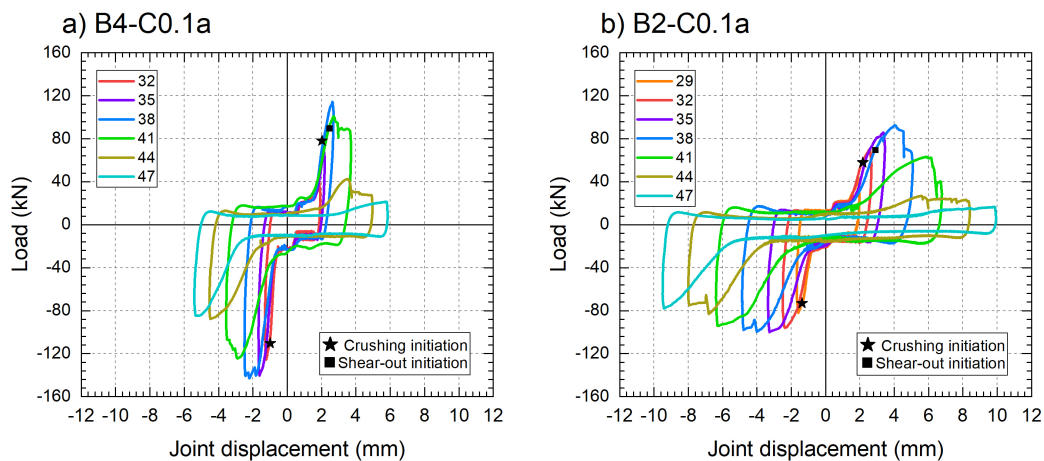


Figure 2.15: Load-joint displacement responses of bolted joints under cyclic loading, a) B4-C0.1a, b) B2-C0.1a.

Prior to crushing initiation, the “plateau” segment without load increase, shown in each cycle, corresponded to the hole clearance. During crushing and after shear-out initiation,

2.3 Experimental results

this plateau extended to include the cumulated crushing and shear-out deformations of the previous cycle. The small fluctuations and non-zero values of the load in the plateau region were attributed to friction between the bolts and the inside of the rugged and deformed bolt-holes.

As mentioned above, since under compression loading shear-out failure was not possible, the specimens were still able to bear load under compression, while under tension, after shear-out failure, only the plateau, caused by the bolt friction, was maintained. Failure of the specimen was thus defined at the first primary cycle where the load under tension no longer noticeably increased above the plateau value.

The envelope curves of the cyclic load-joint displacement responses are shown in Fig. 2.16. The denomination of the compression envelopes was again complemented by “-c”. The envelope curves clearly showed the non-symmetric behavior, i.e. the higher peak loads in compression compared to tension, and the much faster softening in tension due to shear-out, compared to the slower softening in compression where only crushing occurred. The peak loads in the four-bolt joints were higher and the displacements at failure smaller compared to the two-bolt joints, as was also the case in the monotonic experiments for the same reasons (see above).

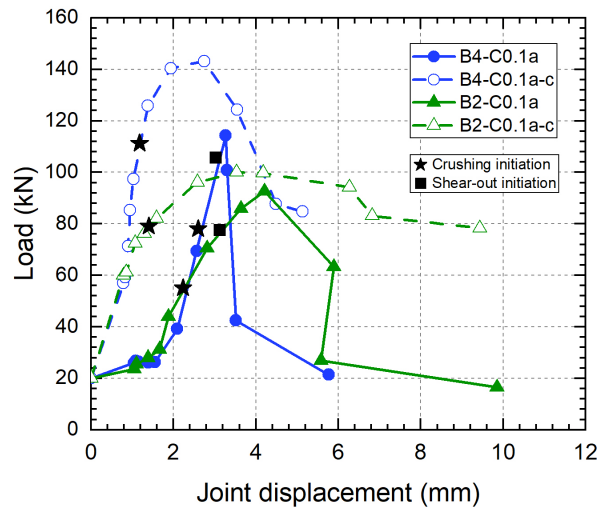


Figure 2.16: Envelope curves of load-joint displacement responses of bolted joints.

The failure modes of the four- and two-bolt joints are shown in Fig. 2.17. The crushing and shear-out patterns in the inner laminates were similar to those under monotonic loading, except that crushing occurred in both directions under cyclic loading. The crushing deformation

Chapter 2. Pseudo-ductile adhesive and bolted linear double lap joints

in the two-bolt joints was much larger than in the four-bolt joints, as also shown in the much longer plateaus of the failure cycles in Fig. 2.15. The photos also show that the laminates were still able to bear compression loading since no shear-out could occur in that direction. Again, the outer laminates and steel bolts were not damaged.

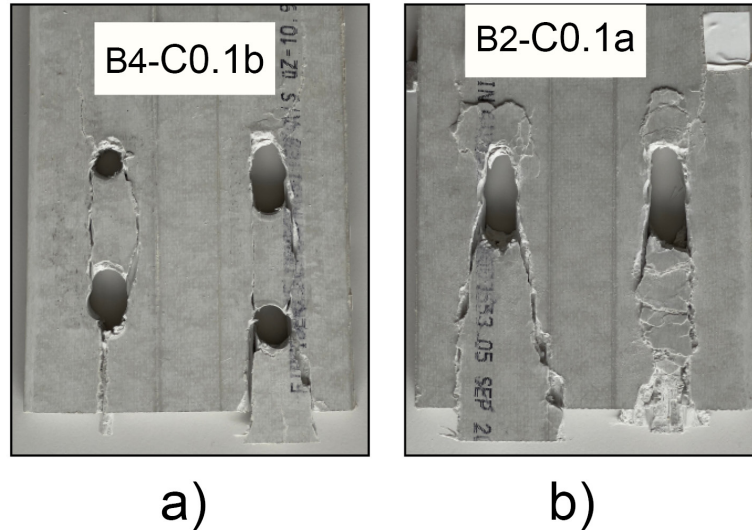


Figure 2.17: Combined crushing and shear-out failure modes of bolted joints under cyclic loading, a) B4-C0.1b b) B2-C0.1a.

2.4 Discussion

2.4.1 Comparison of monotonic and cyclic behavior

The monotonic load–displacement responses and the tensile envelope curves of the cyclic responses of both adhesive and bolted joints are compared in Fig. 2.18. With regard to the adhesive joints, shown in Fig. 2.18(a), the monotonic and cyclic envelope curves were similar at the high rate; the peak loads and failure modes, i.e. fiber-tear, were the same, and only the displacements at the peak load and failure were smaller under cyclic loading. At the low and medium rates, however, the envelope curves were clearly below the monotonic curves because more damage was progressively accumulated during the cyclic loading compared to the monotonic loading. Since the cyclic peak loads were thus below the monotonic maximum (failure) loads, the cyclic displacements up to failure, occurring mainly in the adhesive layer, could increase compared to the monotonic displacements, particularly at the medium rate where they tripled. The failure modes thus changed from fiber-tear to cohesive failure, which occurred after damage accumulation during stretching and alignment of the adhesive's

molecular chains.

In the case of bolted joints, monotonic and cyclic responses were again similar, as in the case of the high rate in the adhesive joints, see Fig. 2.18(b), i.e. the maximum loads were similar and only the displacements at maximum load were smaller under cyclic loading; the failure modes remained basically the same.

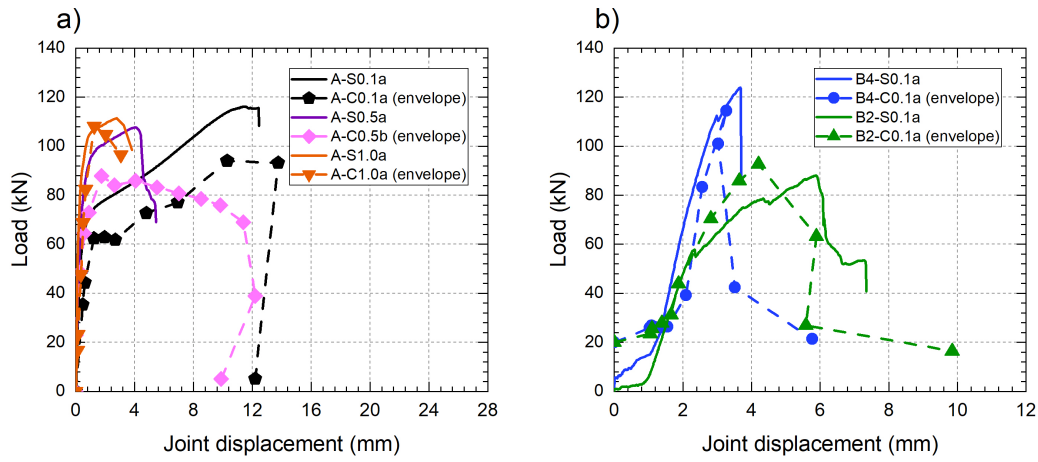


Figure 2.18: Comparison of monotonic load-joint displacement curves and tensile cyclic loading envelope for a) adhesive and b) bolted joints.

2.4.2 Stiffness degradation

The cycle-to-cycle stiffness degradation of all joints, during the tensile cycles, is shown in Fig. 2.19. To appropriately compare the behaviors, the cycle secant stiffnesses, K_i , were normalized by the elastic stiffnesses of the corresponding envelopes, K_e , and the cycle displacements, Δ_i , by the yield displacements, Δ_y , of the envelopes. The elastic stiffnesses and yield displacements were determined according to [22], and the results are shown in Table 2.3. For the bolted joints, the clearance was excluded from the displacements. The resulting rate-dependent trend of the envelope stiffnesses of the adhesive joints were similar to that of the initial stiffness, S , of the monotonic experiments, as described above, see Table 2.1; the latter values were however higher since the tangential stiffnesses were calculated in that case. The normalization of the stiffnesses almost led to an overlap of all degradation curves. In the adhesive joints at the low and medium rates, a rapid decrease occurred in the first damage phase at low amplitudes and high frequencies, while subsequently, during the molecular stretching, the stiffness degradation significantly slowed. The bolted joints and the adhesive joints at the high rate exhibited only one significant, almost linear, stiffness drop up to failure.

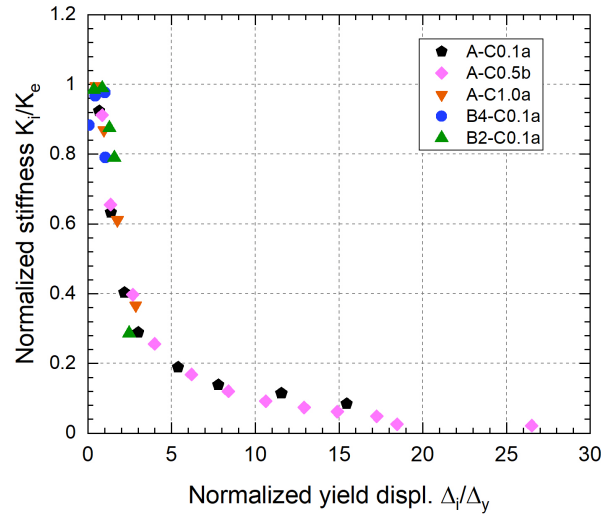


Figure 2.19: Normalized cycle-to-cycle stiffness degradation as a function of normalized displacement.

Table 2.3: Elastic stiffness and yield displacement of envelopes determined according to [19].

Specimen	K_e (kN/mm)	Δ_y (mm)
A-C0.1a	80	0.89
A-C0.1b	94	0.79
A-C0.5a	124	0.76
A-C0.5b	125	0.66
A-C1.0a	141	0.71
A-C1.0b	154	0.66
B4-C0.1a	65	1.24
B4-C0.1b	64	1.42
B2-C0.1a	29	1.90
B2-C0.1b	33	0.90

2.4.3 Energy dissipation capacity

2.4.3.1 Energy dissipation per cycle

The energy dissipation per cycle of both adhesive and bolted joints up to joint failure was determined and compared. The dissipated energy was taken equivalent to the enclosed area of the load-joint displacement hysteresis loops shown in Fig. 2.12, Fig. 2.15. For the bolted joints, the energy dissipated by bolt friction, i.e. the areas between the two plateaus in Fig. 2.15,

was also taken into account.

The resulting dissipated energies per cycle are shown in Fig. 2.20. The highest amount of energy per cycle was dissipated in the adhesive joints at the low rate, followed by the adhesive joints at the medium rate. Both curves exhibited a maximum reached before the significant drop of the load, see Fig. 2.12. During the last cycles preceding failure, the energy dissipated per cycle thus significantly decreased. The adhesive joints at the high rate dissipated the lowest amount of energy per cycle.

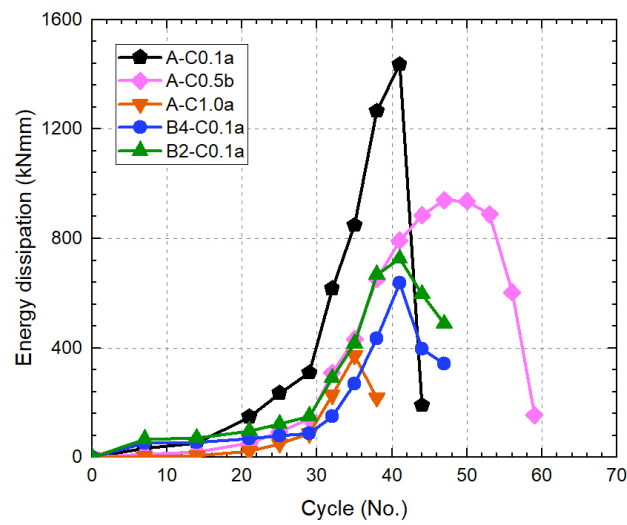


Figure 2.20: Energy dissipation per cycle of adhesive and bolted joints up to failure.

The bolted joints also exhibited a maximum energy dissipation per cycle before the values decreased. The maximum was higher for the two-bolt than for the four-bolt joints, but both were lower than the maxima of the adhesive joints at the two lower rates. The maximum energy per cycle was dissipated at the cycle after shear-out initiation.

2.4.3.2 Cumulative energy dissipation

The cumulative dissipated energy was obtained from the summation of the energies dissipated in all cycles, including primary and trailing cycles. For the bolted joints, the summation was stopped at the primary cycle, which no longer exhibited any noticeable load increase under tension, previously defined as joint failure. The resulting cumulative dissipated energies are shown in Fig. 2.21, as a function of the number of cycles (a), and joint displacements (b).

The largest amounts of cumulative energy were dissipated by the adhesive joints at the low and medium rates, while the joints at the medium rate dissipated more energy than those at the low

Chapter 2. Pseudo-ductile adhesive and bolted linear double lap joints

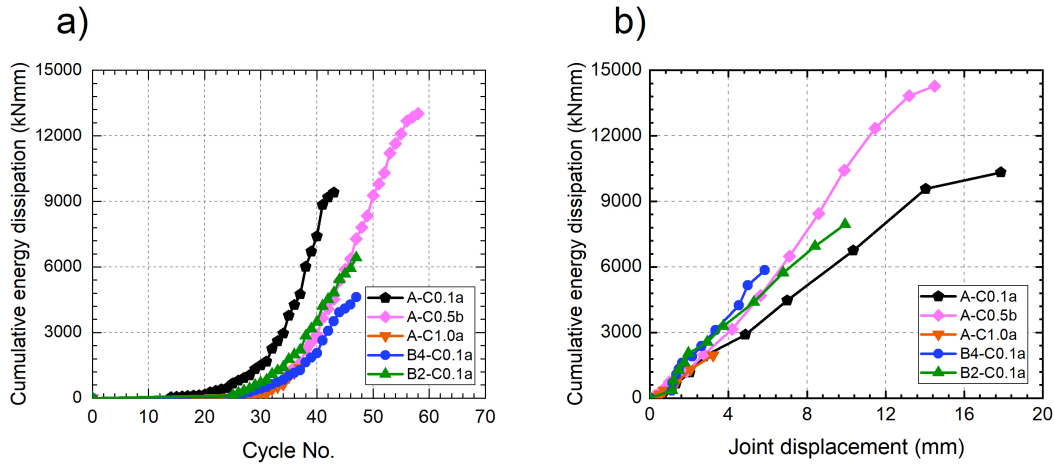


Figure 2.21: Cumulative energy dissipation of adhesive and bolted joints up to failure, as a function of a) cycle number, b) joint displacement.

rate, see Fig. 2.21. At a certain cycle, however, the joints at the low rate dissipated more energy than those at the medium rate, as shown in Fig. 2.21(a), since the imposed displacements were higher (see reference displacements in Table 2.1). At the same imposed displacement however, the joints at the low rate dissipated less energy, as shown in Fig. 2.21(b), since fewer cycles were completed than in the joints at the medium rate. Finally, since, independent of the rate, both joints failed at almost the same displacement – achieved mainly in the adhesive layer – the joints at the medium rate and fewer imposed displacements per cycle were able to sustain more cycles and thus dissipated more energy. The lowest amount of energy was dissipated in the adhesive joints subjected to the high displacement rate, since the adhesive was not able to enter the second branch of its bilinear behavior and thus to dissipate a significant amount of energy.

The bolted joints dissipated much less energy than the adhesive joints subjected to the low and medium rates. The two-bolt joints dissipated more energy per cycle than the four-bolt joints, see Fig. 2.21(a), since the imposed joint displacements per cycle were larger (see Table 2.1). These displacements were directly transformed into crushing and shear-out deformations. On the other hand, for the same imposed joint displacement, the two-bolt joints dissipated less energy than the four bolt joints, as shown in Fig. 2.21(b), since the same crushing and shear-out deformation was produced only twice (by two bolts) and not four times (by four bolts). Due to the longer laminate length between bolts and laminate ends, the two-bolt joints were able to sustain much larger displacements up to failure and thus finally dissipated more energy than the four-bolt joints, although they exhibited a significantly lower monotonic

strength (under tension).

In adhesive joints, an optimum displacement rate seems to exist, at which a maximum number of cycles can be sustained by the joint while the adhesive still maintains a high deformation capacity, see Fig. 2.22. On the other hand, an adhesive can also be designed or selected accordingly, adapted to the design displacement rate, in order to dissipate a maximum amount of energy.

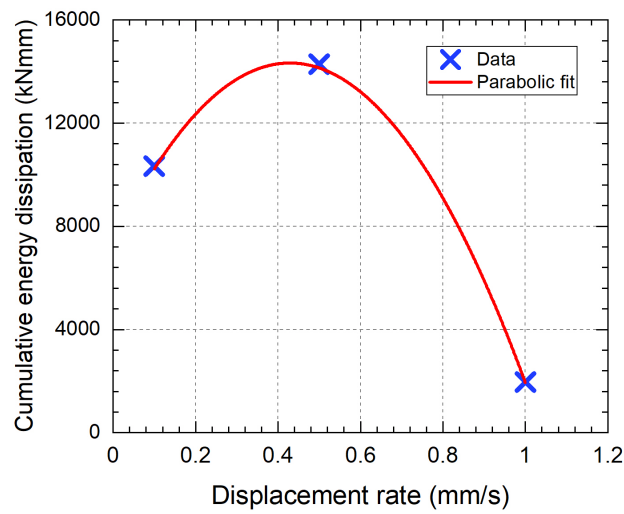


Figure 2.22: Dissipated cumulative energy as a function of displacement rate for adhesive joints.

2.4.3.3 Normalized energy dissipation

The energy dissipated per cycle was normalized by the input energy, i.e. the sum of the elastic and dissipated energy, in order to further compare the different joints, as shown in Fig. 2.23. In all the joints, at least approximately 90% of the input energy was dissipated, reaching almost 100% towards failure. Closer investigation, however, permitted further differentiation of the energy share of the different damage mechanisms. The adhesive joints exhibited two maxima and a minimum of normalized energy dissipation in between, as shown in Fig. 2.23(a). The first maximum was obtained during damage formation at small amplitudes and high frequencies where the elastic energy portion was small. With increasing deformation at lower frequencies, stretching of the molecule chains became dominant and the elastic energy portion increased, i.e. the dissipated/input energy ratio decreased and reached a minimum. In the last cycles before failure, damage again became dominant and the dissipated energy

Chapter 2. Pseudo-ductile adhesive and bolted linear double lap joints

portion increased and the ratio exhibited the second maximum. The three stages coincided well with the consecutive softening-hardening-softening behavior discussed in Section 2.3.2.1 based on Fig. 2.12. The first two stages also agreed well with the trend of stiffness degradation shown in Fig. 2.19, i.e. significant stiffness drop during the first damage phase and leveling-off of stiffness degradation during molecular stretching.

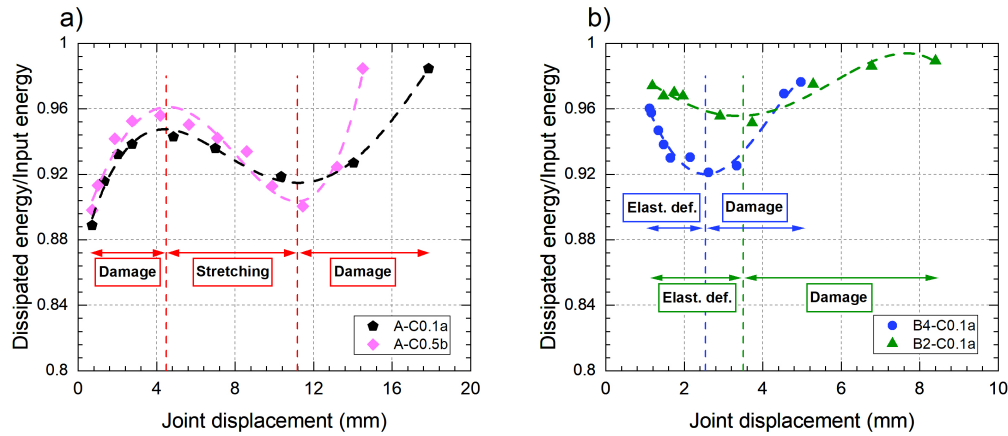


Figure 2.23: Energy dissipation per cycle normalized by input energy as a function of joint displacement for a) adhesive and b) bolted joint, dominant mechanisms are indicated.

In the bolted joints, the first cycles were dominated by friction of the bolt in the hole, i.e. the whole input energy was dissipated (ratio of 1.0). Subsequently elastic deformation became significant and the ratio decreased. With the initiation of crushing, the decreasing trend was halted, and the dissipated energy became dominant and the ratio increased during crushing and shear-out up to failure.

2.5 Conclusions

Monotonic tension and reversed cyclic loading experiments were performed on adhesive and bolted double-lap joints composed of pultruded GFRP profiles. A flexible adhesive and two or four steel bolts were used in the adhesive and bolted joints, respectively. The joint dimensions in all configurations were similar and the monotonic strengths of the adhesive and four-bolt joints were also similar, only those of the two-bolt joints were slightly lower. The effects of the displacement rate in the adhesive joints and the bolt configuration in the bolted joints on the energy dissipation capacity were investigated and adhesive and bolted joints were compared in this respect. The conclusions from this experimental investigation are as follows:

2.5 Conclusions

1. A significant amount of energy was dissipated in the adhesive joints by viscoelastic friction, including molecular chain stretching and damage in the adhesive layer at lower and medium joint displacement rates, while almost no energy dissipation occurred at the highest rate.
2. Energy in the bolted joints was dissipated by progressive crushing and shear-out failures in the inner laminates. Two-bolt joints dissipated significantly more energy than four-bolt joints, although their monotonic strength was lower, mainly due to the longer edge distances in the two-bolt joints.
3. The adhesive joints subjected to the two lower displacement rates dissipated significantly more energy than the bolted joints although the joint dimensions were similar and their monotonic strength was similar or only slightly higher than that of the four- or two-bolt joints, respectively.
4. In adhesive joints an optimum displacement rate was observed, at which a maximum amount of energy was dissipated. Furthermore, a higher portion of the input energy was dissipated and stiffness degradation was more pronounced during predominant damage formation than during predominant molecular stretching.

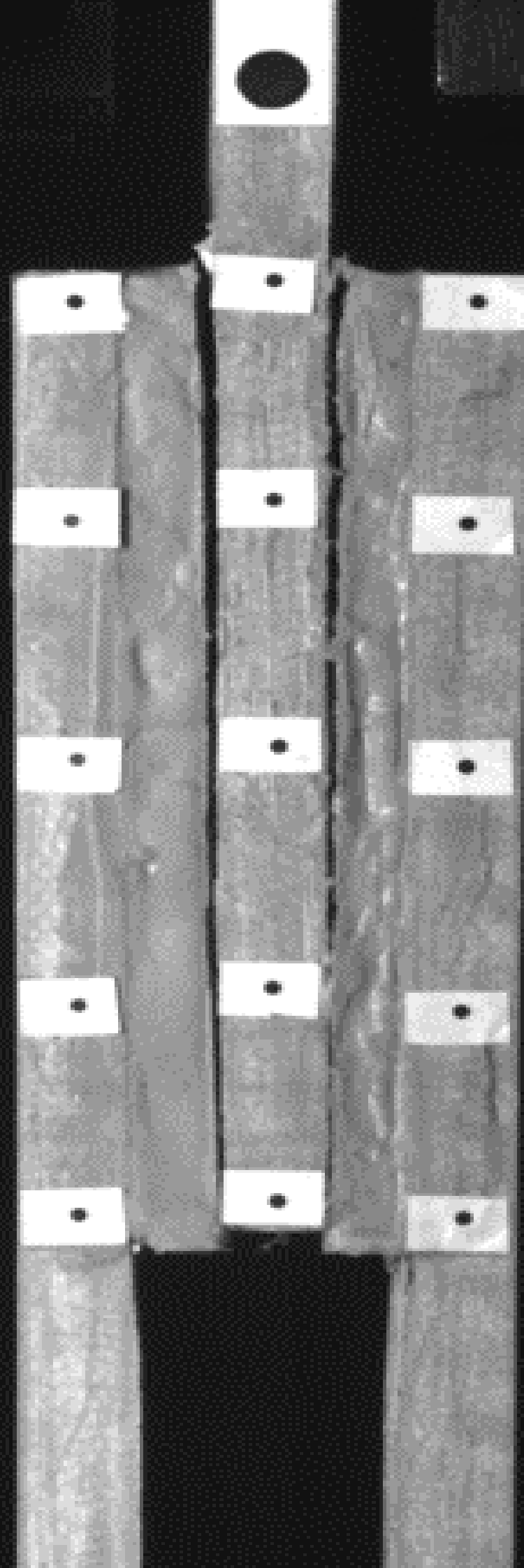
References

- [1] T. Keller and J. de Castro, “System ductility and redundancy of frp beam structures with ductile adhesive joints”, *Composites Part B: Engineering*, vol. 36, no. 8, pp. 586–596, 2005.
- [2] T. Keller and H. Gürtler, “Composite action and adhesive bond between fiber-reinforced polymer bridge decks and main girders”, *Journal of composites for construction*, vol. 9, no. 4, pp. 360–368, 2005.
- [3] S. Yanes-Armas, J. De Castro, and T. Keller, “Energy dissipation and recovery in web–flange junctions of pultruded gfrp decks”, *Composite Structures*, vol. 148, pp. 168–180, 2016.
- [4] M. Angelidi, A. P. Vassilopoulos, and T. Keller, “Ductile adhesively-bonded timber joints–part 1: Experimental investigation”, *Construction and Building Materials*, vol. 179, pp. 692–703, 2018.
- [5] R. Avendaño, R. Carbas, E. Marques, L. Da Silva, and A. Fernandes, “Effect of temperature and strain rate on single lap joints with dissimilar lightweight adherends bonded with an acrylic adhesive”, *Composite Structures*, vol. 152, pp. 34–44, 2016.
- [6] “Fiberline composites a/s”, 2003.
- [7] A. Othman and K. J. Jadee, “Specific bearing strength of bolted composite joint with different glass fiber reinforcement”, *ARPJ Eng Appl Sci*, vol. 11, no. 20, pp. 12 039–12 044, 2016.
- [8] N. Gattesco, A. Gubana, M. Buttazzi, and M. Melotto, “Experimental investigation on the behavior of glued-in rod joints in timber beams subjected to monotonic and cyclic loading”, *Engineering Structures*, vol. 147, pp. 372–384, 2017.
- [9] R. Žarnić, V. Rajčić, and M. Kržan, “Response of laminated glass-clt structural components to reverse-cyclic lateral loading”, *Construction and building materials*, vol. 235, p. 117 509, 2020.
- [10] J. Ye, S. M. Mojtabaei, and I. Hajirasouliha, “Seismic performance of cold-formed steel bolted moment connections with bolting friction-slip mechanism”, *Journal of Constructional Steel Research*, vol. 156, pp. 122–136, 2019.

-
- [11] L. Dai, X. Zhao, and K. J. Rasmussen, “Cyclic performance of steel storage rack beam-to-upright bolted connections”, *Journal of Constructional Steel Research*, vol. 148, pp. 28–48, 2018.
 - [12] X. Xiao, Z. Zhang, and Y. Bai, “Comparative study of energy dissipation capacity of steel and glass fibre-reinforced polymer frames with bonded sleeve connections”, *Journal of Reinforced Plastics and Composites*, vol. 36, no. 22, pp. 1665–1679, 2017.
 - [13] Z. Zhang, Y. Bai, X. He, L. Jin, and L. Zhu, “Cyclic performance of bonded sleeve beam-column connections for frp tubular sections”, *Composites Part B: Engineering*, vol. 142, pp. 171–182, 2018.
 - [14] C. Qiu, Y. Bai, Z. Cai, and Z. Zhang, “Cyclic performance of splice connections for hollow section fibre reinforced polymer members”, *Composite Structures*, vol. 243, p. 112 222, 2020.
 - [15] D. Martins, M. Proenca, J. A. Gonilha, M. F. Sa, J. R. Correia, and N. Silvestre, “Experimental and numerical analysis of gfrp frame structures. part 1: Cyclic behaviour at the connection level”, *Composite Structures*, vol. 220, pp. 304–317, 2019.
 - [16] T. Keller, J. Rothe, J. De Castro, and M. Osei-Antwi, “Gfrp-balsa sandwich bridge deck: Concept, design, and experimental validation”, *Journal of Composites for Construction*, vol. 18, no. 2, p. 04 013 043, 2014.
 - [17] M. Angelidi, A. P. Vassilopoulos, and T. Keller, “Ductility, recovery and strain rate dependency of an acrylic structural adhesive”, *Construction and Building Materials*, vol. 140, pp. 184–193, 2017.
 - [18] H. Krawinkler, F. Parisi, L. Ibarra, A. Ayoub, and R. Medina, *Development of a testing protocol for woodframe structures*. CUREe Richmond, CA, 2001, vol. 102.
 - [19] ASTM, “Standard test methods for cyclic (reversed) load test for shear resistance of vertical elements of the lateral force resisting systems for buildings”, *ASTM E2126*, 2019.
 - [20] I. ISO, “16670 timber structures–joints made with mechanical fasteners–quasi-static reversed-cyclic test method”, *Geneva, Switzerland*, 2003.
 - [21] A. S. for Testing Materials (ASTM). D5573-99, *Standard practice for classifying failure modes in fiber-reinforced-plastic (frp) joints*, 2012.

Chapter 2. Pseudo-ductile adhesive and bolted linear double lap joints

- [22] CEN, “Timber structures - test methods - cyclic testing of joints made with mechanical fasteners [including amendment a1:2005]”, *BS EN 1251*, 2005.



Viscoelastic adhesive modeling of ductile adhesive-composite joints during cyclic loading

Authors: Ghazaleh Eslami*, Abdolvahid Movahedirad*, Thomas Keller*

* Composite Construction Laboratory, École Polytechnique Fédérale de Lausanne (EPFL), Switzerland

Published: *International Journal of Adhesion and Adhesives* (2022), 119, art. no. 103241,

Cited 0 times, DOI: 10.1016/j.ijadhadh.2022.103241

3.1 Introduction

High specific strength- and stiffness-to-weight ratios are among the qualities of fiber-polymer composites that make them attractive for bridge and building construction. Epoxy adhesives are common means of connections in composites structures. Together with the already brittle nature of composites, the relatively high stiffness of these adhesives leads however to also brittle failure in the joints [1]. On the other hand, in load-bearing structures composed of brittle members, pseudo-ductility can be obtained by using pseudo-ductile adhesives in the joints [2]. Due to the relatively high stiffness of the composite laminates compared to the flexible adhesive, the joints' response to an applied displacement mainly depends on the behavior of the adhesive.

The adhesives used for structural purposes are mostly thermoset polymers and exhibit viscoelastic behavior [3], [4], non-recoverable viscoplastic strains do thus not remain. The viscoelastic behavior consists of both an elastic component, with a linear or nonlinear relationship between stress and strain, and a viscous component, with a linear or nonlinear relation-

Contributions: Ghazaleh Eslami conducted the ideation and development of the constitutive model under the supervision of Dr. Abdolvahid Movahedirad and Prof. Thomas Keller. The analysis of the results was carried out by Ghazaleh Eslami in collaboration with Dr. Abdolvahid Movahedirad and Prof. Thomas Keller.

Chapter 3. Phenomenological model for pseudo-ductile adhesives

ship between stress and strain rate [5]. In thermoset polymers, the viscoelastic behavior is a result of molecular chain movements, which are both strain rate- and temperature-dependent [6]. Different applied strain rates can result in different mechanical responses in the polymer, varying from brittle to pseudo-ductile, with different yield load and post-yield behavior [7]. The thermoset molecular chain structure consists of both primary bonds (in the chains and cross-links between the chains, mainly covalent bonds) and secondary bonds (van der Waals and hydrogen bonds), whose strength decreases as the distance between the chains increases. The molecular chains in lightly cross-linked thermosets, denominated elastomer thermosets, are formed in random coils and are in an amorphous state [8]. Under applied low strain rates, the coiled chains have sufficient time to uncoil. After the yield point, chains start to lose secondary bonds and subsequently become aligned or stretched [9]. The stiffness thus significantly decreases and the deformability significantly increases; stretching may result in a hardening behavior. During unloading, the stretched chains tend to become coiled again and the secondary bonds reform. On the other hand, under high strain rates, the chains do not have sufficient time to rearrange and respond to the imposed displacement, and the molecular mobility of the chains is reduced. Consequently, the stiffness remains high and deformability low [10], [11]. Broken primary and lost secondary bonds contribute to the initiation and propagation of damage and energy dissipation in viscoelastic polymers [12]. Damage formation and propagation can change the viscoelastic behavior and parameters of polymers [13], [14]. Depending on the amount of energy dissipation, the response is brittle (low amount, at high strain rate or low temperature) or pseudo-ductile (high amount, at low strain rate or high temperature).

Comprehensive constitutive models are valuable assets for analysis and design purposes and a wide range of constitutive models has therefore been developed for viscoelastic materials. The simplest mechanical model for viscoelastic behavior consists of two elements, each representing a mechanical characteristic of the behavior: a spring and a dashpot (or damper). A Hookean (linear) spring and a Newtonian (linear) dashpot are used for modeling the elastic component and the viscous component, respectively, where the spring constant is the modulus of elasticity, E , and the dashpot constant is the viscosity, η [15]. Spring and dashpot elements can be combined in a variety of configurations to produce a desired viscoelastic response. Maxwell and Kelvin are the most basic models that combine a linear spring with a dashpot, in series and in parallel, respectively [16].

The combination of a simple spring and a dashpot element has been used since 1952 for simulating the rate-dependent behavior of viscoelastic materials [17]. The rheological representation of some of the constitutive models discussed in the following is shown in Fig. 3.1; the linearity or nonlinearity of the spring and dashpot (L = linear, N = nonlinear), and the number

of their parameters are indicated. The simplest combination of springs and dashpots to capture the recovery and relaxation of viscoelastic materials is the standard linear solid model (SLS Model), also known as Zener model which contains a spring in parallel to a Maxwell unit or a spring in series with a Kelvin unit (Fig. 3.1 (a) and (b)) [18]. Subsequently, in 1953, the generalized Maxwell model comprising an elastic spring in parallel with multiple Maxwell units [19] was established to represent linear viscoelasticity. The generalized Maxwell model was shown to be further applicable to the nonlinear viscoelastic behavior [20], and for different classes of polymers such as cross-linked polymers [21], [22], and rubber-like elastomers [23]. However, the generalized Maxwell model typically involves a high number of parameters and high computational cost.

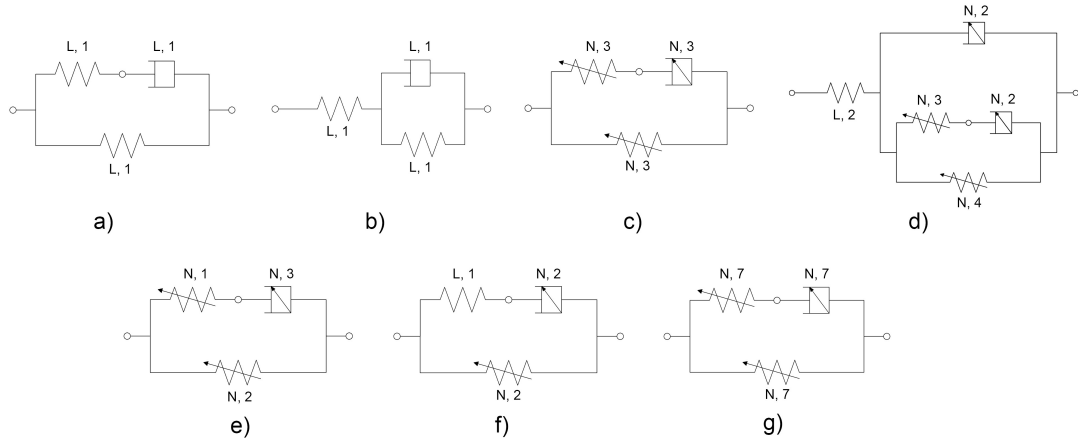


Figure 3.1: Rheological representation of the constitutive models (a) SLS model with Maxwell representation [18], (b) SLS model with Kelvin representation [18], (c) model addressed in Ref. [24], (d) [25], (e) [26], (f) [27], (g) [28] (L = linear, N = nonlinear).

Bergström and Boyce performed a study on the large-strain time-dependent behavior of elastomeric materials using two parallel units, one capturing the equilibrium response represented by a three-parameter nonlinear spring and the other one capturing the time-dependent response represented by another three parameter-nonlinear spring in series with a three-parameter nonlinear dashpot (Fig. 3.1 (c)) [24]. Later, they applied the concept of chain networks to simulate the viscoelastic behavior of highly cross-linked polyethylene materials [25]. Their model included 13 different parameters (Fig. 3.1 (d)) to decompose the mechanical behavior into an elastic and a time-dependent segment with a linear spring in series with a combination of nonlinear springs and dashpots, respectively. They found the model to be in good agreement for different strain rates and relaxation behavior.

Liu et al. [26] found that the initial Bergström and Boyce model (Fig. 3.1 (c)) was unable to identify the damage accumulation in filled rubbers to capture their rupture under cyclic

Chapter 3. Phenomenological model for pseudo-ductile adhesives

loading. Therefore, basing their model on a different theory, they proposed a model with different parameters but the same spring and dashpot combination as the Bergström and Boyce model (Fig. 3.1 (e)). Similarly, the parallel combination of a nonlinear spring with a nonlinear Maxwell unit (Fig. 3.1 (f)), including five parameters, used by Pramanik et al. [27], could only capture strain-hardening of different soft polymers, but not their stress-softening. To capture stress-softening, i.e. damage accumulation, Ayoub et al. [28] proposed a phenomenological model integrating the physics of polymer chains and their alteration under cyclic tension loading for rubber-like materials based on the Zener-type framework. Their proposed model comprised a nonlinear spring in parallel with a nonlinear Maxwell element, which itself was composed of a nonlinear spring in series with a nonlinear dashpot, see Fig. 3.1 (g), each containing seven parameters. In their model, they identified the average length of the chains and the average number of chains per unit volume as the physical parameters, increasing and decreasing due to the chain rearrangement, respectively. These two parameters were modified by a variable damage parameter. Their model was able to reproduce the cyclic tension response of a carbon black-filled rubber.

As previously mentioned, the structural behavior of pseudo-ductile composite adhesive joints mainly depends on the adhesive behavior. Therefore, in this study, to allow a simulation of the pseudo-ductile behavior of adhesively-bonded fiber-polymer composite joints under various applied displacement rates, a novel phenomenological model is proposed for the viscoelastic behavior of pseudo-ductile adhesives. The phenomenological model consists of two parallel units: a conventional-linear Maxwell unit characterizing the linear viscoelastic behavior before the onset of adhesive chain stretching, and an extended-nonlinear Maxwell unit with a variable stiffness spring that characterizes the nonlinear viscoelastic behavior during the molecular chain stretching. A novel constitutive equation is derived for modeling both the monotonic and reversed cyclic behavior of the pseudo-ductile adhesive, the latter is based on a novel cyclic decomposition. Supplementary to the models in the existing literature, the derived model is able to simulate a cyclic behavior with increasing amplitudes, taking into account strain hardening and softening. Furthermore, the model consists of the least possible number of elements and parameters so that it can be efficiently used in the numerical analyses of full-scale structural models under various loading conditions. The model parameters were calibrated with the results of monotonic and reversed cyclic experiments, previously performed in Ref. [29]. The focus of the model is to finally simulate the inelastic energy dissipation capacity, which is a measure of the pseudo-ductile behavior.

3.2 Summary of experimental work

3.2.1 Experimental setup

Double-lap joint specimens consisting of fiber-polymer composite adherends and a ductile adhesive were subjected to a series of monotonic tension and reversed cyclic tension-compression experiments; details of the experimental work and its motivation can be found in Ref. [29].

The joint geometry is shown in Fig. 3.2, the joint area was $100 \times 100 \text{ mm}^2$ and the adhesive layer thickness was 5 mm, which is in the range of applications in bridge and building construction [30], [31]. The adherends consisted of pultruded composite laminates composed of E-glass fibers and an isophthalic polyester resin. The adhesive was a structural two-part acrylic material, SikaFast®-5221 NT, supplied by Sika AG Switzerland. The load-displacement behavior of the adhesive is highly rate-dependent and pseudo-ductile at low to moderate displacement rates [32].

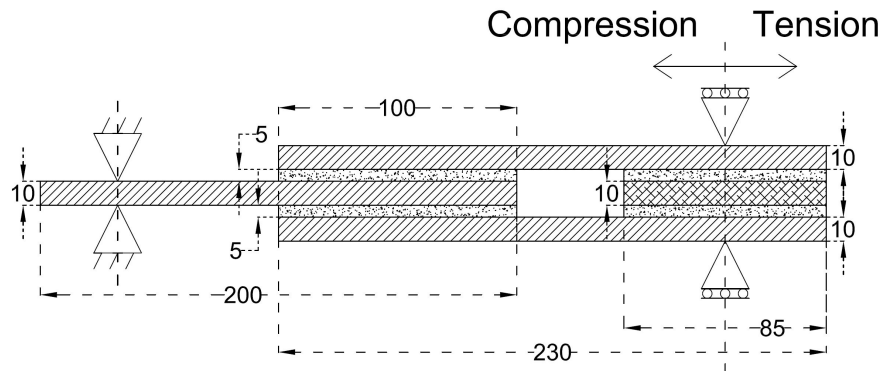


Figure 3.2: Longitudinal section of joint specimen, dimensions in (mm) [29].

The CUREE protocol [33] was selected for the cyclic loading since no such protocol exists for fiber-polymer composite joints. According to Refs. [33], [34], the reference displacement or amplitude of the applied cycles, Δ , is defined based on the load-displacement curves obtained from monotonic experiments, and is equal to 60% of the joint displacement at 80% of the maximum load, taken from the post-peak softening branch. The applied displacement history consisted of primary cycles, whose amplitude was continuously increased (by 50% above Δ), and two intermediate trailing cycles of 75% of the amplitude of the previous primary cycle, see Fig. 3.3. Three displacement rates of 0.1, 0.5, and 1.0 mm/s were used for the monotonic and cyclic experiments.

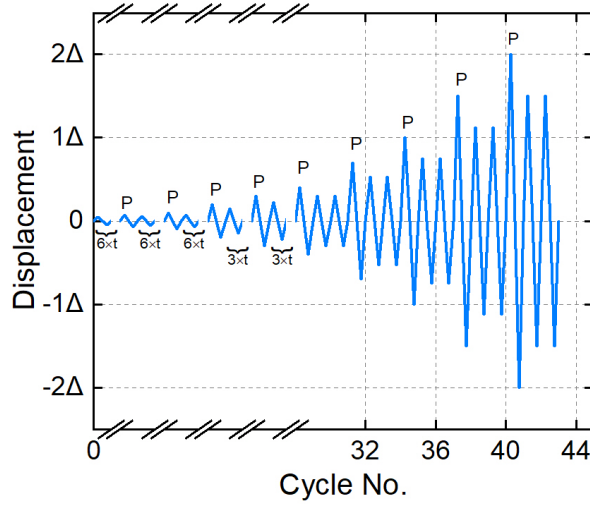


Figure 3.3: Cyclic displacement scheme (P = primary cycle, t = trailing cycle) [29].

The joint denominations included the joint type (A), loading type (Static or Cyclic), rate (0.1, 0.5, 1.0), and joint replicate (a or b). “A-S1.0b” for instance indicates the second adhesive joint under monotonic (static) loading at a rate of 1.0 mm/s.

3.2.2 Experimental results

The load-joint displacement responses of the adhesive joints under monotonic loading are summarized in Fig. 3.4. The yield loads and the displacements at failure were significantly influenced by the displacement rate, and their highest values were attained at the highest and lowest applied displacement rates, respectively. At the lowest rate, a significant hardening occurred in the post-yield branch.

The load-joint displacement responses under cyclic loading of one of the two specimens of each displacement rate are shown in Fig. 3.5. The remaining specimens showed consistent results. Due to the short segment or absence of the post-peak branch in the monotonic responses, Δ is considered to be 60% of the failure displacement, equal to 7.15, 2.9, and 2.3 mm for displacement rates of 0.1, 0.5, 1.0 mm/s, respectively. Since the trailing cycles always overlapped each other and also overlapped the subsequent primary cycle, only the primary cycles are shown, and their cycle number is indicated. The hysteresis loops were almost tension-compression symmetric in all cases. Specimens under the medium rate exhibited the highest number of cycles up to failure, followed by those under the lowest and highest rates. However, the failure displacements were similar for both the low and medium rates. The

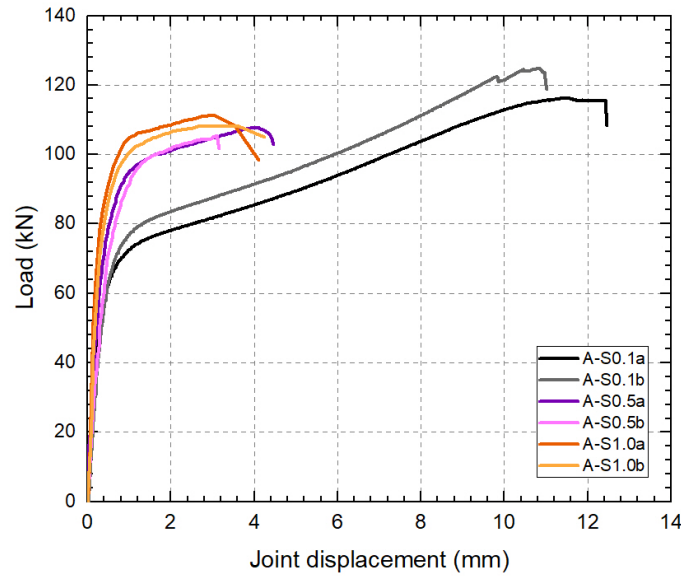


Figure 3.4: Load-joint displacement responses [29].

specimens failed after approximately 12 mm elongation in each direction, which was taken as the ultimate displacement capacity of the adhesive layer in the stretched molecular chains state (aligned to the loading direction), beyond which failure occurred.

The hysteresis loops under displacement rates of 0.1 and 0.5 mm/s in the tension-compression reversals were of a parabolic shape in the earlier cycles but then changed to a sigmoid shape in the later cycles. The changes in this behavior occurred at cycles no. 32 and 41 for displacement rates of 0.1 mm/s and 0.5 mm/s, respectively. The specimens under 1.0 mm/s displacement rate, however, failed before entering the sigmoid phase. Two opposing mechanisms of hardening due to molecule chain stretching, and softening due to microcrack formation and propagation were active under both the displacement rates of 0.1 and 0.5 mm/s. At 0.1 mm/s displacement rate, hardening dominated up to the penultimate primary cycle, indicated by an increasing slope of the post-yield branch, as well as an increasing level of the peak load in the sigmoid phase. At the 0.5 mm/s displacement rate, softening dominated up to the ultimate primary cycle indicated by a continuous decrease of the post-yield slope, as well as a decreasing level of the peak load in the sigmoid phase [29].

3.3 General phenomenological model

Since the laminate stiffness was significantly greater than the adhesive stiffness and the contribution of the laminates to the joint displacements was thus negligible [29], the measured joint

Chapter 3. Phenomenological model for pseudo-ductile adhesives

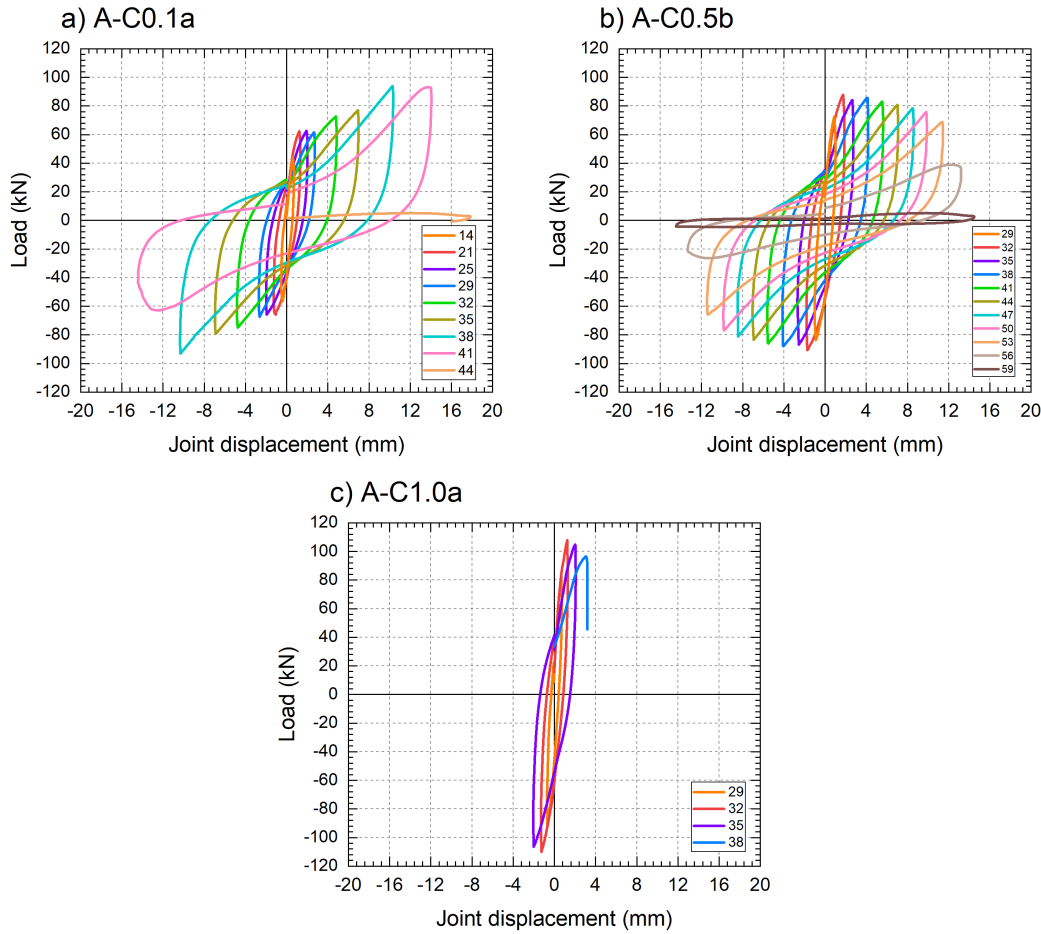


Figure 3.5: Load-joint displacement responses under cyclic loading, primary cycles of a) A-C0.1a, b) A-C0.5b, c) A-C1.0a [29].

displacements, shown in Fig. 3.4, Fig. 3.5, could be directly used for modeling the viscoelastic behavior of the adhesive. Furthermore, the displacement rate in the adhesive layer (internal displacement rate) was constant and equal to the applied displacement rate of the machine (external displacement rate) since the shear stress distribution in the adhesive layer was uniform due to the large post-yielding deformations [29]. Moreover, the load-displacement and stress-strain responses of the joints were equivalent; the strain rate in the adhesive was thus equal to the displacement rate of the joint specimens divided by the overlap length. The load-displacement responses and displacement rates are used in the following since they were directly measured and also used in Ref. [29].

The phenomenological model was derived from the monotonic responses and then also applied to the cyclic responses. This was possible since the responses between the two reversal

points of each cycle (Fig. 3.5), as well as the obtained envelop curves of the cyclic responses [29], exhibited similar nonlinear shapes as obtained from the monotonic responses. These similar shapes resulted from the same mechanisms of hardening and softening.

3.3.1 Constitutive equation

The investigated monotonic load-displacement curves were almost bilinear and thus consisted of two main branches, i.e., a pre-yield linear viscoelastic and a post-yield nonlinear viscoelastic branch, see Fig. 3.4. Consequently, a phenomenological model composed of two dissimilar parallel Maxwell units was introduced, as shown in Fig. 3.6 (a). The first (conventional-linear) Maxwell unit includes a spring of constant stiffness and a dashpot in series, while the second (extended-nonlinear) unit consists of a spring with variable stiffness and a dashpot in series. The first Maxwell unit simulates the rate-dependent initial branch up to the yield point level, during the uncoiling of the molecular chains up to the onset of the loss of secondary bonds, as shown in Fig. 3.6 (b) (red line). The second Maxwell unit simulates the nonlinear stiffening due to the molecular chains' rate-dependent stretching up to the failure level, see blue line in Fig. 3.6 (b). The two Maxwell units are parallel since they are acting concurrently during the specimen deformation. However, the contribution of the first unit is dominant prior to the yield point but becomes negligible beyond the yield point while the second unit acts in the opposite way.

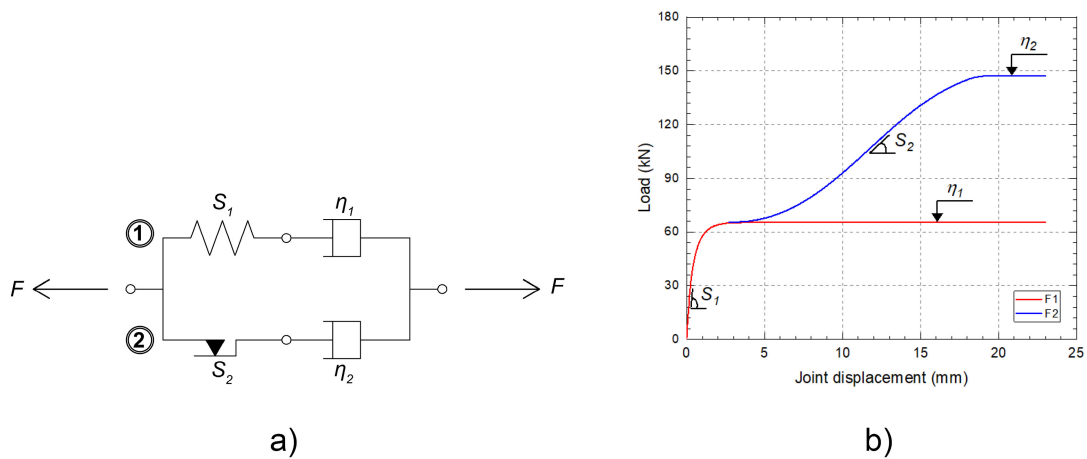


Figure 3.6: Rheological structure of phenomenological model.

A mathematical model can be derived by combining the constitutive relationships of each Maxwell unit, considering force-displacement equilibrium and boundary conditions as follows:

Chapter 3. Phenomenological model for pseudo-ductile adhesives

$$X = X_1 = X_2 = \dot{X} \cdot t \quad (3.1)$$

$$F = F_1 + F_2 \quad (3.2)$$

where X is the total applied displacement, equal to the displacements of the first and second Maxwell units (X_1, X_2) in [mm], \dot{X} is the applied displacement rate in [mm/s], and t is the time in [s]. Similarly, F is the total force, which is equal to the sum of the first and second Maxwell unit forces, F_1 and F_2 , respectively, in [kN].

The force-displacement relationships in the first and second Maxwell units can be expressed as follows [35]:

$$X = \left(\frac{1}{S_n} + \frac{1}{\eta_n \cdot \frac{\partial}{\partial t}} \right) \cdot F_n, \quad n = 1, 2 \quad (3.3)$$

where n is the number representing each of the Maxwell units. For the first Maxwell unit ($n = 1$), S_1 is the constant stiffness of the spring in [kN/mm], and η_1 is the viscosity coefficient of the dashpot in [kN.s/mm]. It should be noted that the displacement (or strain) rate is applied to the whole Maxwell unit and the force-displacement relationship of Eq. (3.3) was obtained, considering the respective internal strain rates of the Maxwell elements.

For the second Maxwell unit ($n = 2$), S_2 is the variable stiffness of the spring to simulate the chain stretching effect on the load-displacement response, and η_2 is the viscosity coefficient of the second dashpot. Since the chain stretching causes a nonlinear increase in the adhesive stiffness, S_2 can be defined by a power-law relationship as follows [36]:

$$S_2 = \alpha \left(\frac{X}{\dot{X}} \right)^\beta \quad (3.4)$$

where α and β are fitting parameters.

By substituting the displacement equation (Eq. (3.1)) into the Maxwell unit relationship (Eq. (3.3)) and Eq. (3.4), the total load (Eq. (3.2)) can be calculated as follows (see Appendix for more details):

$$F = \dot{X} \cdot \eta_1 (1 - e^{-\lambda_1 \cdot t}) + \dot{X} \cdot \eta_2 (1 - e^{-\frac{\lambda_2 \cdot t}{\beta+1}}) \quad (3.5)$$

where λ_1 and λ_2 are equal to S_1/η_1 and S_2/η_2 , respectively. Parameters S_1 , η_1 , α , β , and η_2 are considered as the viscoelastic parameters, to be determined for the development of the phenomenological model.

3.3.2 Parameter optimization method

The optimization method used to estimate the viscoelastic parameters solved a nonlinear least squares problem using the Trust Region Reflective (TRF) algorithm to apply error minimizing. The optimization task was performed using Scipy.optimize library [37] in Python. Details of the optimization method are as follows:

3.3.2.1 Nonlinear least square problem

In a nonlinear least square problem, the goal is to find a local minimum of the cost function $CF(x)$, i.e., Eq. (3.6), considering the residuals $cf_i(x)$ and the loss function rho with m sampling points [37], [38]:

$$\text{minimize } CF(x) = 0.5 \sum_{i=0}^{m-1} rho(cf_i(x)^2), lb \leq x \leq ub \quad (3.6)$$

The optimization parameter, x , is limited by the lower bound (lb) and the upper bound (ub) values, defined according to the mathematical and physical descriptions of the problem. The loss function rho is selected such that the effect of the outliers on the final solution is minimized. In this case, a standard linear loss function was selected as follows:

$$rho(CF(x)) = CF(x) \quad (3.7)$$

The residuals $cf_i(x)$ were calculated based on the difference between the experimental data and the estimations from the developed model.

3.3.2.2 Trust Region Reflective (TRF) algorithm

Trust region is a powerful optimization concept specifically suitable for large sparse problems with bounds [37]. This method was selected since the viscoelastic parameters subjected to optimization were bounded, see below.

Chapter 3. Phenomenological model for pseudo-ductile adhesives

3.3.2.3 Parameter initial values

The S_1 parameter is the representative parameter of the initial linear segment of the load-displacement curve. Therefore, the initial slope value of the load-displacement curve was set as its initial value.

The η_1 viscosity coefficient is a displacement rate-dependent parameter and mainly simulates the level at which the modeled load-displacement curve exhibits the initiation of yielding, see Fig. 3.6 (b). In this work, the initial value of η_1 was defined based on the yield displacement Δ_y [29], applied displacement rate \dot{X} , and initial value of S_1 as follows:

$$\eta_1 = S_1 \cdot \left(\frac{\Delta_y}{\dot{X}} \right) \quad (3.8)$$

The S_2 parameter contributes to the post-yield stiffness of the modeled response and is a function of α and β (Eq. (3.4)). The value of β should always be > 1.0 , considering the post-yield curvature of the load-displacement curves. Initial values of β equal to 1.1 and α according to the equation below, were assumed:

$$\begin{aligned} \text{monotonic: } \alpha \cdot \left(\frac{\Delta_{fail} - \Delta_y}{\dot{X}} \right)^\beta &= F_{fail} - F_y \\ \text{cyclic: } \alpha \cdot \left(\frac{X_c - \Delta_y}{\dot{X}} \right)^\beta &= F_{Xc} - F_y \end{aligned} \quad (3.9)$$

where Δ_{fail} is the displacement at failure (of monotonic and cyclic loading), F_{fail} is the load at failure, F_y is the yield load, X_c is the applied maximum displacement at each cycle, and F_{Xc} is the load at the maximum displacement of each cycle [29].

The η_2 parameter is a rate-dependent viscosity coefficient that mainly determines the level at which the modeled load-displacement curve exhibits the maximum load capacity in the post-yield segment, see Fig. 3.6 (b). Consequently, the initial value for this parameter was assumed as follows:

$$\begin{aligned} \text{monotonic: } \eta_2 &= S_2 \cdot \left(\frac{\Delta_{fail} - \Delta_y}{\dot{X}} \right) \\ \text{cyclic: } \eta_2 &= S_2 \cdot \left(\frac{X_c - \Delta_y}{\dot{X}} \right) \end{aligned} \quad (3.10)$$

A sensitivity analysis of initial values indicated that the final optimization results were not sensitive to alterations of up to 20% of the initial values defined according to the above-

3.4 Monotonic and cyclic viscoelastic parameter results

mentioned assumptions.

3.3.2.4 Parameter bounds

Parameter bounds are also important in an optimization method. They can effectively prevent convergence issues related to cases where the optimization algorithm is extremely over- or under-shooting in the parameter estimation. The parameter bounds should be representative of the valid value range of parameters while being small enough to remain effective. The lower and upper bound limits for the optimization parameters were considered as 0.5 and 1.5 times the initial values, respectively.

3.4 Monotonic and cyclic viscoelastic parameter results

The viscoelastic parameters were determined by the implementation of the aforementioned optimization algorithm for both the monotonic and cyclic experiments under the different applied displacement rates.

3.4.1 Rate-dependent monotonic viscoelastic parameters

The load-displacement responses, obtained from the derived constitutive equation, are shown in Fig. 3.7 for the applied displacement rates of 0.1, 0.5, and 1.0 mm/s. The modeled load-displacement behavior consists of an initial pre-yield linear segment, yield point, post-yield stiffening, and maximum load capacity. The models agree well with the experimental results. The slight differences in the pre-yield linear segments of the phenomenological model and experimental curves were mainly due to the contribution of the laminate deformations, which became negligible after the yield points since the deformations in the adhesive increased significantly.

The variations of the estimated viscoelastic parameters of the phenomenological model versus the applied displacement rates or joint displacement are shown in Fig. 3.8. The estimated values of S_1 , η_1 , η_2 , for the applied displacement rates of 0.1, 0.5, and 1.0 mm/s are shown with solid circles in Fig. 3.8 (a), (b), and (d) respectively, with added power-law fitted curves represented by dashed lines; the variable S_2 parameter is shown in Fig. 3.8 (c). By increasing the applied displacement rate, S_1 parameter increased, while η_1 , S_2 , and η_2 decreased.

Since a higher displacement rate results in a higher stiffness in the pre-yield linear branch [39], the S_1 parameter increased with an increase in the applied displacement rate (Fig. 3.8 (a)).

Chapter 3. Phenomenological model for pseudo-ductile adhesives

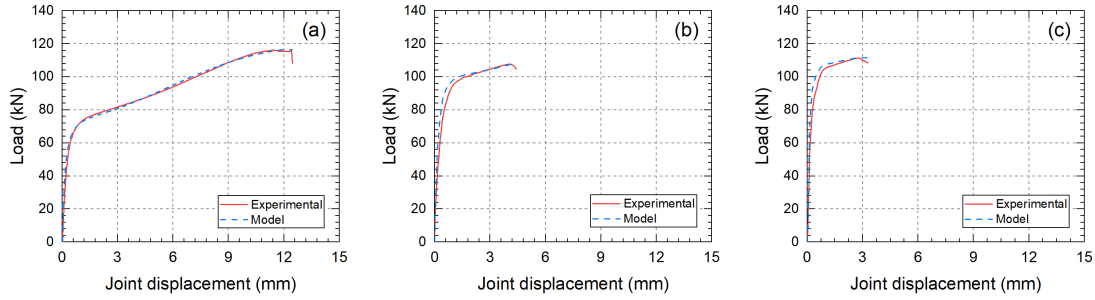


Figure 3.7: Phenomenological model and experimental load-displacement curves for displacement rates of: (a) 0.1 mm/s, (b) 0.5 mm/s, and (c) 1.0 mm/s.

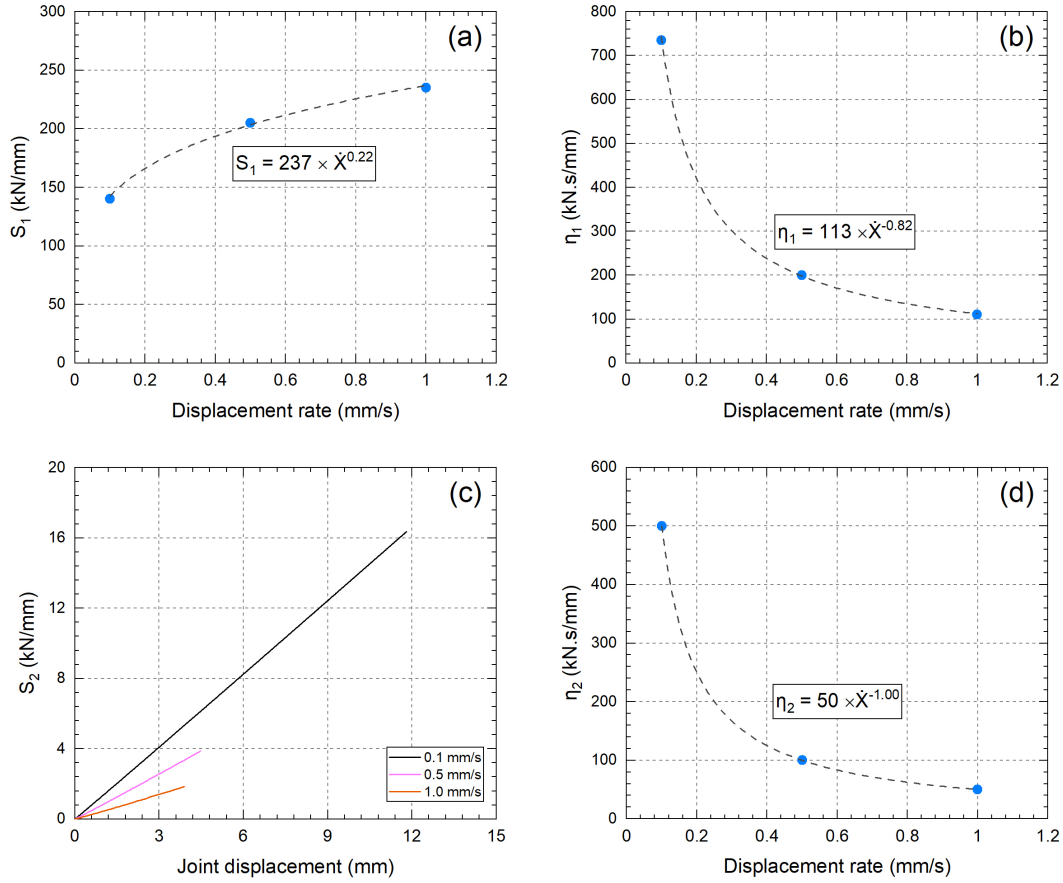


Figure 3.8: Rate-dependent variation of monotonic viscoelastic parameters a) S_1 , b) η_1 , c) S_2 , d) η_2 versus displacement rate.

Under lower applied displacement rates, the polymer chains had more time to uncoil and thus reach the onset of the loss of secondary bonds. Consequently, lower applied displacement rates resulted in higher η_1 values (Fig. 3.8 (b)).

3.4 Monotonic and cyclic viscoelastic parameter results

With the alignment of the stretched polymer chains along the load direction and the resulting hardening, the post-yield stiffness, S_2 parameter, was increasing with the applied displacement for all displacement rates (Fig. 3.8(c)). The lower the displacement rate, the more the polymer chains could become stretched and aligned. As a result, under the lowest applied displacement rate, the highest S_2 maximum value was obtained. The slope of the curves decreased with increasing displacement rate due to the formation and accumulation of damage. Finally, by increasing the displacement rate, a lower number of chains were aligned to the loading direction and participated in load bearing when the failure occurred. Therefore, the failure load level and, accordingly, the η_2 parameter, decreased (Fig. 3.8 (d)).

3.4.2 Rate-dependent cyclic viscoelastic parameters

3.4.2.1 Cycle decomposition

The cyclic responses of the specimens comprised primary and trailing cycles. At the reversal points of each primary cycle, specimens experienced the highest displacements and thus the highest degree of chain stretching. At the following trailing cycle reversal points, specimens underwent a lower displacement than in the previous primary cycle, resulting in less stretched or partially stretched chains. To take into account these different states at the reversal points, each response of the primary cycle was decomposed into two segments, as shown in Fig. 3.9, i.e., a segment starting 1) from the partially stretched state of the adhesive at the reversal point of the trailing cycle (T2 in Fig. 3.9 (a)) up to an almost fully stretched state at the first reversal point of the primary cycle (P1 in Fig. 3.9 (a)), and 2) from the latter (P1) to the also almost fully stretched state at the second reversal point of the primary cycle (P2). By translating the origin of the coordinate system for each segment of the cycles to the reversal point at their beginning, the decomposed segments of the cycles can be shown as in Fig. 3.9 (b) and (c). The nomenclature used for the curves is composed of a first number indicating the applied displacement rate, a second term indicating the segments starting from either the partially stretched state, “T-P”, or the almost fully stretched state, “P-P”, and a fourth number indicating the cycle number. Instead of “almost fully” just “fully” stretched state will be used in the following to clearly differentiate “partially” from “fully”. The trailing cycle responses up to their maximum displacements were fully overlapped by the response of the next primary cycle; they were thus not separately modeled.

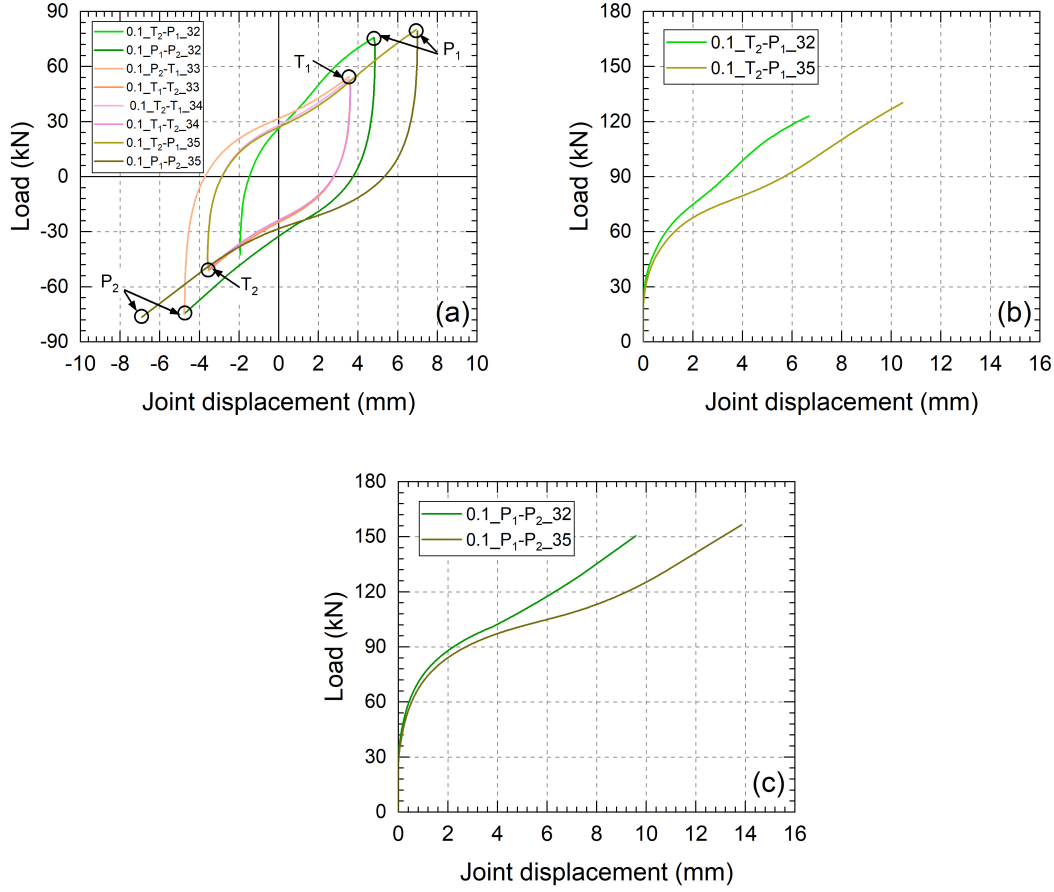


Figure 3.9: Decomposition of cycles of specimen A-C0.1a: a) cycle numbers 32–35 including primary cycles (T-P and P-P) and trailing cycles (P-T and T-T), b) segments T2-P1 (cycle nos. 32 and 35), and c) segments P1-P2 (nos. 32 and 35) of primary cycles.

3.4.2.2 Cyclic viscoelastic parameter estimation procedure

For each of the six combinations of displacement rate and segment (T-P and P-P) a power-law relationship was assumed between the viscoelastic parameters of the phenomenological model (S_1 , η_1 , α , β , η_2) and the maximum applied displacement at each primary cycle as follows:

$$S_{1,i} = a_{S1,i} \cdot X_c^{b_{S1,i}} \quad (3.11)$$

$$\eta_{1,i} = a_{\eta1,i} \cdot X_c^{b_{\eta1,i}} \quad (3.12)$$

$$\alpha_i = a_{\alpha,i} \cdot X_c^{b_{\alpha,i}} \quad (3.13)$$

3.4 Monotonic and cyclic viscoelastic parameter results

$$\beta_i = a_{\beta,i} \cdot X_c^{b_{\beta,i}} \quad (3.14)$$

$$\eta_{2,i} = a_{\eta_{2,i}} \cdot X_c^{b_{\eta_{2,i}}} \quad (3.15)$$

where a_{S1} , a_{η_1} , a_α , a_β , a_{η_2} , b_{S1} , b_{η_1} , b_α , b_β , b_{η_2} are parameter constants calibrated with the experimental results; and the subscript i for these parameters indicates the number of optimization iterations, see below.

The optimization procedure for the estimation of the viscoelastic parameters consists of two iterative steps, as shown in Fig. 3.10. In the first step, the viscoelastic parameters are estimated for each primary cycle according to Eq. (3.5), with R^2 higher than 0.95. For the first optimization iteration, $i = 1$, the initial values are selected as defined in Section 3.3.2.3. The estimation is performed for all of the primary cycles while the maximum cycle displacement, X_c , is lower than the ultimate displacement in the cyclic responses, Δ_{fail} . In the second step, the fitting parameters are estimated according to (3.11), (3.12), (3.13), (3.14), (3.15) so that each of the estimated viscoelastic parameters follows a power-law relationship with the maximum cycle displacement.

The viscoelastic parameters are then re-calculated using the estimated fitting parameters, which are set as the initial values for the next iteration ($i > 1$). The first and second steps are repeated until the normalized differences, e_i , of the estimated fitting parameters compared to their corresponding values of the last iteration (e.g., $e_{S1,i} = (a_{S1,i} - a_{S1,i-1}) / a_{S1,i-1}$) are lower than 0.1%.

3.4.2.3 Cyclic viscoelastic parameter development

The estimated viscoelastic parameters versus maximum cycle displacement (for S_1 , η_1 , and η_2) and cyclic displacement (for S_2), at each primary cycle, are shown in Fig. 3.11 for the applied displacement rates, for partially and fully stretched states. The S_2 and η_2 , parameters are not shown for the highest applied displacement rate of 1.0 mm/s due to the negligible amount of stretching.

The trends of the viscoelastic parameters were affected by two opposing mechanisms, i.e., 1) stiffening (hardening) caused by the molecular chain realignment and stretching in the direction of the applied displacements, and 2) softening caused by the damage formation and accumulation. The applied displacements generated a shear stress state in the adhesive layer of the joint, which could be decomposed into a concurrent set of compression and tension principal stresses. The tension component realigned and stretched the molecular

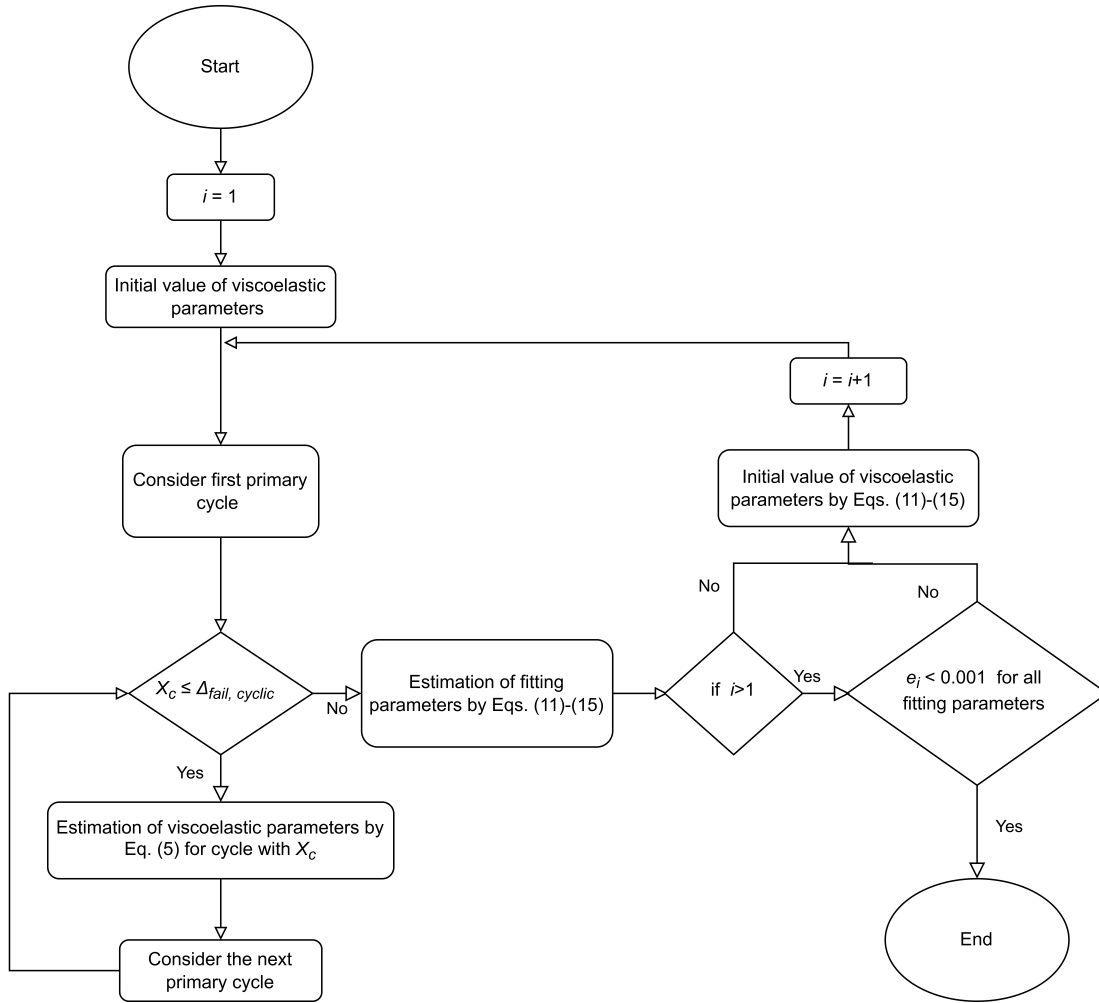


Figure 3.10: Cyclic viscoelastic parameter determination flowchart (Δ_{fail} = displacement at cyclic joint failure).

chains, leading to stiffening. At the displacement reversal point, the compression component induced “buckling” [40] of the stretched chains followed by realignment in the other direction due to the tension (which changed the direction). This continuous change of the molecular realignment caused damage, which accumulated until it became dominant over the stiffening and softening thus occurred.

The S_1 parameter values were initially higher at higher rates, see Fig. 3.11(a), but then decreased much faster than at the lower rate due to the higher loads (see Fig. 3.5), which increased damage formation and the associated softening. Damage accumulation, as described above, also decreased the stiffness at lower rates. No significant differences could be observed for either of the states starting from partially or fully stretched materials.

3.4 Monotonic and cyclic viscoelastic parameter results

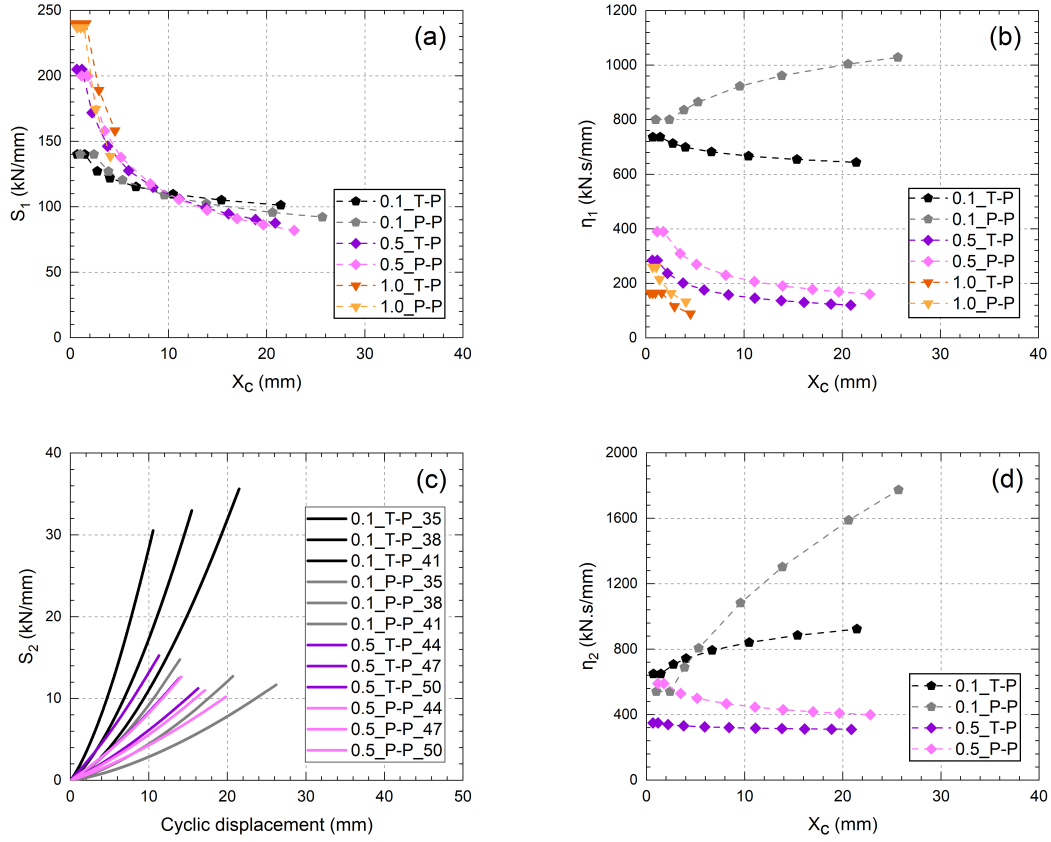


Figure 3.11: Variation of cyclic viscoelastic parameters, a) S_1 , b) η_1 , d) η_2 , versus maximum cycle displacement, and c) S_2 , versus cyclic displacement, under the applied displacement rates.

The η_1 parameter values were higher at the lower rate and followed a decreasing trend with increasing applied maximum cycle displacements for all cases, except for the initially fully stretched material under the lowest 0.1 mm/s displacement rate, see Fig. 3.11(b). The accumulated damage generally decreased the viscosity parameters of the linear segment. In 0.1_P-P, however, the decreasing trend was reversed since the highly stretched chains at the reversal point first resisted the reversed load until they “buckled” and could be realigned in the opposite direction. Consequently, with increasing displacement, i.e., degree of previous stretching, η_1 increased. In general, the η_1 values were higher for more stretched materials for the same reason.

The development of the S_2 parameter during each segment of the primary cycles is shown in Fig. 3.11(c). In all cases, the S_2 parameter exhibited an increasing trend due to an increasing number of aligned molecular chains with an increasing cyclic displacement. Under the lower applied displacement rate, in addition to the high number of secondary bonds lost

Chapter 3. Phenomenological model for pseudo-ductile adhesives

because of molecular chains having more time to deform, a low number of primary bonds were broken, i.e., damage was initiated, due to the large displacement increment of each cycle. In the segment of primary cycles starting from the partially stretched state, T-P (black curves), molecular chains were experiencing the highest cycle maximum displacements up to that cycle, leading to a high realignment of stretched molecular chains and thus high S_2 maximum values. Due to the higher stretching in cycles with higher displacement, the maximum S_2 values increased in the T-P segments from each primary cycle to the next, while the slope of the curves decreased due to damage formation. In the P-P segments, the maximum S_2 values and slope of the curves (gray lines) were lower than in the T-P segments due to a delay in stretching. The delay in stretching occurred since the highly stretched chains at the reversal point first buckled and recoiled before they could realign and stretch in the opposite direction. By increasing the cycle displacement, the delay in stretching in the opposite direction became more dominant and thus the S_2 maximum values decreased from each primary cycle to the next. At the higher applied displacement rate, many more cycles were required until similar displacements were reached as at the low rate, see cycle numbers in Fig. 3.11(c). Much more damage was thus accumulated, which decreased both the S_2 maximum values and the slopes of the curves.

The η_2 parameter values were higher and increased for the lower 0.1 mm/s rate, and lower and decreased for the higher 0.5 mm/s rate (Fig. 3.11 (d)). The increasing-decreasing trends of the η_2 values were in line with the trends of the peak loads of each primary cycle (Fig. 3.5), since the former were determined from the latter (Fig. 3.5). As mentioned in Section 3.2.2, the dominating hardening behavior at the lower rate increased the peak loads and thus η_2 , while the dominating softening at the higher rate decreased the peak loads and η_2 . The η_2 values were generally higher starting from the fully stretched (P-P) than from the partially stretched (T-P) state for maximum displacements of more than 4 mm due to the higher load amplitudes in the P-P segments (Fig. 3.9 (a)).

3.4.2.4 Cyclic viscoelastic parameter constant development

According to (3.11), (3.12), (3.13), (3.14), (3.15) and as shown above, the viscoelastic parameters of the developed phenomenological model all follow a power-law relationship with the applied maximum cycle displacement. Moreover, it could be derived that the parameter constants of (3.11), (3.12), (3.13), (3.14), (3.15) follow a power-law relationship with the applied displacement rate, except for b_{η_1} in fully stretched and b_{η_2} in both partially and fully stretched states, which follow a logarithmic relationship. The derived constant relationships for each of the viscoelastic parameters under the three applied displacement rates, for partially (T-P) or

3.4 Monotonic and cyclic viscoelastic parameter results

fully (P-P) stretched materials, are given in Table 3.1, Table 3.2.

Table 3.1: Cyclic viscoelastic parameter constant values of Eqs. (3.11), (3.12) and their relationships with displacement rate.

Disp. rate	Constants			
	S_1		η_1	
	a_{S1}	b_{S1}	$a_{\eta1}$	$b_{\eta1}$
0.1_T-P	142	-0.12	754	-0.06
0.5_T-P	215	-0.28	301	-0.30
1.0_T-P	265	-0.40	175	-0.40
Formula	$a_{S1} = 265 \times \dot{X}^{0.27}$	$b_{S1} = -0.4 \times \dot{X}^{0.53}$	$a_{\eta1} = 203 \times \dot{X}^{-0.57}$	$b_{\eta1} = -0.6 \times \dot{X}^{1.02}$
0.1_P-P	164	-0.17	697	0.12
0.5_P-P	226	-0.36	489	-0.36
1.0_P-P	260	-0.50	420	-0.57
Formula	$a_{S1} = 260 \times \dot{X}^{0.2}$	$b_{S1} = -0.5 \times \dot{X}^{0.48}$	$a_{\eta1} = 420 \times \dot{X}^{-0.22}$	$b_{\eta1} = -0.3 \times \dot{X}^{-0.57}$

Table 3.2: Cyclic viscoelastic parameter constant values of Eqs. (3.13), (3.14), (3.15) and their relationships with displacement rate.

Disp. rate	Constants					
	α		β		η_2	
	a_α	b_α	a_β	b_β	$a_{\eta2}$	$b_{\eta2}$
0.1_T-P	4.27	-2.05	1.09	0.11	627	0.13
0.5_T-P	56.1	-2.15	1.17	0.03	324	-0.03
1.0_T-P	170	-2.20	1.20	0.02	244	-0.10
Formula	$a_\alpha = 170 \times \dot{X}^{1.6}$	$b_\alpha = -2.2 \times \dot{X}^{-0.03}$	$a_\beta = 1.2 \times \dot{X}^{-0.04}$	$b_\beta = 0.02 \times \dot{X}^{-0.75}$	$a_{\eta2} = 244 \times \dot{X}^{-0.41}$	$b_{\eta2} = -0.1 \times \ln \dot{X} - 0.1$
0.1_P-P	6.02	-2.40	1.21	0.07	351	0.49
0.5_P-P	39.6	-2.08	1.13	0.04	569	-0.15
1.0_P-P	70.0	-2.04	1.10	0.03	700	-0.43
Formula	$a_\alpha = 89 \times \dot{X}^{1.17}$	$b_\alpha = -1.95 \times \dot{X}^{-0.09}$	$a_\beta = 1.1 \times \dot{X}^{-0.04}$	$b_\beta = 0.03 \times \dot{X}^{-0.36}$	$a_{\eta2} = 700 \times \dot{X}^{0.3}$	$b_{\eta2} = 0.4 \times \ln \dot{X} - 0.43$

Knowing that the viscoelastic parameter constants are related to the displacement rates by the relationships given in Table 3.1, Table 3.2, they can be estimated for any other applied displacement rate within the range of 0.1–1.0 mm/s. The viscoelastic parameters can then be

calculated accordingly, and the cyclic responses for the partially or fully stretched state of the material can be obtained.

3.5 Model validation and application

3.5.1 Contributions of first and second Maxwell units

The comparison between the modeled cyclic responses (“mod”) and the corresponding experimental (“exp”) results of primary cycle numbers 41, 44, 47 and 50, starting from their fully stretched state (P), are represented in Fig. 3.12(a) at the medium displacement rate, while Fig. 3.12(b) shows the applied forces (F) and how they are composed of the F_1 and F_2 forces of the individual Maxwell units, according to Eq. (3.2). A good agreement between the phenomenological model predictions and experimental results is demonstrated; the yield points, stretching and softening are well modeled by the constitutive equation. Concerning load sharing, the load increased up to the yield point obtained from the first Maxwell unit (F_1 curves); beyond that point, the first unit no longer contributed (plateau of the red curves). The second Maxwell unit was then activated, beyond the yield point (blue F_2 curves), representing the effects of stretching, and the loads were further increased (dashed curves).

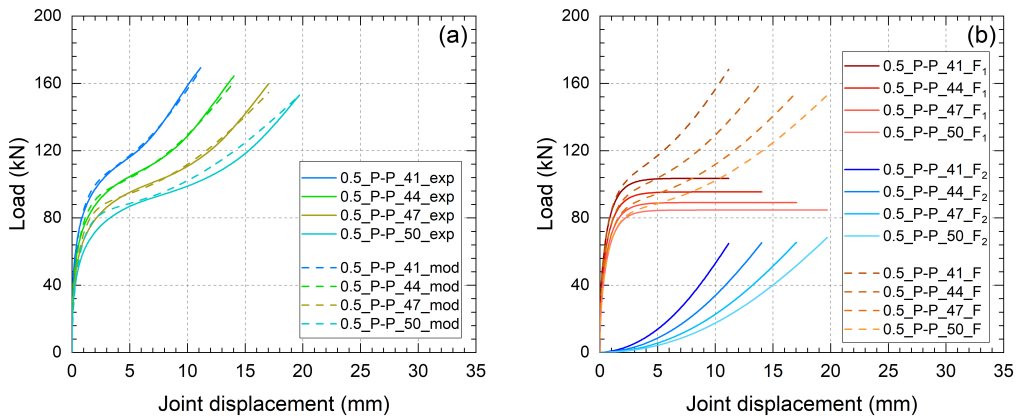


Figure 3.12: (a) Experimental and modeled load-displacement responses of P-P segments for 0.5 mm/s displacement rate, and (b) load sharing between first and second Maxwell units.

3.5.2 Full cycle and envelope curves comparisons

The full cyclic responses of the experimental and phenomenological model under the displacement rate of 0.1 mm/s are compared in Fig. 3.13 (a). The model cyclic curves in Fig. 3.13 (a) were constructed by joining the partially stretched segments, at their peak points, to the reflected fully stretched segments about their origin. The comparison reveals a good agreement between experimental and modeling results.

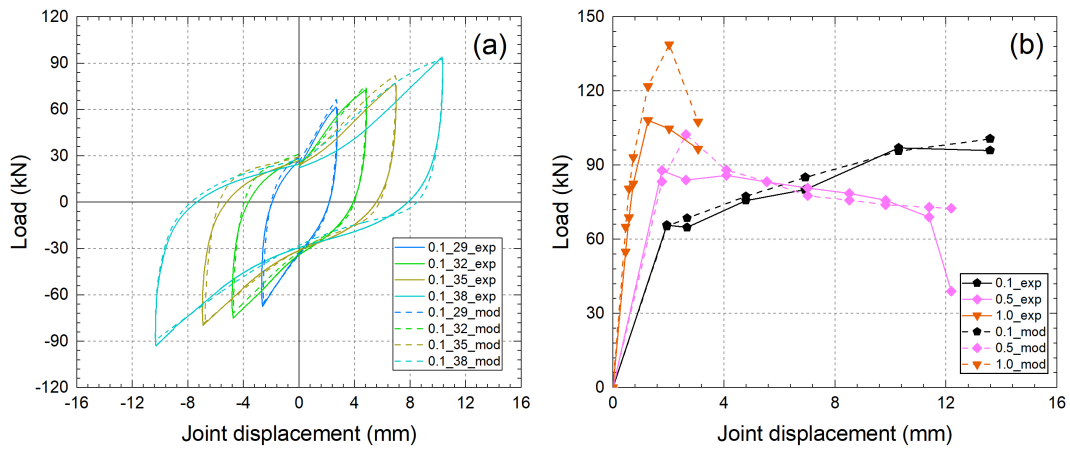


Figure 3.13: (a) Experimental and modeled load-displacement responses of full cycles for 0.1 mm/s displacement rate (specimen A-C0.1a), and (b) experimental and modeled envelope curves for displacement rates of 0.1 mm/s (specimen A-C0.1a), 0.5 mm/s (A-C0.5b), and 1.0 mm/s (A-C1.0a) at P_1 reversal points.

The envelope curves of the experimental cyclic responses, shown in Fig. 3.5, and of the modeled cyclic responses, are further compared in Fig. 3.13 (b). They were constructed by connecting the P_1 peak loads. The comparison reveals that the hardening behavior under 0.1 mm/s and the softening behavior under 0.5 mm/s displacement rate were well represented in the model. The results further show that the peak loads of the final cycles, particularly at 1.0 mm/s, were not well simulated. This is because the final failure, i.e., the complete breakage of the primary bonds, is not comprised in the model. Adding a third parallel unit to the model, consisting of a dashpot element, would also allow the simulation of this last sequence.

The comparison between the curves in Fig. 3.13 validates the capacity of the decomposition procedure and the phenomenological model to simulate the entire cyclic load-displacement behavior of the specimens under the applied displacement rates.

3.5.3 Energy dissipation

Since the energy dissipation capacity is a measure to assess the ductility of a material or structural system, the energy dissipation per primary cycle, obtained from experiments and the model, was determined and compared in Fig. 3.14, for the displacement rates of 0.1 and 0.5 mm/s. The dissipated cyclic energy of the experimental results was obtained from the enclosed area of the load-joint displacement hysteresis loops [41] shown in Fig. 3.5. The dissipated energy values of the model were taken as the enclosed area between the load-displacement responses of the partially stretched and fully stretched segments of each cycle shown in Fig. 3.9, whereby the partially stretched segment was connected at the peak point to the fully stretched segment, reflected about its origin.

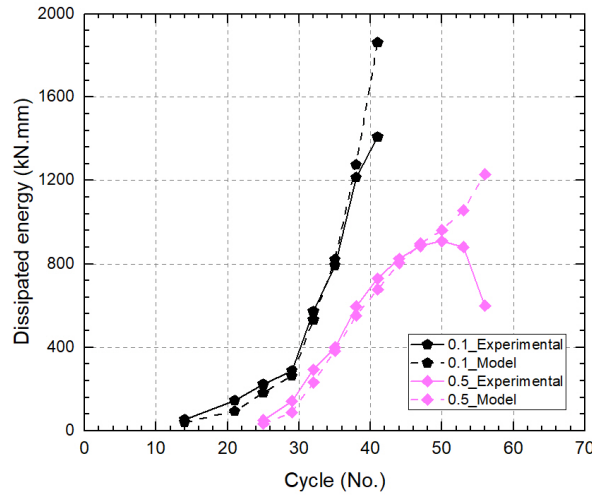


Figure 3.14: Dissipated energy per primary cycle from experimental results and model for displacement rates of 0.1 mm/s (specimen A-C0.1a) and 0.5 mm/s (A-C0.5b).

The greatest amount of energy per cycle was dissipated in the specimens under the lowest displacement rate since the imposed displacements per cycle were higher [29]. Experimental and modeling results agree well in up to approximately 90% of the cycles and thus further validate the model. As mentioned in Section 3.5.2, the significant drops in the peak loads are not covered in the model. Therefore, the dissipated energy for the last cycles, obtained from the model, was overestimated in Fig. 3.14.

3.6 Conclusions

A new phenomenological model was presented, allowing the simulation of the rate-dependent load-displacement responses of a pseudo-ductile adhesive joint under axial monotonic and

cyclic loading. The phenomenological model assumes that the rate-dependent monotonic and decomposed segments of the cyclic responses can be represented by two parallel acting Maxwell units, one conventional-linear and the other extended-nonlinear. By calibrating the viscoelastic parameters of the phenomenological model with the results from experimental monotonic and cyclic investigations, it could be concluded that:

1. The two Maxwell units of the phenomenological model were able to well simulate the rate-dependent pre-yield and post-yield branches of both monotonic and decomposed cyclic responses.
2. The viscoelastic parameters of the Maxwell units did capture well the physical characteristics of the adhesive in both monotonic and decomposed cyclic responses, such as stretching of molecular chains (i.e., strain hardening), and formation and accumulation of damage (i.e., softening) that were captured by the extended-nonlinear Maxwell unit.
3. The effects of the applied displacement rate on the monotonic loading behavior were well represented by power-law relationships between the monotonic viscoelastic parameters and the applied displacement rates.
4. The development of the cyclic viscoelastic parameters could be well related to the maximum cycle displacement by power-law relationships, for each of the decomposed segments and each displacement rate.
5. The constants of the cyclic viscoelastic parameters were related to the applied displacement rate by power-law or exponential relationships. The phenomenological model can thus predict the cyclic responses of the adhesive under any given displacement rate by interpolation.
6. The proposed model could well predict the cyclic envelope curves and the cyclic energy dissipation, except the final failure values of the last cycles. To also model the final chain scission, a third parallel unit could be added to the model, consisting of a dashpot element.
7. The proposed model can be applied to predict the load-bearing behavior of the ductile adhesive under both monotonic and cyclic loading for other displacement rates in the range of 0.1–1.0 mm/s.

Appendix

3.A.1 General relationships

The joint displacement at a constant rate is:

$$X = \dot{X} \cdot t \quad (3.A.1)$$

The constitutive equation for a Maxwell unit consisting of a spring and a dashpot is presented in Eq. (3.3), which can be rearranged as follows [35]:

$$X = \left(\frac{\eta_n \frac{\partial}{\partial t} + S_n}{S_n \cdot \eta_n \frac{\partial}{\partial t}} \right) \cdot F_n \rightarrow S_n \cdot \eta_n \cdot \frac{\partial X}{\partial t} = \eta_n \cdot \frac{\partial F_n}{\partial t} + S_n \cdot F_n, \quad n = 1, 2 \quad (3.A.2)$$

By inserting Eq. (3.A.1) into Eq. (3.A.2), the following equation is obtained:

$$S_n \cdot \eta_n \cdot \dot{X} = \eta_n \cdot \frac{\partial F_n}{\partial t} + S_n \cdot F_n \quad (3.A.3)$$

By dividing Eq. (3.A.2) by η and substituting the resulting S/η with λ , the following relationship is obtained:

$$S_n \cdot \dot{X} = \frac{\partial F_n}{\partial t} + \lambda_n \cdot F_n \quad (3.A.4)$$

3.A.2 Solution for the first Maxwell unit

To find the relationship of F_1 with the other parameters, Eq. (3.A.4) must be integrated. To enable integration, the integration factor $e^{\lambda_1 \cdot t}$ is multiplied to both sides of Eq. (3.A.4), as follows:

$$\int \left(S_1 \cdot \dot{X} \cdot e^{\lambda_1 \cdot t} \right) dt = \int \left[\left(\frac{\partial F_1}{\partial t} \right) e^{\lambda_1 \cdot t} + \lambda_1 \cdot F_1 \cdot e^{\lambda_1 \cdot t} \right] dt \quad (3.A.5)$$

By integrating, substituting $\lambda = S/\eta$, and rearranging the resulting equation, the following relationship is obtained:

$$F_1 = \dot{X} \cdot \eta_1 + \frac{C_1}{e^{\lambda_1 \cdot t}} \quad (3.A.6)$$

As shown in Fig. 3.5, the load function for each Maxwell unit reaches a plateau at a certain point and therefore could be described by a sigmoid function. Consequently, C_1 was assumed to be $C_1 = -\dot{X} \cdot \eta_1$, and the following relationship is obtained:

$$F_1 = \dot{X} \cdot \eta_1 \left(1 - e^{-\lambda_1 \cdot t} \right) \quad (3.A.7)$$

3.A.3 Solution for the second Maxwell unit

A similar procedure was applied for the second Maxwell unit, however, due to the time dependency of S_2 and λ_2 , a different integration factor $\frac{\lambda_2 \cdot t}{e^{\beta+1}}$ was multiplied to both sides of Eq. (3.A.4), as follows:

$$\begin{aligned} \int (S_2 \cdot \dot{X} \cdot \exp(\frac{\lambda_2 \cdot t}{\beta+1})) dt = \\ \int \left[\left(\frac{\partial F_2}{\partial t} \right) \exp(\frac{\lambda_2 \cdot t}{\beta+1}) + \lambda_2 \cdot F_2 \cdot \exp(\frac{\lambda_2 \cdot t}{\beta+1}) \right] dt \end{aligned} \quad (3.A.8)$$

By substituting S_2 from Eq. (3.A.4) and $\lambda = S/\eta$:

$$\begin{aligned} \int (\alpha \cdot t^\beta \cdot \dot{X} \cdot \exp(\frac{\alpha \cdot t^{\beta+1}}{\eta_2 \cdot (\beta+1)})) dt = \\ \int \left[\left(\frac{\partial F_2}{\partial t} \right) \exp(\frac{\alpha \cdot t^{\beta+1}}{\eta_2 \cdot (\beta+1)}) + \frac{\alpha \cdot t^\beta}{\eta_2} \cdot F_2 \cdot \exp(\frac{\alpha \cdot t^{\beta+1}}{\eta_2 \cdot (\beta+1)}) \right] dt \end{aligned} \quad (3.A.9)$$

By integrating and rearranging Eq. (3.A.9), the following equation is obtained:

$$\frac{\alpha \cdot \dot{X}}{\beta+1} \left(\left(\frac{\eta_2 (\beta+1)}{\alpha} \right) \exp \left(\frac{\alpha \cdot t^{\beta+1}}{\eta_2 \cdot (\beta+1)} \right) + c_3 \right) = F_2 \cdot \exp \left(\frac{\lambda_2 \cdot t}{\beta+1} \right) + c_4 \quad (3.A.10)$$

And finally, the following equation results:

$$F_2 = \dot{X} \cdot \eta_2 + \frac{C_2}{\exp(\frac{\lambda_2 \cdot t}{\beta+1})} \quad (3.A.11)$$

Chapter 3. Phenomenological model for pseudo-ductile adhesives

The same assumption as for C_1 can be applied for C_2 , and therefore $C_2 = -\dot{X} \cdot \eta_2$ was assumed. The following relationship is consequently obtained:

$$F_2 = \dot{X} \cdot \eta_2 \left(1 - \exp\left(-\frac{\lambda_2 \cdot t}{\beta + 1}\right) \right) \quad (3.A.12)$$

Substituting [3.A.7](#) and [3.A.12](#) into Eq. [\(3.2\)](#) yields the equation Eq. [\(3.5\)](#).

References

- [1] M. Angelidi, A. P. Vassilopoulos, and T. Keller, “Ductile adhesively-bonded timber joints–part 1: Experimental investigation”, *Construction and Building Materials*, vol. 179, pp. 692–703, 2018.
- [2] T. Keller and J. de Castro, “System ductility and redundancy of frp beam structures with ductile adhesive joints”, *Composites Part B: Engineering*, vol. 36, no. 8, pp. 586–596, 2005.
- [3] J. Lancaster, “The use of adhesives for making structural joints”, *Metallurgy of Welding*, vol. 6, pp. 54–84, 1999.
- [4] L. Hollaway, *Key issues in the use of fiber-reinforced polymer (frp) composites in the rehabilitation and retrofitting of concrete structures: Chapter 1, service life estimation and extension of civil engineering structures*, 2011.
- [5] H.-H. Kausch, *Polymer fracture*. Springer Science & Business Media, 2012, vol. 2.
- [6] I. M. Ward and J. Sweeney, *Mechanical properties of solid polymers*. John Wiley & Sons, 2012.
- [7] M. Angelidi, A. P. Vassilopoulos, and T. Keller, “Displacement rate and structural effects on poisson ratio of a ductile structural adhesive in tension and compression”, *International Journal of Adhesion and Adhesives*, vol. 78, pp. 13–22, 2017.
- [8] J. E. Mark, “Thermoset elastomers”, in *Applied Plastics Engineering Handbook*, Elsevier, 2017, pp. 109–125.
- [9] D. R. Askeland, P. P. Phulé, W. J. Wright, and D. Bhattacharya, “The science and engineering of materials”, 2003.
- [10] J. Foreman, D. Porter, S. Behzadi, P. Curtis, and F. Jones, “Predicting the thermomechanical properties of an epoxy resin blend as a function of temperature and strain rate”, *Composites Part A: Applied Science and Manufacturing*, vol. 41, no. 9, pp. 1072–1076, 2010.
- [11] S.-Q. Wang, S. Ravindranath, Y. Wang, and P. Boukany, “New theoretical considerations in polymer rheology: Elastic breakdown of chain entanglement network”, *The Journal of chemical physics*, vol. 127, no. 6, p. 064 903, 2007.

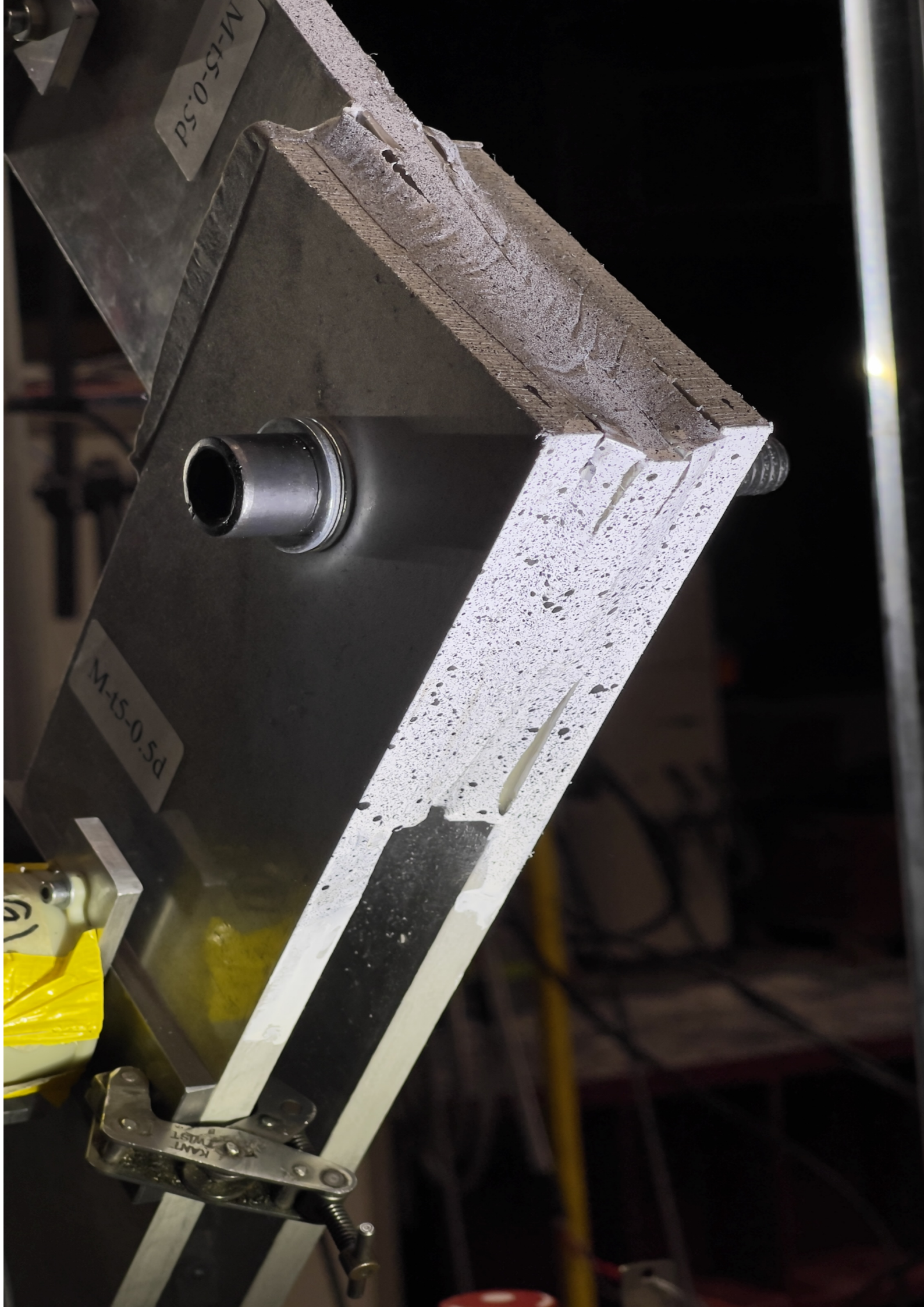
Chapter 3. Phenomenological model for pseudo-ductile adhesives

- [12] R. A. Deblieck, D. Van Beek, K. Remerie, and I. M. Ward, “Failure mechanisms in polyolefines: The role of crazing, shear yielding and the entanglement network”, *Polymer*, vol. 52, no. 14, pp. 2979–2990, 2011.
- [13] S. E. Rangarajan and K. K. Ramarathnam, “Viscoelastic properties of natural rubber with fatigue damage”, *International Journal of Fatigue*, vol. 150, p. 106 344, 2021.
- [14] A. V. Movahedi-Rad, T. Keller, and A. P. Vassilopoulos, “Interrupted tension-tension fatigue behavior of angle-ply gfrp composite laminates”, *International Journal of Fatigue*, vol. 113, pp. 377–388, 2018.
- [15] H. F. Brinson, L. C. Brinson, *et al.*, “Polymer engineering science and viscoelasticity”, *An introduction*, pp. 99–157, 2008.
- [16] T. Alfrey and P. Doty, “The methods of specifying the properties of viscoelastic materials”, *Journal of applied physics*, vol. 16, no. 11, pp. 700–713, 1945.
- [17] F. Schwarzl and A. Staverman, “Time-temperature dependence of linear viscoelastic behavior”, *Journal of Applied Physics*, vol. 23, no. 8, pp. 838–843, 1952.
- [18] D. R. Bland, *The theory of linear viscoelasticity*. Courier Dover Publications, 2016.
- [19] P. E. Rouse Jr, “A theory of the linear viscoelastic properties of dilute solutions of coiling polymers”, *The Journal of Chemical Physics*, vol. 21, no. 7, pp. 1272–1280, 1953.
- [20] W. N. Findley and F. A. Davis, *Creep and relaxation of nonlinear viscoelastic materials*. Courier corporation, 2013.
- [21] Q. Xu and B. Engquist, “A mathematical model for fitting and predicting relaxation modulus and simulating viscoelastic responses”, *Proceedings of the Royal Society A: Mathematical, Physical and Engineering Sciences*, vol. 474, no. 2213, p. 20 170 540, 2018.
- [22] J. Diani, P. Gilormini, C. Frédy, and I. Rousseau, “Predicting thermal shape memory of crosslinked polymer networks from linear viscoelasticity”, *International Journal of Solids and Structures*, vol. 49, no. 5, pp. 793–799, 2012.
- [23] C. Barres, A. Mongruel, M. Cartault, and J. Leblanc, “Linear and nonlinear viscoelasticity of carbon black filled elastomers: Use of complementary rheological characterizations”, *Journal of applied polymer science*, vol. 87, no. 1, pp. 31–41, 2003.

-
- [24] J. S. Bergström and M. Boyce, “Constitutive modeling of the large strain time-dependent behavior of elastomers”, *Journal of the Mechanics and Physics of Solids*, vol. 46, no. 5, pp. 931–954, 1998.
- [25] J. Bergström, C. Rimnac, and S. Kurtz, “An augmented hybrid constitutive model for simulation of unloading and cyclic loading behavior of conventional and highly crosslinked uhmwpe”, *Biomaterials*, vol. 25, no. 11, pp. 2171–2178, 2004.
- [26] M. Liu and M. S. H. Fatt, “A constitutive equation for filled rubber under cyclic loading”, *International Journal of Non-Linear Mechanics*, vol. 46, no. 2, pp. 446–456, 2011.
- [27] R. Pramanik, F. Soni, K. Shanmuganathan, and A. Arockiarajan, “Mechanics of soft polymeric materials using a fractal viscoelastic model”, *Mechanics of Time-Dependent Materials*, pp. 1–14, 2021.
- [28] G. Ayoub, F. Zairi, M. Nait-Abdelaziz, J.-M. Gloaguen, and G. Kridli, “A visco-hyperelastic damage model for cyclic stress-softening, hysteresis and permanent set in rubber using the network alteration theory”, *International Journal of Plasticity*, vol. 54, pp. 19–33, 2014.
- [29] G. Eslami, S. Yanes-Armas, and T. Keller, “Energy dissipation in adhesive and bolted pultruded gfrp double-lap joints under cyclic loading”, *Composite Structures*, vol. 248, p. 112 496, 2020.
- [30] T. Keller, J. Rothe, J. De Castro, and M. Osei-Antwi, “Gfrp-balsa sandwich bridge deck: Concept, design, and experimental validation”, *Journal of Composites for Construction*, vol. 18, no. 2, p. 04 013 043, 2014.
- [31] T. Keller and H. Gürtler, “Design of hybrid bridge girders with adhesively bonded and compositely acting frp deck”, *Composite structures*, vol. 74, no. 2, pp. 202–212, 2006.
- [32] M. Angelidi, A. P. Vassilopoulos, and T. Keller, “Ductility, recovery and strain rate dependency of an acrylic structural adhesive”, *Construction and Building Materials*, vol. 140, pp. 184–193, 2017.
- [33] H. Krawinkler, F. Parisi, L. Ibarra, A. Ayoub, and R. Medina, *Development of a testing protocol for woodframe structures*. CUREe Richmond, CA, 2001, vol. 102.

Chapter 3. Phenomenological model for pseudo-ductile adhesives

- [34] ASTM, “Standard test methods for cyclic (reversed) load test for shear resistance of vertical elements of the lateral force resisting systems for buildings”, *ASTM E2126*, 2019.
- [35] J. D. Ferry, *Viscoelastic properties of polymers*. John Wiley & Sons, 1980.
- [36] A. V. Movahedi-Rad, G. Eslami, and T. Keller, “A novel fatigue life prediction methodology based on energy dissipation in viscoelastic materials”, *International Journal of Fatigue*, vol. 152, p. 106 457, 2021.
- [37] P. Virtanen, R. Gommers, T. E. Oliphant, *et al.*, “Scipy 1.0: Fundamental algorithms for scientific computing in python”, *Nature methods*, vol. 17, no. 3, pp. 261–272, 2020.
- [38] “Scipy.optimize.least_squares - scipy v1.10.1 manual”. (2020), [Online]. Available: https://docs.scipy.org/doc/scipy/reference/generated/scipy.optimize.least_squares.html#scipy.optimize.least_squares.
- [39] J. Gero, *Design optimization*. Elsevier, 2012.
- [40] C. Kurzthaler, “Elastic behavior of a semiflexible polymer in 3d subject to compression and stretching forces”, *Soft Matter*, vol. 14, no. 37, pp. 7634–7644, 2018.
- [41] S. Yanes-Armas, J. de Castro San Roman, and T. Keller, “Energy dissipation in web-flange junctions of pultruded gfrp decks”, in *Proceedings of the 20th International Conference on Composite Materials*, 2015.



Experimental investigation of rotational behavior of pseudo-ductile adhesive angle joints exhibiting variable strain rate

Authors: Ghazaleh Eslami*, Abdolvahid Movahedirad*, Thomas Keller*

* Composite Construction Laboratory, École Polytechnique Fédérale de Lausanne (EPFL), Switzerland

4.1 Introduction

The escalating global demand for lightweight yet durable structural components has led to the adoption of pultruded glass fiber-polymer composite laminates in a variety of construction applications. Composite laminates confer significant benefits, including a high strength-to-weight ratio, corrosion resistance, and expedited erection [1]. Nevertheless, the intrinsic brittleness of glass composite laminates may result in catastrophic failure of composite structures under diverse loading conditions [2]. To circumvent such catastrophic failures, enhancing the ductility of composite structures is imperative, which can be achieved by enhancing their connections, such as bridge deck-girders or beam-column connections, through the introduction of pseudo-ductility. Pseudo-ductility in this respect is understood as nonlinear response caused by progressive damage and associated energy dissipation [3]. Options to achieve pseudo-ductility in the connections are the use of either adhesive-bolt combinations [4] or pseudo-ductile adhesives [5]. Pseudo-ductility in the connections augments the performance of fiber-polymer composite pultruded structures, mainly by increasing their energy dissipation capacity [6].

Contributions: Ghazaleh Eslami conceived, designed and performed the experimental campaign under the supervision of Dr. Abdolvahid Movahedirad and Prof. Thomas Keller. The analysis of the results and development of analytical models were carried out by Ghazaleh Eslami under supervision of Dr. Abdolvahid Movahedirad and Prof. Thomas Keller.

Chapter 4. Pseudo-ductile adhesive angle double lap joints

Since the 1990s, researchers have been investigating hybrid and bolted pultruded beam-column connection configurations with the aim of attaining superior mechanical performance to conventional bolted joints. Bank et al. [7] and [8] conducted comparative analyses of rotational stiffness, strength, and failure modes for eight full-scale glass composite beam-column connections. Among those, six connections comprised different configurations of pultruded angles and built-up components bolted to both beams and columns, while the remaining two were hybrid bolted-bonded beam-column connections using an epoxy adhesive. They found that the studied hybrid connections demonstrated higher rotational stiffness and moment strength. Subsequently, Smith et al. [9] conducted an experimental study on the behavior of the hybrid connections proposed by Bank et al. with pultruded glass composite I- and box-section profiles. Their findings emphasized the superior performance of box-section connections in terms of strength and stiffness relative to I-section connections. The considerable gains in stiffness and strength of glass composite connections obtained using adhesive bonding inspired Carrion et al. [10] to conduct experimental studies on a beam-column box-section connection employing a T-shaped monolithic connector, referred to as "cuff" connection, utilizing a high-strength epoxy. They determined the optimum thickness of their cuff connection that allowed the frame to achieve the full flexural capacity of the pultruded box beams. In 2017, Ascione et al. [11] studied four full-scale glass composite epoxy-bonded I-profile beam-column connections subjected to static loads, focusing on connection location and column strengthening methodologies. The connections composed of seat angles and column stiffeners attained the highest moment capacity. Meanwhile, a primary drawback of adhesive connections identified in the studies was the brittle failure mode, such as adherend or adhesive interface failure, making them less appropriate for being used in structures. The observed limited deformation capacity renders the examined adhesives unsuitable for earthquake resistance as well. To mitigate brittle failure modes of adhesive connections, Ascione et al. [12] modified the proposed connection in [11] to achieve pseudo-ductile failure modes. The modification entailed wrapping the connection at specific locations using a carbon fiber fabric, employing epoxy resin and wet lay-up technique. Their strengthened connection exhibited a pseudo-ductile load-deflection response.

Pseudo-ductile behavior in pultruded structures can even be achieved with simpler joint configurations such as cleated joints [13]. Qureshi et al. [14] studied glass composite beam-to-column connections featuring steel and composite cleats, discovering enhanced torsional moment capacity and stiffness at the expense of diminished rotational deformation. Ascione et al. [15] explored the effect of the bonded area dimensions on the flexural and shear behavior of cleated epoxy connections in large-scale glass composite frames. Their findings indicated that the extension of the bonded area influenced the strength but not the stiffness of the

connections, while the adhesive layer experienced torsional moments.

The two main concerns regarding the beam-column connections investigated in prior experiments involve the durability of hybrid connections and the required ductility. Durability concerns in hybrid connections stem from the need for drilling into composite materials for joint installation [16]. Additionally, neither the brittle adhesive joints nor the hybrid joints using brittle adhesives exhibited a sufficient amount of ductility required for seismic resistant design [17]. Implementing pseudo-ductile adhesives in composite connections can help alleviate these concerns. Unlike brittle adhesives, experiments on linear pseudo-ductile adhesive lap joint connections have shown that the stresses are uniformly distributed over the bonded surfaces [18]. However, the mechanical properties of pseudo-ductile adhesives are sensitive to the applied strain rate [19]. Under low strain rates, pseudo-ductile adhesives exhibit lower stiffness and reduced yield strength, while they can achieve high failure displacement and strength due to molecular chain realignment and stretching into the applied displacement direction [20].

While pseudo-ductile adhesives have previously been examined in composite lap joints, their applications in beam-to-column joints, along with their strain rate-dependent stiffness, moment-rotation resistance, and overall performance have not yet been addressed. The adhesive layer in the studied lap joints experienced a constant strain rate and a uniform stress distribution along the overlap throughout the experiments. However, as noted earlier, in typical bonded beam-column joints (such as those studied in [15]), the adhesive layers will be subjected to torsional moments, inducing variable strain rates and consequently, nonuniform stress distributions in the radial direction from the rotational center. Taking this into consideration, the current study investigates the behavior of a novel adhesive angle double-lap joint under torsional moments, aiming to develop an analytical model with low computational cost for predicting the load bearing capacity under nonuniform stress distribution in the adhesive layers. The basic rate-dependent stress-strain relationships of the adhesive were derived from experiments on adhesive single-lap joints exhibiting a uniform stress distribution. Three different external displacement rates were applied to the angle joints to obtain their moment-rotation responses under different internal strain rate ranges in the adhesive layers. Based on the rate-dependent stress-strain relationships obtained from the single-lap joints, the torsional moment capacities of the angle joints under variable internal strain rate and associated nonuniform stress distributions could be predicted.

4.2 Angle joint concept and experimental program

A novel bonded-bolted angle double-lap joint was designed where a central bolt transfers the section forces, permitting relative joint rotations, while blocking relative translations in the adherend plane. The two pseudo-ductile adhesive layers resist the rotations and thus experience pure torsion, resulting in a nonuniform strain rate in radial direction. An analytical model was suggested to predict the mechanical performance of the pseudo-ductile adhesive under nonuniform strain rate, utilizing strain rate-dependent stress-strain responses as input data. The input data were obtained from linear single-lap joints according to ASTM D1002-10 [21], which exhibited a uniform strain rate and stress distribution along the overlap.

4.2.1 Angle joint experimental approach

The angle joint consists of an inner laminate perpendicularly connected to two outer laminates by a pseudo-ductile adhesive, forming an isosceles right triangle (Fig. 4.1(a)). Fig. 4.1(b) schematically represents the symmetric deformation of each of the inner and outer laminates, θ , under an applied load, F . The load, F , can be decomposed into internal shear and axial loads in the laminates, denoted as F_1 and F_2 , respectively. The bolt placed at the centroid of the adhesively bonded area transfers these internal forces between inner and outer laminates while preventing relative in-plane displacements. The adhesive joint area in Fig. 4.1(b) is represented by a rotational spring, indicating its resistance to rotation. Fig. 4.1(c) presents free-body diagrams of the specimen components and the decomposition of the loads acting on them. Additionally, Fig. 4.1(d)-(f) demonstrate the internal force and moment diagrams of each specimen component shown in Fig. 4.1(c). Each outer laminate carries half the load borne by the inner laminate. The relationship between F_1 , F_2 , and F can be determined as follows:

$$F_1 = F \times \cos(45 + \theta) \quad (4.1)$$

$$F_2 = F \times \sin(45 + \theta) \quad (4.2)$$

By considering equilibrium in the inner laminate, the internal torsional moment borne by the adhesive layers, T , can be calculated as follows:

$$T = F_1 \times L_1 = F \times \cos(45 + \theta) \times (L - a_1 - a_2) \quad (4.3)$$

4.2 Angle joint concept and experimental program

where L_1 is the distance between the point of load application and the bolt, L is the laminates' length, a_1 is the distance of the point of load application to the edge of the laminate, and a_2 is the bolt distance to the edge of the laminate, all shown in Fig. 4.1(a).

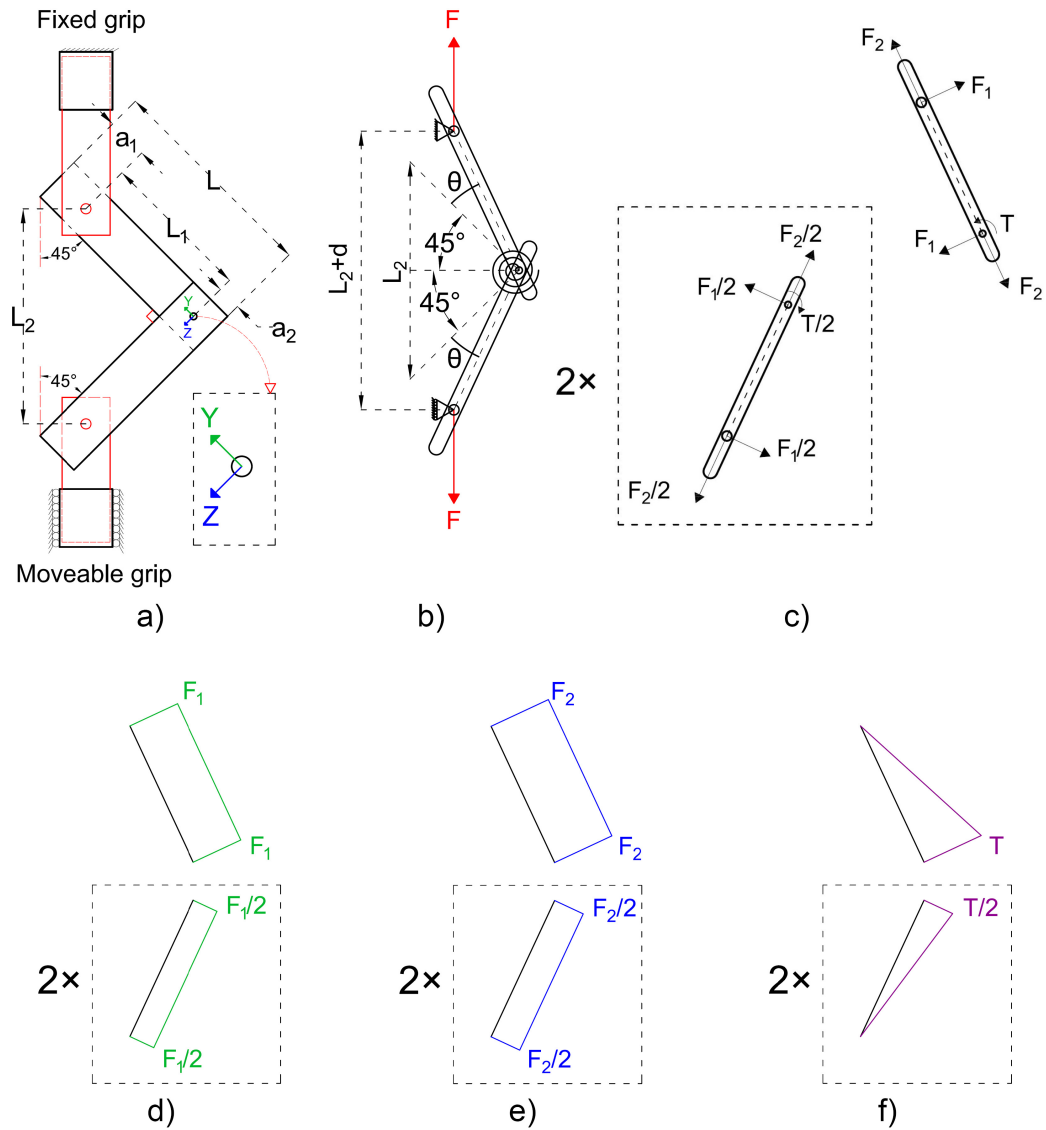


Figure 4.1: Schematic representation of angle joint specimen a) fixed in machine b) deformed state c) acting load decomposition d) internal shear diagram e) internal axial force diagram f) internal bending moment diagram.

4.2.2 Specimen geometry and fabrication

4.2.2.1 Single-lap experiments

The adhesive single-lap joint specimens were fabricated according to [21] from two steel sheets of 1.5 mm thickness, dimensioned as shown in Fig. 4.2, and bonded together over a length of 13 mm. The steel sheets, measuring 101.5 mm \times 25.5 mm \times 1.5 mm, were cut from a plate of 1.5 mm thickness using a waterjet. The shear area of the steel sheets was scratched with a grade 60 sandpaper according to ASTM D2651-01 [22] and then was cleaned with a Sika product (Sika® ADPrep) [23]. The pseudo-ductile adhesive was then applied to the shear area using a mixing gun, with two steel beads of 1.5 mm diameter placed in the shear (bonding) area to guarantee the targeted layer thickness. To have the same total thickness at the ends of the specimen as in the middle, steel tabs measuring 25.5 mm \times 25.5 mm were bonded with an epoxy adhesive (Sikadur-330) to the ends of the steel sheet adherends. The tabs were made of the same steel material as the steel adherends. The joints were then stored for five days under ambient laboratory conditions (23 ± 2 °C and $38 \pm 10\%$ relative humidity) prior to the experiments.

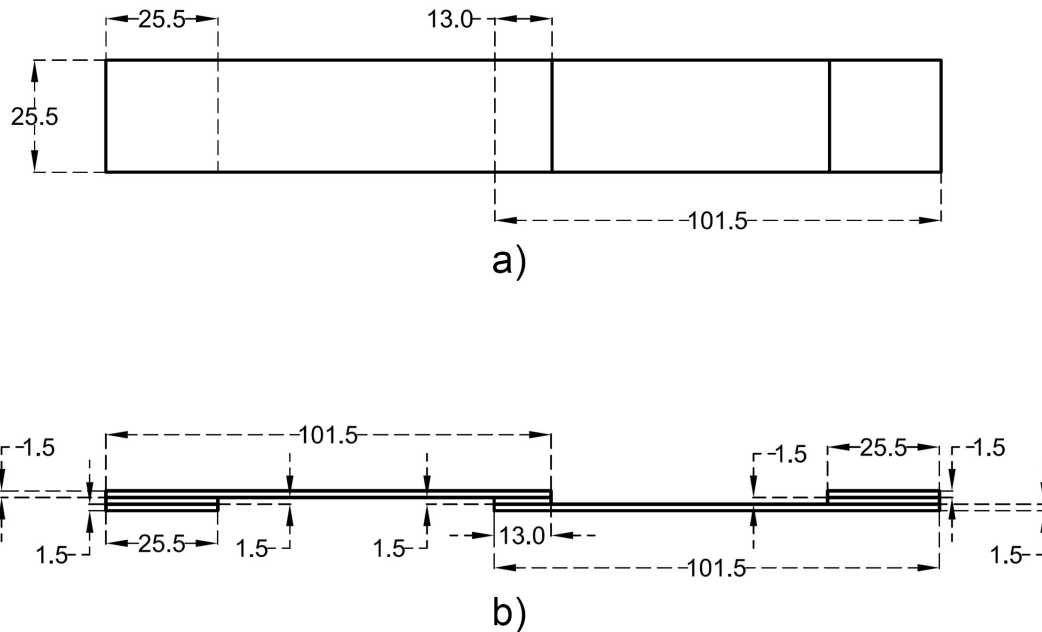


Figure 4.2: Single-lap specimen dimensions according to ASTM D1002 [21] a) top view, b) side view.

4.2 Angle joint concept and experimental program

4.2.2.2 Angle joint experiments

The angle joint specimens comprised an inner laminate and two outer laminates, as shown in Fig. 4.3, each measuring 450 mm × 100 mm × 10 mm in length, width, and thickness, respectively. A joint area of 100 mm × 100 mm, with an adhesive thickness of either 5 mm or 2.5 mm, to represent typical applications in composite bridge and building construction [24], [25], was then considered. To fabricate the angle joints, the composite laminates surface was roughened with sandpaper to remove the polyester layer, revealing the mat layer at a depth of about 0.5 mm. A thin epoxy adhesive layer (Sikadur-330) was then applied to the scratched surface as a bonding promoter using a construction spatula, leaving some marks on the surface. The epoxy layer was left to cure for four hours at 60°C [19]. The inner and outer laminates were then adhesively bonded using the pseudo-ductile adhesive which was applied by a mixing gun. Four steel beads of 5 mm or 2.5 mm in diameter were placed in the bonding area to ensure the desired adhesive layer thickness. After applying the adhesive for each lap, the specimen was cured for one day under ambient laboratory conditions (20±3°C and 38±10% relative humidity). Lastly, the joints were stored in the same room for five days before the experiments. After the curing process was finished, the center of the adhesively bonded area was drilled, at a distance of 50 mm from the laminate's edge, and pinned with a 14 mm diameter bolt.

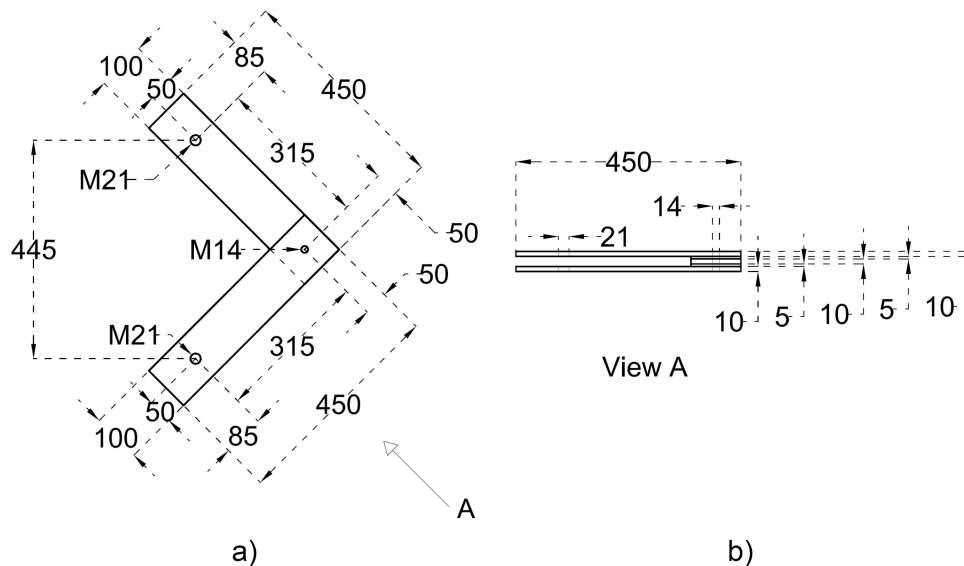


Figure 4.3: Angle joint specimen dimensions in mm from a) top view, b) side view.

Chapter 4. Pseudo-ductile adhesive angle double lap joints

4.2.3 Materials

The pseudo-ductile structural adhesive based on acrylic double performance (ADP) polymer technology, SikaFast®-555L10 (L05), supplied by Sika, Switzerland was used in this study. This two-part adhesive system consists of two components, SikaFast®-555 and SikaFast®-555 L10, which are mixed at a ratio of 10:1 (by volume). Elastic moduli ranging from 340 MPa to 780 MPa were measured in standardized dog-bone specimens, varying with the applied displacement rates of 0.1 mm/s up to 10 mm/s displacement rates [26].

In single-lap adhesively bonded specimens, a DIN EN 1.4034 stainless steel (AISI 420 / X46Cr13) plate was used for the adherends. The material was selected according to the requirements of ASTM D1002-10 [21].

The laminates used in the angle joint specimens were made of glass fiber-polymer composites provided by Fiberline Denmark, and were composed of E-glass fibers in an isophthalic polyester resin matrix with a fiber content of 60% by weight. The laminate structure comprised 70% unidirectional rovings in the core and two outer layers of combined mats, with a polyester surface veil applied to the exterior surfaces. According to the manufacturer, the laminates' longitudinal elastic modulus and tensile strength were 28 GPa and 240 MPa, respectively [27]. Grade 80 stainless steel bolts were used, with an unthreaded length of 35 mm.

4.2.4 Setup, instrumentation, and experimental procedure

4.2.4.1 Single-lap experiments

To conduct tension loading experiments, single-lap shear specimens were fixed at their tabs in the grips of an MTS 25 kN universal testing machine. The experiments were conducted in a displacement-controlled mode, with six applied tensile displacement rates of 0.01, 0.05, 0.1, 0.5, 1.0, and 5.0 mm/s, all referring to the machine's cross-head displacement. The relative displacements in the joint area were measured using a Digital Image Correlation (DIC) system. The DIC system was placed in front of the experimental setup and monitored the movement of the speckles on both steel sheets. Three specimens, each designated by the specimen type (SL), loading rate (0.01, 0.05, 0.1, 0.5, 1.0, and 5.0), and joint replication (1 to 3), were investigated at each displacement rate. As an example, the designation "SL-0.01-1" represents the first single-lap specimen subjected to a displacement rate of 0.01 mm/s.

4.2 Angle joint concept and experimental program

4.2.4.2 Angle joint experiments

Displacement-controlled monotonic experiments were conducted in a laboratory setting at room temperature ($19 \pm 3^\circ\text{C}$) using a Walter+Bai type LFV universal testing machine with a maximum capacity of 200 kN in tension and compression and a maximum displacement of 200 mm. Two steel fixtures were placed in the top and bottom grips of the machine, to which the inner laminate and outer laminates were hinged using a 20 mm bolt, allowing for the free rotation of the end bolts, as shown in Fig. 4.4. The nuts were hand-tightened to prevent the bolts from being pre-stressed. The machine applied the displacement with the desired external rate and measured the resulting loads. The rotation of the laminates was recorded using two inclinometers with an accuracy of 0.001 radians, one attached to the middle of the inner laminate, inclinometer_1, and the other to the middle of an outer laminate, inclinometer_2. To measure the adhesive layer deformations in the angle joint, a two-camera 3D DIC system was used. These cameras enabled the tracking of specimens' motion in 3D space (stereo vision) with an accuracy of $\pm 0.01\%$. A random speckle pattern was applied on the measured surfaces, i.e., edge of the joint area, using both white and black spray in the dashed-line rectangle in Fig. 4.4. The DIC measured area was illuminated with a non-heating LED EFFILUX white light. The light was positioned at a fixed angle and distance from the specimens to provide consistent illumination during the experiments. The post-processing of the results was carried out using Vic-3D software from Correlated Solutions Inc. Furthermore, the specimens were photographed by two additional cameras to monitor them during the experiments.

Three external displacement rates of 0.1, 0.5, and 2.0 mm/min were applied by the machine to the angle joint specimens. During each experiment, the machine applied a constant downward displacement rate to the bottom grip, thus resulting in a range of variable internal strain rates in the joint area.

Three specimens were examined for each displacement rate and thickness of the adhesive layer. The joint designations comprised the joint loading type (M), adhesive thickness (t5 or t2.5), loading rate (0.1, 0.5, 2.0), and joint replication (a, b, c, or d). For example, the designation "M-t5-0.1a" represents the first angle joint subjected to monotonic loading with an adhesive thickness of 5 mm at a rate of 0.1 mm/s.

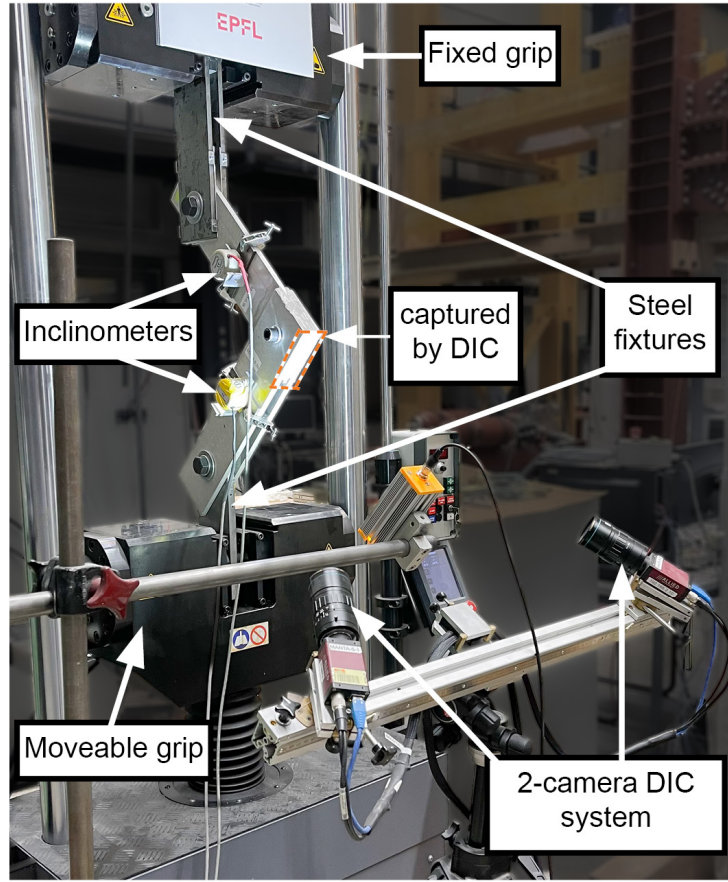


Figure 4.4: Angle-joint specimen experiment setup with two-camera 3D DIC measurement.

4.2.5 Experimental results

4.2.5.1 Single-lap experiments

- Stress-Strain responses

The single-lap experiments investigated the shear stress-strain behavior of the pseudo-ductile adhesive over a wide range of displacement rates. The shear stress, τ , and shear strain, γ , values were calculated from the measured force and deformations using Eq. (4.4) and Eq. (4.5), assuming a uniform stress distribution along the overlap.

$$\tau = \frac{F}{A} \quad (4.4)$$

$$\gamma = \frac{d}{t_s} \quad (4.5)$$

4.2 Angle joint concept and experimental program

where F is the load recorded by the machine, A_s is the joint area, d is the joint displacement, and t_s is the adhesive layer thickness in single-lap joint specimens, equaling 1.5 mm. Fig. 4.5(a) shows the stress-strain curves obtained from Eq. (4.4) and (4.5) for the selected specimens under the applied displacement rates of 0.01, 0.05, 0.1, 0.5, 1.0, and 5.0 mm/s.

The effects of the applied strain rates on the shear behavior of the specimens were studied by analyzing the parameters extracted from the stress-strain curves. The shear modulus, G_1 , was calculated from the slope of a tangent line to the initial section of each specimen's stress-strain curve. The yield points were considered as the points where the tangent line's slope dropped to 20% of the initial slope, and accordingly, the yield stress, τ_y , as well as its corresponding value of strain, γ_y , were obtained. Furthermore, the post-yield modulus, G_2 , was calculated from the slope of a line between the yield point and the maximum stress, the strength was defined as the maximum stress, τ_{max} , and its corresponding value of strain, γ_{max} , as the maximum strain. Table 4.1 summarizes the average values and standard errors of the extracted parameters for each set of specimens subjected to the same applied displacement rates. It can be seen that all parameters increased with increasing the strain rate except for the post-yield modulus and the maximum strain, which decreased as the strain rate increased. The obtained shear strain values from DIC results along the overlap of the joint are shown in Fig. 4.5(b) when the stress was equal to 6 MPa. The shear strain values confirm a uniform strain distribution along the joint area for all displacement rates. For each displacement rate, \dot{d} , the corresponding uniform strain rate, $\dot{\gamma}$, was calculated as follows:

$$\dot{\gamma} = \frac{\dot{d}}{t_s} \quad (4.6)$$

- Failure mode

Fig. 4.6 illustrates the failure surfaces of the single-lap joint area for selected specimens subjected to six different displacement rates. All specimens failed within the adhesive layer, which, based on the classification provided by [28], can be considered as a mixed mode of cohesive failure and adhesive failure. However, the majority of the fracture surface exhibit cohesive failure.

Chapter 4. Pseudo-ductile adhesive angle double lap joints

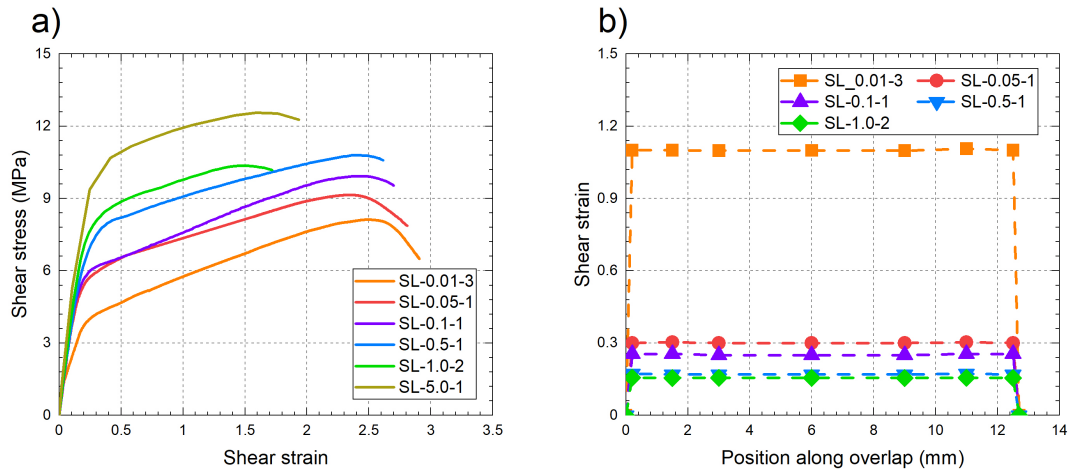


Figure 4.5: a) Shear stress-strain relation under different applied displacement rates for single-lap joints, b) shear strain distribution along single-lap joint overlap under different applied displacement rates at shear stress of 6 MPa.

Table 4.1: Single-lap joint experimental results.

Sp. name	\dot{d} (mm/s)	$\dot{\gamma}$ (1/s)	G_1 (MPa)	γ_y	τ_y (MPa)	G_2 (MPa)	τ_{max} (MPa)	γ_{max}
SL-0.01-1,2,3	0.01	0.007	22.8 ± 0.6	0.19 ± 0.01	3.4 ± 0.1	1.9 ± 0.0	7.4 ± 0.4	2.4 ± 0.0
SL-0.05-1,2,3	0.05	0.033	26.9 ± 2.1	0.22 ± 0.01	5.0 ± 0.3	1.7 ± 0.2	8.9 ± 0.2	2.3 ± 0.0
SL-0.1-1,2,3	0.1	0.066	29.1 ± 0.9	0.23 ± 0.01	5.3 ± 0.4	1.6 ± 0.1	9.3 ± 0.3	2.3 ± 0.2
SL-0.5-1,2,3	0.5	0.330	30.3 ± 1.2	0.27 ± 0.01	6.6 ± 0.4	1.5 ± 0.1	9.4 ± 0.8	2.0 ± 0.3
SL-1.0-1,2,3	1.0	0.660	32.2 ± 1.0	0.28 ± 0.01	8.1 ± 0.4	1.5 ± 0.0	10.5 ± 0.4	1.7 ± 0.1
SL-5.0-1,2,3	5.0	3.300	33.1 ± 1.7	0.31 ± 0.01	9.7 ± 0.9	1.4 ± 0.2	11.9 ± 0.7	1.6 ± 0.1

4.2.5.2 Angle joint experiments

- Rotation rate in the specimens

This section studies the laminate rotation angle and laminate rotation rate, stemming from the external displacement applied by the machine to the angle joint specimens. The rotation angle was measured relative to the initial undeformed state using the two installed inclinometers (Fig. 4.4). Fig. 4.7(a) curves represent the clockwise (positive) and counterclockwise (negative)

4.2 Angle joint concept and experimental program

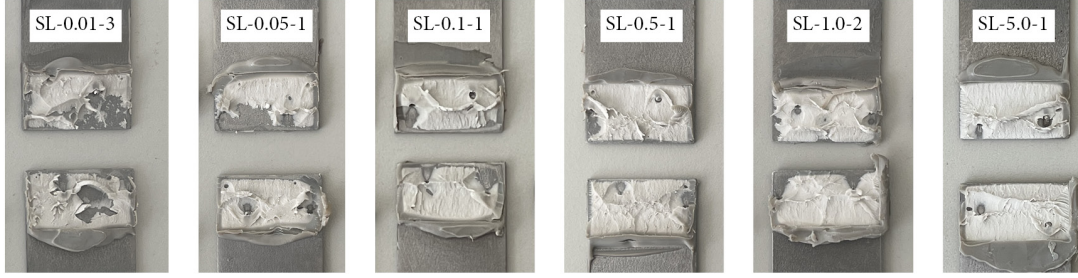


Figure 4.6: Cohesive failure of single-lap specimens under various applied displacement rates.

rotations of the inner and outer laminates, respectively. The identical rotation angles of inner and outer laminates at each load level verify the rotational symmetry around the connecting bolt within the joint area. Therefore, considering the symmetry in rotation and geometry of the specimen, the relation between the edges of the right triangle formed between the bottom load application point, the bolt and the midpoint between the top and bottom application points could be written as follows (according to Fig. 4.1(b)):

$$L_1 \times \sin(45^\circ + \theta) = \frac{L_2 + d}{2} \quad (4.7)$$

where L_2 is the vertical distance between top and bottom load application points (Fig. 4.1(a)), and d is the machine displacement. Then, by rearranging Eq. (4.7), and substituting the values of L_1 and L_2 from Fig. 4.3, the laminate rotation angle can be derived from the machine displacement, as follows:

$$\theta = \left[45^\circ - \arcsin\left(\frac{2 \times 315}{445 + d}\right) \right] \times \left(\frac{\pi}{180}\right) \text{ rad} \quad (4.8)$$

Fig. 4.7(b) illustrates the rotation angles calculated by Eq. (4.8), represented by the dashed lines, and the rotation angles of the inner laminate, measured by the inclinometer depicted by the solid lines, over time for specimens subjected to different displacement rates. The slope of these curves corresponds to the laminate rotation rate of each specimen, denoted as $\dot{\theta}$. The good agreement between the inclinometer rotation measurements and the calculated rotations obtained from Eq. (4.8) further validates the calculations and symmetric deformation of the joint area.

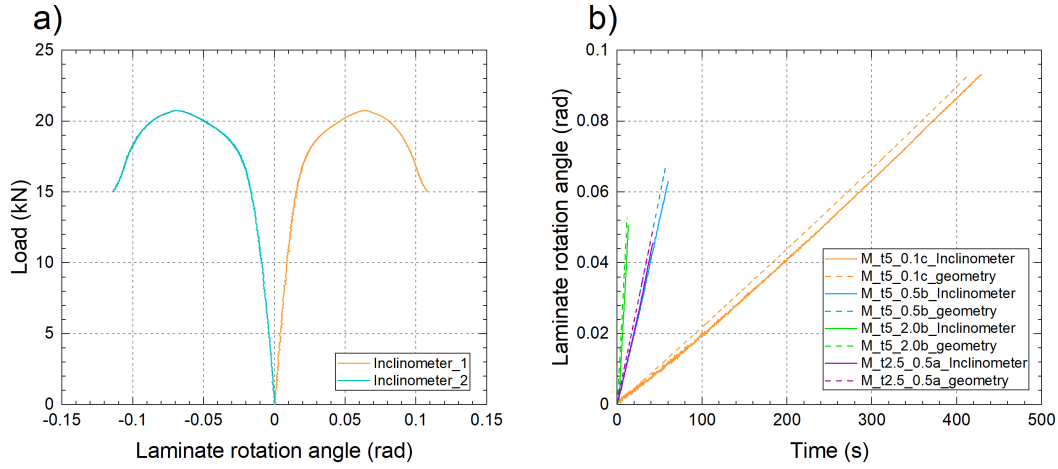


Figure 4.7: Inclinator data: a) Comparing two inclinometers against machine load for specimen M-t5-0.1b; b) Comparing inclinometer data with geometrically calculated rotations over time for specimens M-t5-0.1b, M-t5-0.5b, M-t5-2.0b, M-t2.5-0.5a.

- Torsion-rotation curve analysis

The torsional moment-laminate rotation responses of the angle joints subjected to monotonic loading are presented in Fig. 4.8. The torsional responses were calculated using Eq. (4.3), considering the loads measured by the machine. The laminate rotation angles presented in Fig. 4.8 were calculated using Eq. (4.8). Fig. 4.8(a) illustrates the torsion-laminate rotation responses for specimens with a 5 mm adhesive layer thickness, whereas Fig. 4.8(b) shows the results for specimens subjected to an applied displacement rate of 0.5 mm/s, with adhesive layer thicknesses of 5 mm and 2.5 mm. The torsion-rotation responses of the angle joint specimens can be described by the following two distinct phases: (a) the initial linear segment until the onset of yielding of the joint area, and (b) the continuous decrease in tangential stiffness until the maximum torsional capacity is reached. The stage (a) is characterized by two parameters, the slope of the initial linear segment, S , and the laminate rotation angle at the onset of yielding in the joint area, θ_y . Meanwhile, the stage (b) is characterized by two parameters, the maximum torsional moment, T_{max} , and the laminate rotation angle at maximum torsion, θ_{max} . With the increase of the applied displacement rate, S , θ_y , and T_{max} , increased while θ_{max} , decreased. At the highest displacement rate, T_{max} attained its maximum value, in contrast to θ_{max} , which was the highest at the lowest rate. Compared to the specimens with a 5.0 mm adhesive layer, those with a thinner 2.5 mm adhesive layer thickness exhibited a higher initial stiffness and maximum torsional moment, by 15% and 11%, respectively. However, this reduction in thickness led to a 40% decrease in θ_{max} . Table 4.2 provides a summary of $\dot{\theta}$, S , θ_y , T_{max} , and θ_{max} values for each specimen.

4.2 Angle joint concept and experimental program

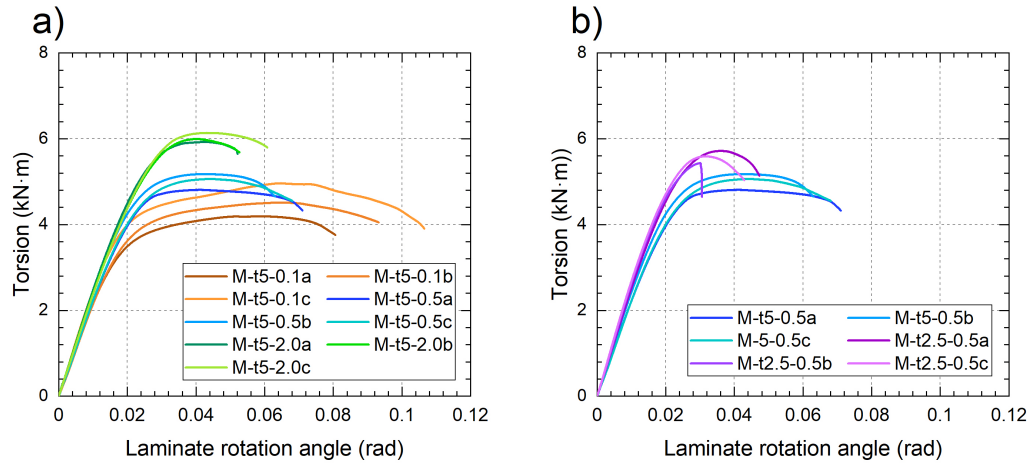


Figure 4.8: Angle joint torsion-rotation relation a) for specimens with 5 mm adhesive layer thickness subjected to various applied displacement rates, b) for specimens with 5 mm and 2.5 mm adhesive layer thickness subjected to 0.5 mm/s applied displacement rate.

Table 4.2: Angle joint experimental results.

Sp. name	$\dot{\theta}$ (rad/s)	S (kN.m/rad)	θ_y (rad)	T_{max} (kN.m)	θ_{max} (rad)
M-t5-0.1a	0.0002	221.43	0.010	4.19	0.060
M-t5-0.1b	0.0002	223.63	0.010	4.51	0.066
M-t5-0.1c	0.0002	250.88	0.011	4.96	0.065
M-t5-0.5a	0.0011	229.41	0.012	4.81	0.041
M-t5-0.5b	0.0011	250.40	0.013	5.17	0.043
M-t5-0.5c	0.0011	228.68	0.012	5.06	0.045
M-t5-2.0a	0.0044	250.41	0.015	5.92	0.044
M-t5-2.0b	0.0044	244.11	0.014	5.99	0.041
M-t5-2.0c	0.0044	240.19	0.014	6.13	0.043
M-t2.5-0.5a	0.0011	255.95	0.013	5.71	0.036
M-t2.5-0.5b	0.0011	271.65	0.013	5.43	0.030
M-t2.5-0.5c	0.0011	274.59	0.014	5.59	0.032

- Shear strain variation

The shear strain at a particular point in the joint area, having a rotational deformation of $2 \times \theta$ about its centroid (Fig. 4.9(a)), can be calculated using the following relationship:

Chapter 4. Pseudo-ductile adhesive angle double lap joints

$$\gamma = \frac{r \times 2 \times \theta}{t_a} \quad (4.9)$$

where r denotes the distance from the point of interest to the center of rotation, and t_a is the adhesive thickness. The shear strain is thus constant through the thickness, as shown in Fig. 4.9(b), and the shear stress distribution is uniform through the thickness at a particular point in the joint area (Fig. 4.9(c)).

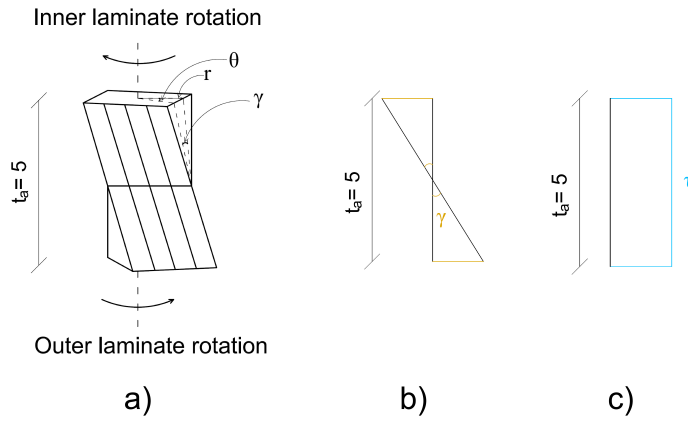


Figure 4.9: a) Schematic representation of deformed adhesive layer subjected to opposite rotation of inner and outer laminates, b) corresponding constant shear strain, c) corresponding uniform shear stress across adhesive thickness.

Fig. 4.10 displays the images of M-t5-0.1c joint along its outer and inner edges. Fig. 4.10(a) and (b) are at the beginning and end of stage (a), when the specimen is at its undeformed state and onset of yield, respectively. Fig. 4.10(c) corresponds to the end of stage (b), with maximum achieved torsion, while Fig. 4.10(d) displays the state at which the torsion was dropped to 80% of its maximum value. For each pair of images, the left one was captured by the DIC system, whereas the right one was taken with a digital camera to track the propagation of failure along the back-facing edges. In Fig. 4.10(b), no failure is apparent in the joint at the onset of yielding. Meanwhile, Fig. 4.10(c) shows cracks initiating at the corners and propagating towards the middle of the edge at maximum torsion. Finally, Fig. 4.10(d) illustrates the final state of the specimens, showing the detached adhesive layer at the edges from laminates on both sides, which propagates towards the center of the joint area with further applied deformation.

Shear strain distributions in the adhesive layer along the edge of the joint area can be calculated using the DIC recordings. The origin of the DIC recorded coordinates was assumed to be on the top face of an outer laminate at the center point of the joint area with X, Y, and Z axes

4.2 Angle joint concept and experimental program

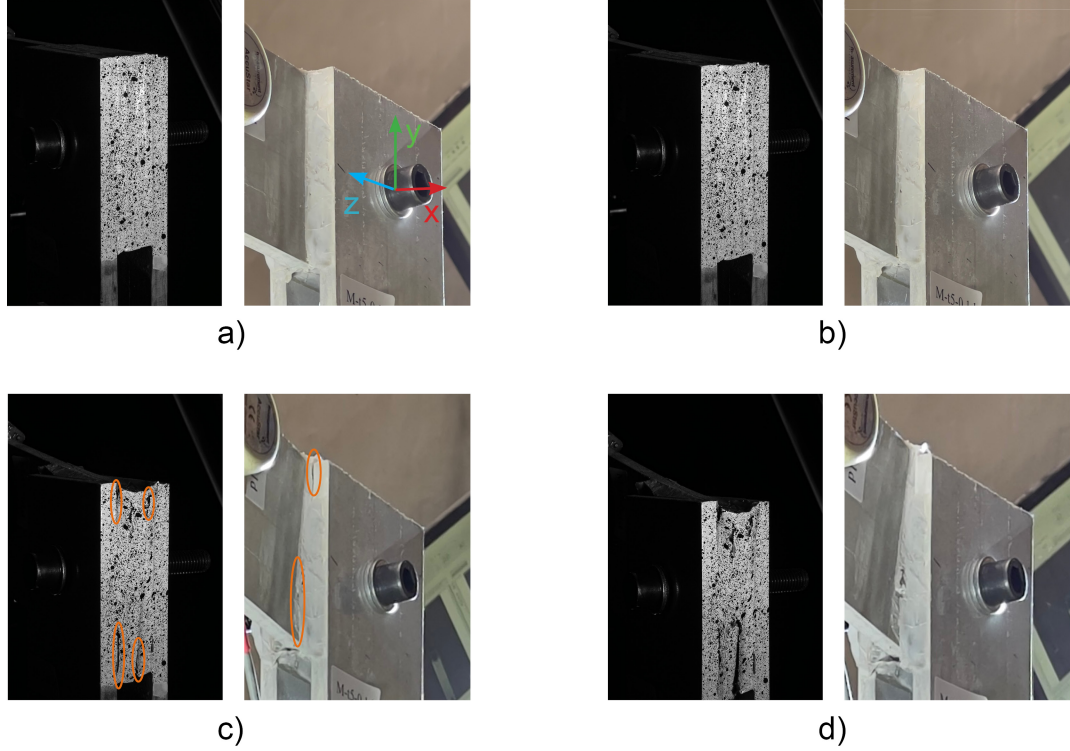


Figure 4.10: DIC and tracking camera captured photos of specimen M-t5-0.1c at a) onset of experiment, b) onset of yielding, c) maximum torsion, and d) when torsion drops to 80% of maximum torsion.

pointing in the joint thickness, vertical, and horizontal directions, respectively, as shown in Fig. 4.10(a). The shear strain for a specific point over the recorded area can be calculated from the DIC data as follows:

$$\gamma_{DIC} = \frac{\sqrt{(y_t - y_0)^2 + (z_t - z_0)^2}}{|x_0 - x_m|} \quad (4.10)$$

where x , y , and z represent the coordinates of a certain point either at the start (undeformed state), x_0 , y_0 , and z_0 , or at a given time of t (deformed state), y_t and z_t . The value of x_m , the x coordinate at the mid-thickness of the adhesive layer, depends on the adhesive layer. Specifically, x_m is -12.5 mm for adhesive layer with x between -10 mm and -15 mm, and -27.5 mm for the one with x between -25 mm and -30 mm. Fig. 4.11(a) and (b) present the γ values calculated along the captured edge of the adhesive layer from the recorded DIC coordinates at ten intervals at stages (a) and (b), as explained previously, for the M-t5-0.1c and M-t5-0.5b joints, respectively. Shear strain values along the captured edge ($y = -50$ mm to 50

Chapter 4. Pseudo-ductile adhesive angle double lap joints

mm at $z = -50$ mm) were also calculated using Eq. (4.9) with r values between 50 mm to 70.7 mm, corresponding to the distance from the edge of the adhesive layer to the joint centroid, and the corresponding rotation, and depicted in Fig. 4.11 as dashed lines. As shown in Fig. 4.11, the values obtained from Eq. (4.9) are in good agreement with DIC results. Yield shear strains at the corners, γ_y , were determined to be 0.32 and 0.38 for M-t5-0.1c and M-t5-0.5b joints, respectively. The maximum shear strain at the corner, γ_{max} , was found to be 1.51 and 1.12 for M-t5-0.1c and M-t5-0.5b joints. The corner points at the adhesive layer edge corresponding to stage (b) in Fig. 4.11 were eliminated from the curve due to the formation of small cracks.

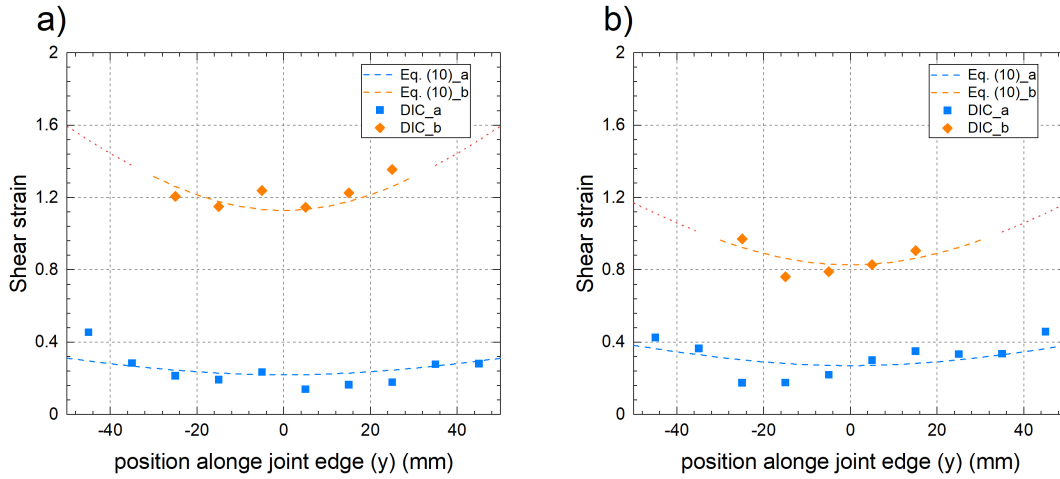


Figure 4.11: Shear strain variation obtained from DIC data along the joint edge at end of stages (a) and (b) of torsion-rotation behavior at $x = 10$ for a) M-t5-0.1c and b) M-t5-0.5b.

Similar to the shear strain relation (Eq. (4.9)), the shear strain rate, $\dot{\gamma}$, can be calculated at each point as follows:

$$\dot{\gamma} = \frac{r \times 2 \times \dot{\theta}}{t_a} \quad (4.11)$$

where $\dot{\theta}$ is reported in Table 4.2 for each displacement rate. Figs. 4.12(a)-(d) illustrate the linear variation of $\dot{\gamma}$ for specimens with 5 mm adhesive layer thickness under laminate rotation rates of 0.0002, 0.0011, and 0.0044 rad/s and specimen with 2.5 mm adhesive layer thickness under laminate rotation rate of 0.0011 rad/s, respectively. Strain rate values are shown along two axes, one passing through the middle of the edges and the other passing through the corners. The strain rate value at the middle of the edge and the corner are denoted as $\dot{\gamma}_m$ and $\dot{\gamma}_c$, respectively.

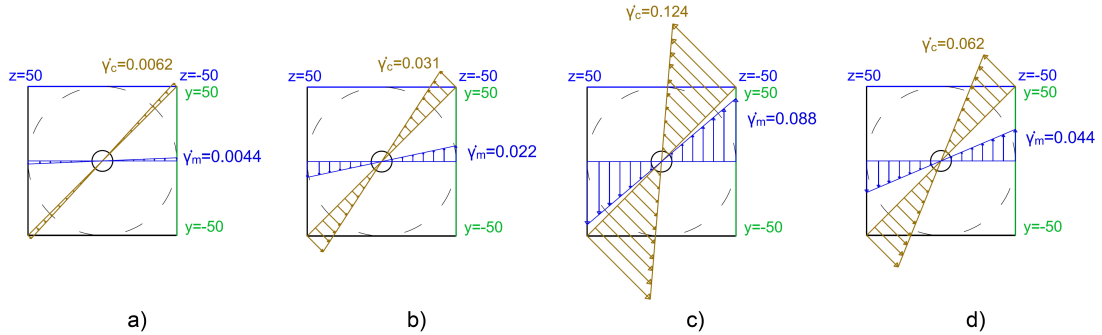


Figure 4.12: Shear strain rate distribution of a) M-t5-0.1 b) M-t5-0.5, c) M-t5-2.0, and d) M-t2.5-0.5.

- Failure mode

Fig. 4.13(a)-(c) illustrate the failure surfaces of the inner and outer laminates of angle joints with 5 mm adhesive thickness subjected to three different laminate rotation rates of 0.00022, 0.0011, and 0.0044 rad/s, respectively. Meanwhile, Fig. 4.13(d) shows the failure surface of an angle joint with 2.5 mm adhesive thickness under a laminate rotation rate of 0.0011 rad/s. Five different failure modes were observed: cohesive failure, C, fiber tear, F, shear-out, S, net tension, N, and adhesive interface failure, A, each specified by a dashed line or an ellipse in Fig. 4.13. The adhesive interface failure precedes all other failure modes, initiating in the corners of the joint area and continuing up to the ultimate failure of the specimen. No evidence of shear-out or net tension failure modes was observed during the experiments up to stage (b) of the torsion-rotation behavior of the specimens. Shear-out and net tension failure modes occurred only after further application of the displacement beyond stage (b). Cohesive failure was mostly observed in angle joints subjected to the lowest applied laminate rotation of 0.00022 rad/s while being only slightly observed in angle joints with a 2.5 mm adhesive layer thickness subjected to the laminate rotation of 0.0011 rad/s. In all other cases, fiber tear failure was observed, followed by shear-out and net tension failure modes after reaching maximum joint capacity.

4.3 Analytical model

An analytical model was developed to predict the behavior of the pseudo-ductile adhesive angle joints torsion-rotation response, considering the rate-dependent characteristics of the pseudo-ductile adhesive. This approach was selected since each point within the adhesive layer of the angle joint experiences a different strain rate relative to its distance from the center of rotation making it challenging to calculate the shear stress distribution using conventional

Chapter 4. Pseudo-ductile adhesive angle double lap joints

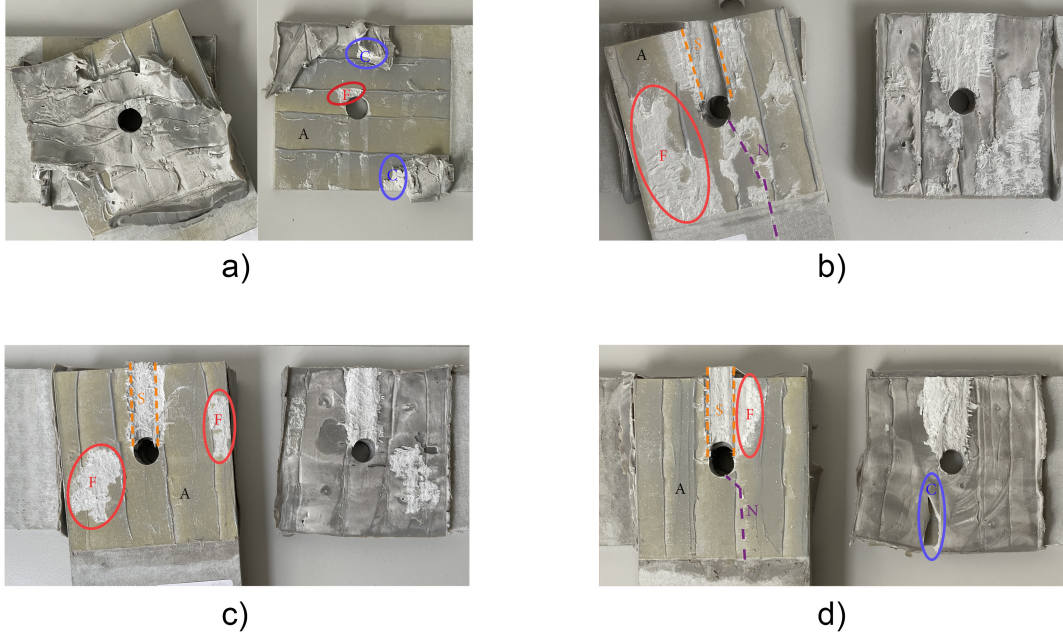


Figure 4.13: Combination of failure modes for angle-joints under a) 0.00022 rad/s (M-t5-0.1b) b) 0.0011 rad/s (M-t5-0.5a) c) 0.0044 rad/s (M-t5-2.0b) d) 0.0011 rad/s (M-t2.5-0.5a) laminate rotation rates, C = cohesive, F = fiber tear, S = shear-out, and N = net tension, A = adhesive/interface.

methods (Eqs. (4.4) and (4.5)).

The initial step in developing the torsional behavior model involved fitting a bilinear model to the single-lap joint experimental results obtained under six distinct shear strain rates (mentioned in Section 4.2.5.1 and Table 4.1). The bilinear model comprises a pre-yield section with two parameters of G_1 , and γ_y , and a post-yield section with two parameters of G_2 and γ_{max} . A power-law relationship was then fitted to G_1 , γ_y , and G_2 parameters, and the corresponding shear strain rate. The power-law relations between the pseudo-ductile adhesive bilinear model parameters and the shear strain rate under the aforementioned laboratory condition of the single-lap joints are expressed as follows:

$$G_1 = 33 \times \dot{\gamma}^{0.09} \quad (4.12)$$

$$\gamma_y = 0.29 \times \dot{\gamma}^{0.05} \quad (4.13)$$

$$G_2 = 1.5 \times \dot{\gamma}^{-0.04} \quad (4.14)$$

Fig. 4.14(a) presents the experimental results (dashed lines) and their corresponding bilinear model (solid lines), while Fig. 4.14(b)-(c) show the fitted power-law relations to G_1 , γ_y , and G_2 data, previously reported in Table 4.1.

Since the failure mode of the single-lap joints was different from that of the angle joints, γ_{max} values were obtained from angle joint experiments and then denominated as $\gamma_{max,angle}$. To estimate the values of $\gamma_{max,angle}$ a power-law relation was fitted to the maximum shear strain over the results of angle joint experiments obtained from the DIC data. The resulting power-law relation is as follows:

$$\gamma_{max,angle} = 0.7 \times \dot{\gamma}^{-0.14} \quad (4.15)$$

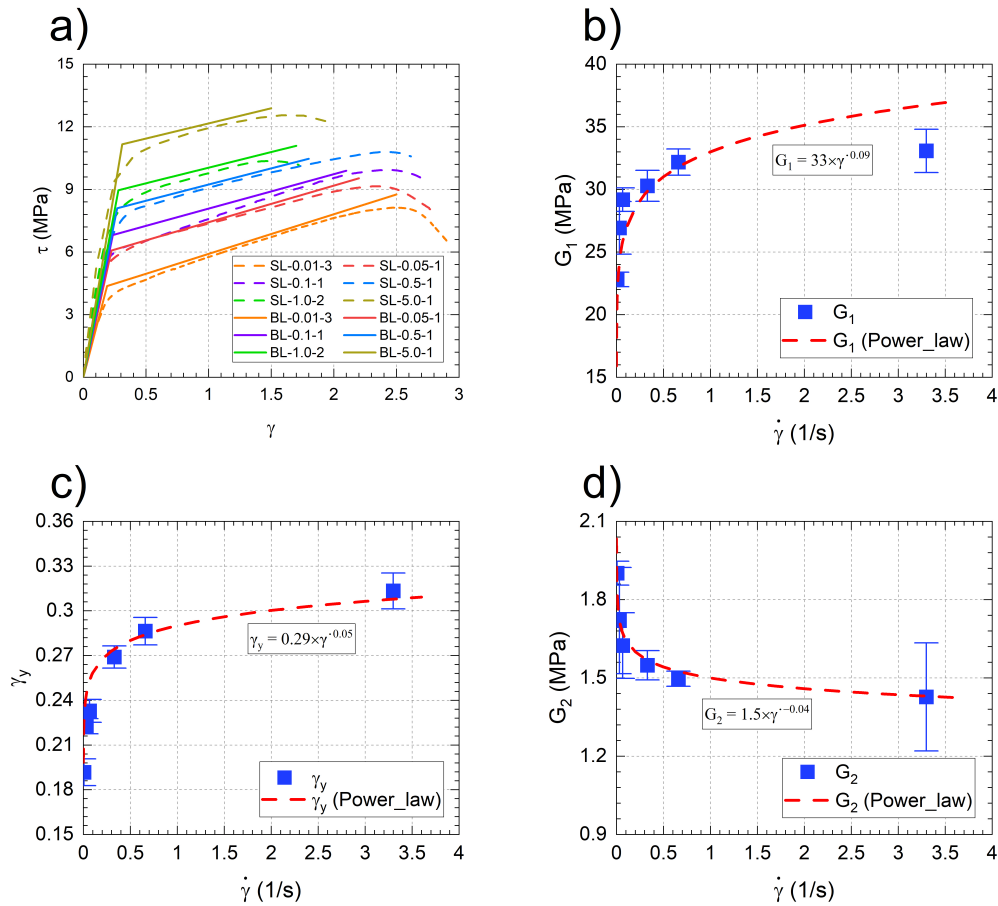


Figure 4.14: Comparison of single-lap joint stress-strain responses between experimental results and bilinear model.

Chapter 4. Pseudo-ductile adhesive angle double lap joints

In the next step, the torsion moment within the adhesive layer, T , can be calculated by integrating torsion moment increments as follows:

$$\int_{-50}^{50} \int_{-50}^{50} r \cdot \tau \cdot dydz \quad (4.16)$$

where $dydz$ is the area increment at each point of the joint area, with y and z ranging from -50 to 50 considering the origin at the center of the middle bolt in Fig. 4.10(a), τ is the shear stress at the corresponding area increment, and r is the length of the arm from the joint center (center of rotation) for a point with y and z coordinates which can be determined as follows:

$$r = \sqrt{y^2 + z^2} \quad (4.17)$$

The stress at each point was derived based on the bilinear model by applying the following conditions:

$$\tau = G_1 \times \gamma \quad \text{if } \gamma \leq \gamma_y \quad (4.18)$$

$$\tau = G_1 \times \gamma_y + G_2 \times (\gamma - \gamma_y) \quad \text{if } \gamma_y < \gamma \leq \gamma_{fail,angle} \quad (4.19)$$

$$\tau = 0 \quad \text{if } \gamma_{fail,angle} < \gamma \quad (4.20)$$

Using the described procedure for each rotation angle of the laminates, θ , the torsion-rotation response of the angle joint can be predicted.

Fig. 4.15 presents the experimental results of angle joints (dashed lines) and the predicted torsion-rotation response (solid lines). Fig. 4.15(a)-(c) depict these responses for the specimens with an adhesive layer thickness of 5 mm subjected to laminate rotation rates of 0.00022, 0.0011, and 0.0044 rad/s, respectively. Meanwhile, Fig. 4.15(d) shows the aforementioned responses and predictions for the specimens with an adhesive layer thickness of 2.5 mm under a laminate rotation rate of 0.0011 rad/s.

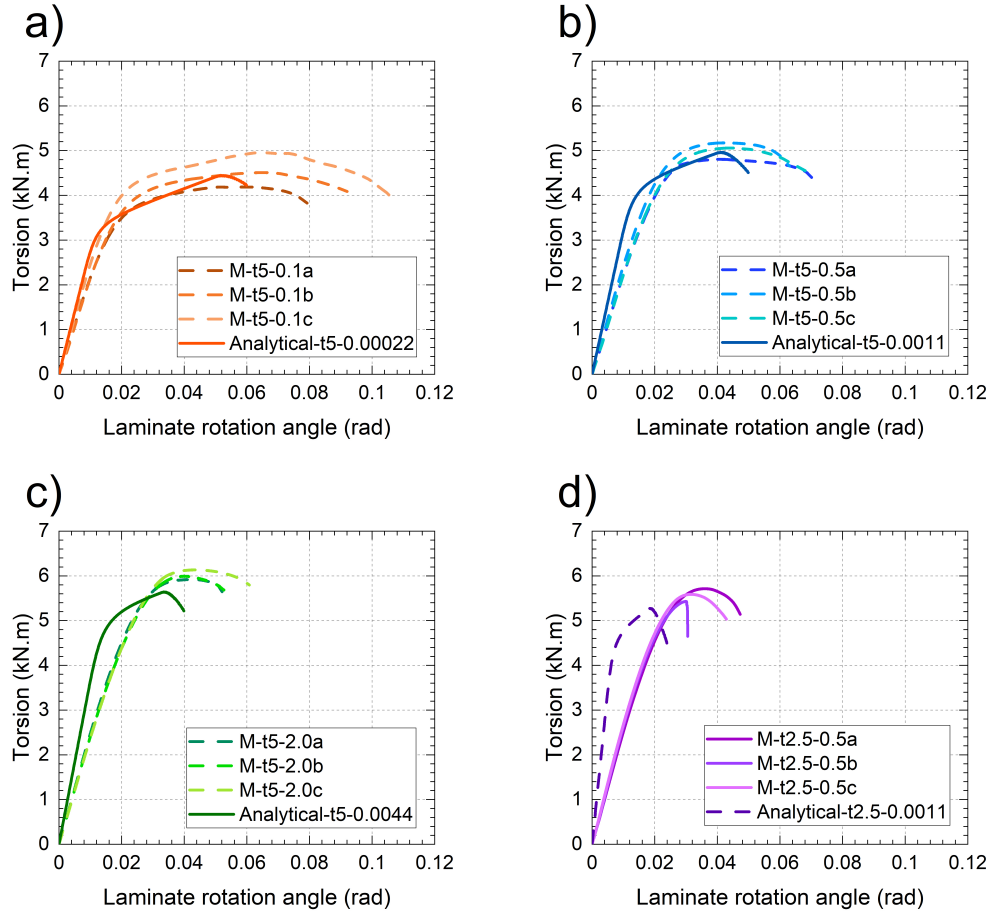


Figure 4.15: Torsion-rotation response comparison of experimental and analytical results for specimens a) M-t5-0.1, $\dot{\theta} = 0.00022$ rad/s, b) M-t5-0.5, $\dot{\theta} = 0.0011$ rad/s, c) M-t5-2.0, $\dot{\theta} = 0.0044$ rad/s, and d) M-t2.5-0.5, $\dot{\theta} = 0.0011$ rad/s.

4.4 Discussion

4.4.1 Analytical model validation and discussion

As it is shown in Fig. 4.5(b), in single-lap joints under tension, the pseudo-ductile adhesive exhibited a uniform shear strain distribution across the joint area. In contrast, in angle joints subjected to torsion, the shear strain distribution is not uniform as it changes depending on the distance from the center of rotation over the joint area of the adhesive layer, as it is shown in Fig. 4.11.

The comparison between experimental results of angle joints and the predicted torsion-

Chapter 4. Pseudo-ductile adhesive angle double lap joints

rotation response for the specimens under different laminate rotation rates, $\dot{\theta}$, and different adhesive layer thicknesses are presented in Fig. 4.15. A good agreement between the analytical model predictions and experimental results is observed, especially for the lower laminate rotation rates (Fig. 4.15(a) and (b)). However, the analytical model and experimental results do not exhibit good agreement at higher strain rates during the pre-yield stage. This discrepancy may be attributed to the basis of the analytical model, in which the stress-strain relationship was obtained from a uniform strain rate distribution. The analytical model, however, demonstrates robust validation for the post-yield stage, with the maximum torsion being of higher importance in the joint design process.

By using the developed analytical model, the stress distribution profile across the joint area in each angle joint specimen can be derived. Fig. 4.16 illustrates the predicted shear stress profile along two axes passing through either the corners or the middle of the edge of the joint area. The stress profiles are depicted at the yield and maximum stages, stage (a) and stage (b), respectively, for a specimen with an adhesive layer thickness of 5 mm subjected to a 0.0044 rad/s laminate rotation rate. The figure highlights the fact that the points lying on a circle at a distance r from the joint centroid have identical shear stress values. The corner stress, τ_c , was calculated to be equal to 7.2 MPa at stage (a) and increased to 8.2 MPa up to stage (b). The shear stress at the middle of the edge, τ_m , rises from 5.0 MPa to 7.5 MPa from the stage (a) up to its maximum (stage (b)). The slight difference between the maximum shear stress at the corners and the middle of the edge can be attributed to the lower shear strain rate at the middle of the edge. This emphasizes the rate-dependent nature of the adhesive and its impact on shear stress distribution within the joint area under torsional loading.

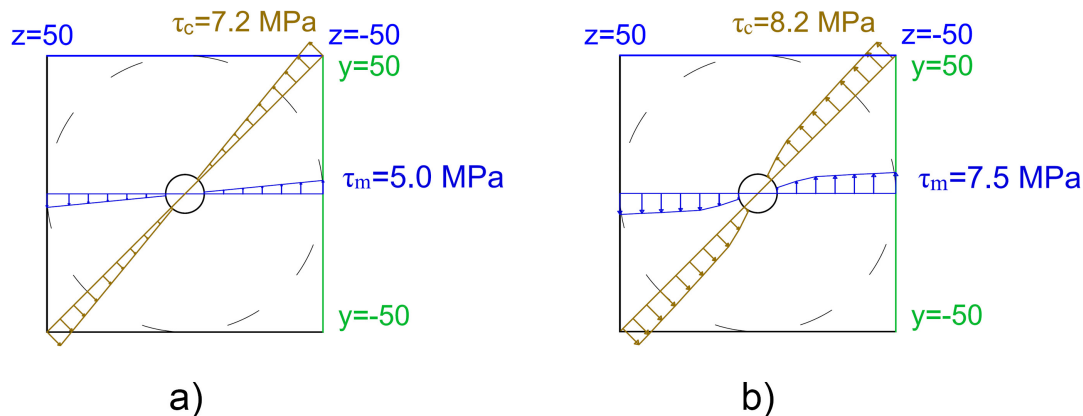


Figure 4.16: Shear stress distribution for M-t5-2.0 with $\dot{\theta} = 0.0044$ at a) stage (a) and b) stage (b).

Fig. 4.17 displays the radial shear stress profiles for r values ranging from 7 to 70.7 mm at

the stage where the whole joint area is in the pre-yield state, end of stage (a), and the state at which the maximum torsion is achieved, end of stage (b). Each case comprises four curves representing: three angle joints with an adhesive layer thickness of 5 mm under laminate rotation of 0.00022, 0.0011, 0.0044 rad/s, and an angle joint with an adhesive layer thickness of 2.5 mm subjected to a 0.0011 rad/s laminate rotation rate. For each specimen, the corresponding rotation angles at which the corner of the joint area reaches its yield and maximum strength, obtained from the analytical model, are reported in the legends of Fig. 4.17(a) and (b), respectively. In Fig. 4.17(a) each stress profile shows a slightly convex (upward) curvature, since the power-law relations of the two pre-yield bilinear model parameters are increasing with the strain rate. In Fig. 4.17(b) the shear stresses at $r = 70.7$ dropped to zero, due to reaching maximum strain at the corners. A significant decrease in the slope of each stress profile in Fig. 4.17(b) indicates the distance, r , beyond which the points are in the post-yield region of the bilinear behavior, whereas the points with a smaller r , are in the pre-yield state. At the end of stage (b), 3% of the joint area ($r < 10$ mm) for specimens subjected to 0.00022 rad/s and 10% of the joint area ($r < 18$ mm) for specimens under 0.0044 rad/s are still in their pre-yield state. The slightly concave (downward) curvature in the post-yield section of the stress profiles in Fig. 4.17(b) was caused by the decreasing power-law relations of the two bilinear model post-yield parameters with the strain rate.

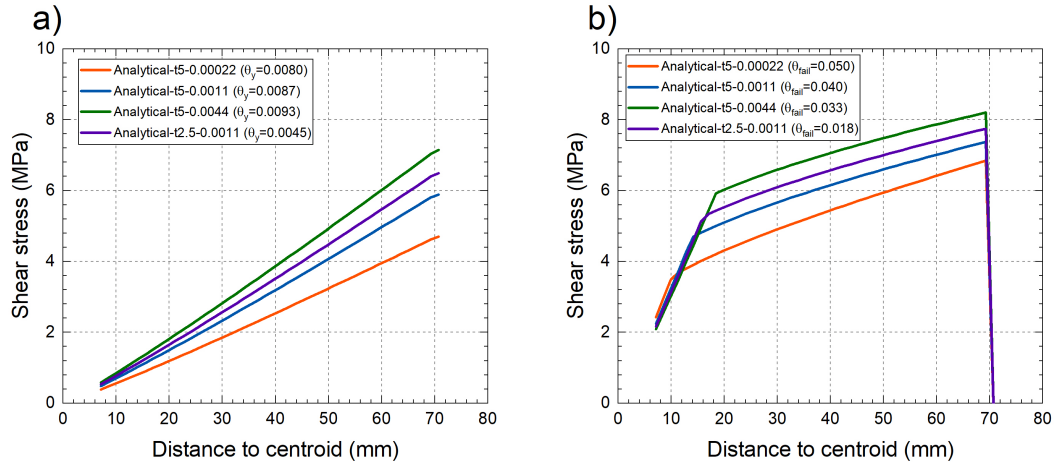


Figure 4.17: Shear stress distribution in radial direction of specimens under different laminate rotation rate and adhesive thickness at end of a) stage (a) and b) stage (b).

The shear stress-strain relationship at the middle point of the edges of the specimens under different laminate rotation rates and adhesive thicknesses with $\dot{\gamma}_m$ of 0.0044, 0.022, 0.088, and 0.044 1/s, displayed in Fig. 4.12, are shown in Fig. 4.18 throughout the experiment. As shown in this figure, the shear stress-strain curve corresponding to the specimen with adhesive

Chapter 4. Pseudo-ductile adhesive angle double lap joints

thickness of 2.5 mm under 0.0011 rad/s laminate rotation rate falls between those of the specimens with a thickness of 5 mm subjected to 0.0011 and 0.0044 rad/s laminate rotation rates, following the magnitude of their shear strain rate.

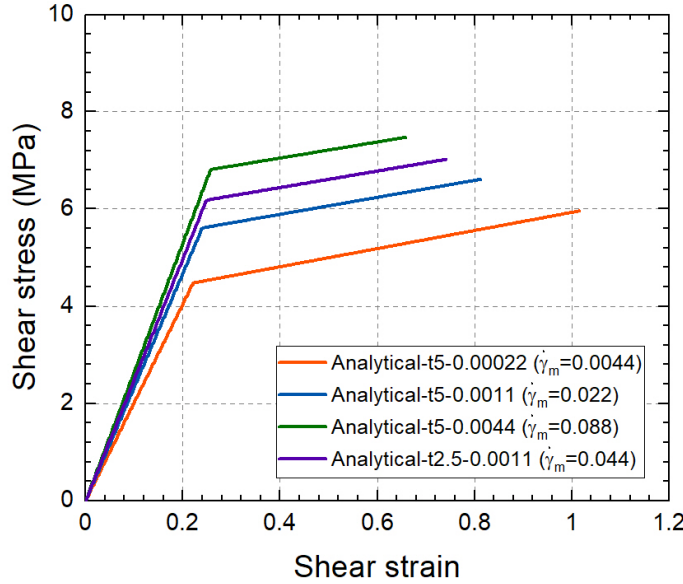


Figure 4.18: Estimated bilinear shear stress-strain at middle point of edges of specimens under different laminate rotation rate and adhesive thickness during experiment.

The shear strain rate at the mid-edge of the joint area, $\dot{\gamma}_m$, was considered as the representative strain rate for each specimen to investigate further the strain rate effects in the following sections.

4.4.2 Variable strain rate effect

To elucidate the effects of strain rate on the torsion-rotation behavior of the angle joints, the average values and corresponding standard errors of S , θ_y , T_{max} , and θ_{max} , were computed for specimens with the same adhesive thickness and under the same laminate rotation rate. These extracted parameters were subsequently plotted against the strain rate, as illustrated in Fig. 4.19(a)-(d), respectively. The analytical bilinear model results are also represented in Fig. 4.19 with a solid line.

An increase in the strain rate resulted in an increase in initial stiffness, yield rotation, and maximum torsional moment, but caused a decrease in maximum rotation. The predicted analytical response overestimated the initial stiffness and underestimated the yield rotation of the experimental data with the difference increasing with the strain rate. However, the predicted analytical response was in good agreement with the experimental data for the

maximum torsion and rotation.

With the increase in strain rate, the molecular chains of the pseudo-ductile adhesive have less time to uncoil and rearrange to the applied load direction. This phenomenon contributes to the higher stiffness within the pre-yield linear region as represented by both the experimental and analytical results in Fig. 4.19(a). The experimental data shows an increase in the initial stiffness by 5% (from 232 to 245 MPa) as the strain rate increases, while the analytical results show a more pronounced 32% increase (from 276 to 365 MPa). The overestimation of the initial stiffness in the torsion-rotation response in the analytical results arises from the incorporated stress-strain relationship from the single-lap joint experimental results with uniform stress distribution.

The stiffer response at higher strain rates leads to an increase in both yield rotation and maximum torsion and a decrease in rotation at the maximum torsion as presented in Fig. 4.19(b)-(d), respectively. In Fig. 4.19(b) the analytical results demonstrate a 22% underestimation compared to the experimental results at lower strain rates, and a more pronounced underestimation of 38% at higher strain rates. This underestimation of the yield rotation can be attributed to the same reason as for initial stiffness. However, the analytical results for maximum torsion and rotation at the maximum torsion, as illustrated in Fig. 4.19(c) and Fig. 4.19(d), respectively, are in good agreement with the experimental results in both values and trend.

4.4.3 Effect of adhesive layer thickness

Both angle joint specimens of M-t5-0.5 and M-t2.5-0.5 with respective adhesive layer thickness of 5 and 2.5 mm were experimented under the same laminate rotation rate of 0.0011 rad/s. By decreasing the adhesive layer thickness, the shear strain rate range expanded from 0-0.031 to 0-0.062, consequently leading to a rise in initial stiffness and yield rotation followed by enhanced strength, as depicted in Fig. 4.19(a)-(c). Conversely, the maximum rotation experienced a decrease, as illustrated in Fig. 4.19(d). These trends are in line with the overall trends of S , θ_y , T_{max} , and θ_{max} for specimens with 5 mm adhesive thickness versus strain rate. The analytical model is also capable of predicting the trend of the variables for the thinner adhesive thickness.

4.4.4 Effect of the adhesive joint type on ductility

In this section, the stress-strain responses from the linear single-lap joints and torsion-rotation responses of the angle joint are compared with the load-displacement behavior of linear double-lap joints with the same materials and adhesive joint area as the angle joints, according

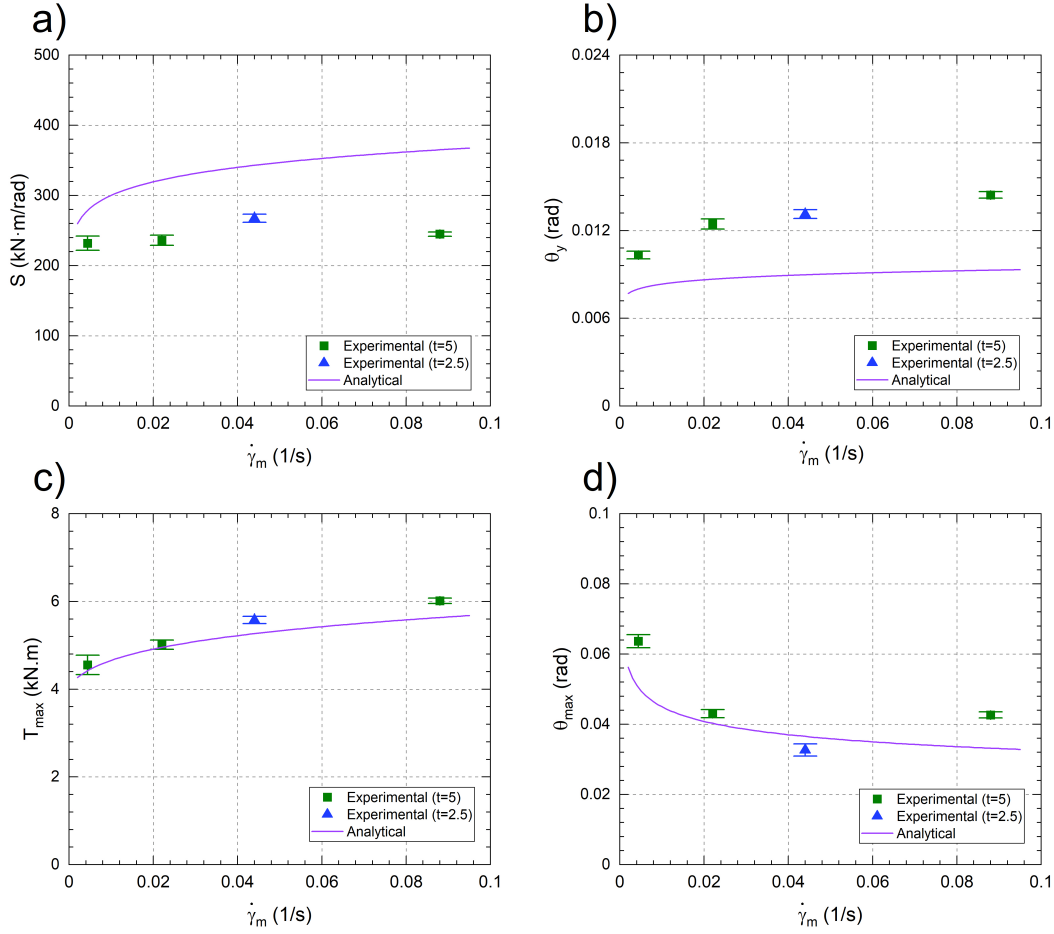


Figure 4.19: Variation of parameters a) S , b) θ_y , c) T_{max} , and d) θ_{max} versus effective strain rate

to the results presented in a previous research [29].

Fig. 4.20(a) provides insight into the effect of strain rate on the ductility of the studied adhesive joint types. The ratio of the area under the post-yield segment of their respective stress-strain, torsion-rotation, or load-displacement curves (i.e., the dissipated inelastic energy), to their total area (i.e., total energy = elastic energy + inelastic energy) [30], ductility ratio, is used to quantify the pseudo-ductility of the adhesive joints. The results show that the ductility ratio, μ , is higher for lower strain rates and decreases with strain rate for all three adhesive joint types (note $\mu = 1.0$ denotes full ductility, neglecting the elastic segment). This behavior is expected for pseudo-ductile adhesives, as higher strain rates result in a more brittle response due to the reduced time available for deformation and energy dissipation. Furthermore, it can be observed that the ductility ratio varies among the different experiment types. Both the linear

double-lap and the linear single-lap joints demonstrate a higher ductility ratio compared to the angle joint, particularly at the lowest strain rate. This difference can be attributed to the uniform strain rate distribution of the linear double-lap and linear single-lap joints, contrasted with the nonuniform strain rate distribution observed in the angle joints. The almost overlapping results of the linear lap joints also demonstrate that, due to the uniform strain rate distributions, the ductility becomes independent of scale, i.e. $13 \times 25.0 \times 1.5$ mm versus $100 \times 100 \times 5$ mm adhesive layer geometries.

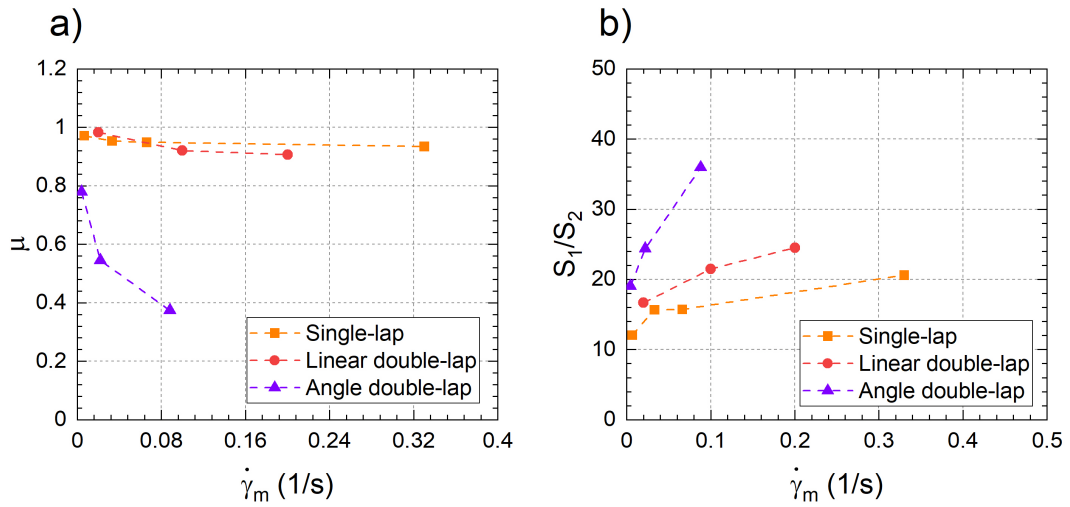


Figure 4.20: Comparison of three adhesive joint experiments for a) inelastic energy to total energy ratio, b) pre-yield to post-yield stiffness ratio, vs. strain rate.

Fig. 4.20(b) shows the pre-yield to post-yield stiffness ratio versus strain rate. This ratio is always higher than one due to the inherently higher stiffness in the pre-yield stage. The results show that the ratio increases with increasing strain rate for all three adhesive joints, consistent with the previously explained behavior of pseudo-ductile adhesives (Fig. 4.14(d)). This behavior results from the slower increase in deformation at lower strain rates, leading to lower pre-yield stiffness, and then allowing the molecular chains to be aligned in the applied deformation direction, leading to a stiffening effect in the post-yield stage. Furthermore, the ratio varies across the joint types. The angle joint exhibits the highest ratio across all strain rates, indicating its inability to effectively exploit the stiffening advantage of the pseudo-ductile adhesives due to the variable strain rate in the adhesive layer. In the adhesive layer, regions close to the center of rotation exhibit lower shear strain and strain rate, consequently remaining in the pre-yield stage characterized by coiled molecular chains. As the distance from the rotation center increases, the molecular chains are subjected to increasing shear strains and strain rates, which enables their uncoiling and reorientation in the tangential direction. However, in the regions furthest from the center of rotation, the molecular chains, which are in

Chapter 4. Pseudo-ductile adhesive angle double lap joints

the post-yield stage, do not have sufficient time to fully uncoil and reorient tangentially before the failure of the joint. This partially rearranged molecular chain structure in the adhesive layer results in a diminished stiffening effect and reduced stiffness after yielding. Consequently, the adhesive layer fails at its interface specially under the highest laminate rotation rate when the joint area experienced the largest range of the strain rate as indicated in Fig. 4.13.

4.5 Conclusions

A novel bonded-bolted angle joint incorporating a central bolt that constrains relative translational deformation but allows for rotational deformation in the adherend plane was developed in this study. Pure torsion moments are imposed in the adhesive layers in this configuration, causing the formation of variable strain rates in the joint in the radial direction from the rotation center. Accordingly, the static behavior of the hybrid bonded-bolted angle joints was investigated, focusing on the effects of induced variable strain rates, adhesive thickness, and adhesive joint type. The results provide insights into the complex performance characteristics of adhesive joints, particularly under variable strain rates. The conclusions from this experimental and analytical investigation are as follows:

1. The angle joint experimental results showed nonuniform shear strain distribution in the radial direction from the rotation center, induced by torsion, in contrast to the single-lap joint experiments.
2. The initial stiffness, yield rotation, and maximum torsion, of the angle-joint experimental results showed increasing trends with the strain rate, while the maximum rotation showed a decreasing trend, all aligned with the rate-dependent molecular chain movement of the pseudo-ductile adhesive.
3. The analytical model developed using the stress-strain relation from single-lap joints with uniform stress distribution overestimated the initial stiffness of the angle joint results with nonuniform stress distribution. However, it could provide good estimations for the strength and post-yield behavior.
4. The angle joint with a thinner adhesive layer exhibited a higher initial stiffness and increased strength in torsion-rotation behavior due to a higher shear strain rate.
5. The adhesive joint ductility is influenced by both strain rate and joint configuration. Lower strain rates enhance ductility in pseudo-ductile adhesives in all joint configurations. Meanwhile, the lower ductility observed in angle joints compared to linear

4.5 Conclusions

double-lap and single-lap joints shows that the pseudo-ductile adhesive capacity may not be fully utilized in the angle configuration, due to the nonuniform strain rate in the radial direction from the rotation center of the adhesive layers.

6. The angle joints exhibited the highest pre-yield stiffness to post-yield stiffness ratio across all strain rates, indicating that they cannot effectively exploit the stiffening advantage of the pseudo-ductile adhesive.

References

- [1] A. Vedernikov, A. Safonov, F. Tucci, P. Carlone, and I. Akhatov, “Pultruded materials and structures: A review”, *Journal of Composite Materials*, vol. 54, no. 26, pp. 4081–4117, 2020.
- [2] H. Xin, Y. Liu, A. S. Mosallam, J. He, and A. Du, “Evaluation on material behaviors of pultruded glass fiber reinforced polymer (gfrp) laminates”, *Composite Structures*, vol. 182, pp. 283–300, 2017.
- [3] L. C. Bank, “Progressive failure and ductility of frp composites for construction”, *Journal of Composites for Construction*, vol. 17, no. 3, pp. 406–419, 2013.
- [4] P. Feng, Y. Wu, Y. Ding, T. Liu, and Y. Tian, “Quasi-plastic flexural behavior of adhesive-bolt hybrid connection for large scale pultruded gfrp frame”, *Engineering Structures*, vol. 238, p. 112 200, 2021.
- [5] J. de Castro and T. Keller, “Design of robust and ductile frp structures incorporating ductile adhesive joints”, *Composites Part B: Engineering*, vol. 41, no. 2, pp. 148–156, 2010.
- [6] T. Keller and J. de Castro, “System ductility and redundancy of frp beam structures with ductile adhesive joints”, *Composites Part B: Engineering*, vol. 36, no. 8, pp. 586–596, 2005.
- [7] L. C. Bank, A. S. Mosallam, and G. T. McCoy, “Design and performance of connections for pultruded frame structures”, *Journal of reinforced plastics and composites*, vol. 13, no. 3, pp. 199–212, 1994.
- [8] L. C. Bank, J. Yin, L. Moore, D. J. Evans, and R. W. Allison, “Experimental and numerical evaluation of beam-to-column connections for pultruded structures”, *Journal of reinforced plastics and composites*, vol. 15, no. 10, pp. 1052–1067, 1996.
- [9] S. Smith, I. Parsons, and K. Hjelmstad, “An experimental study of the behavior of connections for pultruded gfrp i-beams and rectangular tubes”, *Composite structures*, vol. 42, no. 3, pp. 281–290, 1998.
- [10] J. E. Carrion, J. M. LaFave, and K. D. Hjelmstad, “Experimental behavior of monolithic composite cuff connections for fiber reinforced plastic box sections”, *Composite structures*, vol. 67, no. 3, pp. 333–345, 2005.

-
- [11] F. Ascione, M. Lamberti, A. Razaqpur, and S. Spadea, “Strength and stiffness of adhesively bonded gfrp beam-column moment resisting connections”, *Composite Structures*, vol. 160, pp. 1248–1257, 2017.
 - [12] F. Ascione, M. Lamberti, A. G. Razaqpur, S. Spadea, and M. Malagic, “Pseudo-ductile failure of adhesively joined gfrp beam-column connections: An experimental and numerical investigation”, *Composite Structures*, vol. 200, pp. 864–873, 2018.
 - [13] J. Mottram and Y. Zheng, “State-of-the-art review on the design of beam-to-column connections for pultruded frames”, *Composite structures*, vol. 35, no. 4, pp. 387–401, 1996.
 - [14] J. Qureshi, Y. Nadir, and S. K. John, “Bolted and bonded frp beam-column joints with semi-rigid end conditions”, *Composite Structures*, vol. 247, p. 112 500, 2020.
 - [15] F. Ascione, L. Granata, and G. Carozzi, “Flexural and shear behaviour of adhesive connections for large scale gfrp frames: Influence of the bonded area and hygro-thermal aging”, *Composite Structures*, vol. 283, p. 115 122, 2022.
 - [16] A. M. G. Coelho and J. T. Mottram, “A review of the behaviour and analysis of bolted connections and joints in pultruded fibre reinforced polymers”, *Materials & Design*, vol. 74, pp. 86–107, 2015.
 - [17] P. Code, “Eurocode 8: Design of structures for earthquake resistance-part 1: General rules, seismic actions and rules for buildings”, *Brussels: European Committee for Standardization*, 2005.
 - [18] J. de Castro and T. Keller, “Ductile double-lap joints from brittle gfrp laminates and ductile adhesives, part i: Experimental investigation”, *Composites Part B: Engineering*, vol. 39, no. 2, pp. 271–281, 2008.
 - [19] M. Angelidi, A. P. Vassilopoulos, and T. Keller, “Ductility, recovery and strain rate dependency of an acrylic structural adhesive”, *Construction and Building Materials*, vol. 140, pp. 184–193, 2017.
 - [20] G. Eslami, A. V. Movahedi-Rad, and T. Keller, “Viscoelastic adhesive modeling of ductile adhesive-composite joints during cyclic loading”, *International Journal of Adhesion and Adhesives*, vol. 119, p. 103 241, 2022.

Chapter 4. Pseudo-ductile adhesive angle double lap joints

- [21] ASTM, “Standard test method for apparent shear strength of single-lap-joint adhesively bonded metal specimens by tension loading (metal-to-metal)”, *ASTM D1002-10*, ASTM International, West Conshohocken, Pa, Usa, 2010.
- [22] D. ASTM, “2651-01 standard guide for the preparation of metal surfaces for adhesive bonding”, ASTM, 2001.
- [23] SIKA, *Sikafast-555 l03*, <https://industry.sika.com/en/home/appliance-and-equipment/hvac/sikafast-555-l03.html>, 2022.
- [24] T. Keller, J. Rothe, J. De Castro, and M. Osei-Antwi, “Gfrp-balsa sandwich bridge deck: Concept, design, and experimental validation”, *Journal of Composites for Construction*, vol. 18, no. 2, p. 04 013 043, 2014.
- [25] T. Keller and H. Gürtler, “Design of hybrid bridge girders with adhesively bonded and compositely acting frp deck”, *Composite structures*, vol. 74, no. 2, pp. 202–212, 2006.
- [26] G. Eslami, A. Movahedirad, and T. Keller, “Energy dissipation in fiber-polymer composites adhesive joints under cyclic loading”, Ph.D. dissertation, 2023.
- [27] “Fiberline composites a/s”, 2003.
- [28] A. S. for Testing Materials (ASTM). D5573-99, *Standard practice for classifying failure modes in fiber-reinforced-plastic (frp) joints*, 2012.
- [29] G. Eslami, S. Yanes-Armas, and T. Keller, “Energy dissipation in adhesive and bolted pultruded gfrp double-lap joints under cyclic loading”, *Composite Structures*, vol. 248, p. 112 496, 2020.
- [30] N. F. Grace, A. Soliman, G. Abdel-Sayed, and K. Saleh, “Behavior and ductility of simple and continuous frp reinforced beams”, *Journal of composites for construction*, vol. 2, no. 4, pp. 186–194, 1998.



Conclusions and future work

5.1 Conclusion

This thesis attempts to contribute to the field of lightweight construction by conducting a comprehensive investigation into the performance of composite joints, which possess a remarkable strength-to-weight ratio compared to conventional construction materials. Common composite joints tend to exhibit suboptimal performance under seismic actions, as their inherent brittleness results in limited energy dissipation capacity. Consequently, pseudo-ductile adhesive bonded joints were selected to be the subject of studies, having the potential to introduce pseudo-ductility in the joints of brittle composite structures.

Given the scarcity of literature on the behavior of pseudo-ductile adhesives, as well as their intricate, nonlinear, and rate-dependent properties, this research program was conducted, as detailed in the preceding chapters of this thesis. The main conclusions derived from this research are presented below:

- Pseudo-ductile adhesives are known to exhibit strain rate-dependent mechanical behavior. This dependency originates from the molecular chain structure arrangement of the adhesive in its initial state and its change dependent on the applied strain rate. The effect of various phenomena at the molecular level, namely, coiling and uncoiling, stretching, and damage accumulation on the response of a pseudo-ductile adhesive to the applied displacement were studied and discussed in detail.
- The strain rate effects on pseudo-ductile adhesive's mechanical behavior were studied for both uniform strain distribution along the joint area, for linear double lap and single-lap joints, and for gradient strain distribution, for angle double lap joints.

Chapter 5. Conclusions and future work

- Experimental results revealed that, in general, the response of pseudo-ductile adhesive joints had a higher initial stiffness with the increase of the applied displacement rate due to insufficient time for the uncoiling of the molecular chains.
 - With a stiffer pre-yield response at higher rates, pseudo-ductile adhesives exhibit a higher yield load. In linear double lap joints, the pseudo-ductile adhesive exhibited significant stiffening in the post-yield stage, due to stretching and re-alignment of the molecular chains, leading to an increased peak load at lower rates. Conversely, in angle joints, the pseudo-ductile adhesive could not fully exploit its stiffening capacity, as for the linear double lap joints, due to the presence of nonuniform strain rates within the joint area. Consequently, the peak load is increased with the strain rate in the angle joints.
 - In all joint types, a decreasing trend was observed for the failure deformation with the increase of the strain rate, due to less time available for the rearrangement of molecular chains, leading to brittle behavior of the pseudo-ductile adhesive and failure at lower deformations.
- To compare the ductility of the pseudo-ductile adhesive joints subjected to monotonic loading, the ratio of the total absorbed energy to the pre-yield energy for all three types of single-lap, linear and angle double-lap joints could be compared versus their respective strain rate. This provides a unitless measure for the comparison of the ductility of the joints undergoing shear deformations. It was found that linear joints exhibit a significantly higher ductility compared to the angle joints, mainly attributed to the presence of variable strain rates within the adhesive layer of the angle joint.
 - The results of monotonic experiments on linear double lap adhesive joints were used as a basis for definition of the displacement pattern applied to joints in cyclic experiments. It was observed that the pseudo-ductile adhesive joints may exhibit varying behavioral responses when subjected to monotonic or cyclic displacements. These variations were found to be rate-dependent.
 - Cyclic loading results in progressive damage accumulation in the pseudo-ductile adhesive and consequently, the envelope curve defined by the cycles peak load, is lower than that of the monotonic loading. For the cases in which the adhesive undergoes a lower number of cycles, i.e., under the highest applied displacement rate, damage accumulation is insignificant and therefore, a similar peak load was measured for both monotonic and cyclic experiments.

- Being subjected to unloading phase, pseudo-ductile adhesive layers could partially recover the lost secondary bonds and undergo larger displacements under cyclic loading than those under monotonic loading, with an observed increase of up to three times at medium rate. Consequently, a transition in failure mode was also observed, from fiber-tear failure in monotonic experiments to cohesive failure in cyclic experiments.
- Characterizing the rate-dependent behavior of pseudo-ductile adhesives often proves to be time and resource-intensive due to the necessity for comprehensive experimental campaigns to identify the complex behavior of the adhesives under various loading conditions. In this context, having a constitutive behavioral model could be very beneficial as it significantly reduces the dependency on the experimental results for understanding the adhesives behavior. However, it shall be noted that a certain number of experimental results are still required to calibrate the behavioral constitutive model effectively.
 - Due to the significantly larger stiffness of laminates compared to the pseudo-ductile adhesive, the response of the pseudo-ductile adhesive joints can be primarily attributed to the adhesive. Additionally, a behavioral model can be developed for linear double lap joints based on the observation of uniform shear stress distribution in the adhesive layers. Pseudo-ductile adhesive joints subjected to cyclic loading exhibited a similar nonlinear response between the two reversal points of each cycle and the envelop curves to the cycles when compared to joints subjected to monotonic loading. Consequently, the phenomenological model designated to simulate the behavior of the pseudo-ductile adhesive joints under monotonic loading can be expanded to simulate each segment of a cycle in cyclic loading response.
 - Given that the observed monotonic behavior of the pseudo-ductile adhesive consisted of two branches, a phenomenological model composed of two dissimilar parallel Maxwell units was employed to simulate the rate-dependent pre-yield and post-yield branch of the behavior, each.
 - Constitutive models must strike a balance between precise and computational efficiency, two factors that are usually contradictory. However, in this thesis, a computation model of only five parameters, comparatively fewer than the models introduced in literature, could well capture both the response of the adhesive and its physical characteristics, such as stretching of molecular chains (i.e., strain hardening) and formation and accumulation of damage (i.e., softening), in both monotonic and decomposed cyclic responses.

Chapter 5. Conclusions and future work

- An analytical model was also developed for predicting the torsion-rotation behavior of the angle joints, based on the parameterization of their behavior. The analytical model was also found to predict the behavior of the angle joints desirably, particularly under lower strain rates.
- Both constitutive and analytical models for linear and angle double lap joints were developed based on parameterization of the corresponding rate-dependent behavior of the joints. The parameters used to develop both models were found to have power-law relationships with respective strain rate. Moreover, the parameters used in the constitutive model to simulate each segment of the cyclic response were also found to have a power-law or an exponential relationship with the maximum displacement of that cycle.
- The energy dissipation capacity of the pseudo-ductile adhesive joints was one of the main key parameters that necessitated the investigations conducted in this thesis.
 - The energy dissipation capacity of the linear double lap pseudo-ductile adhesive joints was found to be significantly higher than that of the bolted joints when adhesive joints were subjected to lower strain rates. Meanwhile, bolted joints could only dissipate energy through the undesirable irreversible crushing and shear-out damage, making their replacement after a seismic event mandatory. While the deformation of the pseudo-ductile adhesive joints remains within less than 25% of their failure deformation, they contribute to the continuous serviceability of all-composite structures. Moreover, they can help in collapse prevention in severe seismic events up until they reach 75% of their failure deformation.
 - The energy dissipation per-cycle in linear double lap pseudo-ductile adhesive joints increased with the applied displacement rate. However, due to the definition of cycle displacements according to the monotonic response at each rate, specimens under the medium rate undergone smaller displacement at each cycle compared to those subjected to the lower rate. Consequently, because of their similar ultimate displacement, specimens subjected to medium rate experienced a higher number of cycles up to their failure and therefore, dissipated the highest energy in total.

5.2 Original contributions

The original contributions of this thesis with regard to existing knowledge on this research topic are the following:

1. A comparative study of the monotonic response of pseudo-ductile adhesive glass composite double-lap joints with two configurations of bolted glass composite double-lap joints having similar geometry and strength was conducted. The rate-dependent monotonic response behavior of the pseudo-ductile adhesive was studied under three levels of applied displacement rates. The experimental design effectively demonstrates the superior deformation capacity of pseudo-ductile adhesive joints to bolted joints with equivalent load-bearing capacity.
2. Novel reversed cyclic experiments were conducted on pseudo-ductile adhesive double-lap joints enabling a comparison of their energy dissipation capacity with similar bolted joints. The effects of the applied displacement rate on the cyclic behavior and energy dissipation capacity of the pseudo-ductile adhesive double-lap joints were also investigated.
3. A new phenomenological model was developed to simulate the monotonic viscoelastic behavior of the pseudo-ductile adhesive under various displacement rates. The developed model incorporated both linear and nonlinear viscoelastic behavior and utilized only five parameters, each exhibiting a power-law relationship with the applied displacement rate.
4. The constitutive equation derived from the proposed phenomenological model was adapted to the cyclic experimental results by introducing the concept of cycle decomposition. A prediction process for the cyclic response was proposed and validated with cyclic envelope curves and energy dissipation capacity. However, the accuracy of the proposed procedure is limited to the uniform displacement rate values between the minimum and the maximum rates used in the experiments.
5. A new experimental setup, named angle joint, was specifically designed for investigating pseudo-ductile adhesives under variable strain rates. The angle joint configuration provided pure torsion within the adhesive layer and, therefore, a varying strain rate within the adhesive layer area with a value relative to the distance from the center of rotation.
6. The pseudo-ductile adhesive angle joints were subjected to three levels of displacement rates to measure their moment-rotation response. The ductility achieved from the adhesive angle double-lap joints was then compared to that of linear adhesive double-lap joints.
7. An analytical method was proposed for estimating the torsion-rotation response of pseudo-ductile angle joints. The method employed a developed bilinear model based

on the pseudo-ductile adhesive single-lap experimental results under six different strain rates, which was then used to obtain the nonuniform stress distribution across the joint area induced by torsion.

5.3 Recommendations for future work

5.3.1 Phenomenological model of the pseudo-ductile adhesive containing failure criteria

The present research has focused on the rate-dependent pre-and post-yield behaviors of a pseudo-ductile adhesive through the investigation of two stages of adhesive molecular chains, namely uncoiling and loss of secondary bonds. Stiffening is an advantageous phenomenon that was achieved under low strain rates due to the stretching of the molecular chains in the absence of recoverable secondary bonds. Considering that by increasing the displacement, the unrecoverable primary bonds in the chains and between them tend to be broken, knowing this capacity is essential for enhancing the phenomenological model capabilities. In order to characterize the rate-dependent failure properties of the pseudo-ductile adhesive, it is necessary to find its energy release rate properties [1]. The development of appropriate new experimental setups (e.g., Mode I, Mode II, and Mode III experiments) would be required so that the analyzed results be used to achieve a phenomenological model with failure criteria [2], [3].

5.3.2 Time evolution, thickness, and geometry effects

The results obtained from the pseudo-ductile adhesive linear double- and single-lap joints in this thesis demonstrated a uniform stress distribution across the joint area. However, in experiments of double-lap joints under torsion, a nonuniform stress distribution was formed due to the variable strain rate across the joint area. While the effects of adhesive thickness were negligible under uniform stress distribution, the presence of nonuniform distribution magnified the impacts of adhesive thickness [4], [5]. This study also noted distinct behaviors when altering the thickness of the adhesive layer, highlighting the need for further investigation on the subject. Moreover, applying torsional moments on geometries more complex than the investigated square configuration may result in different critical conditions within the adhesive layer, potentially resulting in more complex strain rate patterns within the joint area. Another key aspect is the potential time evolution of adhesives at room temperature, such as physical aging under load, which can significantly impact long-term adhesive joint perfor-

mance. Considering the possibility of different aging conditions and joint area geometries in common practice, in comparison to the investigated square geometry cured for five days at room temperature just prior to the experiments, the development of new representative experimental setups (e.g., angle joints with different thicknesses and joint area geometries under different aging conditions), along with a numerical investigation, would be beneficial to achieve a better understanding of pseudo-ductile adhesives under variable strain rates.

5.3.3 Cycle amplitude effects in tension and torsion

In this study, the CUREE loading pattern, one of the proposed cyclic loading patterns in ASTM Standard E2126 [6], was utilized to determine the history of the applied cyclic displacement. However, CUREE is originally intended for wooden structures. It was found that the amplitude of the cycles plays a crucial role in the competition between damage accumulation and stiffening phenomena during the post-yield branch of the load-displacement response of the pseudo-ductile adhesive joints under different displacement rates. Consequently, it is valuable to investigate different cyclic loading patterns under various displacement rates. Moreover, the interplay between damage accumulation and stiffening phenomena becomes increasingly critical under variable strain rates. Examining cyclic behavior under variable strain rates, in conjunction with diverse loading patterns, could ultimately assist in developing a cyclic loading pattern dedicated to all-composite structures, a contribution currently absent in the literature.

5.3.4 Frame application

The primary objective of this thesis was to introduce pseudo-ductility in all-composite structures through the use of pseudo-ductile adhesive joints. Achieving ductility is particularly important in seismic-prone areas, as increased ductility contributes to enhanced energy dissipation capacity. Given that the benefits of the proposed pseudo-ductile adhesive joint may be more significant in seismic areas, it is crucial to evaluate the dynamic behavior of all-composite structures. While some studies have examined pultruded glass composite frames with bolted connections [7], [8], there remains a gap in understanding the dynamic performance of pultruded glass composite frames with adhesive joints. To address this, conducting experimental investigations of frames with appropriately designed adhesively bonded beam-column connections under monotonic (push-over) [9], [10] and then cyclic loading [11] would serve as a valuable starting point, followed by analytical and numerical investigations.

5.3.5 Exploring a predictive model using machine learning methods

As interest in glass composite profiles and their pseudo-ductile joints grows, the variety of available adhesives is also increasing. Experimentally investigating every type of adhesive under all probable conditions is both time-consuming and cost-inefficient; therefore, searching for an optimal choice is justified. Recently, machine learning techniques and algorithms have demonstrated their utility in prediction and optimization tasks, offering an alternative to altering a single parameter at a time through experimental investigation. As a result, contemporary studies have begun employing evidence-based machine learning techniques to replace the traditional numerical and experimental methods examining the interplay of adhesive joint design parameters [12]. Consequently, the development of a machine learning-based algorithm tailored to enhancing the behavior of pseudo-ductile adhesive joints is an essential direction for future research.

References

- [1] Y. Zhang, A. P. Vassilopoulos, and T. Keller, “Mode i and ii fracture behavior of adhesively-bonded pultruded composite joints”, *Engineering Fracture Mechanics*, vol. 77, no. 1, pp. 128–143, 2010.
- [2] J. Lei, Z. Li, S. Xu, and Z. Liu, “A mesoscopic network mechanics method to reproduce the large deformation and fracture process of cross-linked elastomers”, *Journal of the Mechanics and Physics of Solids*, vol. 156, p. 104 599, 2021.
- [3] F. J. Vernerey, R. Long, and R. Brighenti, “A statistically-based continuum theory for polymers with transient networks”, *Journal of the Mechanics and Physics of Solids*, vol. 107, pp. 1–20, 2017.
- [4] T. Vallée, J. R. Correia, and T. Keller, “Probabilistic strength prediction for double lap joints composed of pultruded gfrp profiles part i: Experimental and numerical investigations”, *Composites Science and Technology*, vol. 66, no. 13, pp. 1903–1914, 2006.
- [5] R. D. Campilho, D. Moura, M. D. Banea, and L. F. M. da Silva, “Adhesive thickness effects of a ductile adhesive by optical measurement techniques”, *International Journal of Adhesion and Adhesives*, vol. 57, pp. 125–132, 2015.
- [6] ASTM, “Standard test methods for cyclic (reversed) load test for shear resistance of vertical elements of the lateral force resisting systems for buildings”, *ASTM E2126*, 2019.
- [7] G. Boscatto and S. Russo, “Free vibrations of a pultruded gfrp frame with different rotational stiffnesses of bolted joints”, *Mechanics of Composite Materials*, vol. 48, pp. 655–668, 2013.
- [8] S. Russo, “Experimental and finite element analysis of a very large pultruded frp structure subjected to free vibration”, *Composite structures*, vol. 94, no. 3, pp. 1097–1105, 2012.
- [9] C. Wu, J. Tian, Y. Ding, and P. Feng, “Axial compression behavior of pultruded gfrp channel sections”, *Composite Structures*, vol. 289, p. 115 438, 2022.
- [10] Y.-F. Li, J.-Y. Lai, and C.-C. Yu, “The push-over test and numerical analysis study on the mechanical behavior of the gfrp frame for sustainable prefabricated houses”, *Sustainability*, vol. 11, no. 23, p. 6753, 2019.

Chapter 5. Conclusions and future work

- [11] J. W. Van de Lindt, S. E. Pryor, and S. Pei, “Shake table testing of a full-scale seven-story steel–wood apartment building”, *Engineering Structures*, vol. 33, no. 3, pp. 757–766, 2011.
- [12] Z. Gu, Y. Liu, D. J. Hughes, J. Ye, and X. Hou, “A parametric study of adhesive bonded joints with composite material using black-box and grey-box machine learning methods: Deep neuron networks and genetic programming”, *Composites Part B: Engineering*, vol. 217, p. 108 894, 2021.

Fabrication process and experiments on linear adhesive and bolted glass composite double-lap joints

Appendix A provides supplementary information and data related to the fabrication of linear double-lap joints and the results of the experiments that were performed on them, as detailed in Chapter 1.4.

The experimental program involved the application of monotonic and cyclic loadings on bolted and pseudo-ductile adhesive double-lap joints. These joints were comprised of two outer glass composite laminates, each measuring 230 mm in length and 100 mm in width, as well as an inner glass composite laminate of 200 mm length and 100 mm width. All three laminates were of a uniform thickness of 10 mm. The laminates' surface underwent initial treatment with 60 grit sandpaper to remove the polyester surface veil down to an approximate depth of 0.5 mm. A promoter layer of Sikadur 330 epoxy adhesive was then applied and then the specimen was cured for four hours in an oven at a temperature of 60 °C. This procedure ensured prevention of a premature adhesion failure in pseudo-ductile adhesive joints (Fig. 1.1).

The subsequent figures (Figs. 1.2-1.8) of this appendix show the load-displacement curves, along with the failure modes observed in the bolted and pseudo-ductile adhesive linear double-lap joints under monotonic and cyclic loading conditions. These figures provide the results substantiated with two replicates of the specimens.

Furthermore, to verify the quality of the fabrication, tomographic imaging was conducted on a prepared joint before initiating the experiment. These images, capturing the whole joint area, coupled with the known adhesive density, facilitated the computation of the voids percentage within the adhesive layer. It was discovered that voids occupied less than 10% of the adhesive layer's total volume in a fabricated joint. This image can be seen in Fig. 1.9.

Appendix A. Fabrication process and experiments on linear adhesive and bolted glass composite double-lap joints

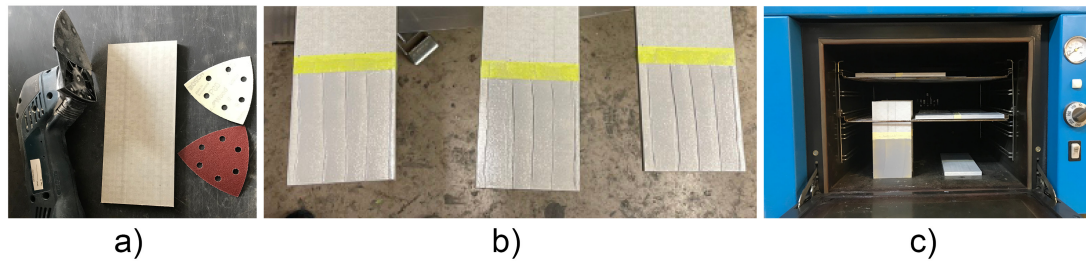


Figure 1.1: a) Scratching of glass composite laminates, b) Applying epoxy promoter coating on glass composite laminates, c) Curing glass composite laminate in the oven.

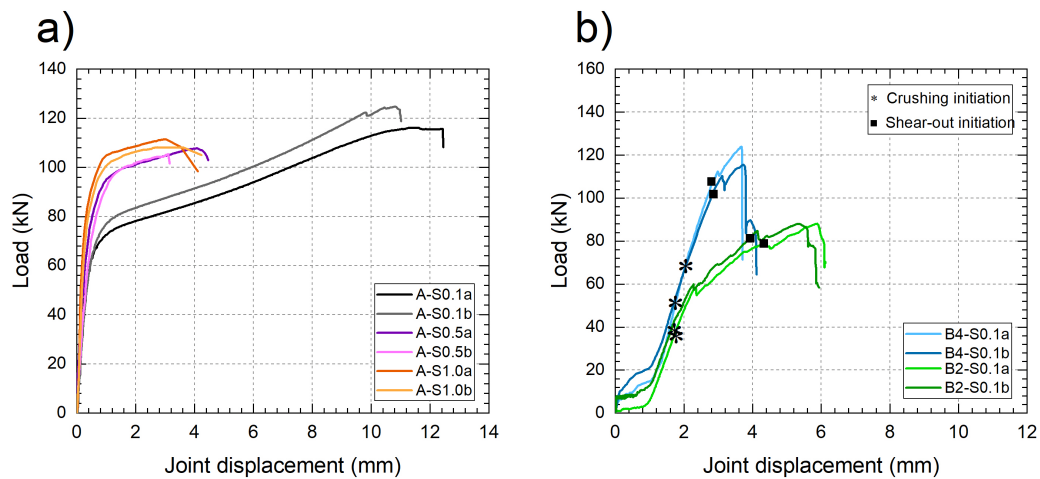


Figure 1.2: Load-joint displacement responses under monotonic loading for a) pseudo-ductile adhesive joints, and b) bolted joints.

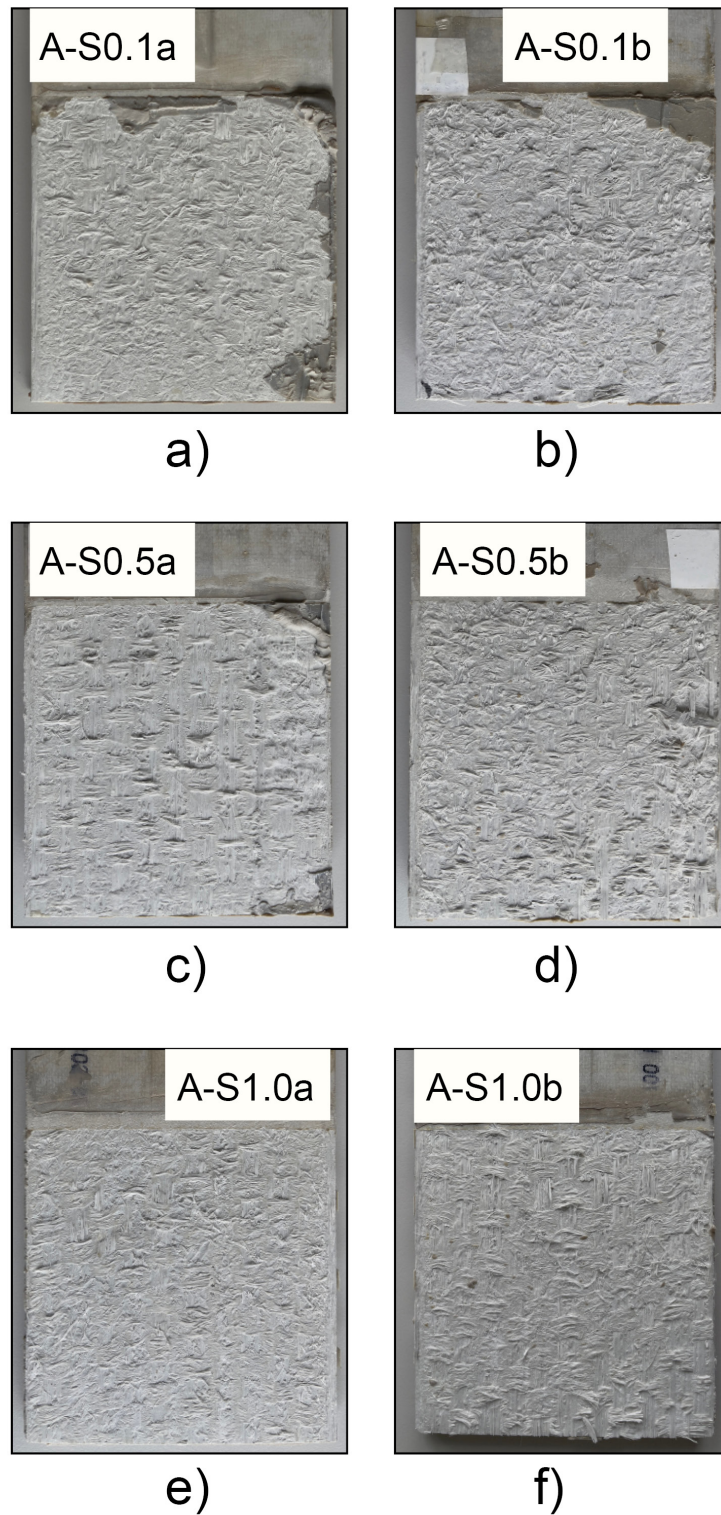
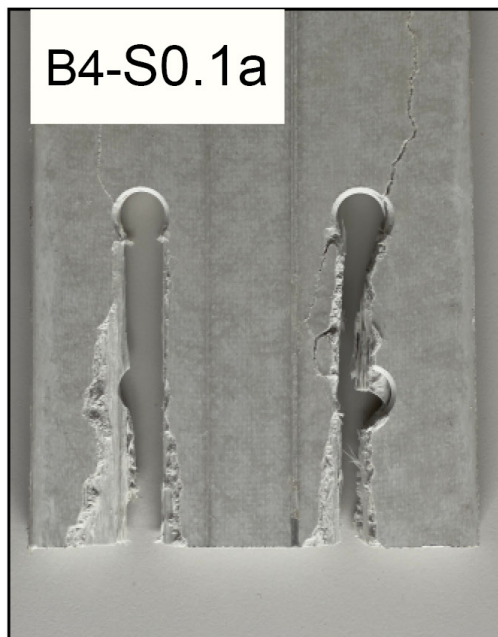
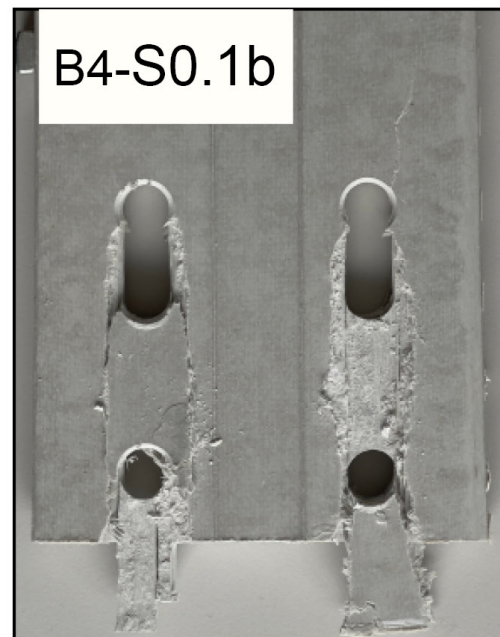


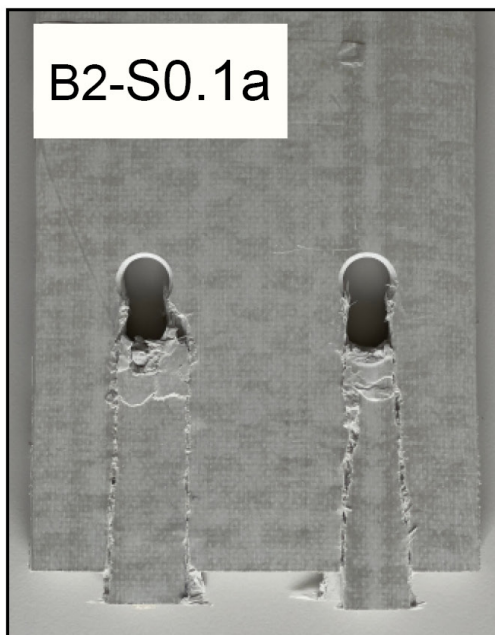
Figure 1.3: Fiber-tear failure modes of adhesive joints under monotonic loading.



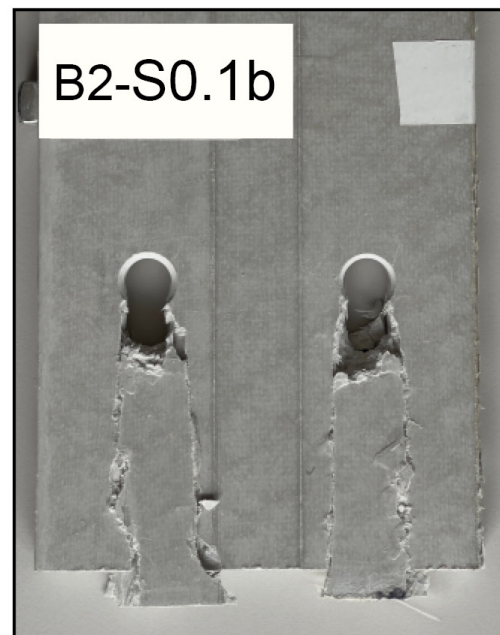
a)



b)



c)



d)

Figure 1.4: Combined crushing and shear-out failure modes of bolted joints under monotonic loading.

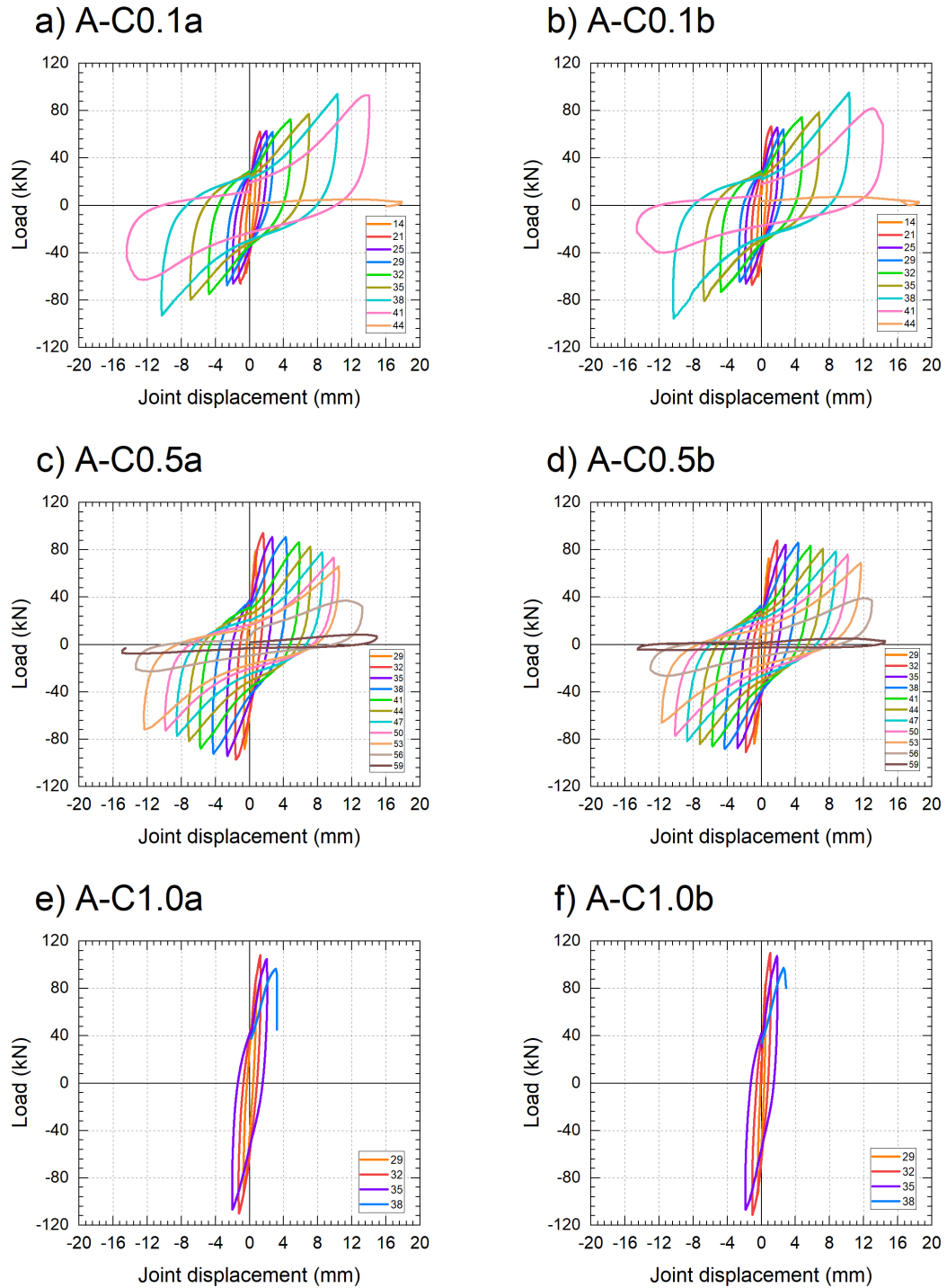


Figure 1.5: Load-joint displacement responses of adhesive joints under cyclic loading.

Appendix A. Fabrication process and experiments on linear adhesive and bolted glass composite double-lap joints

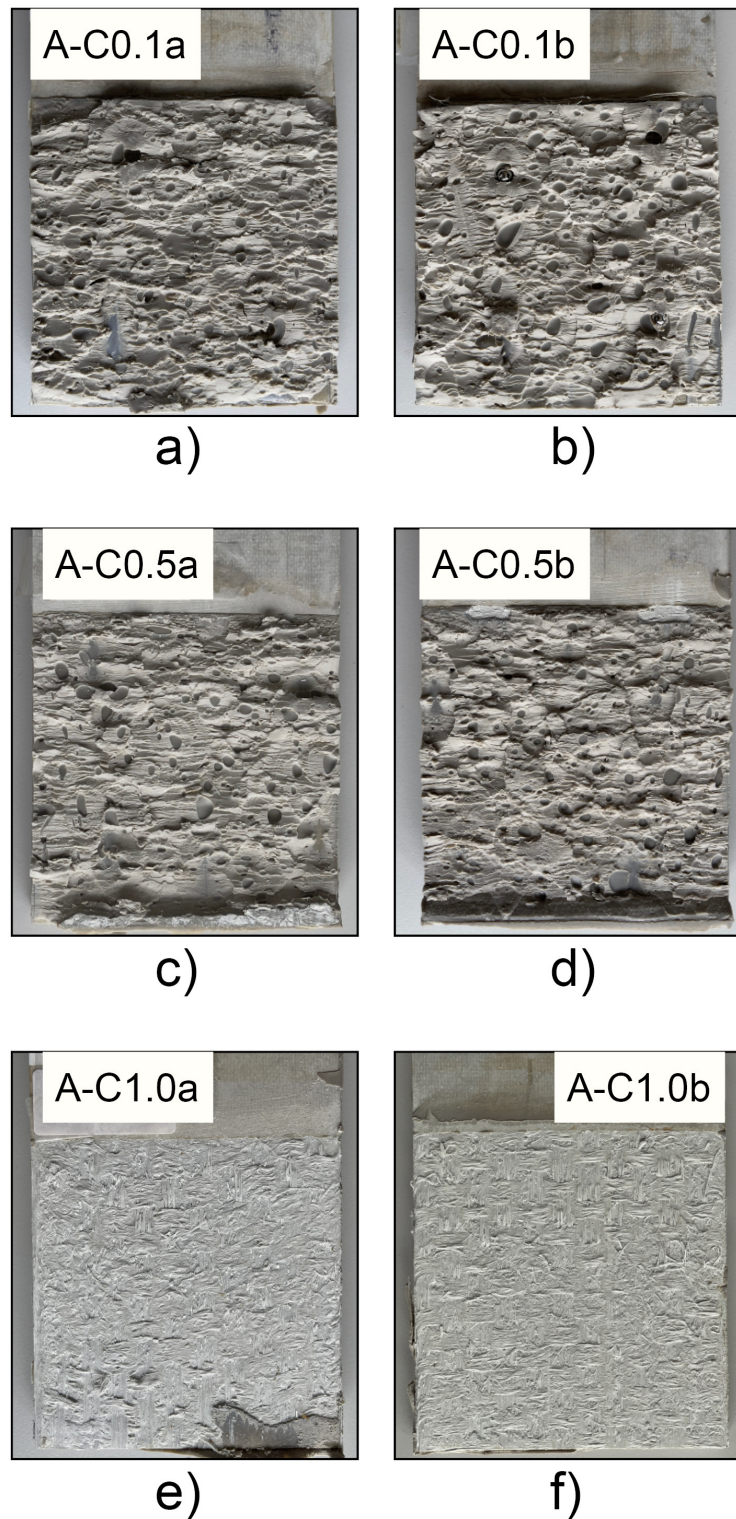


Figure 1.6: Failure modes of adhesive joints under cyclic loading; cohesive failure in a), b), c), and d), fiber-tear failure in e) and f).

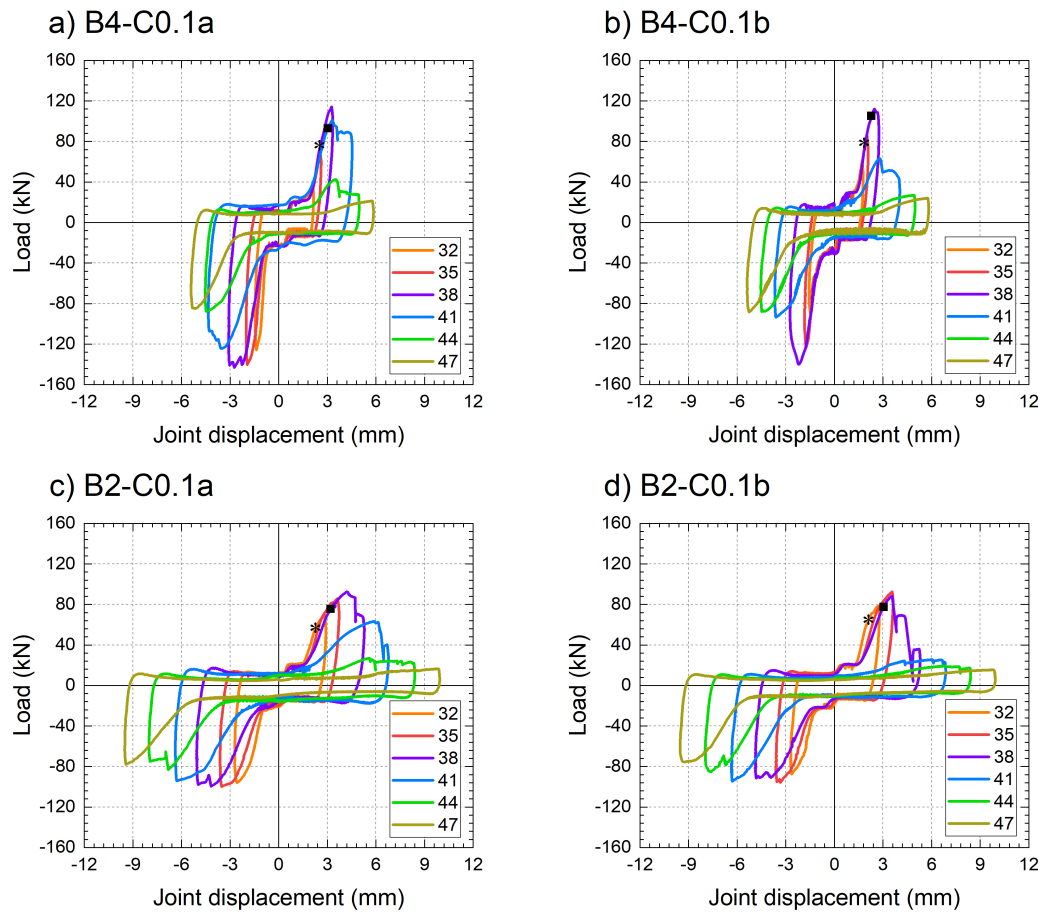
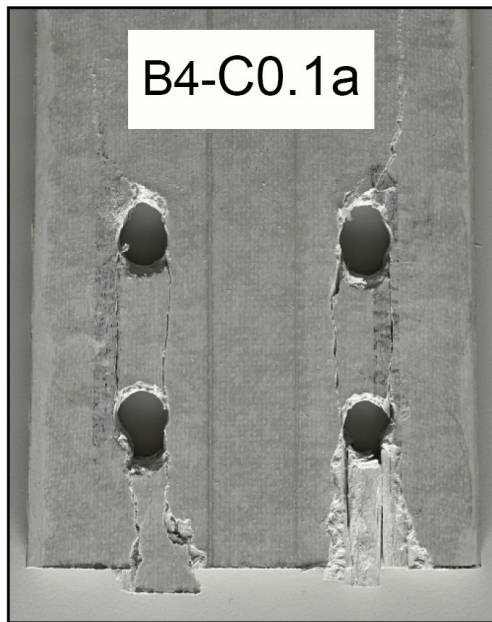
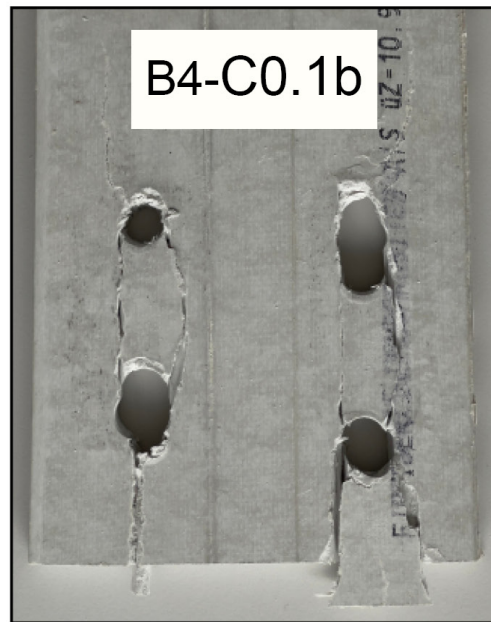


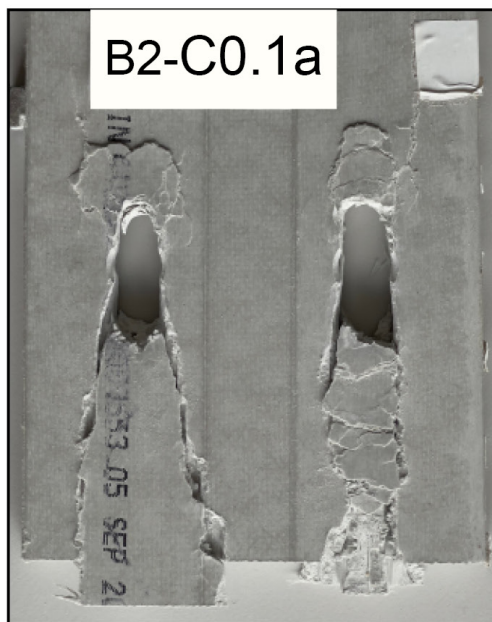
Figure 1.7: Load-joint displacement responses of bolted joints under cyclic loading.



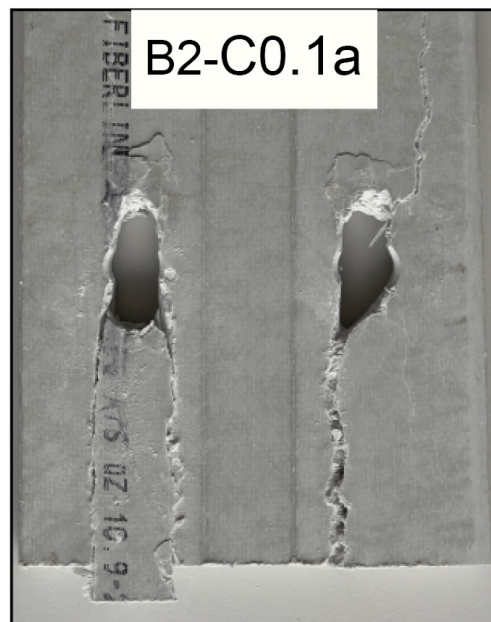
a)



b)



c)



d)

Figure 1.8: Combined crushing and shear-out failure modes of bolted joints under cyclic loading.

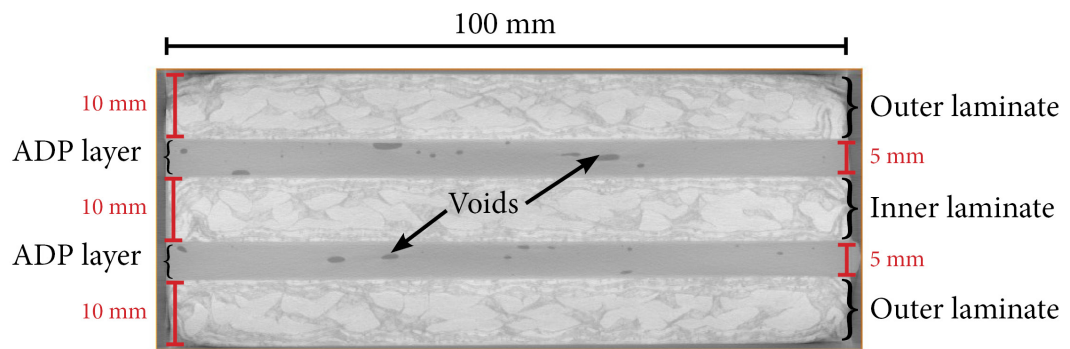


Figure 1.9: Tomography photo at middle section of joint area (100×100).

B

Phenomenological constitutive model development and Python program

Appendix B provides the Python script used for predictions described in Chapter 2.5. This script represents an executable code that performs the computations and analyses described in that chapter. The flowchart presented in Fig. 3.10, which provides a visual overview of the script's sequence of operations, is directly reflected in this script. This makes it easier to understand how the steps outlined in the flowchart are implemented in the code. Additionally, the script is directly linked to the generation of the parameters depicted in Fig. 3.11.

Code:

```
1  # Importing the necessary libraries
2  import pandas as pd
3  import numpy as np
4  import warnings
5  import math
6  import matplotlib.pyplot as plt
7  from scipy import interpolate
8  from scipy.optimize import curve_fit
9  from sklearn.metrics import r2_score
10
11 # Reading the experiment's data as a DataFrame and minor formatting
12 data_joint = pd.read_excel('Cyclic_linear_doublelap.xlsx', sheet_name='A-C0.1a',
13                             skiprows=3, usecols = 'A:C')
14 data_joint = data_joint.rename(columns={'s' : 'Time', 'mm' : 'Joint_displacement',
15                                         'kN': 'Load'})
16
17 ###
18 ### Cleaning Data - Removing the rows where the recorded displacement was noisy
19 ### (e.g. decreasing disps in an increasing disp-control loading)
20 ###
21 noisy_rows_list = []
22 old_len = len(data_joint ["Load"])
23 new_len = old_len - 5
24 while new_len < old_len - 4:
```

Appendix B. Phenomenological constitutive model development and Python program

```
23     for i in range (6, len(data_joint ["Joint_displacement"])-2):
24         disp_increasing_1 = data_joint.loc[i-1, "Joint_displacement"] >= data_
            joint.loc[i-2, "Joint_displacement"]
25         disp_increasing_2 = data_joint.loc[i-1, "Joint_displacement"] >= data_
            joint.loc[i-2, "Joint_displacement"]
26         load_increasing = data_joint.loc[i, "Load"] > data_joint.loc[i-1, "Load"]
27
28         if disp_increasing_1 and disp_increasing_2 and (not load_increasing):
29             noisy_rows_list.append(i)
30         elif not (disp_increasing_1 or disp_increasing_2) and load_increasing:
31             noisy_rows_list.append(i)
32
33     # Dropping the noisy rows
34     data_joint.drop(noisy_rows_list, inplace = True)
35     data_joint.reset_index(drop=True, inplace = True)
36     old_len = new_len
37     new_len = len(data_joint["Load"])
38     noisy_rows_list = []
39
40
41
42
43     ###
44     ### Extracting cycle numbers from the joint data and performing cycle
        decomposition
45     ###
46     data_joint ["new_time"] = np.nan
47     data_joint ["new_disp"] = np.nan
48     data_joint ["new_load"] = np.nan
49     data_joint ["cycle_situation"] = np.nan
50
51     t0 = 0
52     d0 = 0
53     l0 = 0
54     cycle_count = 1
55     cycle_segment = 1
56
57     for i in range (5, len(data_joint["Load"])):
58         if cycle_segment == 2:
59             if data_joint.at[i, "Load"] >= data_joint.at[i-1, "Load"]:
60                 t0 = data_joint.at[i-1, "Time"]
61                 d0 = data_joint.at[i-1, "Joint_displacement"]
62                 l0 = data_joint.at[i-1, "Load"]
63                 cycle_count += 1
64             if data_joint.at[i, "Load"] >= data_joint.at[i-1, "Load"]:
65                 data_joint.at[i, "new_time"] = data_joint.at[i, "Time"] - t0
66                 data_joint.at[i, "new_disp"] = data_joint.at[i, "Joint_displacement"] - d
                    0
67                 data_joint.at[i, "new_load"] = data_joint.at[i, "Load"] - l0
68                 data_joint.loc[i, "cycle_Number"] = cycle_count
69                 data_joint.loc[i, "cycle_situation"] = str(cycle_count) + "_T_P"
70                 cycle_segment = 1
71             else:
```

```

72         if cycle_segment == 1:
73             t0 = data_joint.at[i-1, "Time"]
74             d0 = data_joint.at[i-1, "Joint_displacement"]
75             l0 = data_joint.at[i-1, "Load"]
76
77             data_joint.at[i, "new_time"] = data_joint.at[i, "Time"] - t0
78             data_joint.at[i, "new_disp"] = d0 - data_joint.at[i, "Joint_displacement"]
79             data_joint.at[i, "new_load"] = l0 - data_joint.at[i, "Load"]
80             data_joint.loc[i, "cycle_Number"] = cycle_count
81             data_joint.loc[i, "cycle_situation"] = str(cycle_count) + "_P_P"
82             cycle_segment = 2
83
84     # Storing the cycle segments in a new DataFrame
85     for i in range(1, cycle_count + 1):
86         Name1 = 'data_joint_' + str(i) + '_T_P'
87         cycle_part1 = str(i) + '_T_P'
88
89         Name2 = 'data_joint_' + str(i) + '_P_P'
90         cycle_part2 = str(i) + '_P_P'
91
92         globals()[Name1] = data_joint[data_joint.cycle_situation == cycle_part1][["cycle_Number", "new_time", "Load", "Joint_displacement"]]
93         globals()[Name2] = data_joint[data_joint.cycle_situation == cycle_part2][["cycle_Number", "new_time", "Load", "Joint_displacement"]]
94         globals()[Name1].reset_index(drop=True, inplace = True)
95         globals()[Name2].reset_index(drop=True, inplace = True)
96
97     # Translating the cycle segment to be originated from the coordinate system's origin
98     for i in range (7, cycle_count):
99         name1 = "data_joint_" + str(i) + "_T_P"
100         name2 = "data_joint_" + str(i) + "_P_P"
101         name3 = "data_joint_" + str(i+1) + "_T_P"
102
103         globals()[name2]["New_displacement"] = globals()[name1].iloc[-1,3] - globals()[name2]["Joint_displacement"]
104         globals()[name2]["New_load"] = globals()[name1].iloc[-1,2] - globals()[name2]["Load"]
105         globals()[name2]["New_time"] = globals()[name2]["new_time"] - globals()[name1].iloc[-1,1]
106
107         globals()[name3]["New_displacement"] = globals()[name3]["Joint_displacement"] - globals()[name2].iloc[-1,3]
108         globals()[name3]["New_load"] = globals()[name3]["Load"] - globals()[name2].iloc[-1,2]
109         globals()[name3]["New_time"] = globals()[name3]["new_time"] - globals()[name2].iloc[-1,1]
110
111     ###
112     ### Preparation of data for fitting
113     ### Finding the maximum segment displacement and making the data to be equally spaced

```

Appendix B. Phenomenological constitutive model development and Python program

```
114 ###
115 Disp = pd.DataFrame(columns = ["T_P", "P_P"])
116
117
118 i = 14
119 j = 0
120
121 while j < 8:
122     name1 = "data_joint_" + str(i) + "_T_P"
123     name2 = "data_joint_" + str(i) + "_P_P"
124
125     Disp.at[j, "T_P"] = globals()[name1] ["New_displacement"].max()
126     Disp.at[j, "P_P"] = globals()[name2] ["New_displacement"].max()
127
128     # Creating equally spaced dataframes for each cycle segment
129     name3 = "data_joint_new" + str(i) + "_T_P"
130     name4 = "data_joint_new" + str(i) + "_P_P"
131
132     new_x_1 = np.linspace(globals()[name1] ["New_displacement"].min(), globals()[
133         name1] ["New_displacement"].max(), 500)
134     new_x_2 = np.linspace(globals()[name2] ["New_displacement"].min(), globals()[
135         name2] ["New_displacement"].max(), 500)
136     f1 = interpolate.interp1d(globals()[name1] ["New_displacement"], globals()[
137         name1] ["New_load"], kind="linear", fill_value="extrapolate")
138     f2 = interpolate.interp1d(globals()[name2] ["New_displacement"], globals()[
139         name2] ["New_load"], kind="linear", fill_value="extrapolate")
140     new_y_1 = f1(new_x_1)
141     new_y_2 = f1(new_x_2)
142     globals()[name3] = pd.DataFrame({"New_displacement": new_x_1, "New_load": new
143         _y_1})
144     globals()[name4] = pd.DataFrame({"New_displacement": new_x_2, "New_load": new
145         _y_2})
146
147
148     if j == 0 :
149         i += 7
150     if j >= 1 and j < 3:
151         i += 4
152     if j >= 3 :
153         i += 3
154
155     j += 1
156
157 ###
158 ### Creating initial value DataFrame
159 ###
160 Initial_values = pd.DataFrame(columns = ["T_P", "P_P"])
161
162
163 i = 29
164 j = 0
165
166 while j < 4:
167     name1 = "data_joint_" + str(i) + "_T_P"
168     name2 = "data_joint_" + str(i) + "_P_P"
```

```

161     Initial_values.at[j, "T_P"] = globals()[name1] ["New_displacement"].max()
162     Initial_values.at[j, "P_P"] = globals()[name2] ["New_displacement"].max()
163     i += 3
164     j += 1
165
166     ###
167     ### Define power-law relations
168     ###
169     def S1_def_T_P(cycle_disp, a_S1_T_P, b_S1_T_P):
170         return a_S1_T_P*((cycle_disp)**(-b_S1_T_P))
171
172     def S1_def_P_P(cycle_disp, a_S1_P_P, b_S1_P_P):
173         return a_S1_P_P*((cycle_disp)**(-b_S1_P_P))
174
175
176
177     def n1_def_T_P(cycle_disp, a_P_P1_T_P, b_P_P1_T_P):
178         return a_P_P1_T_P*((cycle_disp)**(-b_P_P1_T_P))
179
180     def n1_def_P_P(cycle_disp, a_P_P1_P_P, b_P_P1_P_P):
181         return a_P_P1_P_P*((cycle_disp)**b_P_P1_P_P)
182
183
184
185     def a_def_T_P(cycle_disp, a_a_T_P, b_a_T_P):
186         return a_a_T_P*((cycle_disp)**(-b_a_T_P))
187
188     def a_def_P_P(cycle_disp, a_a_P_P, b_a_P_P):
189         return a_a_P_P*((cycle_disp)**(-b_a_P_P))
190
191
192
193     def b_def_T_P(cycle_disp, a_b_T_P, b_b_T_P):
194         return a_b_T_P*((cycle_disp)**(b_b_T_P))
195
196     def b_def_P_P(cycle_disp, a_b_P_P, b_b_P_P):
197         return a_b_P_P*((cycle_disp)**(b_b_P_P))
198
199
200
201     def n2_def_T_P(cycle_disp, a_P_P2_T_P, b_P_P2_T_P):
202         return a_P_P2_T_P*((cycle_disp)**(b_P_P2_T_P))
203
204     def n2_def_P_P(cycle_disp, a_P_P2_P_P, b_P_P2_P_P):
205         return a_P_P2_P_P*((cycle_disp)**(b_P_P2_P_P))
206
207
208
209     def load_disp(t, S1, n1, a, b, n2):
210         X_dot = 0.1
211         load_model = (((X_dot*n1)+((-1*X_dot*n1)/(np.exp((S1*t)/n1))))+
212                       ((X_dot*n2)+((-1*X_dot*n2)/(np.exp(((a*(t**b))*t)/
213 (n2*(b+1)))))))

```

Appendix B. Phenomenological constitutive model development and Python program

```
214
215     return load_model
216
217 ###
218 ### Definition the initial values of five main parameters for the displacement
    rate of 0.1 mm/s.
219 ### Two decomposed segments of _T_P and _P_P are considered
220 ### Cycles 29, 32, 35, and 38 are considered for the fitting process
221 ###
222
223 X_dot = 0.1
224 i = 29
225 j = 0
226
227 while j < 4:
228     name1 = "data_joint_" + str(i) + "_T_P"
229     name2 = "data_joint_" + str(i) + "_P_P"
230
231
232     # Initial value of stiffness (from initial stiffness)
233
234     Initial_values.at[j, "S1_T_P"] = ((globals()[name1].at[10,"New_load"]-globals
        ()[name1].at[2,"New_load"])/
        (globals
        ()[name1].at[10,"New_displacement"]-globals()[name1].at[2,"New_displacement
        "]))
235     Initial_values.at[j, "S1_P_P"] = ((globals()[name2].at[15,"New_load"]-globals
        ()[name2].at[5,"New_load"])/
        (globals
        ()[name2].at[15,"New_displacement"]-globals()[name2].at[5,"New_displacement
        "]))
236
237
238     # Initial value of eta 1 (from Eq.8 in chapter 3)
239
240     for k_T_P in range (20, len(globals()[name1]["New_load"])):
241         slope_T_P = ((globals()[name1].at[k_T_P,"New_load"]-globals()[name1].at[(
            k_T_P-8),"New_load"])/ (globals()[name1].at[k_T_P,"New_displacement"]-
            globals()[name1].at[(k_T_P-8),"New_displacement"]))
242
243         if slope_T_P < 0.2*Initial_values.at[j, "S1_T_P"]:
244             X_y_T_P = globals()[name1].at[k_T_P,"New_displacement"]
245             F_y_T_P = globals()[name1].at[k_T_P,"New_load"]
246             Initial_values.at[j, "n1_T_P"] = Initial_values.at[j, "S1_T_P"] * (X_
                y_T_P/X_dot)
247             break
248
249     for k_P_P in range (20, len(globals()[name2]["New_load"])):
250         slope_P_P = ((globals()[name2].at[k_P_P,"New_load"]-globals()[name2].at[(
            k_P_P-8),"New_load"])/
            (globals()[name2].at[k_P_P,"
            New_displacement"]-globals()[name2].at[(k_P_P-8),"New_displacement"]))
251
252         if slope_P_P < 0.2*Initial_values.at[j, "S1_P_P"]:
253             X_y_P_P = globals()[name1].at[k_P_P,"New_displacement"]
254             F_y_P_P = globals()[name1].at[k_P_P,"New_load"]
```

```

255         Initial_values.at[j, "n1_P_P"] = Initial_values.at[j, "S1_P_P"] * (X_
           y_P_P/X_dot)
256         break
257
258
259     # Initial value of alpha and beta for nonlinear stiffness (from Eq.9 in
       chapter 3)
260
261     F_X_c_T_P = globals()[name1]["New_load"].max()
262     X_c_T_P = globals()[name1]["New_displacement"].max()
263     F_X_c_P_P = globals()[name2]["New_load"].max()
264     X_c_P_P = globals()[name2]["New_displacement"].max()
265
266
267     Initial_values.at[j, "beta_T_P"] = 1.1
268     Initial_values.at[j, "beta_P_P"] = 1.1
269
270     Initial_values.at[j, "alpha_T_P"] = ((F_X_c_T_P - F_y_T_P)/(((X_c_T_P - X_y_T
       _P)/X_dot)**Initial_values.at[j, "beta_T_P"]))
271     Initial_values.at[j, "alpha_P_P"] = ((F_X_c_P_P - F_y_P_P)/(((X_c_P_P - X_y_P
       _P)/X_dot)**Initial_values.at[j, "beta_P_P"]))
272
273     S_2_T_P = (F_X_c_T_P - F_y_T_P)/(X_c_T_P - X_y_T_P)
274     S_2_P_P = (F_X_c_P_P - F_y_P_P)/(X_c_P_P - X_y_P_P)
275
276
277     # Initial value of eta 2 (from Eq.10 in chapter 3)
278
279     Initial_values.at[j, "n2_T_P"] = S_2_T_P * ((X_c_T_P - X_y_T_P)/X_dot)
280
281     Initial_values.at[j, "n2_P_P"] = S_2_P_P * ((X_c_P_P - X_y_P_P)/X_dot)
282
283
284     i += 3
285     j += 1
286
287     ###
288     ### Finding the trends between initial parameters and the cycle displacement for
       T_P segments
289     ###
290     S1_T_P_0 = [100, 0.1]
291     S1_opt_T_P, S1_cov_T_P = curve_fit(S1_def_T_P, Initial_values["T_P"].values,
       Initial_values["S1_T_P"].values, S1_T_P_0, bounds = ([S1_T_P_0[0]*0.5, S1_T_P
       _0[1]*0.5], [S1_T_P_0[0]*1.5, S1_T_P_0[1]*1.5]))
292
293     n1_T_P_0 = [500, 0.1]
294     n1_opt_T_P, n1_cov_T_P = curve_fit(n1_def_T_P, Initial_values["T_P"].values,
       Initial_values["n1_T_P"].values, n1_T_P_0, bounds = ([n1_T_P_0[0]*0.5, n1_T_P
       _0[1]*0.5], [n1_T_P_0[0]*1.5, n1_T_P_0[1]*1.5]))
295
296     a_T_P_0 = [5, 1]
297     a_opt_T_P, a_cov_T_P = curve_fit(a_def_T_P, Initial_values["T_P"].values, Initial
       _values["alpha_T_P"].values, a_T_P_0, bounds = ([a_T_P_0[0]*0.5, a_T_P

```

Appendix B. Phenomenological constitutive model development and Python program

```

    _0[1]*0.5], [a_T_P_0[0]*1.5, a_T_P_0[1]*1.5]))
298
299 b_T_P_0 = [1, 0.1]
300 b_opt_T_P, b_cov_T_P = curve_fit(b_def_T_P, Initial_values["T_P"].values, Initial
    _values["beta_T_P"].values, b_T_P_0, bounds = ([b_T_P_0[0]*0.5, b_T_P
    _0[1]*0.5], [b_T_P_0[0]*1.5, b_T_P_0[1]*1.5]))
301
302 n2_T_P_0 = [500, 0.1]
303 n2_opt_T_P, n2_cov_T_P = curve_fit(n2_def_T_P, Initial_values["T_P"].values,
    Initial_values["n2_T_P"].values, n2_T_P_0, bounds = ([n2_T_P_0[0]*0.5, n2_T_P
    _0[1]*0.5], [n2_T_P_0[0]*1.5, n2_T_P_0[1]*1.5]))
304
305 ###
306 ### Finding the trends between initial parameters and the cycle displacement for
    P_P segments
307 ###
308 S1_P_P_0 = [100, 0.1]
309 S1_opt_P_P, S1_cov_P_P = curve_fit(S1_def_P_P, Initial_values["T_P"].values,
    Initial_values["S1_P_P"].values, S1_P_P_0, bounds = ([S1_P_P_0[0]*0.5, S1_P_P
    _0[1]*0.5], [S1_P_P_0[0]*1.5, S1_P_P_0[1]*1.5]))
310
311 n1_P_P_0 = [500, 0.1]
312 n1_opt_P_P, n1_cov_P_P = curve_fit(n1_def_P_P, Initial_values["T_P"].values,
    Initial_values["n1_P_P"].values, n1_P_P_0, bounds = ([n1_P_P_0[0]*0.5, n1_P_P
    _0[1]*0.5], [n1_P_P_0[0]*1.5, n1_P_P_0[1]*1.5]))
313
314 a_P_P_0 = [5, 1]
315 a_opt_P_P, a_cov_P_P = curve_fit(a_def_P_P, Initial_values["T_P"].values, Initial
    _values["alpha_P_P"].values, a_P_P_0, bounds = ([a_P_P_0[0]*0.5, a_P_P
    _0[1]*0.5], [a_P_P_0[0]*1.5, a_P_P_0[1]*1.5]))
316
317 b_P_P_0 = [1, 0.1]
318 b_opt_P_P, b_cov_P_P = curve_fit(b_def_P_P, Initial_values["T_P"].values, Initial
    _values["beta_P_P"].values, b_P_P_0, bounds = ([b_P_P_0[0]*0.5, b_P_P
    _0[1]*0.5], [b_P_P_0[0]*1.5, b_P_P_0[1]*1.5]))
319
320 n2_P_P_0 = [500, 0.1]
321 n2_opt_P_P, n2_cov_P_P = curve_fit(n2_def_P_P, Initial_values["T_P"].values,
    Initial_values["n2_P_P"].values, n2_P_P_0, bounds = ([n2_P_P_0[0]*0.5, n2_P_P
    _0[1]*0.5], [n2_P_P_0[0]*1.5, n2_P_P_0[1]*1.5]))
322
323
324 ###
325 ### Creating the constants DataFrame
326 ### the first row, for T_P, the second row for their error, the third row for P_P
    and the fourth row for their error
327 ###
328 constants = pd.DataFrame(columns=["a_S1", "b_S1", "a_n1", "b_n1", "a_a", "b_a", "
    a_b", "b_b", "a_n2", "b_n2"], index=range(4))
329
330 for i in range (0,2):
331     constants.iloc[0, i] = S1_opt_T_P[i]
332     constants.iloc[2, i] = S1_opt_P_P[i]
```

```

333
334     constants.iloc[0, (i+2)] = n1_opt_T_P[i]
335     constants.iloc[2, (i+2)] = n1_opt_P_P[i]
336
337     constants.iloc[0, (i+4)] = a_opt_T_P[i]
338     constants.iloc[2, (i+4)] = a_opt_P_P[i]
339
340     constants.iloc[0, (i+6)] = b_opt_T_P[i]
341     constants.iloc[2, (i+6)] = b_opt_P_P[i]
342
343     constants.iloc[0, (i+8)] = n2_opt_T_P[i]
344     constants.iloc[2, (i+8)] = n2_opt_P_P[i]
345
346 for i in range(0, 10):
347     constants.iloc[1, i] = 1
348     constants.iloc[3, i] = 1
349
350 ###
351 ### Finding the parameters and their trends for T_P segment of cycles number 29,
352     32, 35, and 38, following the flowchart in the chapter 3
353 ###
354 param_T_P = pd.DataFrame(columns=["S1", "n1", "a", "b", "n2"], index=range(4))
355
356 X_dot = 0.1
357 factor_low = 0.5
358 factor_up = 1.0
359 epsilon = 1
360
361 while epsilon > 0.01:
362     i = 29
363
364     for j in range (0,4):
365
366         name1 = "data_joint_new" + str(i) + "_T_P"
367
368         T_P_0 = [0,0,0,0,0]
369         T_P_0 [0] = S1_def_T_P(Disp.at[j+3, "T_P"], constants.at[0,"a_S1"],
370             constants.at[0,"b_S1"])
371         T_P_0 [1] = n1_def_T_P(Disp.at[j+3, "T_P"], constants.at[0,"a_n1"],
372             constants.at[0,"b_n1"])
373         T_P_0 [2] = a_def_T_P(Disp.at[j+3, "T_P"], constants.at[0,"a_a"],
374             constants.at[0,"b_a"])
375         T_P_0 [3] = b_def_T_P(Disp.at[j+3, "T_P"], constants.at[0,"a_b"],
376             constants.at[0,"b_b"])
377         T_P_0 [4] = n2_def_T_P(Disp.at[j+3, "T_P"], constants.at[0,"a_n2"],
378             constants.at[0,"b_n2"])
379
380         # Finding the parameters
381         popt_T_P, pcov_T_P = curve_fit(load_disp, globals()[name1]["New_
382             displacement"].div(X_dot), globals()[name1]["New_load"], T_P_0, bounds
383             =(p*factor_low for p in T_P_0], [p*factor_up for p in T_P_0]))
384
385

```

Appendix B. Phenomenological constitutive model development and Python program

```
378         for k in range (0,5):
379             param_T_P.iloc[j, k] = popt_T_P[k]
380
381         i = i+3
382
383         # Determining the parameter trends
384         S1_T_P_0 = [constants.iloc[0,0], constants.iloc[0,1]]
385         S1_opt_T_P, S1_cov_T_P = curve_fit(S1_def_T_P, Initial_values["T_P"].values,
386             param_T_P["S1"].values, S1_T_P_0, bounds = ([S1_T_P_0[0]*factor_low, S1_T_P_0[1]*factor_low], [S1_T_P_0[0]*factor_up, S1_T_P_0[1]*factor_up]))
387
388         n1_T_P_0 = [constants.iloc[0,2], constants.iloc[0,3]]
389         n1_opt_T_P, n1_cov_T_P = curve_fit(n1_def_T_P, Initial_values["T_P"].values,
390             param_T_P["n1"].values, n1_T_P_0, bounds = ([n1_T_P_0[0]*factor_low, n1_T_P_0[1]*factor_low], [n1_T_P_0[0]*factor_up, n1_T_P_0[1]*factor_up]))
391
392         a_T_P_0 = [constants.iloc[0,4], constants.iloc[0,5]]
393         a_opt_T_P, a_cov_T_P = curve_fit(a_def_T_P, Initial_values["T_P"].values,
394             param_T_P["a"].values, a_T_P_0, bounds = ([a_T_P_0[0]*factor_low, a_T_P_0[1]*factor_low], [a_T_P_0[0]*factor_up, a_T_P_0[1]*factor_up]))
395
396         b_T_P_0 = [constants.iloc[0,6], constants.iloc[0,7]]
397         b_opt_T_P, b_cov_T_P = curve_fit(b_def_T_P, Initial_values["T_P"].values,
398             param_T_P["b"].values, b_T_P_0, bounds = ([b_T_P_0[0]*factor_low, b_T_P_0[1]*factor_low], [b_T_P_0[0]*factor_up, b_T_P_0[1]*factor_up]))
399
400         n2_T_P_0 = [constants.iloc[0,8], constants.iloc[0,9]]
401         n2_opt_T_P, n2_cov_T_P = curve_fit(n2_def_T_P, Initial_values["T_P"].values,
402             param_T_P["n2"].values, n2_T_P_0, bounds = ([n2_T_P_0[0]*factor_low, n2_T_P_0[1]*factor_low], [n2_T_P_0[0]*factor_up, n2_T_P_0[1]*factor_up]))
403
404         # Finding the trend error
405         constants.iloc[1,0] = abs (S1_opt_T_P[0] - constants.iloc[0,0])
406         constants.iloc[1,1] = abs (S1_opt_T_P[1] - constants.iloc[0,1])
407
408         constants.iloc[1,2] = abs (n1_opt_T_P[0] - constants.iloc[0,2])
409         constants.iloc[1,3] = abs (n1_opt_T_P[1] - constants.iloc[0,3])
410
411         constants.iloc[1,4] = abs (a_opt_T_P[0] - constants.iloc[0,4])
412         constants.iloc[1,5] = abs (a_opt_T_P[1] - constants.iloc[0,5])
413
414         constants.iloc[1,6] = abs (b_opt_T_P[0] - constants.iloc[0,6])
415         constants.iloc[1,7] = abs (b_opt_T_P[1] - constants.iloc[0,7])
416
417         constants.iloc[1,8] = abs (n2_opt_T_P[0] - constants.iloc[0,8])
418         constants.iloc[1,9] = abs (n2_opt_T_P[1] - constants.iloc[0,9])
419
420         # Substituting the new trend constants for the next iteration round
421         for n in range (0,2):
422             constants.iloc[0,n] = S1_opt_T_P[n]
423             constants.iloc[0,(n+2)] = n1_opt_T_P[n]
424             constants.iloc[0,(n+4)] = a_opt_T_P[n]
425             constants.iloc[0,(n+6)] = b_opt_T_P[n]
```

```

421         constants.iloc[0,(n+8)] = n2_opt_T_P[n]
422
423
424     for m in range (0, 10):
425         if m == 0:
426             if constants.iloc[1,m] < 0.01:
427                 epsilon = 0.01
428
429         if m > 0:
430             if epsilon == 0.01:
431                 if constants.iloc[1,m] < 0.01:
432                     epsilon = 0.01
433             else:
434                 epsilon = 1
435
436     ###
437     ### Finding the parameters and their trends for P_P segment of cycles number 29,
438     32, 35, and 38, following the flowchart in the chapter 3
439     ###
440     param_P_P = pd.DataFrame(columns=["S1", "n1", "a", "b", "n2"], index=range(4))
441
442     X_dot = 0.1
443     factor_low_ = 0.5
444     factor_up = 1.0
445     epsilon = 1
446
447     while epsilon > 0.01:
448
449         i = 29
450
451         for j in range (0,4):
452
453             name1 = "data_joint_new" + str(i) + "_P_P"
454
455             P_P_0 = [0,0,0,0,0]
456             P_P_0 [0] = S1_def_P_P(Disp.at[j+3, "P_P"], constants.at[2,"a_S1"],
457                                     constants.at[2,"b_S1"])
458             P_P_0 [1] = n1_def_P_P(Disp.at[j+3, "P_P"], constants.at[2,"a_n1"],
459                                     constants.at[2,"b_n1"])
460             P_P_0 [2] = a_def_P_P(Disp.at[j+3, "P_P"], constants.at[2,"a_a"],
461                                     constants.at[2,"b_a"])
462             P_P_0 [3] = b_def_P_P(Disp.at[j+3, "P_P"], constants.at[2,"a_b"],
463                                     constants.at[2,"b_b"])
464             P_P_0 [4] = n2_def_P_P(Disp.at[j+3, "P_P"], constants.at[2,"a_n2"],
465                                     constants.at[2,"b_n2"])
466
467             # Finding the parameters
468             popt_P_P, pcov_P_P = curve_fit(load_disp, globals()[name1]["New_
469                                     displacement"].div(X_dot), globals()[name1]["New_load"], P_P_0, bounds
470                                     =(p*factor_low_ for p in P_P_0], [p*factor_up_ for p in P_P_0]))
471
472             for k in range (0,5):
473                 param_P_P.iloc[j, k] = popt_P_P[k]

```

Appendix B. Phenomenological constitutive model development and Python program

```
466
467     i = i+3
468
469     # Determining the parameter trends
470     S1_P_P_0 = [constants.iloc[2,0], constants.iloc[2,1]]
471     S1_opt_P_P, S1_cov_P_P = curve_fit(S1_def_P_P, Initial_values["P_P"].values,
472         param_P_P["S1"].values, S1_P_P_0, bounds = ([S1_P_P_0[0]*factor_low, S1_P_P_0[1]*factor_low], [S1_P_P_0[0]*factor_up, S1_P_P_0[1]*factor_up]))
473
474     n1_P_P_0 = [constants.iloc[2,2], constants.iloc[2,3]]
475     n1_opt_P_P, n1_cov_P_P = curve_fit(n1_def_P_P, Initial_values["P_P"].values,
476         param_P_P["n1"].values, n1_P_P_0, bounds = ([n1_P_P_0[0]*factor_low, n1_P_P_0[1]*factor_low], [n1_P_P_0[0]*factor_up, n1_P_P_0[1]*factor_up]))
477
478     a_P_P_0 = [constants.iloc[2,4], constants.iloc[2,5]]
479     a_opt_P_P, a_cov_P_P = curve_fit(a_def_P_P, Initial_values["P_P"].values,
480         param_P_P["a"].values, a_P_P_0, bounds = ([a_P_P_0[0]*factor_low, a_P_P_0[1]*factor_low], [a_P_P_0[0]*factor_up, a_P_P_0[1]*factor_up]))
481
482     b_P_P_0 = [constants.iloc[2,6], constants.iloc[2,7]]
483     b_opt_P_P, b_cov_P_P = curve_fit(b_def_P_P, Initial_values["P_P"].values,
484         param_P_P["b"].values, b_P_P_0, bounds = ([b_P_P_0[0]*factor_low, b_P_P_0[1]*factor_low], [b_P_P_0[0]*factor_up, b_P_P_0[1]*factor_up]))
485
486     n2_P_P_0 = [constants.iloc[2,8], constants.iloc[2,9]]
487     n2_opt_P_P, n2_cov_P_P = curve_fit(n2_def_P_P, Initial_values["P_P"].values,
488         param_P_P["n2"].values, n2_P_P_0, bounds = ([n2_P_P_0[0]*factor_low, n2_P_P_0[1]*factor_low], [n2_P_P_0[0]*factor_up, n2_P_P_0[1]*factor_up]))
489
490     # Finding the trend error
491     constants.iloc[3,0] = abs (S1_opt_P_P[0] - constants.iloc[2,0])
492     constants.iloc[3,1] = abs (S1_opt_P_P[1] - constants.iloc[2,1])
493
494     constants.iloc[3,2] = abs (n1_opt_P_P[0] - constants.iloc[2,2])
495     constants.iloc[3,3] = abs (n1_opt_P_P[1] - constants.iloc[2,3])
496
497     constants.iloc[3,4] = abs (a_opt_P_P[0] - constants.iloc[2,4])
498     constants.iloc[3,5] = abs (a_opt_P_P[1] - constants.iloc[2,5])
499
500     constants.iloc[3,6] = abs (b_opt_P_P[0] - constants.iloc[2,6])
501     constants.iloc[3,7] = abs (b_opt_P_P[1] - constants.iloc[2,7])
502
503     constants.iloc[3,8] = abs (n2_opt_P_P[0] - constants.iloc[2,8])
504     constants.iloc[3,9] = abs (n2_opt_P_P[1] - constants.iloc[2,9])
505
506     # Substituting the new trend constants for the next iteration round
507     for n in range (0,2):
508         constants.iloc[2,n] = S1_opt_P_P[n]
509         constants.iloc[2,(n+2)] = n1_opt_P_P[n]
510         constants.iloc[2,(n+4)] = a_opt_P_P[n]
511         constants.iloc[2,(n+6)] = b_opt_P_P[n]
512         constants.iloc[2,(n+8)] = n2_opt_P_P[n]
```

```
509     for m in range (0, 10):
510         if m == 0:
511             if constants.iloc[3,m] < 0.01:
512                 epsilon = 0.01
513
514         if m > 0:
515             if epsilon == 0.01:
516                 if constants.iloc[3,m] < 0.01:
517                     epsilon = 0.01
518             else:
519                 epsilon = 1
```


Tensile experiments on adhesive dog-bone specimens

In this appendix, the rate-dependent tensile behavior of the pseudo-ductile adhesive, 'SikaFast®-555', is examined using dog-bone specimens, following ASTM D638 [1], at various tensile displacement rates.

3.1 Experimental set-up

- Specimen dimensions and preparation

Type IV dog bone-shaped specimens, with the dimensions shown in Fig. 3.1(a), in line with ASTM D638 [1] recommendations, were employed. Initially, these specimens were fabricated as a plate, then cured at room temperature, and kept in their molds for nineteen days. After demolding, the specimens were cut into the desired dimensions using a waterjet cutting machine.

- Instrumentation

The tensile experiments, which were displacement-controlled, were carried out using an MTS 25 kN universal machine, depicted in Fig. 3.1(b). Aluminum tabs were attached to the ends of the dog bone-shaped specimens, which were then fixed in the machine grips.

The applied displacement and load data was recorded using the MTS machine software. A 2D DIC system was set up to track the strain field on the specimens' surface. A random pattern of black dots was sprayed onto each specimen, allowing the DIC to track their relative displacement during the test. The strains were then calculated using one of three methods, as depicted in Fig. 3.2(a): 1) average displacement of the speckles in a rectangular area covering the whole gauge length, 2) average displacement of the speckles in a rectangular area expanding over

Appendix C. Tensile experiments on adhesive dog-bone specimens

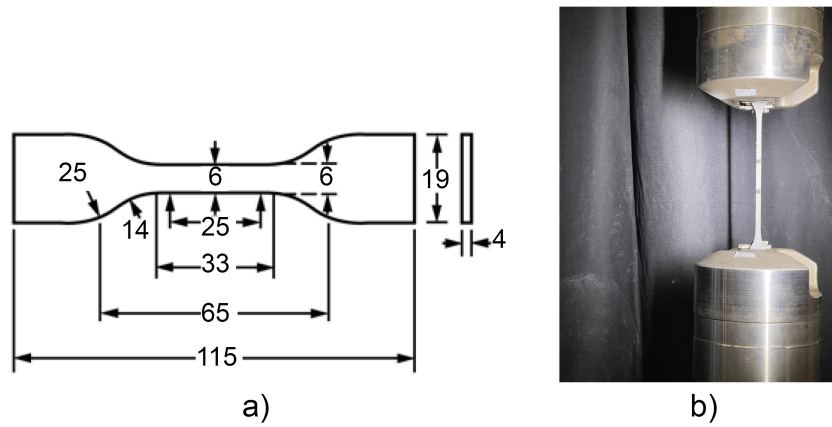


Figure 3.1: a) Geometry of Type IV dog-bone shaped specimens used for tensile experiments according to ASTM D638 [1], b) Specimen being loaded in MTS 25kN machine.

a smaller length in the center of the specimens, 3) average elongation between three lines with different lengths along the length of the specimen. A comparison of the strain values calculated for the specimens shows that they were almost identical among the three adopted approaches, as shown in Fig. 3.1(b). The accuracy of the measurements was ± 0.001 for strains.

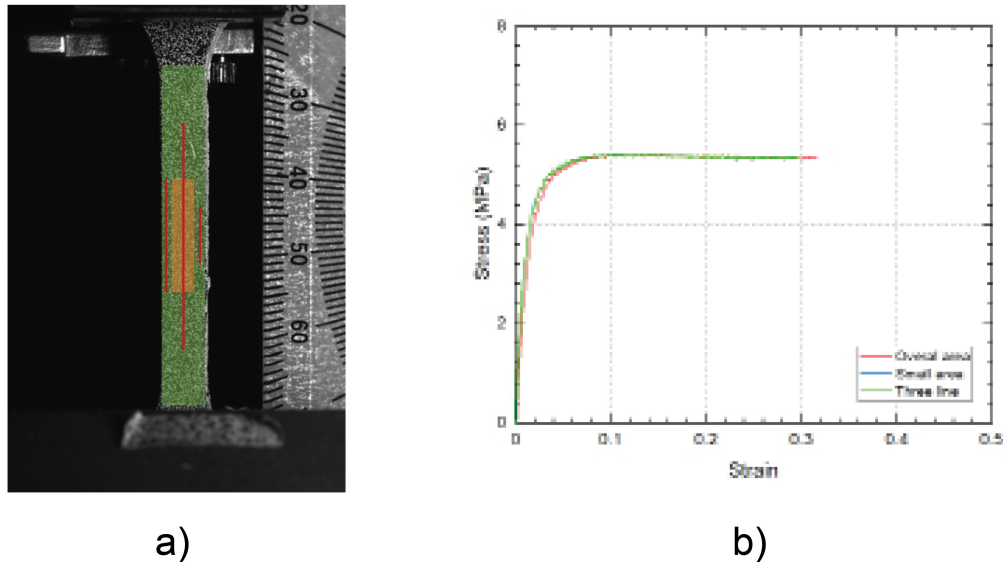


Figure 3.2: a) DIC captured image for strain measurement, and b) Comparison of the various measurement methods using DIC images.

3.2 Experimental results

Fig. 3.3(a)-(e) illustrate the engineering stress-strain curves derived from tensile experiments conducted on the specimens at displacement rates of 0.1, 0.5, 1.0, 5.0, and 10 mm/s, respectively. The engineering stresses, σ_{eng} , were determined by dividing the machine-recorded load by the average initial cross-sectional area, measured at three different positions along the gauge length of the specimens prior to the start of the experiments. Surface degradation of the specimens led to the loss of black speckles, limiting the strains measured by DIC to approximately 30% of the maximum applied deformation. For strains up to this limit, a comparison was made between the DIC-measured strains and those calculated by dividing the machine-recorded displacement by the specimen gauge length (65 mm as per Fig. 3.1(a)). The comparison demonstrated a good agreement between the measured strains and the calculated values. Consequently, the engineering strains, ϵ_{eng} , were determined by dividing the machine-recorded displacement by the specimen gauge length.

The comparison of the engineering stress-strain curves for the specimens under various applied displacement rates is shown in Fig. 3.4(a).

The true stress, σ_{true} , and strain, ϵ_{true} , were calculated using the following equations:

$$\sigma_{true} = \sigma_{eng} \cdot (\epsilon_{eng} + 1) \quad (C.1)$$

$$\epsilon_{true} = \ln(\epsilon_{eng} + 1) \quad (C.2)$$

Fig. 3.4(b) displays the calculated true stress-strain curves for selected specimens under displacement rates of 0.1, 0.5, 1.0, 5.0, and 10 mm/s.

The calculated Poisson's ratio from DIC data versus the true strain under four applied displacement rates is shown in Fig. 3.5.

The specimens exhibited two different deformation modes regardless of the applied displacement rate. In most cases, a uniform deformation was observed along the specimen until a sudden failure. However, a few specimens experienced a non-uniform local deformation, resulting in necking and failure at the necking position.

Appendix C. Tensile experiments on adhesive dog-bone specimens

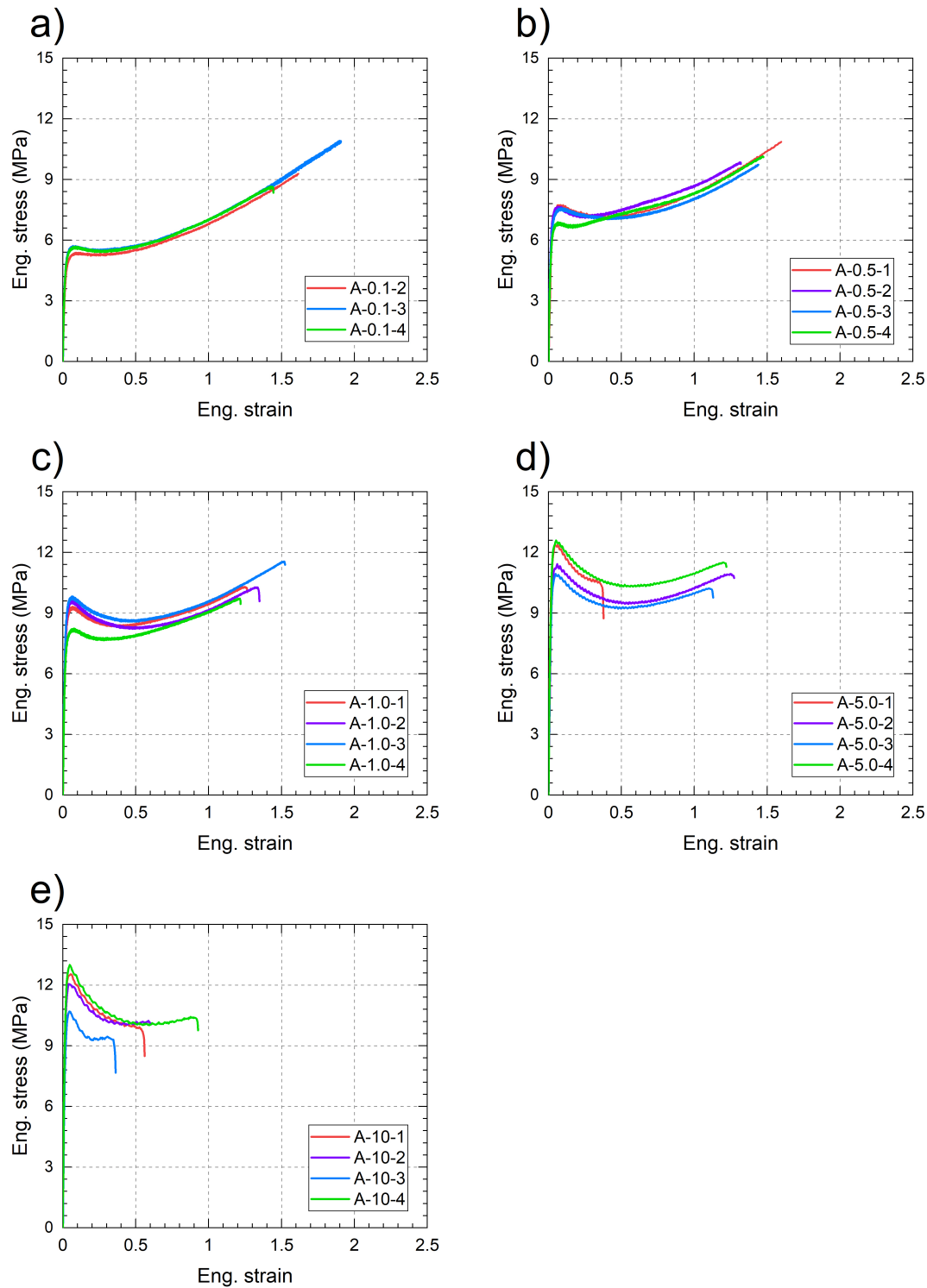


Figure 3.3: Engineering stress-strain curves for dog-bone specimens under a) 0.1, b) 0.5, c) 1.0, d) 5.0, e) 10.0 mm/s displacement rates.

3.2 Experimental results

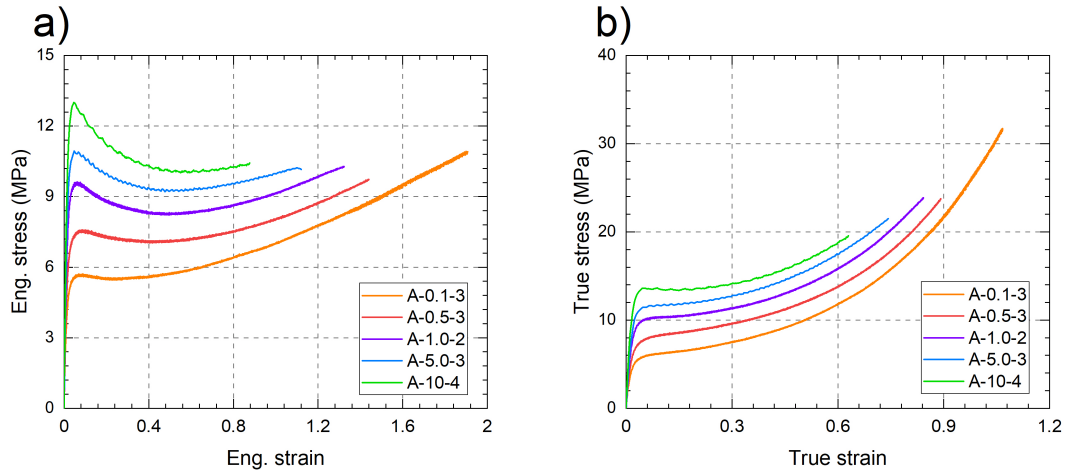


Figure 3.4: Comparison between the stress-strain results under five applied displacement rates, for a) engineering stress-strain, and b) true stress-strain.

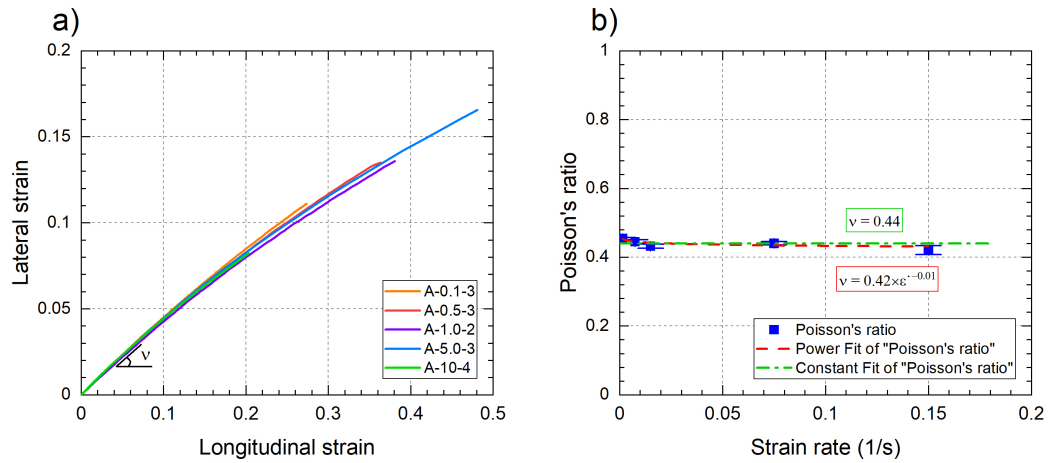


Figure 3.5: Comparison of Poisson's ratio versus true strain under five strain rates.

Table 3.1 provides a summary of the specimens' dimensional properties, elastic modulus, E , yield strain, ϵ_y , yield stress, σ_y , ultimate tensile strength (UTS) strain, ϵ_{UTS} , and UTS stress, σ_{UTS} . The variation of σ_{true} , E , ϵ_y , σ_y , ϵ_{UTS} , and σ_{UTS} are presented in Fig. 3.6. All these mechanical properties followed a power-law relation versus strain rate shown in Fig. 3.6 by a dashed line and their equation written in each curve. As seen from Fig. 3.6, an increase in elastic modulus with the strain rate was observed, while the yield strain showed less dependency on the strain rate. In contrast, both failure strain and failure stress decreased as the strain rate increased.

Appendix C. Tensile experiments on adhesive dog-bone specimens

Table 3.1: Specimens measured dimensional and mechanical properties.

Sp. name	Thickness (mm)	Width (mm)	E (MPa)	ϵ_y	σ_y (MPa)	ϵ_{UTS}	σ_{UTS} (MPa)
A-0.1-1	3.87	6.07	301	0.0094	2.8	0.9611	24.3
A-0.1-2	3.93	6.09	348	0.0094	3.2	1.0669	31.7
A-0.1-3	3.84	6.11	340	0.0097	3.3	0.8917	21.1
A-0.5-1	3.96	6.07	423	0.0102	4.3	0.9538	28.2
A-0.5-2	3.62	6.03	480	0.0089	4.3	0.8401	22.8
A-0.5-3	3.97	6.05	445	0.0091	4.0	0.8918	23.8
A-0.5-4	4.12	6.02	405	0.0090	3.7	0.9048	25.1
A-1.0-1	4.42	5.98	546	0.0091	5.0	0.8144	23.2
A-1.0-2	4.08	5.92	549	0.0100	5.5	0.8482	24.0
A-1.0-3	4.13	6.02	583	0.0095	5.5	0.9238	29.1
A-1.0-4	3.25	6.06	503	0.0087	4.4	0.7947	21.5
A-5.0-1	3.91	5.98	717	0.0085	6.4	0.3002	14.2
A-5.0-2	3.75	6.01	650	0.0093	5.2	0.8128	24.6
A-5.0-3	3.86	6.19	649	0.0095	6.0	0.7519	21.6
A-5.0-4	3.89	6.08	730	0.0089	6.3	0.7958	25.4
A-10-1	3.79	6.00	793	0.0087	6.8	0.4240	15.1
A-10-2	3.38	6.01	758	0.0093	7.0	0.4625	16.3
A-10-3	3.08	6.02	659	0.0083	5.5	0.2973	12.5
A-10-4	3.90	6.11	789	0.0097	7.6	0.6484	19.8

3.2 Experimental results

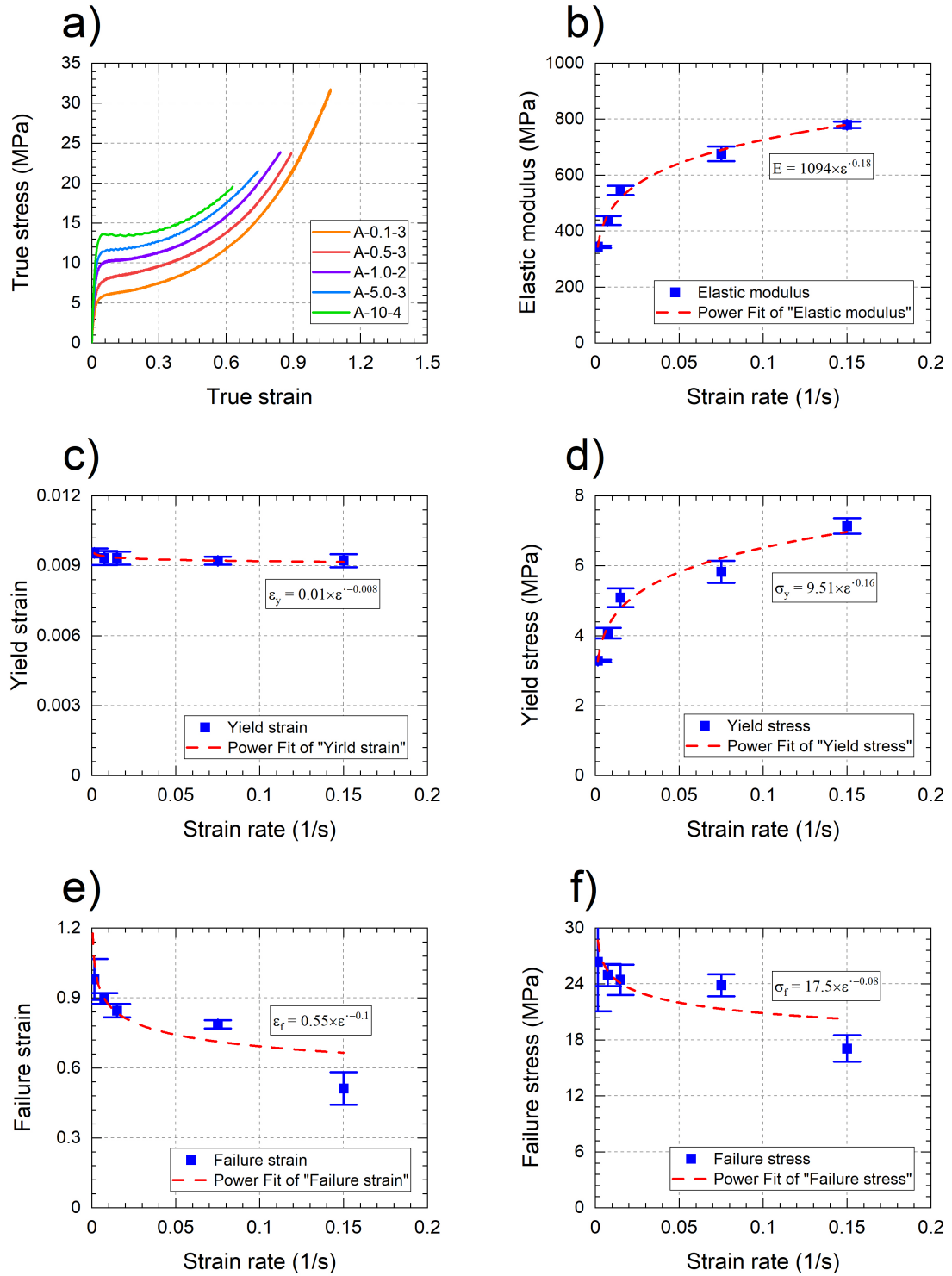


Figure 3.6: Rate-dependent variation of parameters a) true stress b) elastic modulus, c) yield strain, d) yield stress e) failure strain, and f) failure stress versus displacement rate.

References

- [1] ASTM, “Standard test method for tensile properties of plastics”, *ASTM D638*, *ASTM International*, West Conshohocken, Pa, Usa, 2003.

D

Adhesive glass composite angle double-lap and single-lap experiments

Appendix D presents supplementary information related to the experimental results of the linear single-lap and angle double-lap joints. The stress-strain relationships of the linear single-lap joints and their failure modes for all three replicates under six displacement rates of 0.01, 0.05, 0.1, 0.5, 1.0, and 5.0 mm/s are presented in the following. For angle double-lap joints, the load-displacement data recorded by W+B 200 kN machine and the load-rotation data recorded by inclinometers are depicted in Fig. 4.3. The angle double-lap joints failure modes for specimens with 5 mm adhesive layer thickness under displacement rates of 0.1, 0.5, and 2.0 mm/s and specimens with 2.5 mm adhesive layer thickness under displacement rate of 0.5 mm/s are shown in Fig. 4.4 and Fig. 4.5.

Appendix D. Adhesive glass composite angle double-lap and single-lap experiments

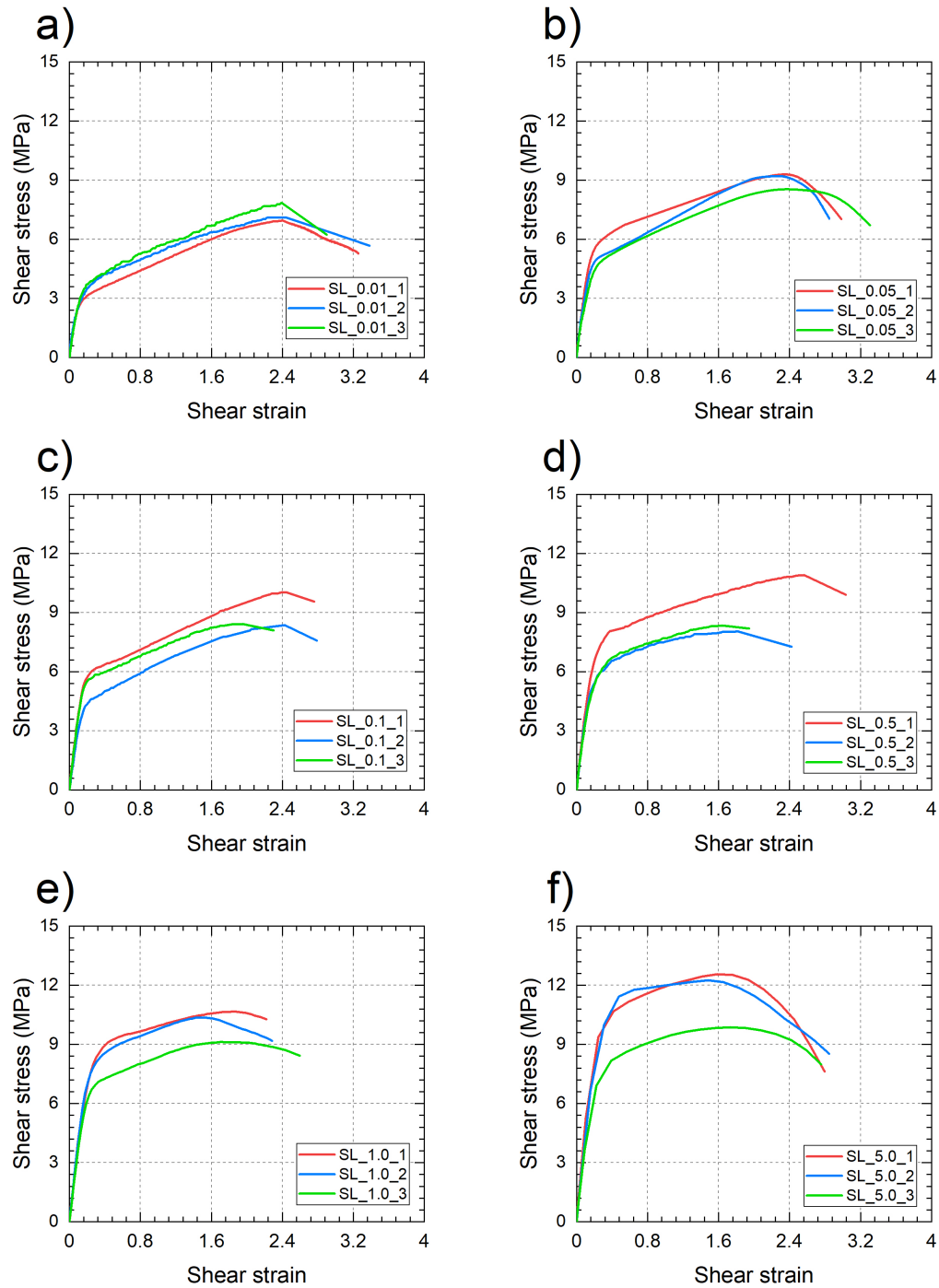


Figure 4.1: Stress-strain curves of single-lap experiments under a) 0.01, b) 0.05, c) 0.1, d) 0.5, e) 1.0, f) 5.0 mm/s displacement rates.

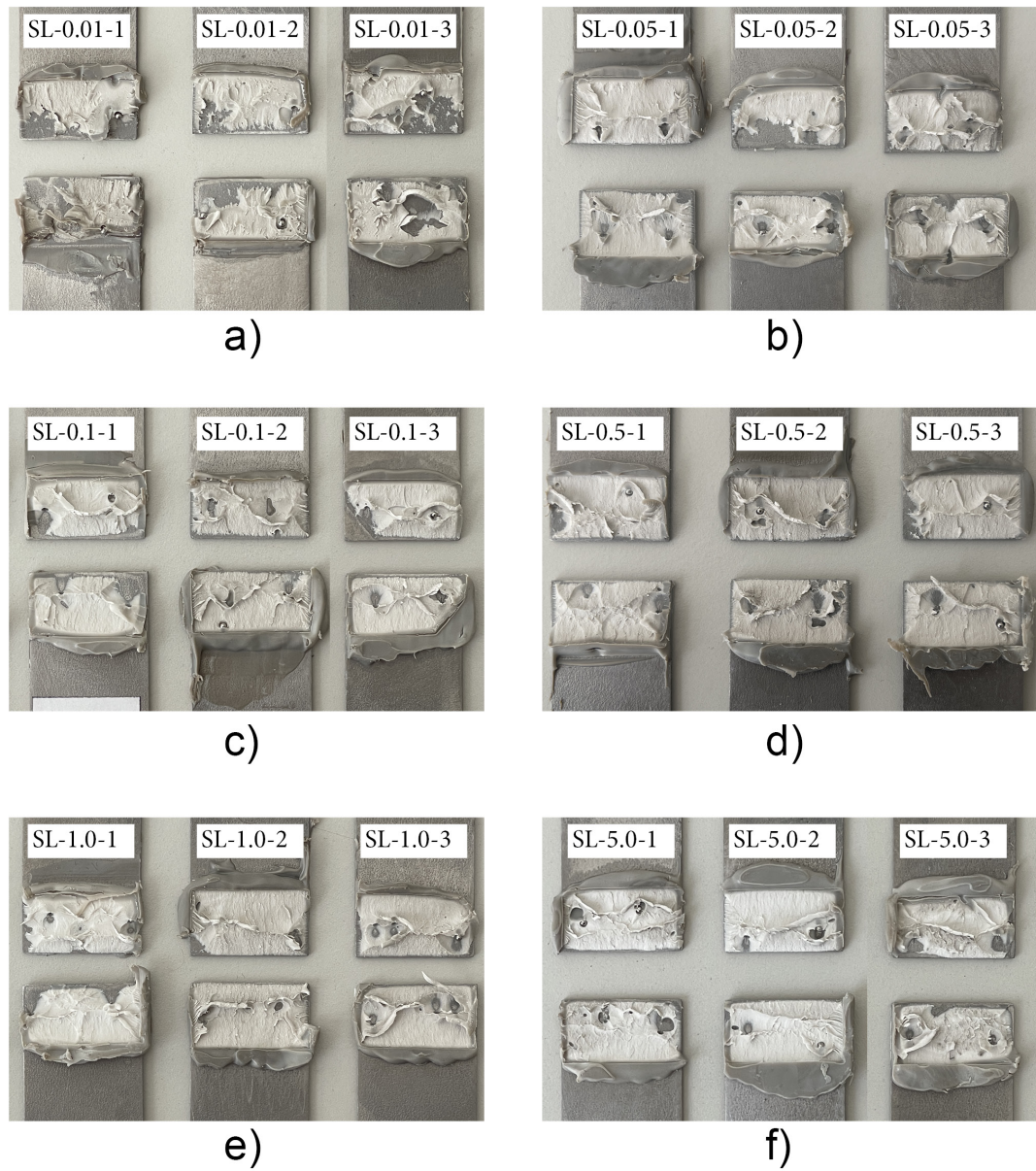


Figure 4.2: Failure surfaces of single-lap specimens under various applied displacement rates of a) 0.01 mm/s, b) 0.05 mm/s, c) 0.1 mm/s, d) 0.5 mm/s, e) 1.0 mm/s, and f) 5.0 mm/s.

Appendix D. Adhesive glass composite angle double-lap and single-lap experiments

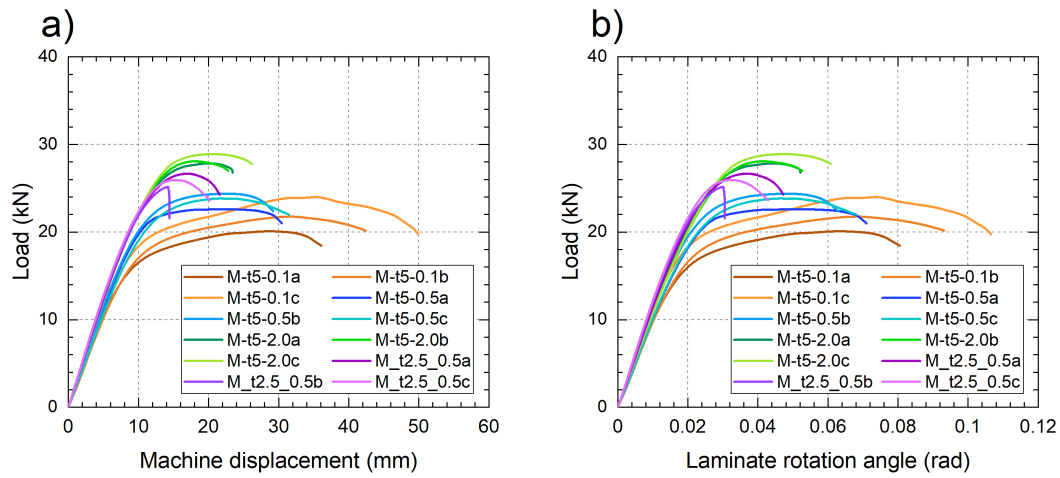
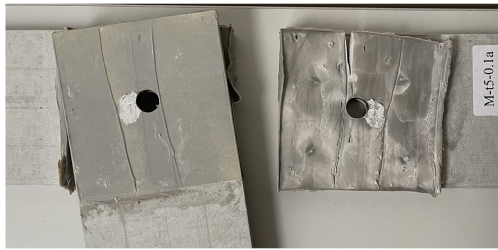


Figure 4.3: Angle joints results for specimens with 5 mm adhesive layer thickness subjected to various applied displacement rates and specimens with 2.5 mm adhesive layer thickness subjected to displacement rate of 0.5 mm/s, a) load-displacement curves, and b) load-laminate rotation curves.



a) M-t5-0.1a



b) M-t5-0.1b



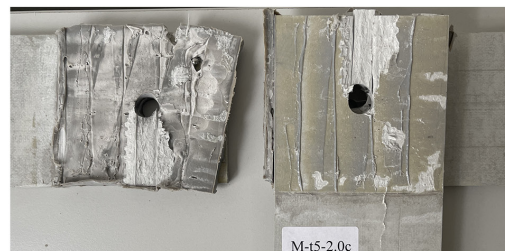
c) M-t5-0.1c



d) M-t5-2.0a



e) M-t5-2.0b



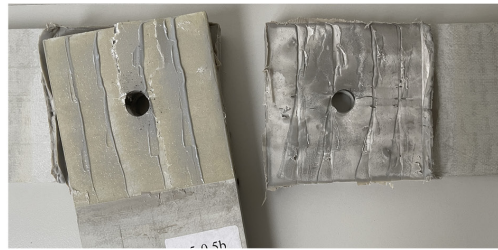
f) M-t5-2.0c

Figure 4.4: Combined failure modes for angle-joints with 5 mm adhesive layer thickness under 0.1 and 2.0 mm/s displacement rates.

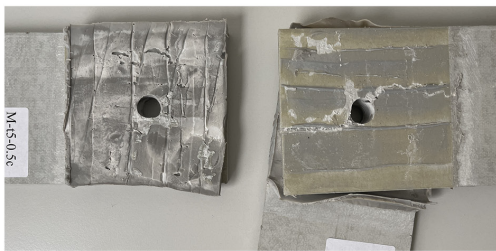
Appendix D. Adhesive glass composite angle double-lap and single-lap experiments



a) M-t5-0.5a



b) M-t5-0.5b



c) M-t5-0.5c



d) M-t2.5-0.5a



e) M-t2.5-0.5b



f) M-t2.5-0.5c

Figure 4.5: Combined failure modes for angle-joints with 5 mm and 2.5 mm adhesive layer thickness under 0.5 mm/s displacement rates.

GHAZALEH ESLAMI | RESUME

- Status: Ph.D. Candidate at École polytechnique fédérale de Lausanne
- Fields: Civil engineering, Machine learning, Programming
- Activities: Civil Eng. Design composites, AI app. Image Proc.
- Residence Permit: Formation avec activite (B)
- Find Me Online: github.com/Ghazaleh1991
[linkedin.com/in/ghazaleh-eslami](https://www.linkedin.com/in/ghazaleh-eslami)



Education

2019/07 - 2023/07 **Ph.D. Candidate in Composite Construction** EPFL, Lausanne, Switzerland

- **Thesis:** Pseudo-ductility in Fiber-polymer Composites Adhesive Joints under Cyclic Loading
- **Main Research Activity:**
 - Conducted tensile, shear, and **DMA experiments** on **SIKA** ductile structural adhesives
 - **Data-driven** experimental investigation on the performance of **SIKA** ductile adhesive joints compared to bolted-GFRP joints using **Python** and numerical verification in **Abaqus**
 - Experimental and numerical investigation on constant & variable rate-dependant behavior of double lap **SIKA** ductile adhesive joints
 - Development and **optimization** of a **constitutive model** for rate-dependent behavior of ductile adhesives in joints with **Python**
 - **Data cleaning**, analysis, syncing, and **management** for the experimental projects
 - Designed the test setups and conducted experiments
- **Notable Courses:** Applied Data Analysis; Scientific Programming for Engineers (in C++); New Concretes for Structures
- **Notable Activities:** Member of operations committee in **ECCM20 Conference** at **EPFL**:
 - Managed, organized, and categorized articles database using **Python**
 - Assisted in event scheduling through **code-based management** of admitted articles
 - **Code-based creation** of the conference booklet

2011/10 - 2013/10 **M. Sc. in Structural Engineering** Amirkabir Univ. of Tech., Iran

- **Thesis:** Progressive collapse prevention in steel moment frames by connection improvement
- **Main Research Activity:**
 - Numerical simulation of welded side-plate beam-column connections using **ABAQUS**
 - Developed **Python scripts** for **interactive optimization** of plastic hinge locations in steel frames in **SAP2000** software, through **nonlinear dynamic analysis**
 - Utilized **VBA programming for Excel** to post-process results
- **Notable Courses:** Nonlinear Structural Analysis; Structural Stability; Optimization of Structure; Mechanics of Composite Materials

2007/10 - 2011/09 **B. Sc. in Civil Engineering** University of Science and Culture, Iran

- **Notable Courses:** Steel Structures; Concrete Structures
- **Notable Remarks:**
 - Contributed to authoring the **Iranian National Building Code - Part 11**
 - Completed one-year **on-site internship** in excavation, concrete casting, foundation, structure and ceiling casting for building projects
- **GPA:** 18.19 (out of 20) - **Ranked 1st** among 60 others

»»» Experience

2017/10 - 2019/06 **Guest Researcher** EPFL, Lausanne, Switzerland

- » **Project 1:** Fatigue Behavior of a Two-component **SIKA** Adhesive under Various Stress Ratios
- » **Main Responsibilities:** Managing the Conduct of Fatigue Experiments and Performing the Measurements and Results Post-Processing:
 - Design and fabrication of specimens
 - Configuration of test setup and **video-extension technique** & conducting the tests
 - Analysis of data using **Python scripting** & preparing the technical reports
- » **Project 2:** Mechanical Property Determination of a Newly Developed Adhesive by **SIKA**
- » **Main Responsibilities:** Experiment Conduct and Analysis of Data:
 - Performed **DMA experiments** to determine **glassy transition temperature** of the adhesive
 - Conducted **tensile experiments** under **various displacement rates and temperatures**
 - **Data analysis** to gain insights on **temperature- and rate-dependent behavior** of the adhesive
 - Preparation of technical reports and presentations for the provider company
- » **Project 3:** CCLAB GFRP Conference Table with Foam Core
- » **Main Responsibilities:** Numerical **Analysis** and **Design** of the GFRP Conference Table:
 - Numerical analysis of the **egg-shaped GFRP table** in **Abaqus**
 - **Optimization of the GFRP layers** in top and bottom sheets and **design of the foam core thickness** to ensure stability and minimizing deflection in the cantilevered end
- » **Notable Remarks:** Member of the operations committee for **ICSS-12 Conference** at **EPFL**

2014/09 - 2017/09 **Research Assistant** Amirkabir Univ. of Tech., Iran

- » **Project:** Seismic Behavior of Composite Shear Walls
- » **Main Research & Teaching Activities:**
 - Designed an optimal steel-concrete composite shear wall
 - Designed test setup and conducted experiments
 - Performed numerical analysis of the tested shear wall in **Abaqus**
- » **Attended Courses:** Structural Reliability & Safety (**17.6 out of 20**); Control of Structures (**18.25 out of 20**); Seismic Design of Structures; Creep, Fatigue, and Fracture Mechanics
- » **Notable Activities:**
 - Member of operations committee for **International Bridge Conference** ([Jan. 2015](#)), and **New Materials & Structures in Civil Engineering** ([Oct. 2016](#)) at Amirkabir Univ. of Tech.
 - Assistant editor in **Amirkabir Journal of Science and Research (AJSR)** ([Oct. 2015 - Oct. 2017](#))
 - Contributed to translation and authoring of a book entitled "Strengthening of Reinforced Concrete using FRP Bonds ([in Persian](#))"

2016/04 - 2016/10 **R&D Engineer (Part Time - 40%)** Vandidad Co., Iran

- » **Project:** Leveraging Ultra-Light Structural Nano-Concrete
- » **Main Responsibilities:**
 - Optimized the design of the nano-particle concrete mixture
 - Conducted and managed QC experiments on the concrete samples

Skills

Language Skills

English: C2

French: B1 (*Learning*)

Persian: Native

Programming-related Skills

Python

C++

Version Control Systems (Git)

Cloud-Based Platforms

Amazon Web Services (AWS)

Python Related Knowledge and Skills

SciKit-Learn

Keras

TensorFlow

SciPy

Matplotlib

Seaborn

Numpy

Pandas

Scientific, Research and Misc. Programs

MATLAB

OpenSees

ABAQUS

VIC3D

Misc.

Experimental Data Mngmt.

Data Wrangling

Adhesive Materials

Material Testing

Data-driven Optimization

Fatigue Analysis

Certificates

March 2023

Certified Cloud Practitioner

Amazon Web Services

➤ **AWS Foundational Certification:** AWS Cloud concepts, services, and terminology

➤ Main Topics Covered:

- Cloud computing, storage, scalability and availability on AWS Cloud
- Core AWS services and their use cases; security best practices; billing and pricing models; how cloud impacts the businesses

December 2022

Artificial Intelligence Nanodegree

UDACITY

➤ **3-Month Duration:** Python programming for **foundational AI algorithms**; Mastering classical AI algorithms, Bayes Networks, Hidden Markov Models, and more.

➤ Main Topics Covered:

- **Artificial Intelligence and Classical Search:** Sudoku solver in **Python** for **constraint satisfaction problems**; Mastering classical graph informed and uninformed **search algorithms**
- **Automated Planning:** Representing general problem domains with symbolic logic; Building a **forward planning agent** to find **optimal plans** for the agent's goals.
- **Optimization Problems:** Solving **iterative improvement optimization problems** using gradient-free methods
- **Adversarial Search:** Developing an **adversarial game playing agent** for decision making in competitive environments using the minimax theorem
- **Fundamentals of Probabilistic Graphical Models:** Using **Bayes Nets** to represent complex probability distributions; Leveraging **Hidden Markov Models** for pattern recognition.

January 2019

Applied Data Science: ML Diploma

EPFL Extension School, Switzerland

➤ **4-Month Duration:** Mastering the techniques and tools for data acquisition, transformation and predictive analysis, ensuring the ability to work with the entire data pipeline.

➤ Main Topics Covered:

- **Applied Data Analysis with Python:** Data cleaning, manipulation, and feature engineering in Python
- **Applied Machine Learning:** Advanced machine learning techniques, deep learning and convolutional neural networks